
Electronic Thesis and Dissertation Repository

8-23-2016 12:00 AM

Photo-Isomerizable Self-Complementary Hydrogen Bond Arrays

Iamnica Janic Linares Mendez
The University of Western Ontario

Supervisor
James A. Wisner
The University of Western Ontario

Graduate Program in Chemistry
A thesis submitted in partial fulfillment of the requirements for the degree in Doctor of
Philosophy
© Iamnica Janic Linares Mendez 2016

Follow this and additional works at: <https://ir.lib.uwo.ca/etd>

 Part of the [Organic Chemistry Commons](#), and the [Physical Chemistry Commons](#)

Recommended Citation

Linares Mendez, Iamnica Janic, "Photo-Isomerizable Self-Complementary Hydrogen Bond Arrays" (2016).
Electronic Thesis and Dissertation Repository. 3999.
<https://ir.lib.uwo.ca/etd/3999>

This Dissertation/Thesis is brought to you for free and open access by Scholarship@Western. It has been accepted for inclusion in Electronic Thesis and Dissertation Repository by an authorized administrator of Scholarship@Western. For more information, please contact wlsadmin@uwo.ca.

Abstract

The combination of photoswitchable molecules and supramolecular complexes has provided valuable contributions to materials science. The scope of applications where these smart materials could contribute drives the efforts toward developing systems that provide a range of responses, sensibilities and stabilities. This thesis exploits the use of a well-known photochromic system in a self-complementary hydrogen bond array; i.e. the azo group, R-N=N-R. The novelty of the approach described in this thesis resides in the double function of the azo group within the array: as a hydrogen bond acceptor site and as a functional element that promotes a structural change capable of disrupting the complexation equilibrium when irradiated with light.

The photo-isomerizable self-complementary hydrogen bond arrays presented in this document are obtained by a general and practical synthetic method from inexpensive starting materials. Their self-complementary recognition was corroborated by ^1H NMR dilution experiments and single crystal X-ray structures. In the course of these studies, it was observed that the electron withdrawing character of the substituents employed, the presence of solvent-solute interactions and the disposition of the binding sites have a significant effect over the dimerization constants obtained.

Likewise, some photochemical properties of these systems were studied, such as their UV-Vis absorption spectra, the *cis/trans* ratio at their photostationary state after *trans*- to *cis*-photoisomerization, the stability of the complexes present in solution after UV- light irradiation, and the decay profile of their *cis*-isomeric forms. The distribution profiles (or speciation diagrams) of monomers and dimers in toluene- d_8 solutions at different *cis/trans*

ratios of four of our photoswitchable self-complementary hydrogen bond arrays were obtained. From these speciation diagrams we were able to confirm that the mathematical approach employed to describe the systems' equilibria provided us a reliable approximation of all complexation constants in solution after photoisomerization.

Keywords

azoheteroaromatic compounds, photoisomerization, self-complementary arrays, smart materials, hydrogen bond.

Co-Authorship Statement

Jeffrey S. Pleizier synthesized and crystallized compound **4a**. All X-ray crystal structure were solved by Dr. Paul D. Boyle (X-Ray facility manager). Mass spectrometry of all compounds presented in this work was carried out by Doug Hairsine (Mass Spec facility manager).

Scheme 1.5 and Figure1.13 were reproduced with permission from: John Wiley & Sons (License number 3910300843589) and Royal Society of Chemistry (License number 3910310008235)

All of the remaining work in this thesis was performed by the author herself.

Acknowledgments

“Science, my lad, is made up of mistakes, but they are mistakes which it is useful to make, because they lead little by little to the truth”

-Jules Verne

This thesis is the result of a five years journey where I had the opportunity to work and learn in the company of many people. I want to take these lines to publicly acknowledge their contribution to this project.

Foremost, I want to thank Professor James A. Wisner for letting me work under his supervision, for trusting in my capabilities to overcome all daily difficulties. His understanding, encouragement and patience towards my performance as a Chemist have created a significant impact in my professional development. I take to the heart all the advice and experience I earned working for him.

Likewise, I am thankful to the members of the examination committee: Dr. Paul J. Ragona, Dr. Michael A. Kerr, Dr. Giovanni Fanchini and Dr. Donal Macartney. Thanks for the time employed reading and outlining the areas where I can polish the quality of the work presented. To Dr. Paul J. Ragona for keeping track of my progress all this time and being coherent with the forms and procedures that rule the Graduate Program in Chemistry. To Dr. Michael A. Kerr for pushing me to think outside the box during the courses I had the opportunity to take with him.

I am grateful to Bhanu Mudrboyina and Jeffrey S. Pleizier (former and present labmates at Professor Wisner’s group) for their warm welcome into the lab and their guidance. In

particular, I want to thank Jeff for his patience over 5 years of working side by side providing ideas and comments on this project and for all the fun we had (regardless that most of the times it was he making fun of my “Mexicanity”). I am glad to have you at my side sharing the ups and downs of grad school.

The project I am presenting through these pages would not be possible without all the faculty and staff from the Chemistry Department. Thanks to Mathew Willans (NMR facility manager), Doug Hairsine (Mass Spec facility manager) and Paul D. Boyle (X-Ray facility manager) for their aid towards in the characterization of the compounds obtained. Likewise, I want to thank to Dr. Estefania Ruiz for her assistance in the mathematical model approach and the statistics figures employed.

Por último, y no por ello menos importante, a mis padres Lucia Méndez Delgado y José Luis Linares García por apoyarme en estos ocho años lejos de casa. Por mantener una estrecha comunicación constante con la cual los siento tan cerca como si estuvieran todos los días a mi lado. Por insistir en enseñarme a perseguir mis sueños con la vista fija en la meta y la mente abierta a aprender de los errores que tendré que cometer para madurar y salir adelante. Y por nunca perder la fe en mí, a pesar de que en veces yo misma no la tenga. A mi hermano Elder Linares Méndez por enseñarme a aferrarme menos a lo que tengo y puedo lograr, porque, citando sus palabras, “*eso no es todo lo que me define*”. Gracias por ser mi cómplice y confidente.

Table of Contents

Abstract	i
Co-Authorship Statement.....	iii
Acknowledgments.....	iv
Table of Contents	vi
List of Tables	x
List of Figures	xiii
List of Schemes.....	xxv
List of Abbreviations and Symbols.....	xxviii
Chapter 1	1
1 Introduction	1
1.1 Supramolecular Chemistry.....	1
1.2 Molecular Recognition.....	2
1.3 Intermolecular Interactions	3
1.4 Hydrogen Bond.....	5
1.4.1 Definition.....	5
1.4.2 Classification.....	6
1.4.3 Strength of the Hydrogen Bond in Supramolecular Arrays.....	8
1.5 Supramolecular Complexes.....	14
1.6 Preorganization	16
1.7 Tautomerization	18
1.8 Solvent Effect.....	21
1.9 Smart Materials.....	24
1.10 Supramolecular Photochemistry.....	25
1.11 Photoswitches	25

1.11.1 Photo Stationary State.....	32
1.11.2 Fatigue or Photodegradation.....	34
1.12 Azoaromatic Compounds.....	36
1.12.1 Azoaromatic Compounds in Self-Assembly Systems.....	41
1.13 Scope of the Thesis.....	45
1.14 References.....	46
Chapter 2.....	53
2 Synthesis and Characterization of Photoswitchable Self-Complementary DDAAA Hydrogen Bond Arrays.....	53
2.1 Introduction.....	53
2.2 Design of Photoswitchable Self-Complementary Hydrogen Bond Arrays.....	57
2.3 Results and Discussion.....	61
2.3.1 Synthesis of Photoswitchable Self-Complementary Hydrogen Bond Arrays.....	61
2.3.2 ¹ H NMR Dilution Experiments: Stability of <i>trans-trans</i> dimers.....	65
2.3.3 X-Ray Analysis of Self-Complementary Arrays.....	79
2.4 Summary and Conclusion.....	94
2.5 Experimental Methodology.....	95
2.5.1 Generalities.....	95
2.5.2 Synthetic Methods.....	97
2.5.3 ¹ H NMR Dilution Experiments.....	128
2.6 References.....	129
Chapter 3.....	132
3 Photochemistry of Photoswitchable Self-Complementary DDAAA Hydrogen Bond Arrays.....	132
3.1 Introduction.....	132
3.2 Results and Discussion.....	139

3.2.1	UV-Vis Characterization	139
3.2.2	Photoisomerization <i>Trans</i> to <i>Cis</i>	145
3.2.3	Complexation Constants in Solution After Photoisomerization.....	151
3.2.4	<i>Cis</i> to <i>Trans</i> Reversion Kinetics	174
3.3	Summary and Conclusions	178
3.4	Experimental Methodology	179
3.4.1	Generalities	179
3.4.2	Photostationary State Experiments	180
3.4.3	Synthesis of (Z)-4-(pyridin-2-yl diazenyl)-1,3,5-triazin-2-amine derivatives ((<i>c</i>)- 4c , (<i>c</i>)- 4f and (<i>c</i>)- 4k).	181
3.4.4	¹ H NMR Reversion Experiments.....	181
3.5	References.....	182
Chapter 4	184
4	Synthesis and Characterization of Second Generation Photoswitchable Self-Complementary DDAAA Hydrogen Bond Arrays.....	184
4.1	Introduction: Design of Second Generation Photoswitchable Self-Complementary Hydrogen Bond Arrays.	184
4.2	Results and Discussion.	190
4.2.1	Synthesis of Second Generation Photoswitchable Self-Complementary Hydrogen Bond Arrays.	190
4.2.2	¹ H NMR Dilution Experiments: Stability of <i>trans-trans</i> dimers.....	192
4.2.3	X-Ray Analysis of Self-Complementary Arrays	201
4.2.4	UV-Vis Characterization	215
4.2.5	Photoisomerization <i>Trans</i> to <i>Cis</i>	218
4.2.6	Complexation Constants in Solution After Photoisomerization.....	224
4.2.7	<i>Cis</i> to <i>Trans</i> Reversion Kinetics	234
4.3	Summary and Conclusions	237
4.4	Experimental Methodology	239

4.4.1	Generalities	239
4.4.2	Synthetic Methods	240
4.4.3	Synthesis of (Z)-4-butoxy-6-((2-methoxyphenyl)diazenyl)-1,3,5-triazin-2-amine, (c)-7c.	246
4.5	References.....	247
Chapter 5	248
5	Conclusions and Outlook.....	248
5.1	Conclusions.....	248
5.2	Outlook	250
Curriculum Vitae	252

List of Tables

Table 1.1 Intermolecular Interactions.....	4
Table 1.2 Categories of hydrogen bond interaction and some of their important properties. ..	6
Table 1.3 Comparison of the effect of electron-withdrawing functional groups attached to DDD units on the association constant (K_a) in CDCl ₃ at 298 K.....	10
Table 1.4 Association constant of the six modalities of the 1·2 complex in CDCl ₃ at 296 K.....	42
Table 2.1 Reactants, yields of intermediates 2a-p and overall yields of photoswitchable self-complementary hydrogen bond arrays 4a-p	64
Table 2.2 Dimerization constants, free energies of dimerization, calculated chemical shifts of monomer (δ_m) and dimer (δ_d) species studied, and the total change in chemical shift (Δδ_{max}) in CDCl ₃ at 298 K.....	68
Table 2.3 Dimerization constants, free energies of dimerization, calculated chemical shifts of monomer (δ_m) and dimer (δ_d) species studied, and the total change in chemical shift (Δδ_{max}) in Toluene- <i>d</i> ₈ at 298 K.....	76
Table 2.4 Crystallographic parameters for 4a , 4d , 4f and 4k crystals.....	80
Table 2.5 Hydrogen bond distances and angles of complex 4a·4a X-ray crystal structure data.....	82
Table 2.6 Hydrogen bond distances and angles of complex 4d·4d X-ray from the crystal structure data.....	85
Table 2.7 Hydrogen bond distances and angles of complex 4f·4f X-ray from the crystal structure data.....	88
Table 2.8 Hydrogen bond distances and angles of complex 4k·4k X-ray from the crystal structure data.....	91

Table 2.9 Summary of hydrogen bond distances, intramolecular and intermolecular ring's planes angles of 4a , 4d , 4f and 4k from their crystal structure data.	93
Table 3.1 Characteristic $n \rightarrow \pi^*$ and $\pi \rightarrow \pi^*$ transition bands of derivatives (t)- 4a-p from UV-Vis spectroscopy in acetonitrile at 298 K.	141
Table 3.2 Characteristic $n \rightarrow \pi^*$ and $\pi \rightarrow \pi^*$ transition bands of derivatives (c)- 4 from UV-Vis spectroscopy in acetonitrile at 298 K.	142
Table 3.3 <i>Trans</i> to <i>cis</i> interconversion yields at PSS after irradiation with UV Light (360 nm) at 298 K.	148
Table 3.4 Complexation constants, free energies of complexation and chemical shifts of the <i>trans</i> -isomer in the complex δ_{tc} studied in Toluene- <i>d</i> ₈ (at 298 K).	164
Table 3.5 Rate constants calculated for <i>cis</i> to <i>trans</i> thermal reversion of derivatives 4c , 4f and 4k studied in Toluene- <i>d</i> ₈ at 298 K.	175
Table 4.1 Ranges and mean values of the lengths (Å) and angles (°) of hydrogen bonds in crystal structures of purines and pyrimidines, nucleosides, and nucleotides. ^a	188
Table 4.2 Reactants and overall yields of photoswitchable self-complementary hydrogen bond arrays 7	191
Table 4.3 Dimerization constants, free energies of dimerization, chemical shifts of monomer (δ_m) and dimer (δ_d) species studied, and the total change in the chemical shift ($\Delta\delta_{max}$) in CDCl ₃ at 298 K.	192
Table 4.4 Dimerization constants, free energies of dimerization, chemical shifts of monomer (δ_m) and dimer (δ_d) species studied, and the total change in the chemical shift ($\Delta\delta_{max}$) in toluene- <i>d</i> ₈ at 298 K.	198
Table 4.5 Crystallographic parameters for 7c , 7f , 7k and 7n crystals.	202
Table 4.6 Hydrogen bond distances and angles of complex 7c · 7c X-ray crystal structure data.	204

Table 4.7 Hydrogen bond distances and angles of complex 7f·7f X-ray from the crystal structure data.	207
Table 4.8 Hydrogen bond distances and angles of the array 7k X-ray from the crystal structure data.	211
Table 4.9 Hydrogen bond distances and angles of complex 7n·7n X-ray from the crystal structure data.	213
Table 4.10 Summary of hydrogen bond distances, intramolecular and intermolecular ring's planes angles of 7c , 7f , 7k and 7n from their crystal structure data.	214
Table 4.11 Comparison of intermolecular distances in 4f and 7f dimer structures in the solid state.	215
Table 4.12 Characteristic $n \rightarrow \pi^*$ and $\pi \rightarrow \pi^*$ transition bands of derivatives (t)- 7 from UV-Vis spectroscopy in acetonitrile at 298 K.	216
Table 4.13 Characteristic $n \rightarrow \pi^*$ and $\pi \rightarrow \pi^*$ transition bands of derivative (c)- 7c from UV-Vis spectroscopy in acetonitrile at 298 K.	218
Table 4.14 <i>Trans</i> to <i>cis</i> interconversion yields at PSS after irradiation with UV Light (360 nm) at 298 K.	221
Table 4.15 Dimerization constant ($K_{t,t}$), complexation constant ($K_{t,c}$), free energy of dimerization ($\Delta G_{t,t}$), free energy of complexation ($\Delta G_{t,c}$), calculated chemical shifts of monomer (δ_m), dimer (δ_d) and complex (δ_{tc}) species studied in Toluene- d_8 at 263 K.	232

List of Figures

Figure 1.1 Types of hydrogen bond arrays: Linear, Bent, Donating Bifurcated, Accepting Bifurcated, Trifurcated, and Three Center Bifurcated.	8
Figure 1.2 DDD-AAA hydrogen bond arrays studied by Wisner and coworkers.	9
Figure 1.3 The effect of the number of hydrogen bonding sites on the stability (K_a) of different arrays.	11
Figure 1.4 Hydrogen Bond Arrays studied by Jørgensen and Pranata.	12
Figure 1.5 Secondary hydrogen bond interactions in triply hydrogen bonded arrays.	13
Figure 1.6 Triple hydrogen bond complexes studied by Zimmerman and Murray.	13
Figure 1.7 Nucleotide base pairs in DNA.	15
Figure 1.8 (A) A guanidine tetramer reported by Sundquist and Klung; (B) A molecular duplex reported by Chu and coworkers.	15
Figure 1.9 Murray and Zimmerman DAA-ADD complex structures. Association constants (K_{ass}) calculated in a 5% DMSO- d_6 - $CDCl_3$ solvent system.	17
Figure 1.10 Generalized profile of hydrogen bond interactions between solute and solvent.	23
Figure 1.11 Absorption spectra of A and B.	33
Figure 1.12 Cyclization plots of a (A) fatigue resistant material and (b) a non-fatigue resistant material after 10 cycles	35
Figure 1.13 Changes in the absorption spectrum of <i>trans</i> -azobenzene (<i>E</i> isomer) upon irradiation with 316 nm light.	37
Figure 1.14 Ghadiri's peptide photoswitchable system.	44
Figure 2.1 Theoretical plot of the relation between association constant and degree of polymerization as a function of concentration of a self-associating (A-A) monomer.	54

Figure 2.2 Examples of aromatic azo compounds that display intramolecular hydrogen bonds.	56
Figure 2.3 (A) Schematic representation of 2,6-diaminopyridinium tetraphenylborate-1,2-bis(5,7-dimethyl-1,8-naphthyridin-2-yl)diazene (1/1) complex. (B) Solid state structure obtained by X-Ray diffraction of single crystal.....	56
Figure 2.4 Structures of the different locations of a donor group in an azoheteroaromatic backbone and their putative dimers using six-membered azoheteroaromatics.....	59
Figure 2.5 (A) Selective systematic substitution of cyanuric chloride at different temperatures. (B) Selective systematic substitution strategy employed.....	60
Figure 2.6 ¹ H NMR spectra displaying the concentration-dependent behavior of 4o in CDCl ₃ at 298 K. (i) 5.59 x 10 ⁻⁴ M, and (ii) 1.61 x 10 ⁻² M.....	69
Figure 2.7 ¹ H NMR spectra displaying the concentration-dependent behavior of 4f in Toluene- <i>d</i> ₈ at 298 K. (i) 2.45 x 10 ⁻³ M (H _a signal covered by the toluene reference signal), (ii) 8.56 x 10 ⁻³ M, and (iii) 1.61 x 10 ⁻² M.	69
Figure 2.8 Amino's proton assignment based on chemical shift in compounds 4a-p	70
Figure 2.9 Dimerization isotherm of 4a with K_{t-t} value and free energy calculated from fitting of the data to a 1:1 dimerization model. Blue, green and red dots correspond to first, second and third separate dilution experiments, respectively. Solid line corresponds to the theoretical dilution curve obtained from the average K_{t-t} of three separate dilution experiments.....	71
Figure 2.10 Dimerization isotherm of 4n with K_{t-t} value and free energy calculated from fitting of the data to a 1:1 dimerization model. Blue, green and red dots correspond to first, second and third separate dilution experiments, respectively. Solid line corresponds to the theoretical dilution curve obtained from the average K_{t-t} of three separate dilution experiments.	72
Figure 2.11 Plot of ΔG_{t-t} vs $\Delta \delta_{max}$ for derivatives 4a-p in CDCl ₃ at 298 K. Dotted line corresponds to the linear least squares correlation for derivatives 4a-p excluding 4a (r = -0.81396).....	73

Figure 2.12 Plot of ΔG_{t-t} vs σ_m of derivatives 4a , 4c , 4d , 4f , 4i , 4k and 4n in $CDCl_3$ at 298 K. Dotted line corresponds to the least squares correlation line ($r = -0.9861$).	74
Figure 2.13 Plot of ΔG_{t-t} vs I of derivatives 4a , 4c , 4d , 4f , 4i , 4k and 4n in $CDCl_3$ at 298 K. Dotted line corresponds to the least squares correlation line ($r = -0.9848$).	74
Figure 2.14 Dimerization isotherm of 5c with K_{t-t} value and free energy calculated from fitting of the data to a 1:1 dimerization model. Blue, green and red dots correspond to first, second and third separate dilution experiments, respectively. Solid line corresponds to the theoretical dilution curve obtained from the average K_{t-t} of three separate dilution experiments.....	78
Figure 2.15 Dimerization isotherm of 4c with K_{t-t} value and free energy calculated from fitting of the data to a 1:1 dimerization model. Blue, green and red dots correspond to first, second and third separate dilution experiments, respectively. Solid line corresponds to the theoretical dilution curve obtained from the average K_{t-t} of three separate dilution experiments.....	78
Figure 2.16 Stick representation of the X-ray crystal structure of 4a dimer with intermolecular hydrogen bonds indicated (dashed orange lines). Blue, grey and white correspond to nitrogen, carbon and hydrogen atoms, respectively.	82
Figure 2.17 Stick representation of the X-ray crystal structure of 4d dimers with intermolecular hydrogen bonds indicated (dashed orange lines). Blue, grey, white and red correspond to nitrogen, carbon, hydrogen and oxygen atoms, respectively.....	84
Figure 2.18 Stick representation of the X-ray crystal structure of 4d with C-H \cdots N interactions indicated (dashed orange lines). Blue, grey, white and red correspond to nitrogen, carbon, hydrogen and oxygen atoms, respectively.	86
Figure 2.19 Stick representation of the X-ray crystal structure of 4f dimer with intermolecular hydrogen bonds indicated (dashed orange lines). Blue, grey, white and yellow correspond to nitrogen, carbon, hydrogen and sulfur atoms, respectively.	88
Figure 2.20 Stick representation of the X-ray crystal structure of 4f with indicating C-H \cdots N interactions (dashed orange lines). Blue, grey, white and yellow correspond to nitrogen, carbon, hydrogen and sulfur atoms, respectively.....	89

Figure 2.21 Stick representation of the X-ray crystal structure of 4k dimers with intermolecular hydrogen bonds indicated (dashed orange lines). Blue, grey, white and red correspond to nitrogen, carbon, hydrogen and oxygen atoms, respectively.....	91
Figure 2.22 Stick representation of the X-ray crystal structure of 4k with indicating C-H \cdots π interactions (dashed orange lines). Blue, grey, white and red correspond to nitrogen, carbon, hydrogen and oxygen atoms, respectively.	92
Figure 2.23 Donor and acceptor sites assignment of 4a , 4d , 4f and 4k dimers.....	93
Figure 3.1 Normalized UV-Vis Absorption Spectra of derivatives (t)- 4a-p in acetonitrile at 298 K.....	140
Figure 3.2 UV-Vis absorption spectra of (c)- 4c and its thermal reversion to (t)- 4c in acetonitrile at 298 K (4c total concentration = 1.71×10^{-4} M).	143
Figure 3.3 UV-Vis absorption spectra of (c)- 4f and its thermal reversion to (t)- 4f in acetonitrile at 298 K (4f total concentration = 1.67×10^{-4} M).....	144
Figure 3.4 UV-Vis absorption spectra of (c)- 4k and its thermal reversion to (t)- 4k in acetonitrile at 298 K (4k total concentration = 3.72×10^{-5} M).....	145
Figure 3.5 ^1H NMR spectra displaying derivative 4p at PSS in CDCl_3 at 298 K. RX = 4'-tritylphenoxy.	146
Figure 3.6 ^1H NMR spectra displaying derivative 4d at (i) PSS, and (ii) after complete <i>cis</i> - to <i>trans</i> - thermal reversion in CD_3CN at 298 K. RX = <i>n</i> -octyloxy.	147
Figure 3.7 Cyclization plot of 4c ($[\mathbf{4c}] = 9.1 \times 10^{-4}$ M). Purple areas correspond to the N-H chemical shift change after UV light irradiation (centered at 360 nm for 1h). White areas correspond to the N-H chemical shift change after visible light irradiation ($\lambda > 400$ nm for 10 minutes). Yellow area correspond to the N-H chemical shift observed after thermal reversion of the solution over 72h.....	149
Figure 3.8 Chemical structures of intermediates 1 and 2b	155

Figure 3.9 Relationship between K_{t-c} and δ_{tc} . $\delta_{obs} = 5.61$ ppm at a *cis/trans* ratio = 1.85 for a total concentration $[4c] = 3.42 \times 10^{-3}$ M. 158

Figure 3.10 1H NMR spectra displaying the concentration-dependent behavior of **4c** in toluene-*d*₈ at 298 K. Total concentration $[4c] = 3.27 \times 10^{-3}$ M, (i) $[c]_0/[t]_0 = 1.73$ (ii) $[c]_0/[t]_0 = 0.93$, (iii) $[c]_0/[t]_0 = 0.59$, (iv) $[c]_0/[t]_0 = 0.33$, (v) $[c]_0/[t]_0 = 0.22$, and (vi) $[c]_0/[t]_0 = 0$ 159

Figure 3.11 Relationship between δ_{obs} vs $[t]_0$ during a thermal reversion experiment of derivative **4c**. Red dots correspond to a reversion experiments ($[4c] =$ and 2.90×10^{-3} M). Solid line corresponds to the theoretical dilution curve obtained from the average of three separate dilution experiments with (*t*)-**4c**. 160

Figure 3.12 Top Plot: Theoretical K_{t-c} vs δ_{tc} curves for the set of δ_{obs} from the least squares line that describes third reversion experiment of derivative **4c** (Green dots at Figure 3.10, $[4c] = 3.42 \times 10^{-3}$ M). Bottom Plot: Theoretical *CV* vs δ_{tc} curve for the set of K_{t-c} calculated from the third reversion experiment of derivative **4c** (Green dots at Figure 3.8, $[4c] = 3.42 \times 10^{-3}$ M). 161

Figure 3.13 Top Plot: K_{t-c} vs δ_{tc} curves for the set of δ_{obs} from the third reversion experiment of derivative **4c** (green dots at Figure 3.10, $[4c] = 3.42 \times 10^{-3}$ M). Bottom Plot: *CV* vs δ_{tc} curve for the set of K_{t-c} calculated from the third reversion experiment of derivative **4c** (Green dots at Figure 3.8, $[4c] = 3.42 \times 10^{-3}$ M). 162

Figure 3.14 Relationship between δ_{obs} vs $[t]_0$ for three reversion experiments of derivative **4c**. Blue, red and green dots correspond to first, second and third separate reversion experiments, respectively. Blue, red and green dashed lines correspond to the calculated δ_{obs} vs $[t]_0$ plots for the first, second and third reversion experiments with the K_{t-c} and δ_{tc} values with minimum *CV* (sample standard deviations of 0.003, 0.003 and 0.008 ppm, respectively). Solid line corresponds to the dilution curve obtained for (*t*)-**4c** from the average of three separate dilution experiments. 164

Figure 3.15 Relationship between δ_{obs} vs $[t]_0$ for three reversion experiments of derivative **4f**. Blue, red and green dots correspond to first, second and third separate reversion experiments, respectively. Blue, red and green dashed lines correspond to the calculated δ_{obs}

vs $[t]_0$ plots for the first, second and third reversion experiments with the K_{t-c} and δ_{tc} values with minimum CV (sample standard deviations of 0.01, 0.005 and 0.02 ppm, respectively). Solid line corresponds to the dilution curve obtained for (t)-**4f** from the average of three separate dilution experiments. 165

Figure 3.16 Relationship between δ_{obs} vs $[t]_0$ for three reversion experiments of derivative **4k**. Blue, red and green dots correspond to first, second and third separate reversion experiments, respectively. Blue, red and green dashed lines correspond to the calculated δ_{obs} vs $[t]_0$ plots for the first, second and third reversion experiments with the K_{t-c} and δ_{tc} values with minimum CV (sample standard deviations of 0.03, 0.02 and 0.04 ppm, respectively). Solid line corresponds to the dilution curve obtained for (t)-**4k** from the average of three separate dilution experiments..... 166

Figure 3.17 Structural similarities between *trans-trans*, *cis-cis* dimers and the *trans-cis* complex in mixed solution of **4a-p**..... 167

Figure 3.18 Relationship between δ_{obs} vs $[t]_0$ through three reversion experiments of the derivative **4k**. Blue, red and green dots correspond to first, second and third separated reversion experiments, respectively. Blue, red and green dashed lines correspond to the predicted δ_{obs} vs $[t]_0$ plots for the first, second and third reversion experiments with the expected ΔG values (sample standard deviations of 0.05, 0.12, 0.11 ppm, respectively). Solid line corresponds to the dilution curve obtained from the average of three separated dilution experiments. 169

Figure 3.19 Potential N-H/ π intermolecular interactions in (A) **4k** *trans-cis* complex structure; and (B) **5k** dimer structure..... 169

Figure 3.20 Theoretical speciation diagram of derivative **4c** at the third reversion experiment (green dots at Figure 3.10, $[4c] = 3.42 \times 10^{-3}$ M) at 298 K. Solid lines correspond to the first scenario ($K_{c-c} = 0$) and dotted-star marked lines correspond to the second scenario ($K_{c-c} = 18$ M⁻¹) respectively. Blue, red, orange, yellow and brown colors correspond to $[t]$, $[t \cdot t]$, $[t \cdot c]$, $[c]$, and $[c \cdot c]$, respectively. Black dotted line corresponds to maximum *cis/trans* ratio in reversion experiment. Grey dotted line corresponds to *cis/trans* ratio at PSS..... 171

Figure 3.21 Theoretical speciation diagram of derivative **4f** at the third reversion experiment (green dots at Figure 3.14, $[4f] = 2.35 \times 10^{-3} \text{ M}$) at 298 K. Solid lines correspond to the first scenario ($K_{c-c} = 0$) and dotted-star marked lines correspond to the second scenario ($K_{c-c} = 26 \text{ M}^{-1}$) respectively. Blue, red, orange, yellow and brown colors correspond to $[t]$, $[t \cdot t]$, $[t \cdot c]$, $[c]$, and $[c \cdot c]$, respectively. Black dotted line corresponds to maximum *cis/trans* ratio in reversion experiment. Grey dotted line corresponds to *cis/trans* ratio at PSS..... 172

Figure 3.22 Theoretical speciation diagram of derivative **4k** at the third reversion experiment (green dots at Figure 3.15, $[4k] = 1.84 \times 10^{-3} \text{ M}$) at 298 K. Solid lines correspond to the first scenario ($K_{c-c} = 0$) and dotted-star marked lines correspond to the second scenario ($K_{c-c} = 46 \text{ M}^{-1}$) respectively. Blue, red, orange, yellow and brown colors correspond to $[t]$, $[t \cdot t]$, $[t \cdot c]$, $[c]$, and $[c \cdot c]$, respectively. Black dotted line corresponds to maximum *cis/trans* ratio in reversion experiment..... 173

Figure 3.23 Decay profiles of (c)-**4c** isomer in toluene- d_8 at 298 K. Blue, red and green dots correspond to first, second and third separate reversion experiments ($r = -0.9973, -0.9982$ and -0.9981) respectively. Blue, red and green dashed lines correspond to the calculated values obtained by linear least squares regression of the first, second and third separate reversion experiments, respectively..... 175

Figure 3.24 Decay profiles of (c)-**4f** isomer in toluene- d_8 at 298 K. Blue, red and green dots correspond to first, second and third separate reversion experiments ($r = -0.9995, -0.9981$ and -0.9987) respectively. Blue, red and green dashed lines correspond to the calculated values obtained by linear least squares regression of the first, second and third separate reversion experiments, respectively..... 176

Figure 3.24 Decay profiles of (c)-**4k** isomer in toluene- d_8 at 298 K. Blue, red and green dots correspond to first, second and third separate reversion experiments ($r = -0.9954, -0.9907$ and -0.9962) respectively. Blue, red and green dashed lines correspond to the calculated values obtained by linear least squares regression of the first, second and third separate reversion experiments, respectively..... 177

Figure 4.1 Average N-H...N(pyridine) angle in dimer structures of **4** observed in the solid state. 185

Figure 4.2 Proposed design for second generation photoswitchable self-complementary DDAAA hydrogen bond arrays.	186
Figure 4.3 Dimerization isotherm of 7c with K_{t-t} value and free energy calculated from fitting of the data to a 1:1 dimerization model. Blue, green and red dots correspond to first, second and third separate dilution experiments, respectively. Solid line corresponds to the theoretical dilution curve obtained from the average K_{t-t} of three separate dilution experiments.....	193
Figure 4.4 Dimerization isotherm of 7g with K_{t-t} value and free energy calculated from fitting of the data to a 1:1 dimerization model. Blue, green and red dots correspond to first, second and third separate dilution experiments, respectively. Solid line corresponds to the theoretical dilution curve obtained from the average K_{t-t} of three separate dilution experiments.....	194
Figure 4.5 Correlation plot of $\ln K_{t-t}$ vs $\Delta\delta_{max}$ for all derivatives 7 in CDCl ₃ at 298 K (r = 0.8595).	195
Figure 4.6 Correlation plot of ΔG_{t-t} vs σ_m of derivatives 7c , 7f , 7g , 7i and 7k in toluene- <i>d</i> ₈ at 298 K. Dotted line corresponds to the least squares correlation line (r = -0.91784).	196
Figure 4.7 Correlation plot of ΔG_{t-t} vs <i>I</i> of derivatives 7c , 7f , 7g , 7i , and 7k in CDCl ₃ at 298 K. Dotted line corresponds to the least squares correlation line (r = -0.86027).	196
Figure 4.8 Dimerization isotherm of 7n with K_{t-t} value and free energy calculated from fitting of the data to a 1:1 dimerization model. Blue, green and red dots correspond to first, second and third separate dilution experiments, respectively. Solid line corresponds to the theoretical dilution curve obtained from the average K_{t-t} of three separate dilution experiments.....	197
Figure 4.9 Dimerization isotherm of 7c with K_{t-t} value and free energy calculated from fitting of the data to a 1:1 dimerization model. Blue, green and red dots correspond to first, second and third separate dilution experiments, respectively. Solid line corresponds to the theoretical dilution curve obtained from the average K_{t-t} of three separate dilution experiments.....	198
Figure 4.10 Dimerization isotherm of 7f with K_{t-t} value and free energy calculated from fitting of the data to a 1:1 dimerization model. Blue, green and red dots correspond to first, second	

and third separate dilution experiments, respectively. Solid line corresponds to the theoretical dilution curve obtained from the average $K_{t,t}$ of three separate dilution experiments..... 198

Figure 4.11 Stick representation of the X-ray crystal structure of **7c** dimer with intermolecular hydrogen bond indicated (dashed orange lines). Blue, grey, white and red correspond to nitrogen, carbon, hydrogen and oxygen atoms, respectively..... 204

Figure 4.12 Stick representation of the X-ray crystal structure of **7f** dimer A-A' with intermolecular hydrogen bonds indicated (dashed orange lines). Blue, grey, white, red and yellow correspond to nitrogen, carbon, hydrogen, oxygen and sulfur atoms, respectively.. 206

Figure 4.13 Stick representation of the X-ray crystal structure of **7f** dimer B-B' with intermolecular hydrogen bonds indicated (dashed orange lines). Blue, grey, white, red and yellow correspond to nitrogen, carbon, hydrogen, oxygen and sulfur atoms, respectively.. 207

Figure 4.14 Selected molecules in the crystal lattice of **7f**. Green and blue structures correspond to dimer A-A' and dimer B-B', respectively. 208

Figure 4.15 Stick representation of the X-ray crystal structure of **7f** with C-H...N interactions indicated (dashed orange lines). Blue, grey, white, red and yellow correspond to nitrogen, carbon, hydrogen, oxygen and sulfur atoms, respectively..... 208

Figure 4.16 Stick representation of the X-ray crystal structure of **7k** array with intermolecular hydrogen bond indicated (dashed orange lines). Blue, grey, white and red correspond to nitrogen, carbon, hydrogen and oxygen atoms, respectively. View perpendicular to *ab* plane. All C-H hydrogen atoms removed for clarity. 210

Figure 4.17 Stick representation of the X-ray crystal structure of **7k** layout with intermolecular hydrogen bond indicated (dashed orange lines). Blue, grey, white and red correspond to nitrogen, carbon hydrogen and oxygen atoms, respectively. View perpendicular to the *bc* plane. All C-H hydrogen atoms removed for clarity. 210

Figure 4.18 Stick representation of the X-ray crystal structure of **7n** dimer with intermolecular hydrogen bond indicated (dashed orange lines). Blue, grey, white, red and green correspond to nitrogen, carbon hydrogen oxygen and fluor atoms, respectively. 212

Figure 4.19 Donor and acceptor sites assignment of 7c , 7f , 7k and 7n dimers.....	213
Figure 4.20 Normalized UV-Vis Absorption Spectra of derivatives (t)- 7 in acetonitrile at 298 K.....	215
Figure 4.21 UV-Vis absorption spectra of (c)- 7c and its thermal reversion to (t)- 7c in acetonitrile at 298 K (7c total concentration = 1.26×10^{-4} M).	217
Figure 4.22 ^1H NMR spectra displaying derivative 7c at PSS in toluene- d_8 at 298 K. RX = <i>n</i> -butoxy.	219
Figure 4.23 ^1H NMR spectra displaying derivative 7c at PSS in toluene- d_8 at 298 K. RX = <i>n</i> -butoxy.	220
Figure 4.24 Cyclization plot of 7c ($[\mathbf{7c}] = 9.11 \times 10^{-4}$ M). Purple areas correspond to the N-H chemical shift change after UV light irradiation (centered at 360 nm for 1h). White areas correspond to the N-H chemical shift change after visible light irradiation ($\lambda > 400$ nm for 10 minutes). Yellow area correspond to the N-H chemical shift observed after thermal reversion of the solution over 72h	221
Figure 4.25 Complexation equilibria present in mixed <i>cis/trans</i> solutions of derivatives 7 in non-polar solvents.....	224
Figure 4.26 Dimerization isotherm of 7c with K_{t-t} value and free energy calculated from fitting of the data to a 1:1 dimerization model. Blue and green dots correspond to first and second separate dilution experiments, respectively. Solid line corresponds to the theoretical dilution curve obtained from the average K_{t-t} of two separate dilution experiments.....	227
Figure 4.27 ^1H NMR spectra displaying the concentration-dependent behavior of 7c in toluene- d_8 at 298 K. Total concentration $[\mathbf{7c}] = 5.84 \times 10^{-3}$ M, (i) $[c]_0/[t]_0 = 1.11$ (ii) $[c]_0/[t]_0 = 0.33$	228
Figure 4.28 Relationship between δ_{obs} vs $[t]_0$ during a thermal reversion experiment of derivative 7c . Blue dots correspond to a reversion experiment ($[\mathbf{7c}] = 8.8 \times 10^{-4}$ M). Solid line corresponds to the theoretical dilution curve obtained from the average of two separate dilution experiments with (t)- 7c	228

Figure 4.29 Top Plot: Top Plot: Theoretical K_{t-c} vs δ_{tc} curves for the set of δ_{obs} from the least squares curve that describes the third reversion experiment of derivative **7c** (red dots in Figure 4.31, $[7c] = 1.47 \times 10^{-3}$ M). Bottom Plot: Theoretical CV vs δ_{tc} curve for the set of K_{t-c} calculated from the third reversion experiment of derivative **7c** (red dots at Figure 4.31, $[7c] = 1.47 \times 10^{-3}$ M). 230

Figure 4.30 Top Plot: K_{t-c} vs δ_{tc} curves for the set of δ_{obs} from the third reversion experiment of derivative **7c** (red dots in Figure 4.31, $[7c] = 1.47 \times 10^{-3}$ M). Bottom Plot: CV vs δ_{tc} curve for the set of K_{t-c} calculated from the third reversion experiment of derivative **7c** (red dots at Figure 4.31, $[7c] = 1.47 \times 10^{-3}$ M). 231

Figure 4.31 Relationship between δ_{obs} vs $[t]_0$ through three reversion experiments of the derivative **7c**. Blue, green and red dots correspond to first, second and third separate reversion experiments, respectively. Blue, green and red dashed lines correspond to the predicted δ_{obs} vs $[t]_0$ plots for the first, second and third reversion experiments with the expected ΔG values (sample standard deviations of 0.006, 0.003, 0.01 ppm, respectively). Solid line corresponds to the dilution curve obtained from the average of two separate dilution experiments. 232

Figure 4.32 Theoretical speciation diagram of derivative **7c** at the third reversion experiment (red dots at Figure 4.31, $[7c] = 1.47 \times 10^{-3}$ M) at 263 K. Solid lines correspond to the first scenario ($K_{c-c} = 0$) and dotted-star marked lines correspond to the second scenario ($K_{c-c} = 68$ M⁻¹) respectively. Blue, red, orange, yellow and brown colors correspond to $[t]$, $[t \cdot t]$, $[t \cdot c]$, $[c]$, and $[c \cdot c]$, respectively. Black dotted line corresponds to maximum *cis/trans* ratio in reversion experiment. Grey dotted line corresponds to *cis/trans* ratio at PSS..... 233

Figure 4.33 Decay profiles of (**c**)-**7c** isomer in toluene-*d*₈ at 298 K. Blue, red and green dots correspond to first, second and third separate reversion experiments ($r = -0.9934, -0.9966, -0.9981$) respectively. Blue, red and green dashed lines correspond to the calculated values obtained by linear least squares regression of the first, second and third separate reversion experiments, respectively..... 235

Figure 4.34 Decay profiles of (**c**)-**7c** isomer in toluene-*d*₈ at 263 K. Blue, green and red dots correspond to first, second and third separate reversion experiments ($r = -0.9816, -0.9574$ and -0.9885), respectively. Blue, green and red dashed lines correspond to the calculated values

obtained by linear least squares regression of the first, second and third separate reversion experiments, respectively..... 236

List of Schemes

Scheme 1.1 Hydrogen Bond Interaction.....	5
Scheme 1.2 Preorganization Principle.....	16
Scheme 1.3 Equilibria between tautomeric forms of 6[1H]-pyrimidinone.....	19
Scheme 1.4 Zimmerman's group system tautomers.....	20
Scheme 1.5 Monomers desolvation upon complex formation.....	21
Scheme 1.6 Photochromic compounds which transform via <i>cis-trans</i> (<i>Z/E</i>) isomerization ($h\nu_1 < h\nu_2$).....	26
Scheme 1.7 Photochromic compounds which transform via intermolecular pericyclic reactions ($h\nu_1 < h\nu_2$).....	26
Scheme 1.8 Photochromic compounds which transform via intramolecular pericyclic reactions ($h\nu_1 < h\nu_2$).....	27
Scheme 1.9 Photochromic compounds which transform via intramolecular group transfer ($h\nu_1 < h\nu_2$).....	28
Scheme 1.10 The visual cycle of Retinal/Retinol.....	29
Scheme 1.11 Hecht and Gostl small molecules release system controlled via photoswitching.....	30
Scheme 1.12 Branda and coworkers polymer with adhesive properties controlled by photoswitching.....	31
Scheme 1.13 Photodegradation of Spirooxazines and Spiropyrans.....	34
Scheme 1.14 Photoisomerization of Azobenzene.....	36
Scheme 1.15 Proposed mechanism for the <i>E/Z</i> (<i>trans/cis</i>) isomerization of azoaromatic compounds.....	40

Scheme 1.16 Multi-stage host-guest complex.	42
Scheme 1.17 Photo-controlled assembly of pseudorotaxane.....	43
Scheme 1.18 Aggregation pattern changes after photoisomerization.....	44
Scheme 1.19 Photoswitchable catalyst by Pericas and coworkers.	45
Scheme 2.1 Supramolecular thermoplastic elastomer obtained by functionalizing poly(ethylene-butylene) with self-associating ureidopyrimidinone ending groups.....	54
Scheme 2.2 A proposed photoswitchable self-complementary DDAAA hydrogen bond array and its idealized function.	61
Scheme 2.3 Synthesis of photoswitchable self-complementary DDAAA hydrogen bond arrays 4a-p	61
Scheme 2.4 Dimerization equilibrium of 4a-p	65
Scheme 2.5 Synthesis of (<i>E</i>)- 6-(phenyldiazenyl)-1,3,5-triazin-2-amine, derivatives 5c , 5f and 5k	75
Scheme 3.1 Takeshita's photoreversible supramolecular polymer.....	133
Scheme 3.2 Yokoyama's indolyfulgimide – bis(acylamino)pyridine complex.	135
Scheme 3.3 Photoswitchable triple hydrogen bond motif studied by Hecht and coworkers.	135
Scheme 3.4 Photoisomerization of derivatives 4a-p	136
Scheme 3.5 Complexation equilibria present in mixed <i>cis/trans</i> solutions of derivatives 4a-p in non-polar solvents.....	138
Scheme 3.6 Complexation equilibria involving the 4a-p <i>trans</i> -isomer.....	152
Scheme 3.7 Complexation equilibria involving the 4a-p <i>cis</i> -isomer.	153
Scheme 4.1 Synthetic strategy to add quinoline ring as acceptor at the third step.	186

Scheme 4.2 Synthetic strategy to add quinoline ring at the second step.	187
Scheme 4.3 Improved photoswitchable self-complementary AAADD hydrogen bond array.	191
Scheme 4.4 Amended photoswitchable self-complementary AAADD hydrogen bond array and its idealized function.....	190
Scheme 4.5 Synthesis of second generation photoswitchable self-complementary DDAAA hydrogen bond arrays.....	190
Scheme 5.1 Preorganized photo-isomerizable self-complementary hydrogen bond arrays. n = 1 or 2.....	249
Scheme 5.2 Proposed inclusion of photo-isomerizable self-complementary hydrogen bond arrays.....	249

List of Abbreviations and Symbols

(+R)	electron donating resonance effect
(-I)	electron withdrawing inductive effect
A	hydrogen bond acceptor
α	hydrogen bond donor properties
β	hydrogen bond acceptor properties
χ	molar fraction
CD ₃ CN	deuterated acetonitrile
CDCl ₃	deuterated chloroform
CV	coefficient of variation
D	hydrogen bond donor
Δ	Heat
δ	chemical shift
D	Donor
δ_d	chemical shift of dimer
ΔG	free energy
$\Delta\Delta G$	free energy difference
δ_m	chemical shift of monomer
DMSO-d ₆	deuterated dimethylsulfoxide
DNA	deoxyribonucleic acid
δ_{obs}	chemical shift observed
δ_{tc}	chemical shift of trans-cis complex
<i>E</i>	entgegen or cis
ε	extinction coefficient
EI-HRMS	Electron Impact Ionization High Resolution Mass Spectrometry
eq.	Equivalent
ϕ	quantum yield
g	Grams
h	Hours
h ν	wavelength

Hz	Hertz
IR	Infrared
IUPAC	International Union of Pure and Applied Chemistry
K	rate of reaction
K	Kelvin
K_a	association constant
$K_{c:c}$	<i>cis-cis</i> dimerization constant
kcal	Kilocalories
kJ	kiloJoules
$K_{t:c}$	trans-cis complexation constant
$K_{t:t}$	trans-trans complexation constant
λ	wavelength
LRAT	Lechtin retinol acyltransferase
M	Multiplet
m.p.	melting point
M^{-1}	per molar
min	Minutes
mL	mililiters
μL	Microliters
mmol	Milimole
mol^{-1}	per mole
NMR	Nuclear Magnetic Resonance
NOESY	Nuclear Overhauser Effect Spectroscopy
$^{\circ}\text{C}$	Celsius
π	pi orbital
pH	minus logarithm of proton concentration
ppm	parts per million
PSS	Photostationary State
R	linear correlation coefficient
RDH12	all- <i>trans</i> retinol dehydrogenase
RDH5	11- <i>cis</i> retinol dehydrogenase

RHO	Rhodopsin
RNA	Ribonucleic acid
RPE65	Retinoid isomerase
R.T.	room temperature
RX	substituent group
S	Singlet
σ_m	substituent constant at meta-position
T	Triplet
T	Temperature
THF	Tetrahydrofuran
TLC	thin layer chromatography
UV	ultraviolet light
Vis	visible light
vs.	Versus
Z	zusammen or cis

Chapter 1

1 Introduction

1.1 Supramolecular Chemistry

In Jean-Marie Lehn's words, Supramolecular Chemistry is "... a *highly interdisciplinary field of science covering the chemical, physical, and biological features of chemical species of higher complexity, which are held together and organized by means of intermolecular (noncovalent) binding interactions*".¹

The roots of this relatively young area can be traced back to the nineteenth century with contributions from studies in organic chemical and biological systems. The synthesis of the first (and arguably most employed) host molecules, the cyclodextrins by Antoine Villiers in 1891,² the introduction of "lock-and-key" concept by Emil Fischer in 1894,³ the "induced fit" concept by Daniel E. Koshland in 1958,⁴ and the description of an observed carboxylic acid complex as "Übermoleküle" (supramolecule in German) by Karl Lothar Wolf in 1937,⁵ were some of the earliest contributions that made possible the emergence of more advanced tailored hosts such as the crown ethers of Charles Pedersen in 1967,^{6,7} the cation and anion cryptates of Jean-Marie Lehn in 1969^{8,9} and the spherands of Donald J. Cram in 1973.^{10,11} The latter three were awarded the Nobel Prize for Chemistry in 1987 for their work in supramolecular chemistry.¹²

More recently, supramolecular chemistry has evolved and broadened its scope. It no longer only serves as a means to explain physical properties of pure substances and

mixtures such as the transportation of alkali metal ions through cell membranes,^{13,14} and the enzyme-substrate catalysis in living systems.¹³⁻¹⁶ Supramolecular chemistry now creates its own subjects to study by developing sophisticated and complex arrays to serve specific purposes in different fields.¹⁹⁻²¹

The aim of this first chapter is to provide the context to understand and locate the contribution of the systems presented in the following chapters. It will cover basic concepts that describe supramolecular complexes and the specific intermolecular interactions that operate in our arrays. Likewise, this chapter will present the photochemical basis that operates in our proposed arrays and the state of the art regarding the use of photochromic compounds in supramolecular chemistry.

1.2 Molecular Recognition

Molecular recognition is known as the strong, selective and reversible stabilizing interaction of one molecule with another to form a well-defined spatial arrangement between them. Initially, the term molecular recognition was exclusively employed to describe biological systems. However, it was discovered that the occurrence and effects of this event were not limited to that discipline and that it could be applied in a wide range of other scientific and technologic fields.²²

Based on the definition provided in the previous paragraph, it could be said that there are two main features that characterize molecular recognition: the intermolecular interactions and their spatial arrangement.

1.3 Intermolecular Interactions

Also known as supramolecular and non-covalent interactions, intermolecular interactions are the overall result of attractive and repulsive forces between identified separated entities, i.e. molecules, chemical groups within the same molecule, ions, and/or atoms. The energies associated with these interactions range from $< 2 \text{ kJ mol}^{-1}$ for dispersion interactions to 300 kJ mol^{-1} for ion – ion interactions in non-polar media²³ (Table 1.1).

At a macroscopic level, these interactions are responsible for aspects of many important physical properties of matter such as density, boiling point, solvation, surface tension and redox potentials. In biology, intramolecular interactions explain the three dimensional structures of proteins,²⁴⁻²⁶ DNA²⁷ and RNA. Likewise, they participate in well-known processes such as carbohydrate recognition^{28,29} and the transport of cations in biological systems.^{30,31} Lastly, these interactions are useful in materials science to create specific crystal packing systems (crystal engineering),^{32,33} molecular systems with mechanical properties for specific environments,³⁴ and to modulate optical properties of some materials.^{35,36}

Table 1.1 Intermolecular Interactions.²³

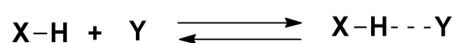
Interaction	Strength (kJ mol ⁻¹)	Example	Directionality
Ion – ion	200 – 300	Tetrabutylammonium chloride	Low
Ion – dipole	50 – 200	Sodium[15]crown-5	Medium
Dipole – dipole	5 – 50	Acetone	Medium
Hydrogen Bonding	4 – 120		Medium
Cation - π	5 – 180	K ⁺ in benzene	Medium
π - π	0 – 50	Benzene and graphite	Medium
van der Waals	< 5	Argon, packing in molecular crystals	Low
Hydrophobic (solvophobic)	Related to solvent – solvent interaction energy	Cyclodextrin inclusion compounds.	Low

From the intermolecular interactions listed above, hydrogen bonds have arguably received the most attention since they are often a central interaction in determining molecular recognition and aggregation in chemical and biological systems. Similarly, due to their strength and directionality, hydrogen bonds have been one of the primary strategies employed in the construction of many novel materials.

1.4 Hydrogen Bond.

1.4.1 Definition.

In 2011, IUPAC presented a technical report in which a new definition of hydrogen bond was provided. This definition states that *the hydrogen bond is an attractive interaction between a hydrogen atom from a molecule or a molecular fragment X-H in which X is more electronegative than H, and an atom or group of atoms in the same or a different molecule (Y), in which there is evidence of bond formation* (Scheme 1.1).³⁷



Scheme 1.1 Hydrogen Bond Interaction.

The definition provided by IUPAC is broad and requires evidence of bond formation. According to IUPAC, there are some criteria of what is considered bond formation evidence which includes:

- 1) Geometry: The angle formed between the three atoms that participate in the hydrogen bond interaction usually tends to be linear.
- 2) The nature of the physical forces involved: Although a hydrogen bond is not considered to be purely electrostatic, it is recognized for its substantial contribution due to the directionality of this interaction. Other contributions to the hydrogen bond are polarization, charge transfer, exchange repulsion and dispersion forces (the last two included in van der Waals interactions).^{38,39}

- 3) Spectroscopy: The effects of the hydrogen bond in the absorption of different types of energy is observed in the red shifting in the X-H vibrational frequency in an IR spectrum and the deshielding of H in HX in a ^1H NMR spectrum.

1.4.2 Classification.

Throughout the literature, the hydrogen bond has been classified into three main categories based on geometry, energy, thermodynamics and function in nature, which are summarized in Table 1.2.⁴⁰⁻⁴²

Table 1.2 Categories of hydrogen bond interaction and some of their important properties.

	Very Strong or Strong	Strong or Moderate	Weak
Bond Energy (kcal/mol)	60 – 170	15- 60	< 15
Interaction Type	Strongly Covalent	Mostly Electrostatic	Electrostatic/Dispersed
Directionality	Strong	Moderate	Weak
D (X····Y) range (Å)	2.2 - 2.5	2.5 - 3.0	3.0 - 4.0
θ (X-H··Y) (°)	175 – 180	130 -180	90 – 180
Effect on Crystal Packing	Strong	Distinctive	Variable
IR ν_s relative shift	> 25 %	5 – 25 %	< 5 %
^1H Chemical Shift Downfield (ppm)	14 – 22	< 14	-
Examples	[F··H··F] ⁻ [N··H··N] ⁻	O – H··O=C N – H··O=C	C – H··O O – H·· π

This classification is meant to be a broad guide to the hydrogen bond interactions observed in nature and used in the design and construction in crystal engineering and supramolecular chemistry. The terminology employed would depend on the author referred. Desiraju and Steiner classified hydrogen bonds as very strong, strong and weak based on the observation that hydrogen bonds that fall into the category of strong are interactions that are able to control crystal and supramolecular structure effectively. On the other hand, Jeffrey named the same categories as strong, moderate and weak in order to be in tune with biological literature since moderate hydrogen bond interactions are usually observed in chemistry and nature, as the other two categories being the minority exception.

Another way to classify the hydrogen bond interaction is in accordance to the different spatial arrays formed between the hydrogen bond donors (which are the molecular fragments **X-H**), **D**, and the hydrogen bond acceptors (the counterparts **Y**), **A** (Scheme 1.1 and Figure 1.1). The appearance of different hydrogen bond arrays is explained due to the attractive force of extra binding sites; i.e. donors and/or acceptors. The angles described are often significantly different from linearity; therefore, these types of arrays are not expected in very strong (or strong according to Jeffrey's classification) hydrogen bond interactions. These configurations are known as donating bifurcated, accepting bifurcated, trifurcated and three centre bifurcated (Figure 1.1).⁴¹⁻⁴⁵

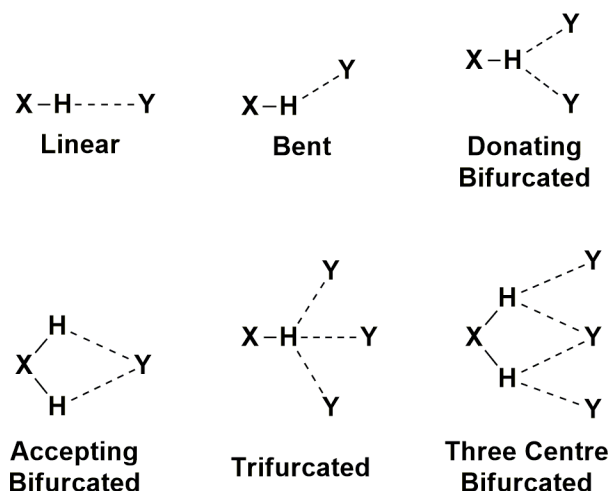


Figure 1.1 Types of hydrogen bond arrays: Linear, Bent, Donating Bifurcated, Accepting Bifurcated, Trifurcated, and Three Center Bifurcated.

1.4.3 Strength of the Hydrogen Bond in Supramolecular Arrays.

There are different ways to modulate the strength of the hydrogen bond interactions in a supramolecular array. The three main strategies are:

- (i) the manipulation of some chemical properties of the hydrogen bond donor and acceptor sites; i.e. the electron density of these sites⁴⁶ and the polarization of the X-H bond;⁴⁷
- (ii) the addition of more intramolecular interactions to create a cooperative effect;⁴⁸ and
- (iii) the arrangement of the hydrogen bond donor and acceptor sites that participate in the interaction.⁴⁹

1.4.3.1 Electron density of binding sites.

The first feature refers to the possibility of controlling the electron density in donor and acceptor sites through substituent effects. In this sense, it is desired to have a low electron density in hydrogen bond donor sites and a high electron density in hydrogen bond acceptor sites in order to observe a strong hydrogen bond interaction. Therefore, it is commonly observed in the literature that electron-withdrawing groups are bonded near hydrogen bond donors and electron-donating groups are bonded near hydrogen bond acceptors.

One example of this effect was reported by Wisner and coworkers through **DDD-AAA** hydrogen bond arrays.⁵⁰ In this work, the comparison of the association constants of a set of different **DDD** units with an **AAA** unit proved that as more electron-withdrawing groups were added to the **DDD** unit higher association constants were obtained (Figure 1.2, Table 1.3). Likewise, the addition of electron-donating groups to the **AAA** unit showed higher association constants than the addition of electron withdrawing groups when complexed to the same **DDD** unit.

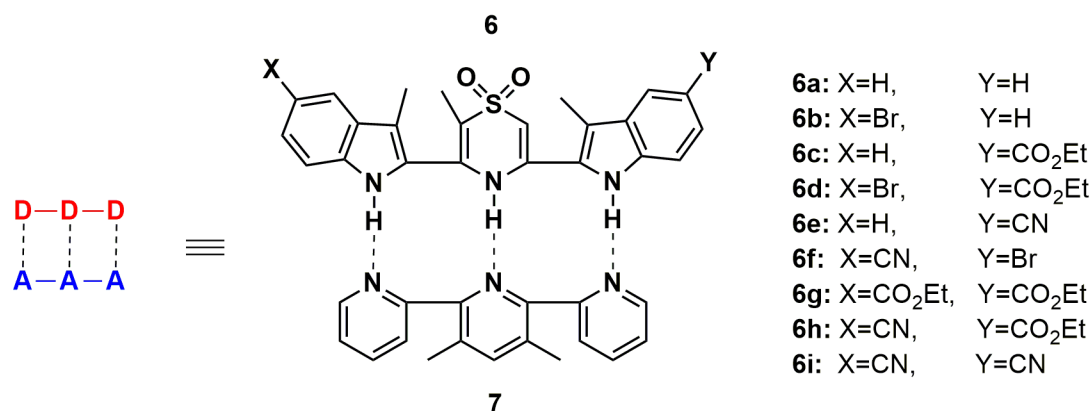


Figure 1.2 DDD-AAA hydrogen bond arrays studied by Wisner and coworkers.

Table 1.3 Comparison of the effect of electron-withdrawing functional groups attached to **DDD** units on the association constant (K_a) in $CDCl_3$ at 298 K.

DDD	X	Y	K_a with 7 [M^{-1}]
6a	H	H	3.7×10^3
6b	Br	H	7×10^3
6c	H	CO_2Et	1.1×10^4
6d	Br	CO_2Et	2.6×10^4
6e	H	CN	2.9×10^4
6f	CN	Br	4.9×10^4
6g	CO_2Et	CO_2Et	5.4×10^4
6h	CN	CN	1.1×10^5

1.4.3.2 Number of hydrogen bond sites.

Cooperativity refers to two or more binding sites acting in a concerted fashion to produce a combined interaction that is stronger than when the binding sites act independently.²³ In other words, the stability of a hydrogen bond array is proportional to the number of hydrogen bond interactions present. This effect is well documented in the literature by Zimmerman and Murray, who reported the effect of extra donors and acceptors on the stability of hydrogen bond complexes.^{51,52}

As illustrated in Figure 1.3, the complex with the highest number of hydrogen bond sites, **DDD-AAA**, has the highest association constant ($K_a \geq 10^5 M^{-1}$),⁵³ whereas the complex with the lowest number of hydrogen bond sites, **DD-AA**, has the lowest association constant ($K_a = 260 M^{-1}$). The authors observed that the addition of an extra

hydrogen bond donor site has a greater influence on the stability of the complex than the addition of an extra hydrogen bond acceptor site. Hence, the **DDD-AA** complex has an association constant of $3 \times 10^3 \text{ M}^{-1}$ compared with the **DD-AAA** complex with an association constant of 848 M^{-1} . It follows that, these last two complexes display higher association constants than the **DD-AA** complex.

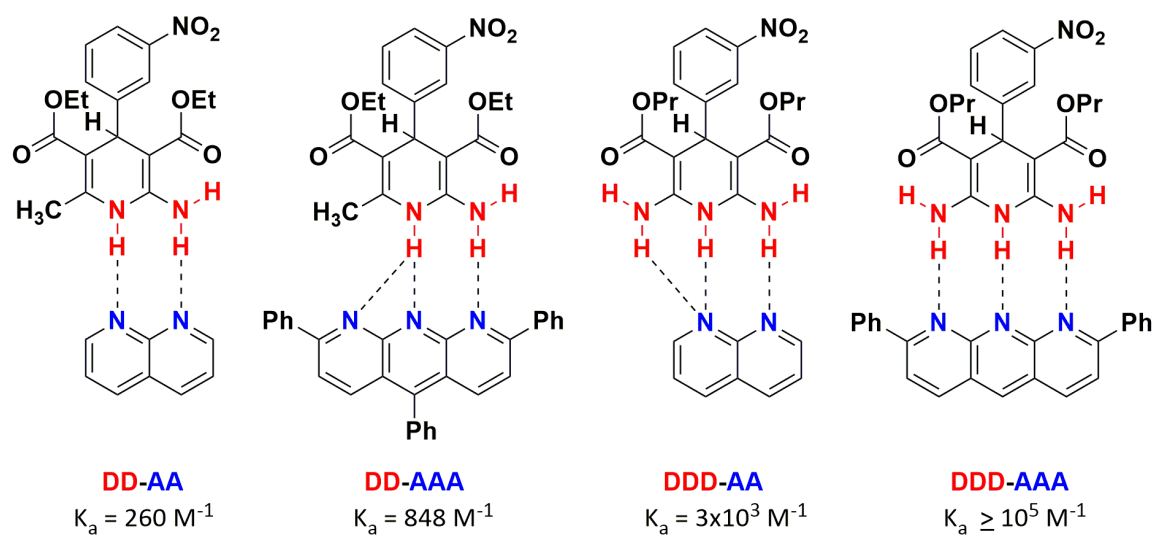


Figure 1.3 The effect of the number of hydrogen bonding sites on the stability (K_a) of different arrays.

1.4.3.3 Secondary Hydrogen Bond Interactions.

The last feature that contributes to the strength of the hydrogen bond array refers to the distribution of the hydrogen bond sites between units. Supramolecular complexes with the same number of donor and acceptor sites have different association constants when the sequence of those binding sites is different.

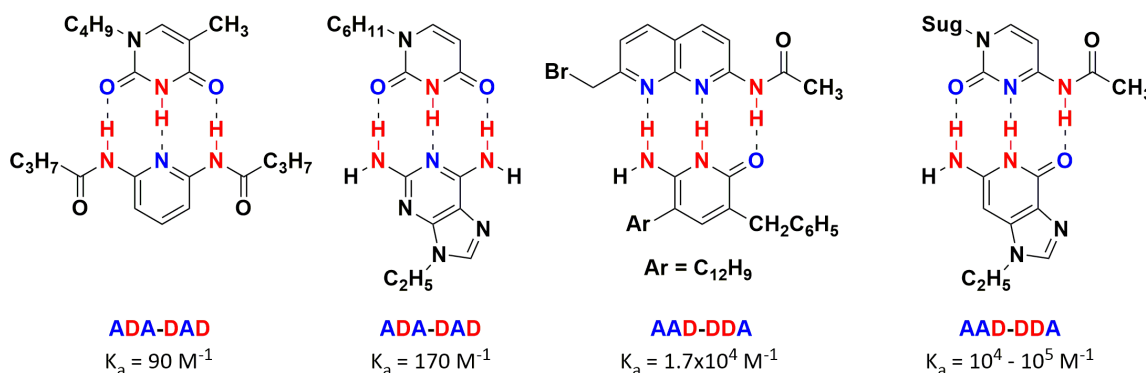


Figure 1.4 Hydrogen Bond Arrays studied by Jørgensen and Pranata.⁵⁵

Jørgensen and Pranata observed this peculiarity in some hydrogen bond complexes,⁵⁵ (Figure 1.4). As can be noted, all complexes in Figure 1.4 comprise the same number of donors and acceptors. However, the difference between the lowest association constant ($K_a = 90 \text{ M}^{-1}$) and the highest one ($K_a = 10^4 - 10^5 \text{ M}^{-1}$) is significant.⁵⁵ The authors explained these differences due to the repulsive or attractive effect of the secondary hydrogen bond interactions. The contribution of these interactions was estimated through different computational methods.^{55,56}

Secondary interactions occur among neighboring hydrogen bond donor/acceptor sites (Figure 1.5). The proximity between them in the arrays (2 - 4 Å) is sufficient to exhibit substantial electrostatic repulsions and attractions. According to this model, an array that

alternates donors and acceptors, **ADA-DAD**, is less favored since it displays four repulsive secondary interactions. On the other hand, the most favored array is the one that comprises all donors on one unit and all acceptors in the other one, **DDD-AAA**. After Jörgensen and Pranata's studies, Zimmerman and Murray supported this model by comparing a set of arrays that represented all the possible combinations with three donors and three acceptors (Figure 1.6).⁵¹

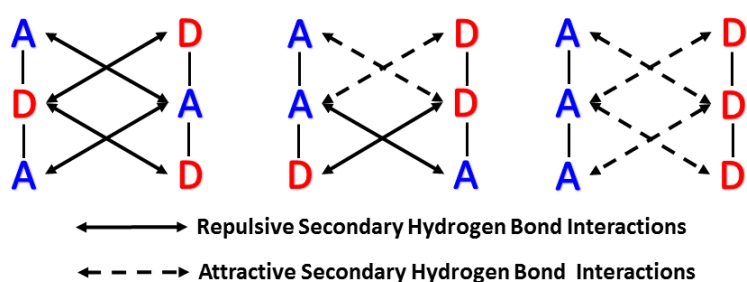


Figure 1.5 Secondary hydrogen bond interactions in triply hydrogen bonded arrays.

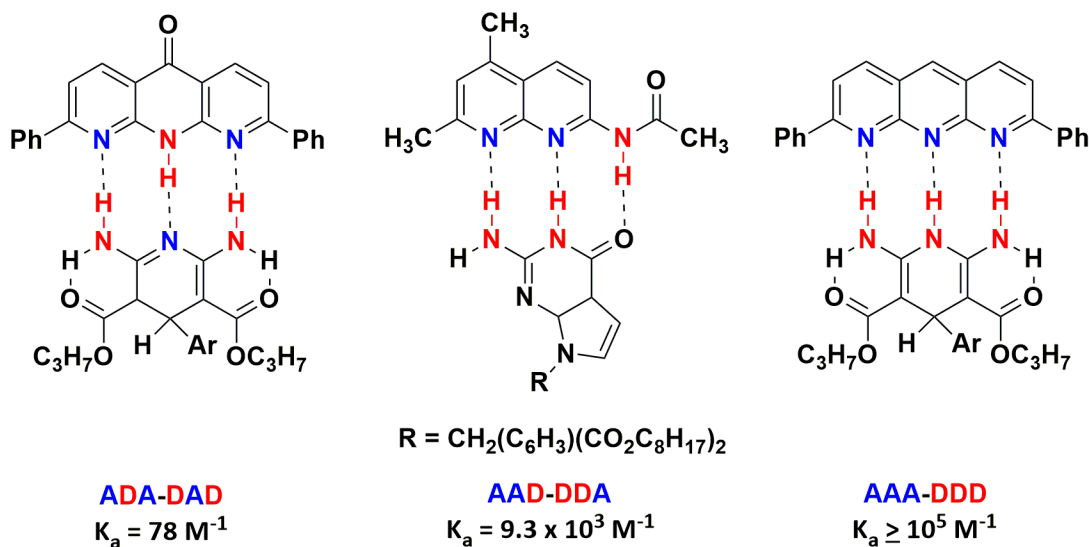


Figure 1.6 Triple hydrogen bond complexes studied by Zimmerman and Murray.

Moreover, the energetic contributions of the primary and secondary hydrogen bond interactions estimated by Jörgensen and Pranata were confirmed by another study carried

out by Sartorius and Schneider.⁵⁷ Based on multiple linear regression analysis of association energies of 58 different complexes, Sartorius and Schneider calculated that the average value of the free energy of a primary hydrogen bond interaction is 7.9 kJ mol^{-1} and for a secondary hydrogen bond interaction is 2.9 kJ mol^{-1} regardless of its character as an attractive or repulsive interaction.⁵⁸

1.5 Supramolecular Complexes.

A supramolecular complex is an entity formed by the molecules that participate in a molecular recognition event. It is characterized by its geometry, thermodynamic and kinetic features.⁵⁹ Since a supramolecular complex requires more than one molecule, each molecule that participates is known as a monomer or monomeric unit. The supramolecular complex can also be defined as a collection of monomers or monomeric units arranged in a specific orientation to each other by intermolecular interactions. The chemical composition of each monomer in a supramolecular complex classifies it as complementary or self-complementary.

Complementary hydrogen bond arrays consist of two or more *different* monomeric units which interact with each other to form a complex. Each monomeric unit incorporates a mutually complementary arrangement of donors and acceptors in order to form the hydrogen bonds. Natural examples of complementary arrays are nucleotide base pairs (Figure 1.7). The complementary arrays illustrated in the preceding pages (Figure 1.2 to 1.4 and 1.6) are the result of the studies and meticulous design of several research groups.

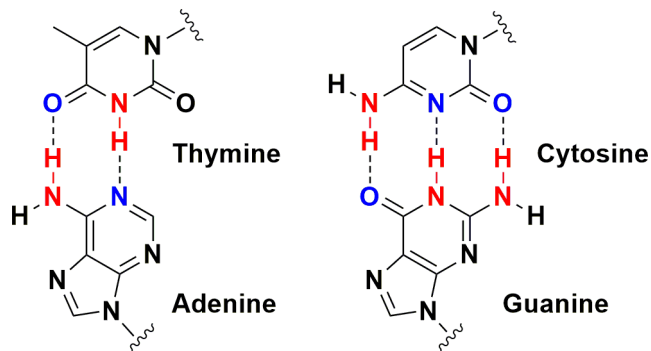


Figure 1.7 Nucleotide base pairs in DNA.

Self-complementary arrays comprise only one type of monomeric unit. The monomeric unit comprises hydrogen bond donors and acceptors disposed in such way that it can form a complex with itself. These complexes are generally characterized by an inversion center. One example of these arrays is provided by guanine tetramers discovered in eukaryotic chromosomes by Sundquist and Klug (Figure 1.8A).⁶⁰ Likewise, there are many reports regarding the design and synthesis of self-complementary arrays, such as the molecular duplex reported by Chu and coworkers, illustrated in Figure 1.8B.⁶¹

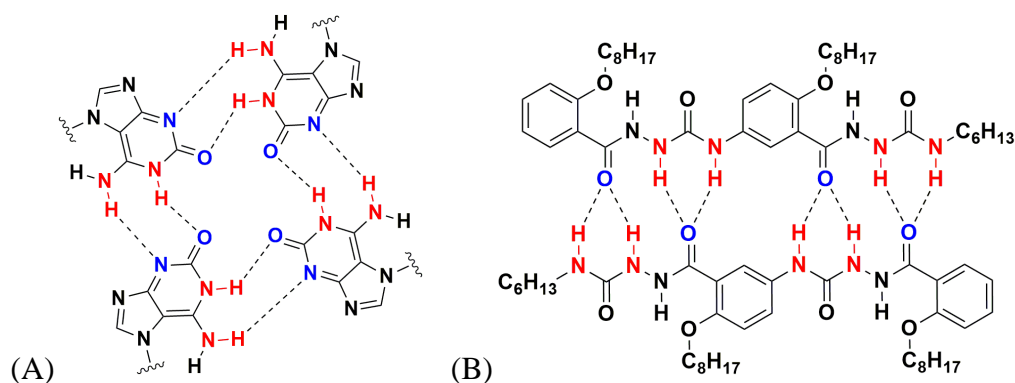
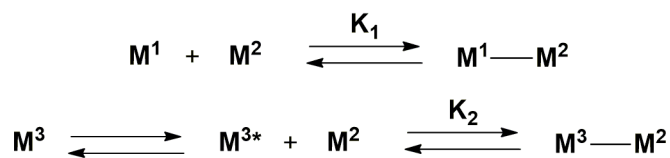


Figure 1.8 (A) A guanine tetramer reported by Sundquist and Klug; (B) A molecular duplex reported by Chu and coworkers.

1.6 Preorganization

Besides the strength of non-covalent interactions present in a supramolecular complex, its stability can be affected by the monomer structure and the conformational disposition of binding sites. These two features are part of the preorganization principle described by Donald J. Cram.^{62,63}

The preorganization principle implies that a monomer (M^1) designed to have the binding sites in a fixed way perfectly complementary to the other monomer's binding sites (M^2), *prior* to their complexation, will bind more strongly than a monomer (M^3) that needs to undergo a conformational rearrangement (M^{3*}) prior to the binding event (Scheme 1.2).⁵ Therefore, a key feature in the design of supramolecular complexes is the stability of the monomers' conformation to ensure a perfect fit with each other. Otherwise, there will be an energetic cost due to the conformational re-arrangement needed to reach the proper binding geometry.



Scheme 1.2 Preorganization Principle.

A good example of the importance of this principle was reported by Murray and Zimmerman through the complementary supramolecular arrays **3·2** and **9·2** (Figure 1.9).⁶⁴ The authors observed that the **3·2** complex exhibited an association constant significantly lower than that anticipated by Jørgensen's secondary interactions model. Molecular

mechanics calculations of the possible conformations for **3** showed that structure **3''**, which presents a steric repulsive interaction with the 4-amino group, is the favorable conformer. Meanwhile, the same calculations showed that the structure where the alkoxy group is optimally positioned to participate in a secondary hydrogen bond interaction, **3'**, is less stable by 4 kcal mol⁻¹. This is, the geometrical prearrangement involved in order to engage monomers **3** and **2** into complexation has an energetic cost that is reflected in the **3·2** complex K_{ass} value. This observation was supported by the association constant of the **9·2** complex. In this complex, monomer **9** was specifically designed and synthesized to have an accessible oxygen acceptor atom to interact with the 4-amino group via a lactone moiety; the result was a higher association constant compared with **3·2** complex. This study confirms that fixing a monomer into a geometrical structure that complements the other monomer's interacting sites disposition has a positive effect on the stability of the complex.

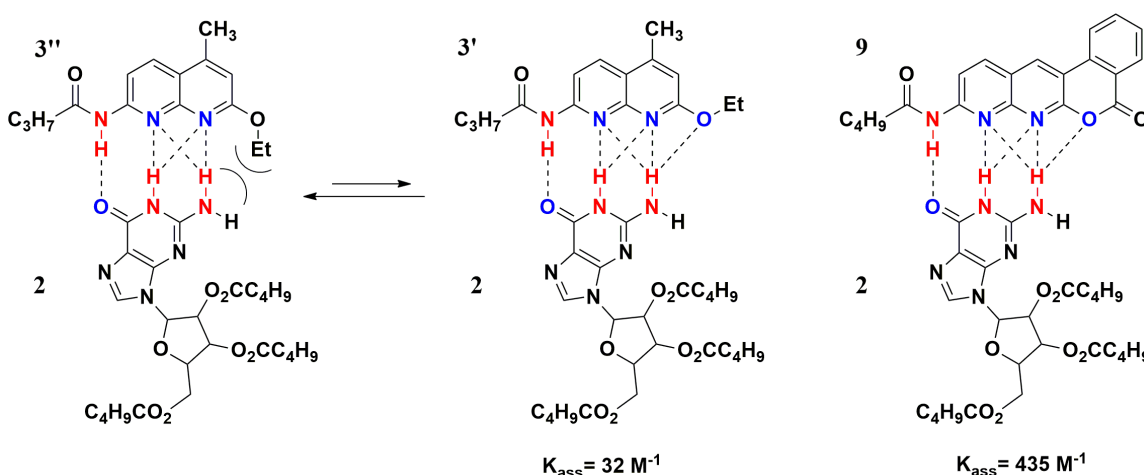
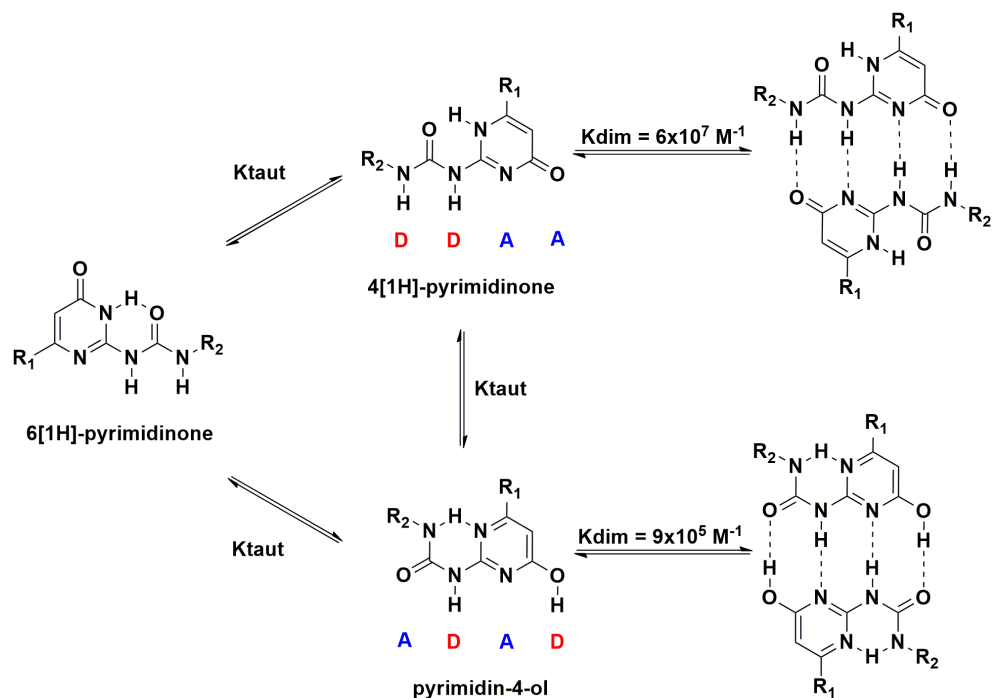


Figure 1.9 Murray and Zimmerman DAA-ADD complex structures. Association constants (K_{ass}) calculated in a 5% DMSO-d₆ – CDCl₃ solvent system.

1.7 Tautomerization

As can be observed in the examples provided in previous sections, most of the hydrogen bonded supramolecular complexes comprise heteroaromatic moieties. They serve as good backbones since they have at least one heteroatom which is used as a hydrogen bond acceptor site. Likewise, different chemical groups (donor and acceptor sites) can be attached to them by known synthetic pathways. However, one of the complications involved with the use of heteroaromatic compounds is their ability to convert to different tautomeric forms due to a proton shift; which is known as prototropy.⁶⁵

Depending on the monomer's design, it is often possible to obtain more than one tautomer (or protomer) able to participate in a hydrogen bond array. One popular example of these systems are the ureidopyrimidones developed by Meijer and coworkers. They noticed that the 6[1H]-pyrimidinone can tautomerize to 4[1H]-pyrimidinone or pyrimidin-4-ol. The last two tautomers can dimerize due to their **DDAA** and **DADA** disposition, respectively. Both arrays are preorganized by an intramolecular hydrogen bond (Scheme 1.3).⁶⁶

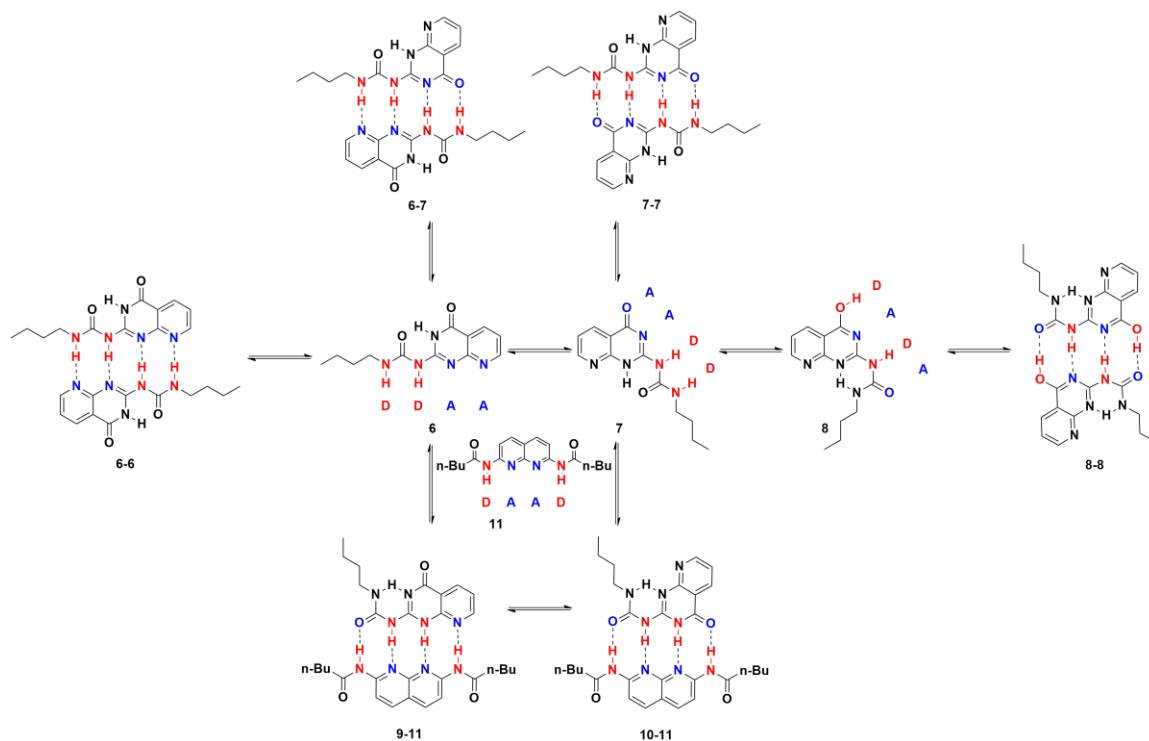


Scheme 1.3 Equilibria between tautomeric forms of 6[1H]-pyrimidinone.

Through this work, the authors observed that the preference of one tautomer over others depends on the nature of the substituent. Systems where \mathbf{R}_1 was an electron-withdrawing group provided the highest fractions of pyrimidin-4-ol tautomer. The rationalization behind this observation was the reduced stability of the enone in 4[1H]-pyrimidinone when an electron-withdrawing 6-substituent is present. In addition, the hydrogen bond acceptor competence of its carbonyl function is reduced.

Besides the effect of substituents, tautomerization can be affected by the solvent employed. In the ureidopyrimidones' example, the dominant tautomers observed in chloroform and toluene correspond to 4[1H]-pyrimidinone and pyrimidin-4-ol in fixed ratios. In THF, the ratio of these two tautomers changes upon dilution. Lastly, in dimethyl sulfoxide solution, the 6[1H]-pyrimidinone is the only tautomer observed.

Another way to control the tautomeric ratio is by the addition of another monomer that forms a complex with only one of the possible tautomers. This strategy was applied by Zimmerman and coworkers who studied self-complementary hydrogen bond arrays able to tautomerize in five different ways⁶⁵ (Scheme 1.4).



Scheme 1.4 Zimmerman's group system tautomers.

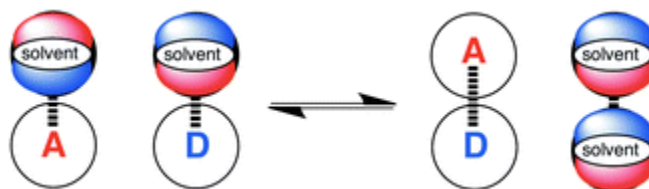
In this study, it was observed that tautomers **6** and **7** were most abundant when toluene and chloroform were employed as solvents, respectively. This observation is reasonable due to the strength of **DDAA-AADD** self-complexation compared to the **DADA-ADAD** tautomeric complex. In both solutions, once a small excess of compound **11** is added, tautomers **6** and **7** fully disassociate to lead the formation of a **DAAD-ADDA**

complementary array with tautomer **9** or **10**. The authors supported the formation of the **9**•**11** complex using computational and NOE studies.

1.8 Solvent Effect

It is likely, with the exception of crystal engineering, that most of the supramolecular chemistry studied to date has been observed in solution. Therefore, solvent plays a significant role in the binding event due to its interaction with the monomers and any complexes formed.

Solvation is the process wherein through intermolecular interactions the dispersed solute is surrounded by a sphere of solvent molecules, the solvation shell. The extent of solvation (i.e. the number and arrangement of solvent molecules around the solute) differs from one solvent to another due to differences in the interactions at work in each case, that are dependent on solvent's nature. The importance of the solvent in complexation lies in the fact that the solvation shell generally blocks the binding sites of the monomers in solution. Hence, there is an amount of energy involved in the dissociation of solvent molecules from these binding sites (Scheme 1.5).⁶⁷



Scheme 1.5 Monomer desolvation upon complex formation.
Scheme reproduce with permission (License number 3910300843589).

In other words, there is a competition for binding sites between solvent and the other monomer(s) involved in the complex. This solvent effect was examined by Taft,⁶⁸ Abraham⁶⁹ and Hunter,⁷⁰ among others. Hunter proposed a model to predict the association constant and the free energy implicated in the formation of a hydrogen bond complex in different solvents (Equations 1 and 2).⁷⁰ The model is a simplification of possible interactions between solute and solvent in terms of their hydrogen bond donor and/or acceptor characteristics: α and α_s describe hydrogen bond donor properties of solute and solvent; and, β and β_s describe hydrogen bond acceptor properties of solute and solvent, respectively (i.e. Kamlet-Taft parameters).⁶⁸

$$\Delta G = -(\alpha - \alpha_s)(\beta - \beta_s) + 6 \text{kJmol}^{-1} \quad \text{Equation 1}$$

$$\Delta G = -\ln K_{Pred} RT \quad \text{Equation 2}$$

As a result of this model, a profile of the dominant interaction in a solute-solvent system can be summarized in Figure 1.10. According to this profile, a hydrogen bond array is favored either because solute - solute interactions or solvent - solvent interactions are dominant over solute - solvent interactions. The first scenario corresponds to designed arrays with a high molecular recognition level; i.e. the structural arrangement and interactions present result in a greatly stable complex. In contrast, the second scenario concerns the solvophobicity of the monomers in solution and the interaction of dissociated solvent molecules with bulk solution.

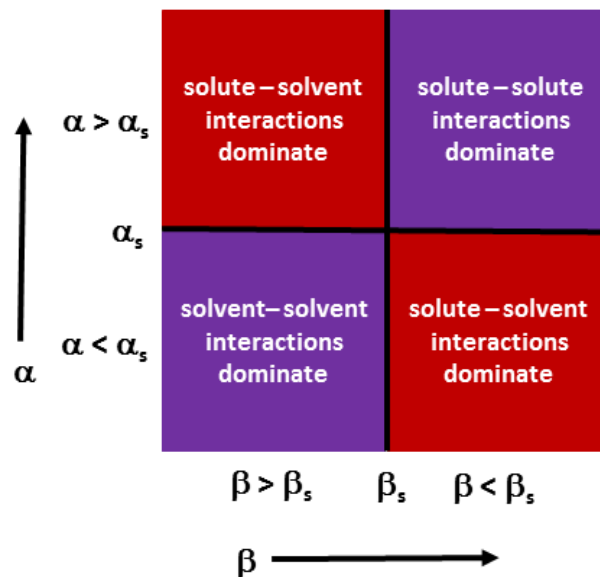


Figure 1.10 Generalized profile of hydrogen bond interactions between solute and solvent.

The accuracy of this model has been corroborated by the author through a number of studies. One of them involved the estimation of the association constant of perfluoro-*tert*-butyl alcohol and tris-*n*-butylphosphine oxide in different solvents.⁷¹ The values obtained applying this model are in agreement with those obtained experimentally, with the exception of alcohols whose case is special due to an underestimation of the polarity of such solvents.⁷²

1.9 Smart Materials.

Thanks to the examination and understanding of the physical properties of different chemical species, materials science now has a broad range of resources available to tailor materials that fulfill a specific purpose. This continued development has led to the emergence of complex and sophisticated materials with the ability to exhibit fast, repeatable, reversible and significant change in one of their physical properties in response to controlled external stimuli. These materials are referred in the literature as “smart” materials.

The nature of the external stimulus used in these materials can be:

- Chemical: changes in the pH,⁷³ the ionic strength,⁷⁴ the solvent system,⁷⁵ gases present⁷⁶ and redox-reactions.⁷⁷
- Physical: electric field,⁷⁸ temperature changes,⁷⁹ light irradiation⁸⁰ and mechanical stress applied.⁸¹
- Biochemical: antigens,⁸² enzymes⁸³ or other biochemical agents present.⁸⁴

Some of the physical properties that can be modified in response to the stimuli can be changes in physical shape or aggregation pattern adopted, volume, viscosity, and porosity.

The increasing interest and development of novel smart materials relate to their potential applications in drug delivery,⁸⁵ bioseparation of proteins, immunoassays,⁸⁶ tissue scaffolds,^{87,88} generation of mechanical work at a microscopic level, sensors and nanowires⁸⁹ and self-healing.⁹⁰

1.10 Supramolecular Photochemistry.

Supramolecular complexes can be described and characterized comparing the properties of each one of the monomers with those of the final resulting complex. In this sense, the properties of the latter cannot be assumed as a mere superposition of those of its units.⁹¹

One property that can be affected after complexation is the interaction with light. The energy provided to a supramolecular system after light irradiation can generate a significant change in the structural and electronic organization of the complex. The study of these changes is the object of the supramolecular photochemistry.⁶⁷

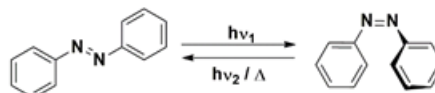
1.11 Photoswitches

Photochromism is the term used to describe the efficient and reversible transformation of some organic molecules between, at least, two (meta) stable isomers induced by light absorption.^{67,92} Molecules that show this property are known as photochromic compounds or photoswitches.

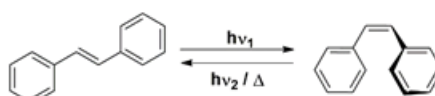
Transformations observed in these compounds include E/Z isomerization, pericyclic reactions, intramolecular hydrogen transfer, intramolecular group transfer, dissociation processes and electron transfers (Scheme 1.6 to 1.9).⁹³ After transformation, photoswitches generally exhibit changes in physicochemical properties such as absorption

spectra,⁹³ dipole moment,⁹⁴ refractive index,⁹⁵ dielectric constant,⁹⁶ oxidation/reduction potential⁹⁷ and geometrical structure.

Azo Aromatic Compounds

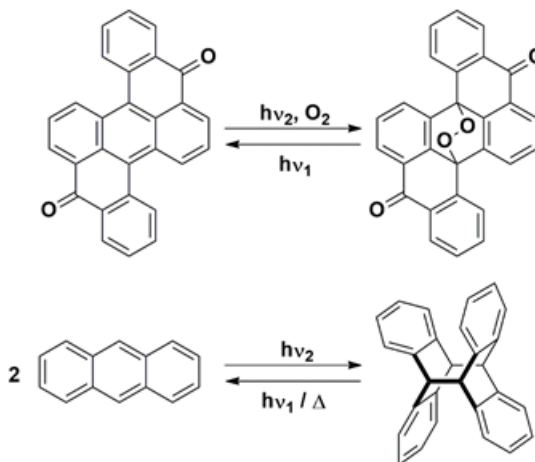


Stilbenes

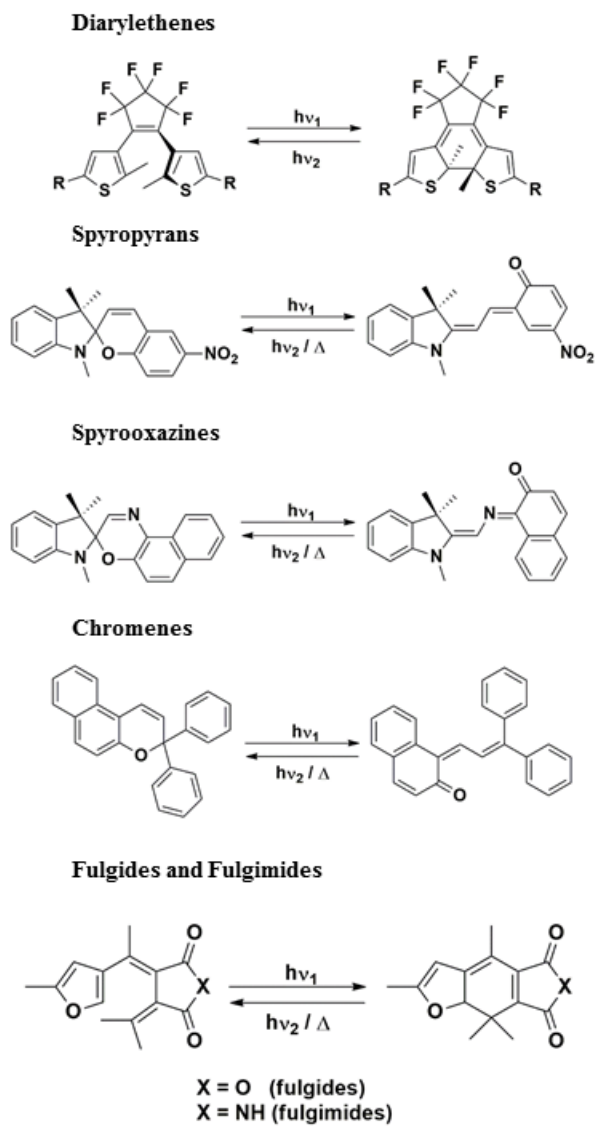


Scheme 1.6 Photochromic compounds which transform via *cis-trans* (Z/E) isomerization ($h\nu_1 < h\nu_2$).

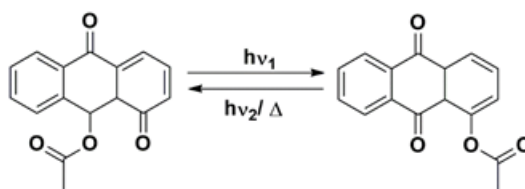
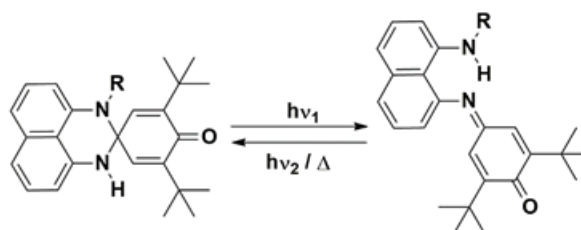
Polycyclic Aromatic Compounds



Scheme 1.7 Photochromic compounds which transform via intermolecular pericyclic reactions ($h\nu_1 < h\nu_2$).



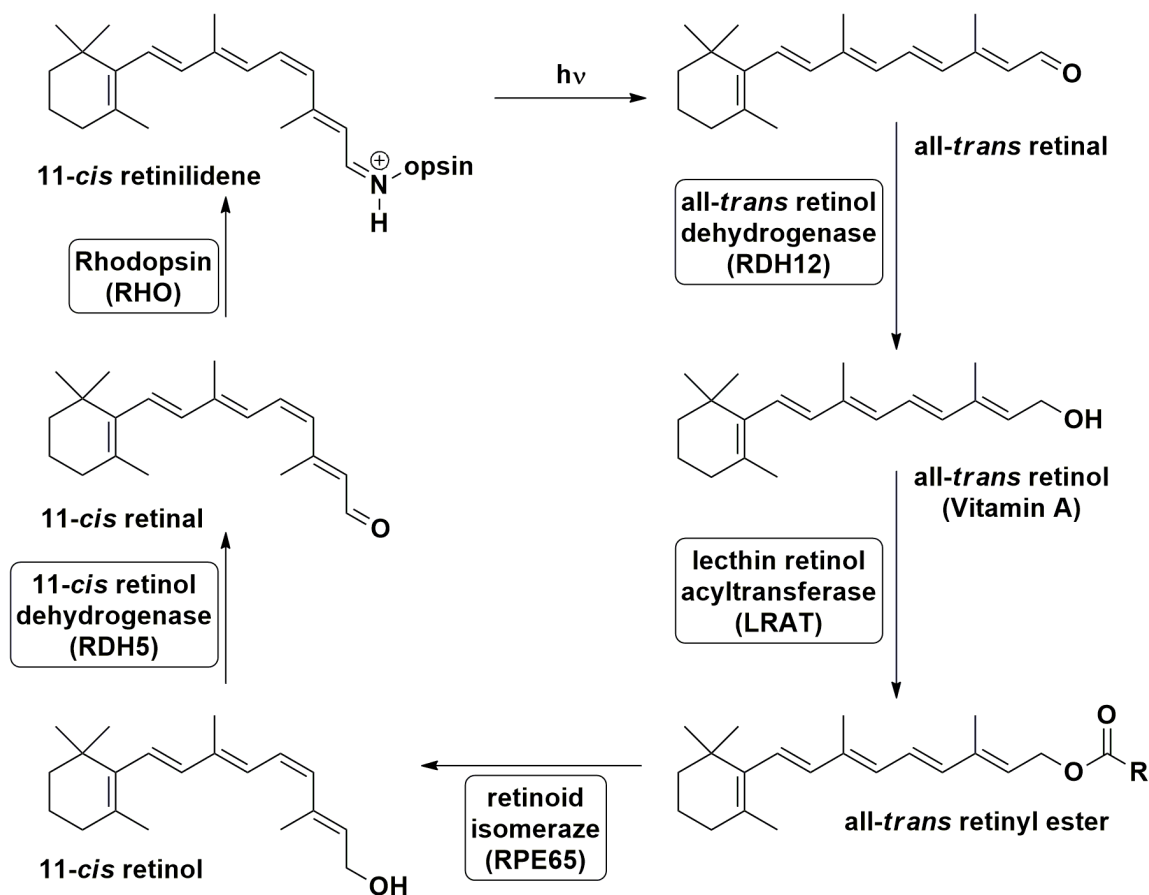
Scheme 1.8 Photochromic compounds which transform via intramolecular pericyclic reactions ($h\nu_1 < h\nu_2$).

Polycyclic Quinones**Perimidinespirocyclohexadienones**

Scheme 1.9 Photochromic compounds which transform via intramolecular group transfer ($h\nu_1 < h\nu_2$).

In living systems, photochromism is responsible for vision. For example, rhodopsin is a protein present in rod cells in the retina. This protein comprises chromophore 11-*cis*-retinal as its protonated Schiff base which isomerizes to all-*trans*-retinal after the visible light stimulus (Scheme 1.10). This structural change generates a cascade of events that lead to a neural signal and visual transduction.⁹⁸

The interest in the study, development, and application of photoswitches lies in the advantages that light provides as a stimulus. It does not necessarily produce waste products and offers an accurate and effective remote control since one can selectively irradiate a specific area.^{92,99} For that reason, it is possible to find in the literature a wide variety of applications of these systems in smart materials.

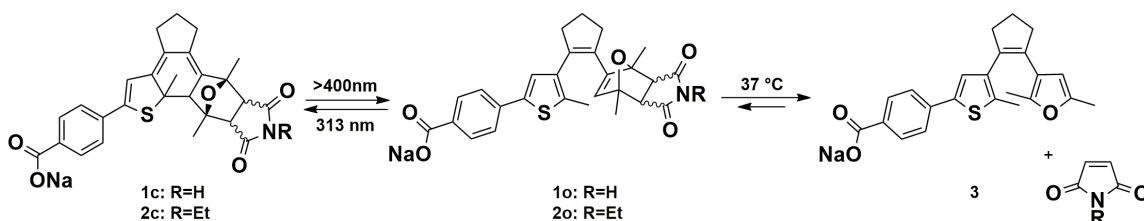


Scheme 1.10 The visual cycle of Retinal/Retinol.

A good example is the control of Diels-Alder and retro Diels-Alder reactions by the use of diarylethenes. This controlled mechanism has been studied and applied by the Hecht and Branda groups as a means to control the release of small molecules and the adhesive properties of a polymer, respectively.

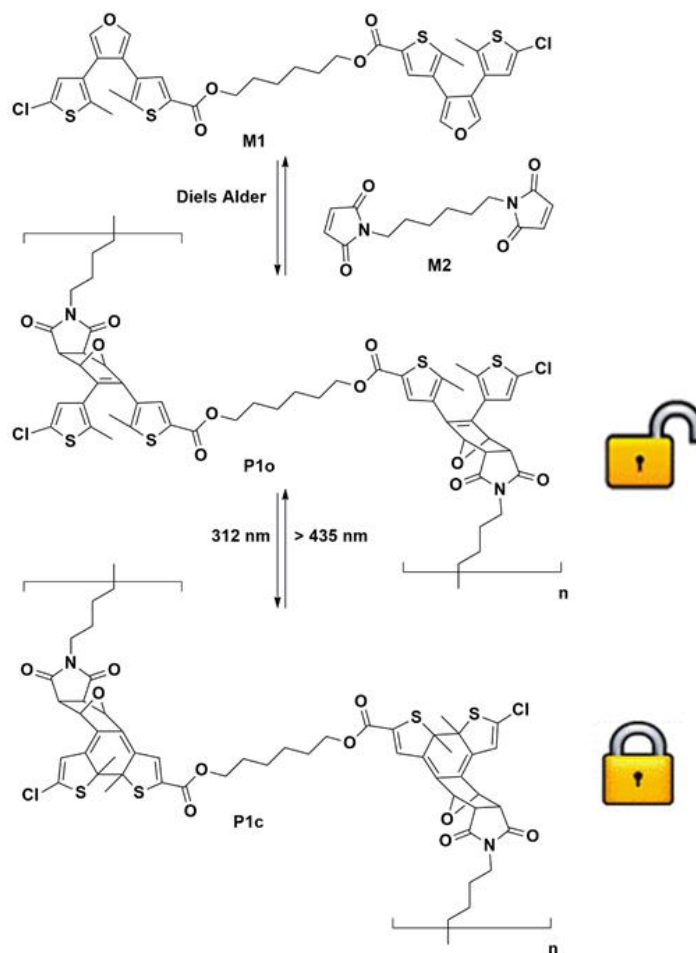
Hecht's approach involved the synthesis of compounds **1c** and **2c** which are intended to retain a molecule of maleimide or N-ethylmaleimide.¹⁰⁰ Once these compounds are irradiated with visible light (wavelengths higher than 400 nm) the compounds **1o** and **2o** are generated in quantitative yield, which under physiological conditions (phosphate-

buffered saline solution, body temperature) release maleimide via a retro-Diels-Alder reaction. The authors claim the potential of this method as a photoswitchable prodrug for maleimide-based reactive inhibitors (Scheme 1.11).



Scheme 1.11 Hecht and Gostl small molecules release system controlled via photoswitching.

On the other hand, Branda and coworkers reported the synthesis of a polymer with self-healing properties that can be turned “on” and “off” by controlling Diels-Alder reaction direction (Scheme 1.12).¹⁰¹ The synthesis of this polymer, **P1o**, involves cycloaddition between diarylfuran moieties of **M1** with maleimide groups of **M2**. Besides the polymerization, cycloaddition forms photochromic diarylethene groups in their open form. Irradiation of the polymer (**P1o**) with UV light triggers ring closing of diarylethene groups, which “locks” the system (**P1c**) and prevents the retro Diels-Alder reaction. Conversely, irradiation of **P1c** with visible light returns the open configuration of the diarylethene groups in the polymer, **P1o**, unlocking the system to a possible retro Diels-Alder reaction.



Scheme 1.12 Branda and coworkers' polymer with adhesive properties controlled by photoswitching.

The last two examples outline the versatile applications of photochromic molecules. Extrapolating this attribute to the entire library of photochromic systems provides a good sense of how extensive the number of applications that could be developed are. In this sense, regardless of the photoswitching system selected for an expected purpose, there are two important properties that need to be evaluated to indicate its effectiveness: the photo-stationary state and photodegradation.

1.11.1 Photo Stationary State.

A photochemical transformation, like any reversible chemical process, will reach an equilibrium; i.e. a state wherein the rate of formation and disappearance are equal for each of the participant species. This is known in photochemistry as the photo stationary state (**PSS**).¹⁰²

Since the absorption of light is required to promote the transformation of a photoswitch from **A** to **B**, the amount of **B** formed, n_B , by irradiating **A** at a specific wavelength, λ_{irr} , is proportional to the absorptivity of **A**, ϵ_A , and the quantum yield of the transformation from **A** to **B**, $\phi_{A \rightarrow B}$ (Equation 3). Likewise, as this transformation is taking place, the formed **B** can absorb λ_{irr} wavelength and trigger the conversion from **B** to **A**; wherein the amount of **A** formed, n_A , is proportional to the absorptivity of **B**, ϵ_B , and the quantum yield of the reverse reaction $\phi_{B \rightarrow A}$ (Equation 4).¹⁰³

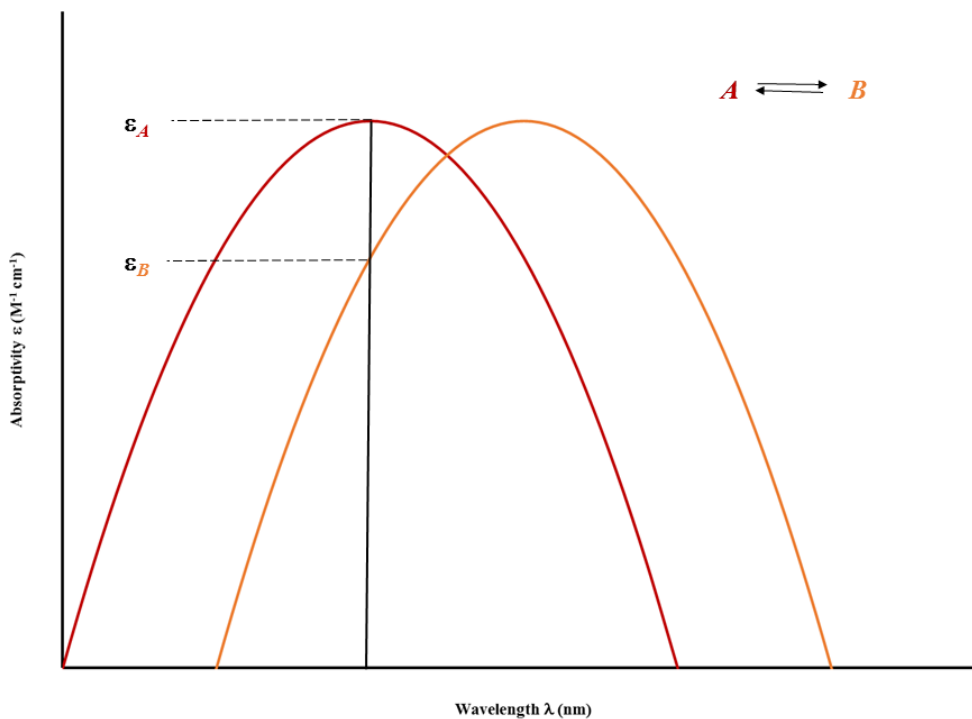


Figure 1.11 Absorption spectra of *A* and *B*.

$$n_B \propto \epsilon'_A \cdot \phi_{A \rightarrow B} \quad \text{Equation 3}$$

$$n_A \propto \epsilon'_B \cdot \phi_{B \rightarrow A} \quad \text{Equation 4}$$

At the photo stationary state, the ratio n_B/n_A is constant since the process has reached an equilibrium. This state can also be described in terms of the absorptivities and quantum yields (Equation 5).

$$\frac{n_B}{n_A} = \frac{\epsilon'_A \phi_{A \rightarrow B}}{\epsilon'_B \phi_{B \rightarrow A}} \quad \text{Equation 5}$$

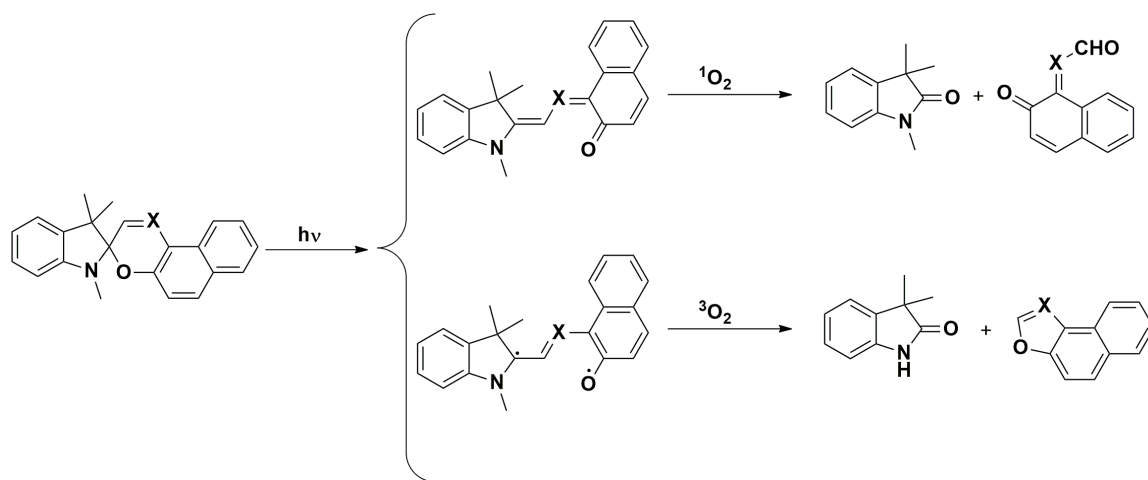
Figure 1.11 and Equations 3 to 5 stress the importance of choosing a wavelength wherein the reactant shows a much higher absorbivity than the product in order to ensure maximum conversion of one form to its isomer (in this case the transformation from *A* to

B, or vice versa). In other words, a wavelength wherein the absorption bands have minimal overlap.

1.11.2 Fatigue or Photodegradation.

One of the main characteristics of a photochromic system is that the two isomeric forms are (meta) stable; however, repeated exposition of light stimulus over time can promote the appearance of side reactions that can deteriorate the expected responses of a system. The loss of performance of a material is known as fatigue; and more specifically for photoresponsive materials, as photodegradation.⁹³

Generally, photodegradation of a photoswitch is caused by the reaction of the photoswitch's excited intermediate with the environment wherein the transformation takes place: e.g. a polymeric matrix, solvent, oxygen, etc. The major cause of photodegradation is often oxidation due to the presence of molecular oxygen.^{104,105}



Scheme 1.13 Photodegradation of Spirooxazines and Spiropyrans.¹⁰⁶

Fatigue is quantitatively described by the number of cycles that a system can significantly respond under well-defined environmental conditions. A complete cycle corresponds to transformation of a photoswitch from state *A* to state *B* and reversion from state *B* to state *A*.

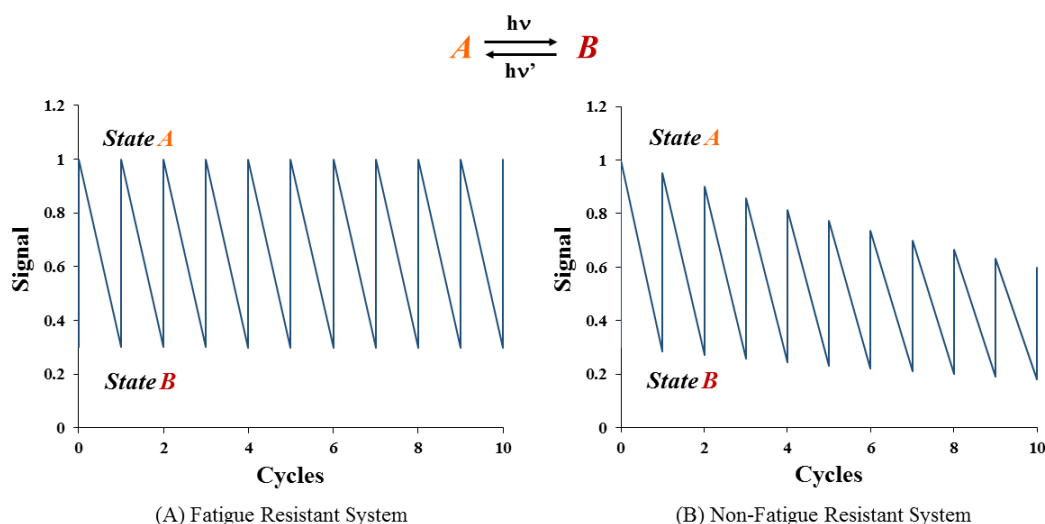


Figure 1.12 Cyclization plots of a (A) fatigue resistant material and (B) a non-fatigue resistant material after 10 cycles.

Alternatively, the degree of degradation allows calculating the fraction of the non-degraded material, y , after n cyclization assuming that x is a fraction of degraded material *per cycle* (Equation 6).

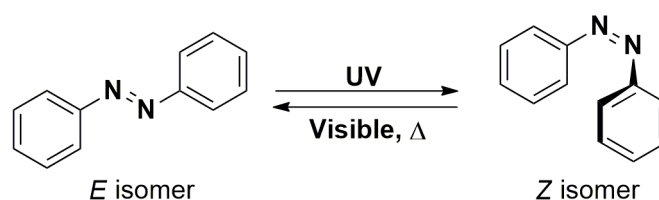
$$y = (1 - x)^n \quad \text{Equation 6}$$

Figure 1.12 shows two cyclization plots of a fatigue resistant system, (A), and a non-fatigue resistant system, (B). The first plot was obtained assuming a photodegradation percent of 0.01 % ($x = 0.0001$). In this case, after 10 cycles it can be extrapolated that 99.9% of the material has not photodegraded. Therefore, it responds very nearly as

efficiently as it did in the first cycle. In contrast; the second plot was obtained assuming a 5 % degradation per cycle ($x = 0.05$). Under this conditions, there is little less than 60% of non-photodegraded active material after 10 cycles. The response is significantly decreasing over only a few cycles.

1.12 Azoaromatic Compounds

From the entire palette of photochromic compounds, azoaromatic compounds, and more specifically azobenzenes, have captured the interest of a large part of the research community. Azoaromatic compounds comprise an azo group (-N=N-) connected to aromatic rings which undergoes *E/Z* isomerization (*trans/cis* isomerization) after absorption of a specific wavelength of light. Of both isomeric forms, the *E* isomer (*trans*) is the most stable, and can be transformed to the *Z* isomer (*cis*) by UV light irradiation. Conversely, the *Z* isomer is the less stable and can be reversed to the *E* isomer by visible light irradiation or heat (Scheme 1.14).¹⁰⁷



Scheme 1.14 Photoisomerization of azobenzene.

The two isomeric forms of azoaromatic compounds are differentiated by their absorption spectra. The UV-Vis absorption spectrum of the *E* isomer comprises two

absorption bands: one at larger wavelengths with lower absorptivity that corresponds to a symmetry forbidden $n \rightarrow \pi^*$ transition, producing the S_1 excited state; and, one at smaller wavelengths with higher absorptivity that corresponds to a symmetry allowed $\pi \rightarrow \pi^*$ transition, giving the S_2 excited state. After isomerization, there is a significant change in absorption spectrum: the $n \rightarrow \pi^*$ band increases its absorptivity; and, the $\pi \rightarrow \pi^*$ band dramatically decreases its absorptivity and shifts to shorter wavelengths (blue shifting or hypsochromic effect). In this way, differences between absorption spectra allow interconversion from one isomer to the other using a specific wavelength. In the case of azobenzene, irradiation at 313 nm produces the *Z* (*cis*) isomer in ~80% yield, and irradiation at 436 nm produces the *E* (*trans*) isomer in ~90% yield.¹⁰⁸

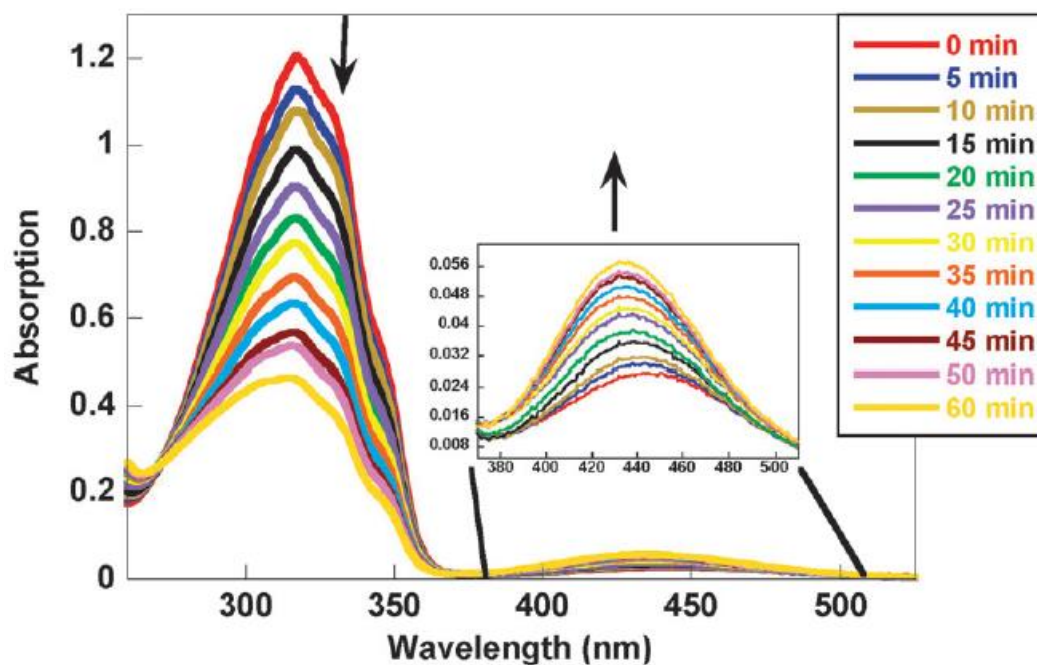


Figure 1.13 Changes in the absorption spectrum of *trans*-azobenzene (*E* isomer) upon irradiation with 316 nm light.

Figure reproduced with permission (License number 3910310008235)

The above description of an azoaromatic UV-Vis absorption profile is a generality since substituents have a substantial effect on absorption spectra. In this sense, azoaromatic compounds have been divided into three families based on their $n\rightarrow\pi^*$ and $\pi\rightarrow\pi^*$ transition energies:^{109,110}

Azobenzenes

Azobenzenes substituted with alkyl, aryl, halide, carbonyl, amide, nitrile, ester, carboxylic acid, nitro, 3-amino and 3-alkoxy groups. Absorption spectra of these compounds are generally similar to unsubstituted azobenzene; i.e. the $\pi\rightarrow\pi^*$ band is very intense in the UV region and the $n\rightarrow\pi^*$ band weaker in the visible region. They usually exhibit a yellow color visually in the *trans*-isomeric form.

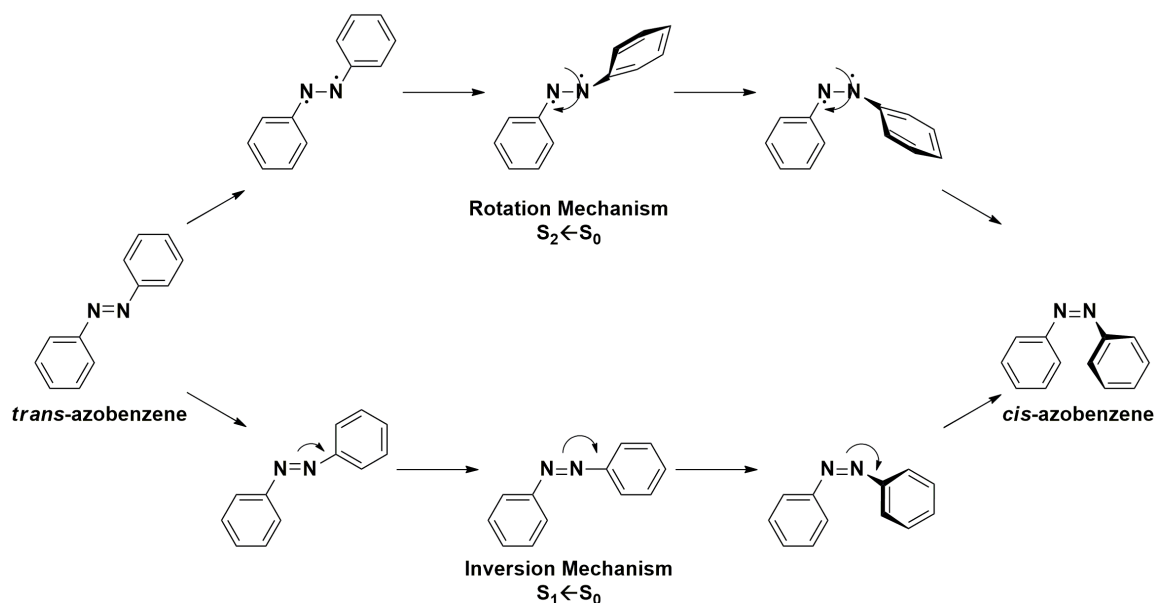
Aminoazobenzenes

This family comprises azobenzenes with electron donor substituents; i.e. with one or more amino or hydroxyl substituents in the 2- or 4- positions. In their absorption spectra, the $\pi\rightarrow\pi^*$ transition band is shifted to higher wavelengths and overlaps with the $n\rightarrow\pi^*$ transition band. In comparison with the preceding family, aminoazobenzenes exhibit higher quantum yields and higher thermal isomerization yields. Due to the presence of amino or hydroxyl groups, hydrogen bond formation and tautomerization can occur. They usually exhibit an orange color in the *trans*-isomeric form.

Pseudostilbenes

This group comprises two types of azobenzenes: (i) protonated azobenzenes, and (ii) azobenzenes substituted with an electron donor and an electron acceptor substituent in the 4- and 4'- positions creating a push-pull effect. In both types, absorption spectra exhibit $n \rightarrow \pi^*$ and $\pi \rightarrow \pi^*$ transitions degenerate in energy, and occur in the visible region; i.e. the $\pi \rightarrow \pi^*$ band is shifted to red, changing the appearance order with respect to the $n \rightarrow \pi^*$ band. These compounds are characterized by an intense red color.

Despite much research, the *E/Z* isomerization mechanism is still being considered by the research community. The debate about the correct mechanism is among two pathways: rotation and inversion (Scheme 1.15). The first pathway involves the cleavage of the π bond between nitrogen atoms allowing rotational isomerization wherein the C-N-N-C dihedral angle changes while the N-N-C angle remains $\sim 120^\circ$. This mechanism proceeds through the S_2 excited state. In the second pathway, the C-N=N-C dihedral angle remains unchanged ($\sim 0^\circ$) as the N=N-C angle increases towards 180° which leads to a transition in one *sp* hybridized nitrogen atom. This mechanism takes place through the S_1 excited state.¹⁰⁹



Scheme 1.15 Proposed mechanism for the *E/Z* (*trans/cis*) photoisomerization of azoaromatic compounds.

Historically, azoaromatic compounds were recognized as dyes and employed in food, fabrics, toys and cosmetics¹¹¹⁻¹¹³ due to their intense red-orange color. However, right after their photochromic properties were identified, these compounds found opportunities in another niche as molecular switches. Some of the features that make azobenzenes one of the most employed photoswitches are:¹¹⁴

- a. relatively small influence that the environment (e.g solvent) has on the absorption profile and isomerization;
- b. minimal photodegradation;
- c. high quantum yield of transformation from one isomer to other;
- d. large achievable concentration differences between *cis* isomer and *trans* isomer in photo stationary state;

- e. ultrafast photoisomerization within few picoseconds and slower thermo-reversion (milliseconds to days); and
- f. large structural differences between isomers.

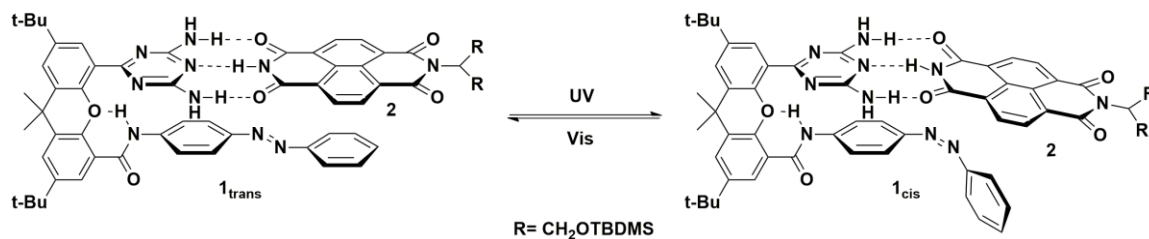
The first two characteristics make azobenzene a reliable and robust photochromic system that can be introduced at a broad range of conditions; whereas the following three are related to the effective response to stimuli. Finally, the last feature refers to the role of the geometry of both isomeric forms in macroscopic properties of the entire system.

1.12.1 Azoaromatic Compounds in Self-Assembly Systems.

The transformation from one isomeric form in azoaromatic compounds to the other induces a significant change in the entire structure to which the photoswitch is a part. The impact of such change is dependent on the intended application of the system. In this sense, some of the most widespread applications in literature involve photoisomerization of the azo group as a means to produce movement;¹¹⁵ to study protein folding-models;¹¹³ and, to control self-assembly¹¹⁶ and/or molecular recognition.

Specifically regarding the control over supramolecular arrays, there are three approaches to the use of azoaromatic compounds. The most modest strategy is related to the planarity of *E* (trans) isomeric form and its π - π interactions with proximal aromatic groups. One example is a multi-stage host-guest complex developed by Rotello and coworkers, (Scheme 1.16). The host, **1**, comprises an azobenzene moiety located parallel

to a diamino-1,3,5-triazine ring. The triazine ring has a **DAD** hydrogen bond array which complements the **ADA** array of the naphthalenediimide guest, **2**.¹¹⁷



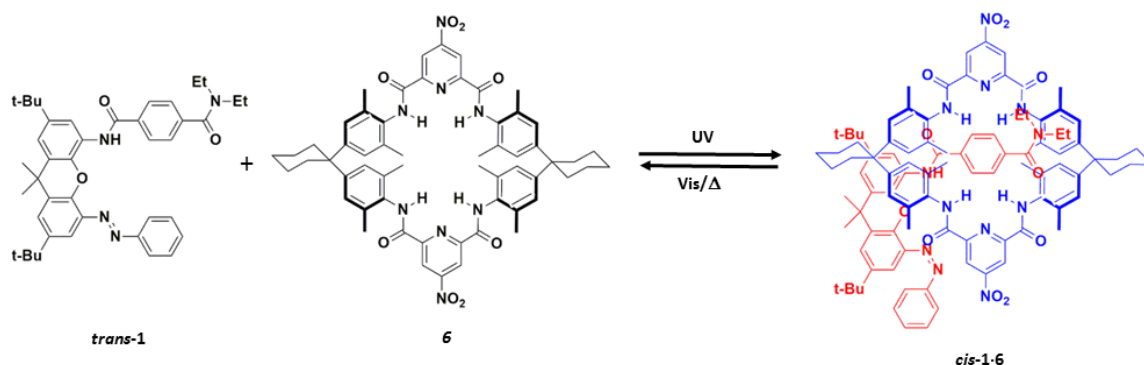
Scheme 1.16 A Multi-stage host-guest complex examined by Rotello and coworkers.

At first sight, hydrogen bonding seems to be the driving complexation interaction; yet, comparison of the association constants of the complex when azobenzene in **1** has a *trans* geometry, **1_{trans}**, against a *cis* geometry, **1_{cis}**, highlights the contribution of π - π interactions in the complex's stability (Table 1.4). Likewise, a π - π contribution is observed in the differences in association constants when guest **2** is in different oxidation states: **2**, **2⁻** and **2⁼**. The highest constant corresponds to **1_{trans}**·**2** complex wherein the electron-rich azobenzene moiety is parallel to the electron-poor oxidized naphthalenediimide. After reduction of guest **2** to **2⁻** and **2⁼**, the association constant decreases due to dipolar repulsion between the electron-rich reduced guest and azobenzene fragment.

Table 1.4 Association constant of the six modalities of the **1**·**2** complex in CDCl₃ at 296 K.

HOST	K _a (2) M ⁻¹	K _a (2⁻) M ⁻¹	K _a (2⁼) M ⁻¹
1_{trans}	9750	2054	591
1_{cis}	575	228	136

A different use of an azoaromatic group to control supramolecular complexation refers to the ability of one isomer to block potential binding sites. Location of an azo group next to binding sites allows control over the surrounding space and the possibility of complementary binding sites' access to that space. Jeong and coworkers reported in 2003 a pseudorotaxane controlled by photoisomerization of an azo group (Scheme 1.17). The axle, **trans-1**, is a complementary terephthalamide group which is located parallel to an azobenzene group. Proximity between the axle and azo group, plus π - π interactions between aromatic groups, in **trans-1** renders threading through the cavity of **6** difficult.¹¹⁸



Scheme 1.17 Photo-controlled assembly of pseudorotaxane.

After irradiating **trans-1** with UV light, the **cis-1** isomer is produced with a 77% yield. The structural disposition of the free aromatic ring in the azo group creates the space required for macrocycle **6** to encircle the terephthalamide axle. Control over the assembly of the pseudorotaxane is supported by the differences between the association constants of **trans-1·6** and **cis-1·6**; which were estimated as ≤ 1 and $5200 \pm 100 \text{ M}^{-1}$, respectively.

Finally, the last strategy to apply azoaromatic groups as a means to manipulate the aggregation pattern of supramolecular systems is by modifying the aromatic rings to

incorporate exogenous non-covalent binding sites. This way, the geometric disposition of the binding sites is affected by *E/Z* (*trans-cis*) isomerization; and, as a consequence, the supramolecular aggregation is affected. A good example is the use of azobenzene in a peptide system by Ghadiri's group¹¹⁹ (Figure 1.14). A change from the *E* (*trans*) isomer to the *Z* (*cis*) isomer results in a rearrangement of hydrogen bonding sites from an intermolecular assembly to an intramolecular one (Scheme 1.18).

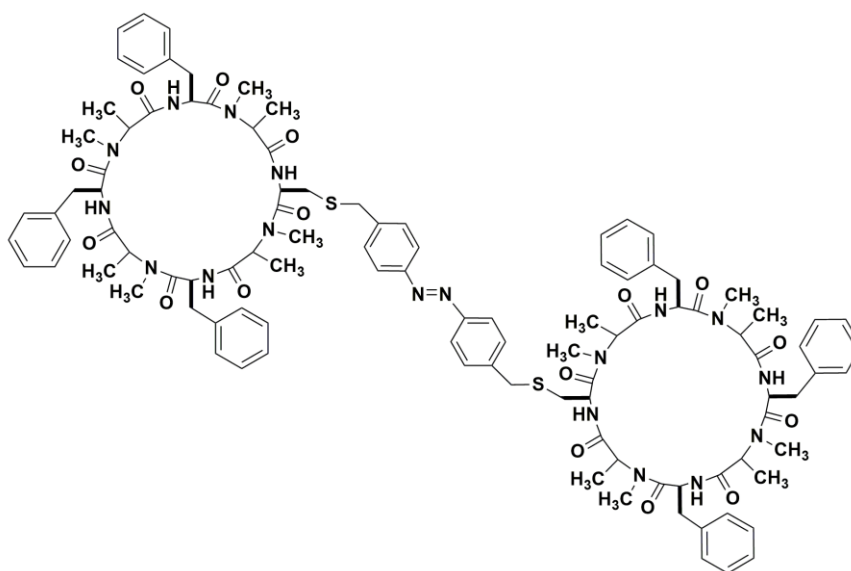
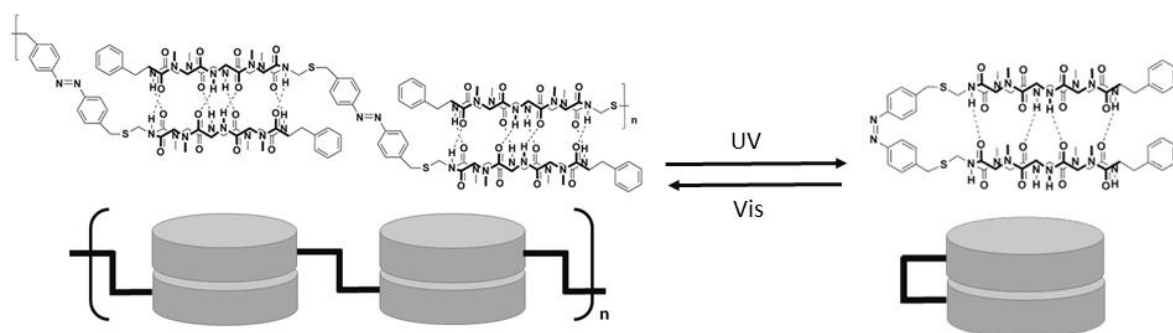
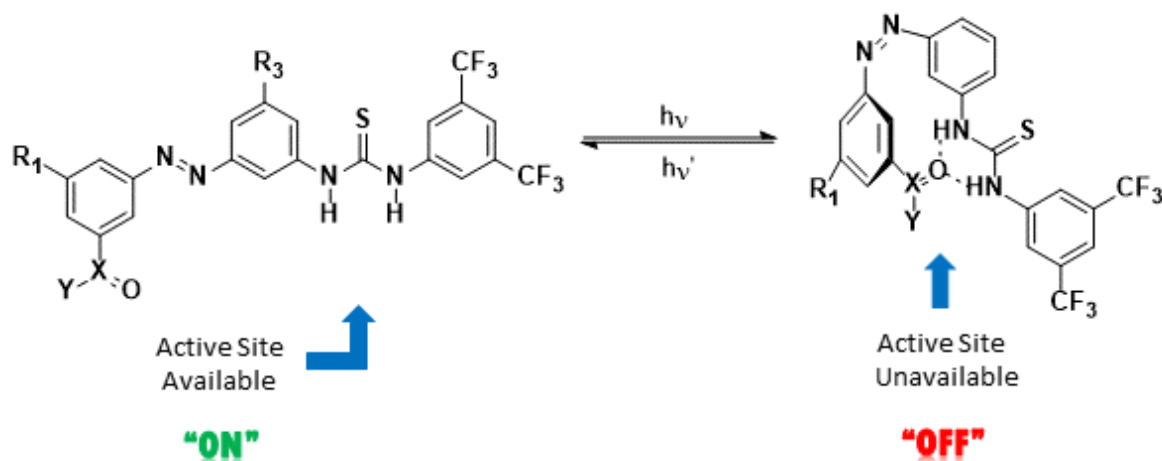


Figure 1.14 Ghadiri's peptide photoswitchable system.



Scheme 1.18 Aggregation pattern changes after photoisomerization.

Beside supramolecular arrays, control over the availability of specific non-covalent binding sites by azoaromatic compounds has been studied in other fields such as catalysis.¹²⁰ Recently, Pericas and coworkers reported the synthesis and effectiveness of a photoswitchable catalyst.¹²¹ The catalyst comprises a thiourea group which is an active catalytic site when the system is in its *E* (*trans*) form. Once the system is switched to its *Z* (*cis*) form, a hydrogen bond acceptor group is located close to the thiourea. An intramolecular hydrogen bond interaction blocks the active site shutting down the catalyst effect in the reaction (Scheme 1.19).



Scheme 1.19 Photoswitchable catalyst by Pericas and coworkers.

1.13 Scope of the Thesis

The development of self-complementary hydrogen bond arrays whose stability can be reversibly modulated by an external stimulus is an opportunity regarding the expansion of the smart materials family. The aim of this Ph.D. project was the development of light responsive self-complementary hydrogen bond arrays. The novelty of these arrays lies in

the use of a photochromic group (i.e. the azo group, $-N=N-$) as a hydrogen bond acceptor in the supramolecular complex. An account of the impact that the external stimulus has in our systems was a key element in order to define the properties that characterize and differentiate these arrays with the present state of the art. Therefore, the main challenge during this project was the description once the structural change of these systems was triggered via light irradiation; i.e. *trans*- to *cis*- photoisomerization. In other words, to measure the stability of the complex(es) present in solution after the photochemical change. In the following chapters, the design, synthesis and characterization of photoswitchable self-complementary **DDAAA** hydrogen bond arrays are reported and discussed. This report includes the approach to the mathematical model employed to describe these systems' change after photoisomerization.

1.14 References

1. Lehn, J.-M. *Science*, **1993**, 260, 1762.
2. Crini, G. *Chem. Rev*, **2014**, 114, 10940.
3. Behr, J.-P. *The lock-and-key principle : the state of the art--100 years on*. Chichester : Wiley & Sons, 1994.
4. Koshland, D. E. Jr. *Angew. Chem. Int. Ed. Engl.*, **1994**, 33, 2375.
5. Schalley, C. *Analytical methods in supramolecular chemistry*. Weinheim : Wiley-VCH, 2007.
6. Pedersen, C. J. *J. Am. Chem. Soc.*, **1967**, 89, 2495.
7. Pedersen, C. J. *Science*, **1988**, 241, 536.
8. Diethich, B., Lehn, J.-M. and Sauvage, J. P. *Tetrahedron Letters*, **1969**, 10 (34), 2885.
9. Lehn, J.-M. *Angew. Chem. Int. Ed. Engl.*, **1988**, 27 (1), 89.

10. Cram, D. J. *Angew. Chem. Int. Ed. Engl.*, **1988**, 27 (8), 1009.
11. Cram, D. J.; Cram, J. M. *Science*, **1974**, 183, 803.
12. Press Release: The 1987 Nobel Prize in Chemistry. *Nobelprize.org*. [Online] http://www.nobelprize.org/nobel_prizes/chemistry/laureates/1987/press.html. (Accessed August 2015)
13. Steed, J. W.; Atwood, J. L. *Supramolecular Chemistry*. Chichester : New York : Wiley, 2000.
14. Safer, B.; Schwartz, A. *Circulation Research*, **1967**, 21, 25.
15. Cragg, P. J. *Supramolecular Chemistry : From Biological Inspiration to Biomedical Applications*. Dordrecht : Springer Science+Business Media B.V., 2010.
16. Román-Meléndez, G. D. von Glehn, P.; Harvey, J. N.; Mulholland, A. J.; Marsh, E. N. G. *Biochemistry*, **2014**, 53 (1), 169.
17. Ballard, S. A., Gingell, C. J.; Tang, K.; Turner, L. A.; Price, M. E.; Naylor, A. M. *The Journal of Urology*, **1998**, 159, 2164.
18. Chen, G.; Wang, H.; Robinson, H.; Cai, J.; Wan, Y.; Ke, H. *Biochemical Pharmacology*, **2008**, 75, 1717.
19. Etxebarria, J.; Ros, M. B. *J. Mater. Chem.*, **2008**, 18, 2919.
20. Buerkle, L. E.; Rowan, S. J. *Chem. Soc. Rev.*, **2012**, 41, 6089.
21. Sangeetha, N. M.; Maitra, U. *Chem. Soc. Rev.*, **2005**, 34, 821.
22. Ariga, K., Ito, H.; Hill, J. P.; Tsukube, H. *Chem. Soc. Rev.*, **2012**, 41, 5800.
23. Steed, J. W., Turner, D. R. and Wallace, K. J. *Core concepts in supramolecular chemistry and nanochemistry*. Chichester : John Wiley, 2007.
24. Hubbard, R. E.; Haider, M. K. Hydrogen Bonds in Proteins: Role and Strength. *Encyclopedia of Life Sciences*. Chichester : John Wiley & Sons, 2010.
25. Stites, W. E. *Chem. Rev.*, **1997**, 97, 1233.
26. Griffiths-Jones, S. R.; Searle, M. S. *J. Am. Chem. Soc.*, **2000**, 122, 8350.
27. Kool, E. T. *Chem. Rev.*, **1997**, 97, 1473.
28. Ke, C.; Destecroix, H.; Crump, M. P.; Davis, A. P.; *Nature Chemistry*, **2012**, 4, 718.
29. Destecroix, H.; Renney, C. M.; Mooibroek, T. J.; Carter, T. S.; Stewart, P. F. N.; Crump, M. P.; Davis, A. P. *Angew. Chem. Int. Ed. Engl.*, **2015**, 54 (7), 2057.
30. Dougherty, D. A.; Kumpf, R. A. *Science*, **1993**, 261, 1708.

31. Dougherty, D. A. *Science*, **1996**, 271, 163.
32. Aakeröy, C. B., Champness, N. R.; Janiak, C. *CrystEngComm*, **2010**, 12, 22.
33. Desiraju, G. R. *Angew, Chem. Int. Ed. Engl.*, **2007**, 46, 8342.
34. Stoddart, J. F. *Chem. Soc. Rev.*, **2009**, 38, 1802.
35. Yan, Z.; Guang, S.; Xu, H.; Liu, X-Y. *Dyes and Pigments*, **2013**, 99 (3), 720.
36. Barooah, N., Mohanty, J.; Pal, H.; Bhasikuttan, A. C. *Org. Biomol. Chem.*, **2012**, 10 (26), 5055.
37. Arunan, E.; Desiraju, G. R.; Klein, R. A.; Sadlej, J.; Scheiner, S.; Alkorta, I.; Clary, D. C.; Crabtree, R. H.; Dannenberg, J. J.; Hobza, P.; Kjaergaard, H. G.; Legon, A. C.; Mennucci, B.; Nesbitt, D. J. *Pure Appl. Chem.*, **2011**, 83 (8), 1619.
38. Morokuma, K., *J. Chem. Phys.*, **1971**, 55, 1236.
39. Umeyama, H.; Morokuma, K. *J. Am. Chem. Soc.*, **1977**, 99, 1316.
40. Desiraju, G. R.; Steiner, T. *The Weak Hydrogen Bond In Structural Chemistry and Biology*. Oxford : New York : Oxford University Press, 1999.
41. Jeffrey, G. A. *An Introduction to Hydrogen Bonding*. New York : Oxford University Press, 1997.
42. Steiner, T., *Angew. Chem. Int. Ed. Engl.*, **2002**, 41, 48.
43. Jeffrey, G. A.; Maluszynska, H. *Int. J. Biol. Macromol.*, **1982**, 4, 173.
44. Saied, O.; Simard, M.; Wuest, J. D. *J. Org. Chem.*, **1998**, 63, 3756.
45. Jeffrey, G. A., *Cryst. Rev.*, **1995**, 4, 213.
46. Wilcox, C. S.; Kim, E.; Romano, D.; Kuo, L. H.; Burt, A. L.; Curran, D. P. *Tetrahedron*, **1995**, 51 (2), 621.
47. Chen, Y.-F.; Dannenberg, J. J. *Journal of Computational Chemistry*, **2011**, 32, 2890.
48. Schneider, H.-J.; Juneja, R. K.; Simova, S. *Chem. Ber.*, **1989**, 122, 1211.
49. Cooke, G.; Rotello, V. M. *Chem. Soc. Rev.*, **2002**, 31, 275.
50. Wang, H.; Mudraboyina, B. P.; Wisner, J. A. *Chem. Eur. J.*, **2012**, 18, 1322.
51. Murray, T. J.; Zimmerman, S. C. *J. Am. Chem. Soc.*, **1992**, 114, 4010.
52. Zimmerman, S. C.; Murray, T. J. *Tetrahedron Letters*, **1994**, 35, 4077.
53. Blight, B. A.; Camara-Campos, A.; Djurdjevic S.; Kaller, M.; Leigh, D. A.; McMillan F. M.; McNab, H.; Slawin A. M. Z. *J. Am. Chem. Soc.*, **2009**, 131 (39), 14116.

54. Kyogoku, Y.; Lord, R. C.; Rich, A. *Biochim. Biophys. Acta.*, **1969**, 179, 10.
55. Jörgensen, W. L.; Pranata, J. *J. Am. Chem. Soc.*, **1990**, 112, 2008.
56. Pranata, J.; Wierschke, S. G.; Jörgensen, W. *J. Am. Chem. Soc.*, **1991**, 113, 2810.
57. Sartorius, J.; Schneider, H-J. *Chem. Eur. J.*, **1996**, 2, 1446.
58. Quinn, J. R., Zimmerman, S. C., Del Bene, J. E. & Shavitt, I. *J. Am. Chem. Soc.*, **2007** 129, 934.
59. Lehn, J.-M. *Supramolecular chemistry : concepts and perspectives : a personal account built upon the George Fisher Baker lectures in chemistry at Cornell University and the Lezione Lincee, Accademia nazionale dei Lincei, Roma*. Weinheim : New York : VCH, 1995.
60. Sundquist, W. I.; Klug, A. *Nature*, **1989**, 342, 825.
61. Chu, W.; Yang, Y.; Chen, C. *Org. Lett.*, **2010**, 12, 3156.
62. Artz, S. P.; Cram, D. J. *J. Am. Chem. Soc.*, **1984**, 106, 2160.
63. Cram, D. J. *Science*, **1988**, 240, 760.
64. Murray. T. J.; S. C. Zimmerman, *Tetrahedron Letters*, **1995**, 36 (42), 7627.
65. Corbin, P.S.; Zimmerman, S. C. *J. Am. Chem. Soc.*, **1998**, 120, 9710.
66. Beijer, F. H.; Sijbesma, R. P.; Kooijman, H.; Spek, A. L.; Meijer, E. W. *J. Am. Chem. Soc.*, **1998**, 120 (27), 6761.
67. Atwood, J. L. Steed, J. W. *Encyclopedia of supramolecular chemistry*. New York : Marcel Dekker, 2004.
68. Kamlet, M. J.; Abboud, J. L. M.; Abraham, M. H.; Taft, R. W.; *J. Org. Chem.*, **1983**, 48 (17), 2877.
69. Abraham, M. H. *Chem. Soc. Rev.*, **1993**, 22, 73.
70. Hunter, C. A.; *Angew. Chem. Int. Ed. Engl.*, **2004**, 43, 5310.
71. Cook, J. L.; Hunter, C. A.; Low, C. M. R.; Perez-Velasco, A.; Vinter, J. G. *Angew. Chem. Int. Ed. Engl.*, **2007**, 46 (20), 3706.
72. Amenta, V.; Cook, J L.; Hunter, C. A.; Low, C. M. R.; Sun, H.; Vinter J. G. *J. Am. Chem. Soc.*, **2013**, 135 (32), 12091.
73. Ma, L., Kang, H.; Liu, R.; Huang, Y.; *Langmuir*, **2010**, 26 (23), 18519.
74. Bai, T.; Han, Y.; Zhang, P.; Wang, W.; Liu, W.; *Soft Matter*, **2012**, 8 (25), 6846.

75. Wang, J.-H.; Li, M.; Li, D., *Chem. Sci.*, **2013**, *4*, 1793.
76. Lin, S.; Theato, P. *Macromol. Rapid Commun.*, **2013**, *34*, 1118.
77. Yan, Q.; Feng, A.; Zhang, H.; Yin, Y.; Yuan, J.; *Polym. Chem.*, **2013**, *4*, 1216.
78. Biggs, J.; Danielmeier, K.; Hitzbleck, J.; Krause, J.; Kridl, T.; Nowak, S.; Orselli, E.; Quan, X.; Schapeler, D.; Sutherland, W.; Wagner, J. *Angew. Chem. Int. Ed. Engl.*, **2013**, *52* (36), 9409.
79. Lagoudas, D. C. *Shape Memory Alloys: Modeling and Engineering Applications*. Boston : Springer-Verlag, 2008.
80. Lendlein, A.; Hongyan Jiang, H.; Jünger, O.; Langer, R. *Nature*, **2005**, *434*, 879.
81. Yu, X.; Chen, L.; Zhang, M.; Yi, T. *Chem. Soc. Rev.*, **2014**, *43*, 5346.
82. Miyata, T.; Asami, N.; Uragami, T. *Nature*, **1999**, *399*, 766.
83. Hu, J.; Zhang, G.; Liu, S. *Chem. Soc. Rev.*, **2012**, *41*, 5933.
84. Ehrick, J. D.; Luckett, M. R.; Khatwani, S.; Wei, Y.; Deo, S. K.; Bachas, L. G.; Daunert S. *Macromol. Biosci.*, **2009**, *9* (9), 864.
85. Meng, F.; Zhong, Z.; Feijen, J.; *Biomacromolecules*, **2009**, *10* (2), 197.
86. Liu, H.; Liu, X.; Meng, J.; Zhang, P.; Yang, G.; Su, B.; Sun, K.; Chen, L.; Han, D.; Wang, S.; Jiang, L. *Adv. Mater.*, **2013**, *25* (6), 922.
87. Furth, M. E.; Atala, A.; Van Dyke, M. E. *Biomaterials*, **2007**, *28*, 5068.
88. Roy, I.; Gupta, M. N. *Chemistry & Biology*, **2003**, *10* (12), 1161.
89. Willner, I.; Basnar, B.; Willner, B. *Adv. Funct. Mater.*, **2007**, *17*, 702.
90. Cohen Stuart, M. A.; Huck, W. T. S.; Genzer, J.; Müller, M.; Ober, C.; Stamm, M.; Sukhorukov, G. B.; Szleifer, I.; Tsukruk, V. V.; Urban, M.; Winnik, F.; Zauscher, S.; Luzinov, I.; Minko, S., *Nature Materials*, **2010**, *9*, 101.
91. Balzani, V.; Scandola, F. *Supramolecular photochemistry*. New York : Ellis Horwood, 1991.
92. Rusew, M.-M.; Hecht, S. *Adv. Mater.*, **2010**, *22*, 3348.
93. Bouas-Laurent, H.; Durr, H. *Pure and Applied Chemistry*, **2001**, *73* (4), 639.
94. Bletz, M.; Pfeifer-Fukumura, U.; Kolb, U.; Baumann, W.; *J. Phys. Chem. A*, **2002**, *106* (10), 2232.
95. Hoshino, M., Ebisawa, F.; Yoshida, T.; Sukegawa, K. *Journal of Photochemistry and Photobiology, A: Chemistry*, **1997**, *105* (1), 75.

96. Kurihara, S.; Ikeda, T.; Tazuke, S. *Japanese Journal of Applied Physics, Part 2: Letters*, **1988**, 27, L1791.
97. Exelby, R. *Journal of the Society of Dyers and Colourists*, 83, **1967**, 450.
98. Nakanishi, K. *Pure and Appl. Chem.*, **1991**, 63 (1), 161.
99. Ercole, F.; Davis, T. P.; Evans, R. A. *Polym. Chem.*, **2010**, 1, 37.
100. Gcstl, R.; Hecht S.; *Chem. Eur. J.*, **2015**, 21, 4422.
101. Asadirad, A. M.; Boutault, S.; Erno, A.; Branda, N. R. *J. Am. Chem. Soc.*, **2014**, 136 (8), 3024.
102. Scaiano, J. C. *CRC handbook of organic photochemistry*. Boca Raton : CRC Press, 1989.
103. Fisher, E. *Journal of Physical Chemistry*, **1967**, 71, 3704.
104. Baillet, G.; Giusti, G.; Guglielmetti, R. *J. Photochem. Photobiol. A: Chem.*, **1993**, 70, 157.
105. Yoshida, T.; Morinaka, A. *J. Photochem. Photobiol. A: Chem.*, **1992**, 63, 227.
106. Crano, J. C.; Guglielmetti, R. J. *Organic photochromic and thermochromic compounds*. New York : Plenum Press, 1999.
107. Klan, P.; Wirz, J. *Photochemistry of Organic Compounds: from concepts to practice*. Chichester : Wiley, 2009.
108. Fischer, E. *J. Am. Chem. Soc.*, **1960**, 82, 3249.
109. Bandarab, H. M. D.; Burdette, S. C. *Chem. Soc. Rev.*, **2012**, 41, 1809.
110. Merino, E.; Ribagorda, M. *Beilstein J. Org. Chem.*, **2012**, 8, 1071.
111. Yamjala, K.; Nainar, M. S.; Ramiseti, N. R. *Food Chemistry*, **2016**, 192, 813.
112. Turgaya, O.; Santana, R. C.; Ataíde, C. H.; Barrozo, M. A. S. *Separation and Purification Technology*, **2011**, 79, 26.
113. Wangz, L-H.; Huang, S-J. *Russian Journal of Electrochemistry*, **2010**, 46, 1414.
114. Renner, C.; Moroder, L. *ChemBioChem*, **2006**, 7, 868.
115. Merino, E.; Ribagorda, M. *Beilstein Journal of Organic Chemistry*, **2012**, 8, 1071.
116. Yagai, S.; Karatsu, T.; Kitamura, A. *Chem. Eur. J.*, **2005**, 11, 4054.
117. Goodman, A.; Breinlinger, E.; Ober, M.; Rotello, V. M. *J. Am. Chem. Soc.*, **2001**, 123 (25), 6213.
118. Jeong, K.-S.; Chang, K.-J.; An, Y.-J. *Chem. Commun.*, **2003**, 1450.

119. Vollmer, M.S.; Clark, T. D.; Steinem, C.; Ghadiri, M. R. *Angew. Chem. Int. Ed. Engl.*, **1999**, (11), 1598.
120. Peters, M. V.; Stoll, R. S.; Kühn, A.; Hecht, S.; *Angew. Chem. Int. Ed. Engl.*, **2008**, 47, 5968
121. Osorio-Planes, L.; Rodriguez-Escrich, C.; Pericas, M. A. *Org. Lett.* , **2014**, 16, 1704.

Chapter 2

2 Synthesis and Characterization of Photoswitchable Self-Complementary DDAAA Hydrogen Bond Arrays

2.1 Introduction

Supramolecular chemistry has evolved from explaining properties associated with molecular aggregation to the design and creation of novel and potentially useful systems. In this sense, supramolecular polymers are examples of applications that supramolecular chemistry can contribute to.¹ Traditional polymers are formed by monomers joined through covalent bonds. Supramolecular monomeric units are independent molecules linked via non-covalent interactions. The reversibility of the interactions makes it possible to obtain materials with improved processing, self-healing behaviour and, if desired, crystallinity.² Meanwhile, polymer-like properties such as viscosity, elasticity, fiber formation and other hierarchical arrangements can be obtained through a careful design of the interacting sites and the use of specific spacers or different monomeric blocks (e.g. Figure 2.1, Scheme 2.1).^{2,3}

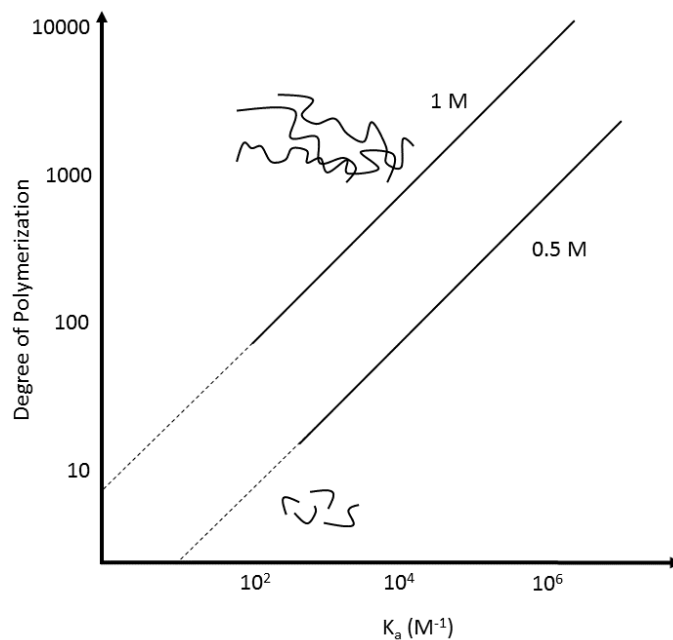
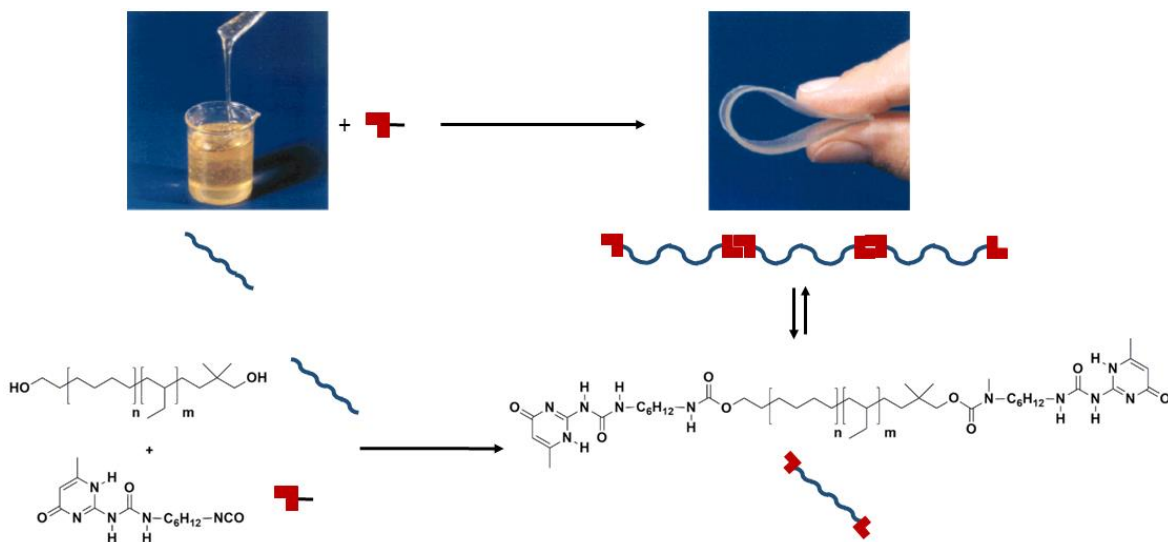


Figure 2.1 Theoretical plot of the relation between association constant and degree of polymerization as a function of concentration of a self-associating (A-A) monomer.



Scheme 2.1 Supramolecular thermoplastic elastomer obtained by functionalizing poly(ethylene-butylene) with self-associating ureidopyrimidinone ending groups.⁴

Efforts toward the development of these types of polymers have responded to specific needs the materials are intended to cover. Applications vary from rheological modifiers,⁵ super-hydrophobic coats,⁶ scaffolds for tissue engineering,^{7,8} self-healing materials,⁹ drug delivery¹⁰ and bioimaging¹¹ among many. In these cases, control over the aggregation relies on environmental changes such as temperature, solvent system,³ pH¹² and enzymatic action.¹³ More sophisticated means of control involve molecular switches. Specifically, aromatic azo compounds have been employed, where changes in the geometric distribution of exogenous binding sites before and after photoisomerization have been the most exploited (Chapter 1 Section 1.12.1).¹⁴ However, this property is not the only possible contribution from the azo group in this context.

In principle, the two sp^2 nitrogen atoms in the azo group ($-N=N-$) can perform as hydrogen bond acceptor sites. This feature has been observed in intramolecular hydrogen bonds between one of the nitrogen atoms of an aromatic azo group and hydroxyl,¹⁵ carboxylic acid¹⁶ and/or amino groups¹⁷ located *ortho*- to the azo function (Figure 2.2). Nevertheless, though this property is well known and documented in the literature, it has not been intentionally employed as part of an intermolecular hydrogen bond array to date.

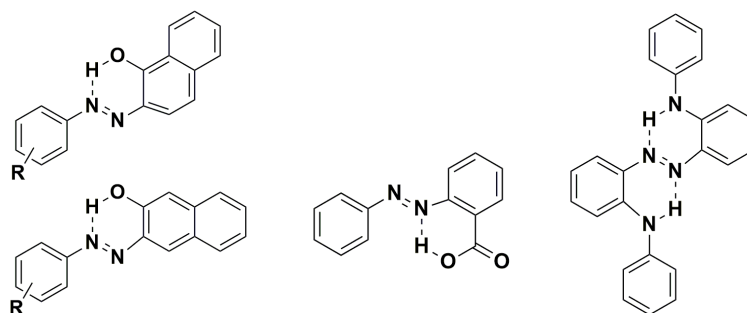


Figure 2.2 Examples of aromatic azo compounds that display intramolecular hydrogen bonds.

Recently, Wisner and coworkers reported the crystal structure of a hydrogen bond complex between 2,6-diaminopyridinium tetraphenylborate and 1,2-bis(5,7-dimethyl-1,8-naphthyridin-2-yl)diazene.¹⁸ The 1,8-naphthyridine moiety is a known hydrogen bond acceptor array.^{19,20} The novelty of this complex lies in the participation of the azo group as an intermolecular hydrogen bond acceptor. Likewise, the *trans* disposition of the azo-group allows the two 1,8-naphthyridine rings to enclose the diaminopyridinium cation with the maximum number of primary hydrogen bond interactions to all but one hydrogen bond donor (Figure 2.3).

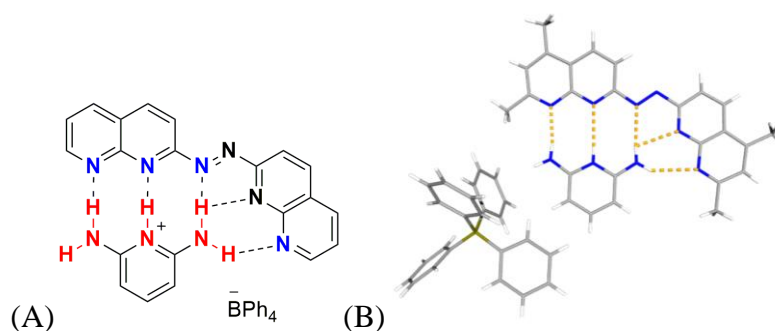


Figure 2.3 (A) Schematic representation of 2,6-diaminopyridinium tetraphenylborate-1,2-bis(5,7-dimethyl-1,8-naphthyridin-2-yl)diazene (1/1) complex. (B) Solid state structure obtained by single crystal X-ray diffraction.

Elucidation of the structure of the complex in the solid state led to speculation whether azoheteroarene-containing species could find further use as host molecules. Furthermore, since some azoheteroaromatic compounds show photoisomerization properties,^{21,22,23} the participation/inclusion of these moieties could potentially be a method to control efficacy of a complexation event.

2.2 Design of Photoswitchable Self-Complementary

Hydrogen Bond Arrays

Once azoheteroaromatic compounds were recognized as potential hydrogen bond acceptor moieties, it was considered how to exploit this feature. As depicted in Figure 2.3, one strategy is the synthesis of two complementary molecules wherein acceptor binding sites are provided by the azoheteroaromatic compound and donor binding sites are provided by a complementary array. An alternative approach involves the synthesis of an array comprising both donor and acceptor sites and able to form a self-complementary complex; a homodimer. This is the aim of this project.

The first element to consider in designing a self-complementary array is the backbone that will hold the donor and acceptor sites. In this case, it was the selection of the azoheteroaromatic component. Based on the complex formed in Figure 2.3, the azo derivative selected has to have a nitrogen atom positioned *ortho* to the azo group on the heteroaromatic ring in order to have at least two acceptor sites at one end of the array. In this sense, 2,2'-azopyridine was a good reference point to start with since its photochemical

properties are similar to those of azobenzene derivative and its synthesis is straightforward.²¹

The second element to deliberate was the hydrogen bond donor group selected and its position in the azoheteroaromatic backbone. In this regard, amino and amido groups have been employed as hydrogen bond donors in most of the hydrogen bond arrays reported in the literature. They are often the best option since the polarization of the N-H bond locates a low electrostatic potential on the hydrogen atom, which is optimal for a good donor site.²⁴ Likewise, the lone pair of electrons on the nitrogen atom can engage in conjugation with the heteroaromatic ring; this adds a resonance-assisted hydrogen bond effect which could further favour dimer stability.²⁵⁻²⁶ Regarding the position of this donor group, a structural analysis indicated that the optimal position was *meta* to the azo group (Figure 2.4). Locating an amino group in the *ortho* position favors an intramolecular hydrogen bond between amino and azo groups, leaving only one hydrogen atom available for an intermolecular hydrogen bond and inhibiting photoisomerization. In the case of the *para* isomer, the amino group would be able only to interact with the nitrogen atom from the pyridine ring, without including the azo group as an acceptor site. The azo and pyridyl nitrogen acceptors could participate in **C-H**⋯**N** interactions with the proton *ortho* to the azo and amino groups from another molecule. However, the **C-H** contribution as a donor site would not be polarized enough in order to obtain a stable dimer.²⁷ Lastly, the *meta* isomer allows the alignment of the amino group hydrogen atoms toward the opposing azo group and pyridine ring acceptors, which could optimally provide six hydrogen bond interactions in a potential **DDAAA** array.

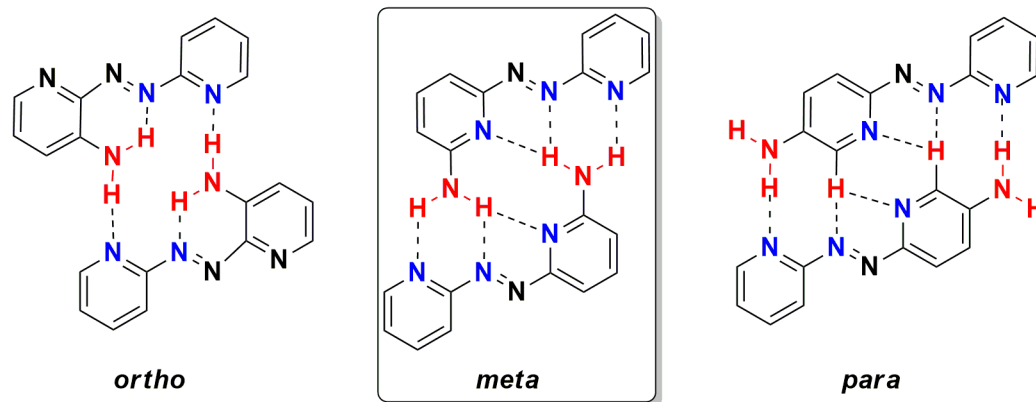


Figure 2.4 Structures of the different locations of a donor group in an azoheteroaromatic backbone and their putative dimers using six-membered azoheteroaromatics.

Based on this model, our first attempts were directed to synthesizing (*E*)-6-(pyridin-2-ylidiazenyl)pyridin-2-amine, the highlighted *meta* isomer in Figure 2.4. However, all known and reported syntheses of azoaromatic compounds were attempted without the desired results. Hence, it was necessary to seek alternatives that provide the structural properties outlined but were more feasible to obtain.

With this in mind, our attention turned to cyanuric chloride (2,4,6-chloro-1,3,5-triazine) which was employed by Whitesides and coworkers as starting material in the synthesis of a variety of melamine derivatives that participate in hydrogen bond arrays.^{28,29,30,31,32} Cyanuric chloride has an advantage over many other heteroaromatic systems due to the possibility to selectively and easily replace each chloride substituent with a nucleophile by controlling the reaction temperature and sequence of nucleophiles applied (Figure 2.5(A)). According to the literature, substitution yields are often over 95% and a trisubstitution is achievable in some cases by one pot synthesis.^{33,34} For the purpose of the desired system, cyanuric chloride offered the opportunity to selectively add: (i) a

donor group, (ii) an RX group, and (iii) an acceptor sites precursor, following a systematic method in order to develop a family of photoswitchable hydrogen bond arrays (Figure 2.5(B)). Likewise, it fulfills the location requirements of donor and acceptor sites in the azoheteroaromatic backbone. Lastly, the addition of an RX group to the photoswitchable hydrogen bond array would allow us to create a library of products wherein the electron withdrawing/donating character of RX could contribute variously to the strength of dimerization.

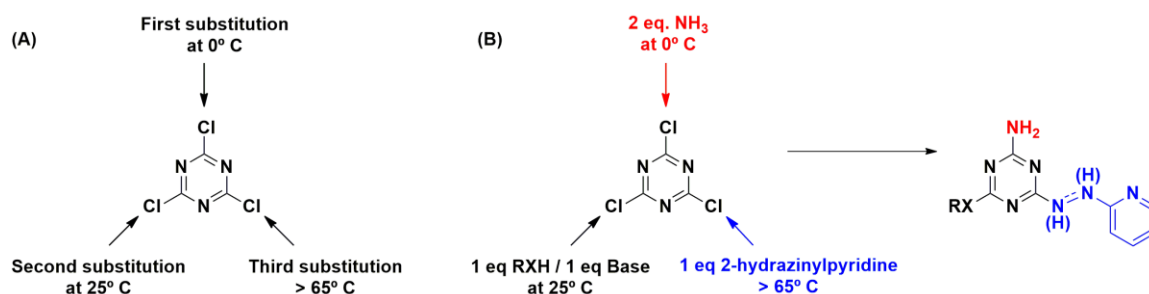
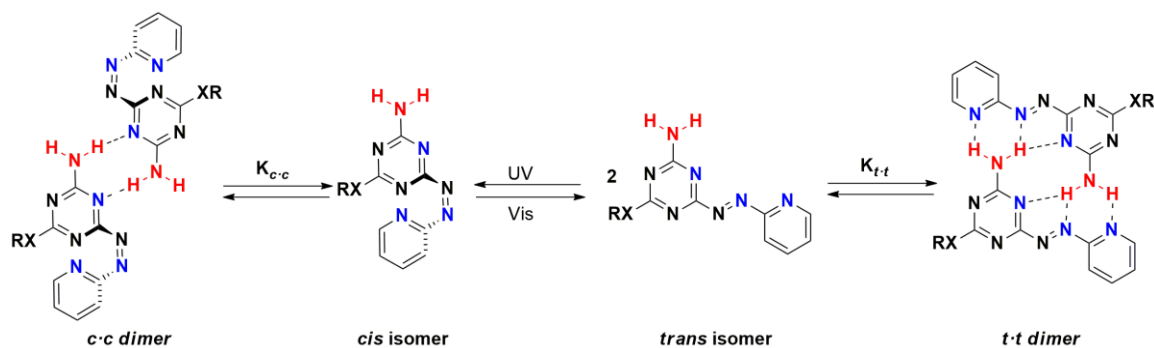


Figure 2.5 (A) Selective systematic substitution of cyanuric chloride at different temperatures. (B) Selective systematic substitution strategy employed.

In this way, the backbone of our photoswitchable self-complementary hydrogen bond array corresponded to the non-symmetrical azoheteroaromatic compound illustrated in Scheme 2.2. The aim of the designed system was to dimerize as the *trans* isomer (or *E* isomer). Control over dimerization would come after irradiating with UV light promoting the formation of *cis* isomer (or *Z* isomer) whose ability to dimerize should be greatly reduced in comparison with the *trans* isomer.

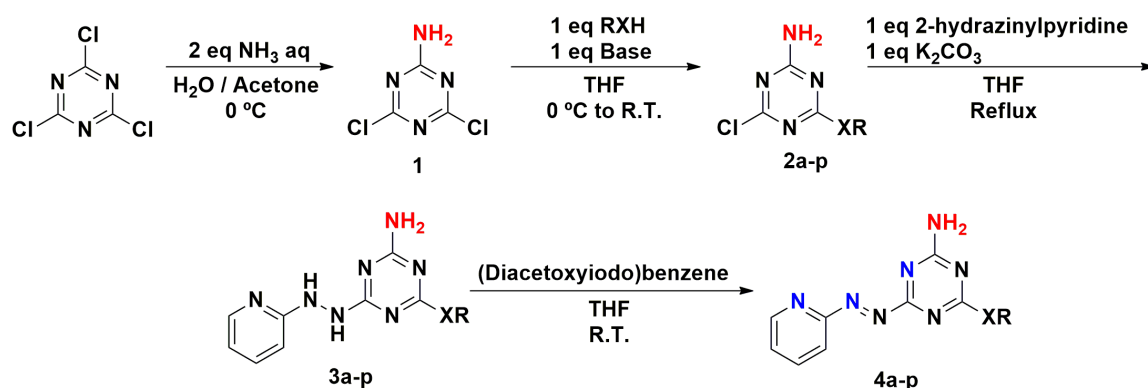


Scheme 2.2 A proposed photoswitchable self-complementary **DDAAA** hydrogen bond array and its idealized function.

2.3 Results and Discussion

2.3.1 Synthesis of Photoswitchable Self-Complementary Hydrogen Bond Arrays

Synthesis of our systems started with cyanuric chloride as shown in Scheme 2.3, and proceeded by typical literature methods.^{34,35}



Scheme 2.3 Synthesis of photoswitchable self-complementary **DDAAA** hydrogen bond arrays **4a-p**.

The first substitution corresponded to the addition of the donor group; i.e. the amino group. Synthesis of intermediate **1** was performed according to a procedure reported by Baliani and coworkers³⁴ to give a 78 % yield in our hands.

Regarding the second substitution, it was our plan to add the acceptor sites' precursor 2-hydrazinylpyridine, and later obtain the azo functionality by oxidation. Finally, we would substitute the final chloride leaving group of a common intermediate with an "RX" group in order to develop a library of arrays. However, after many attempts using this strategy, we concluded that the addition of the RX group was not workable by this synthetic sequence. Therefore, we proceeded to switch the order of addition and add the RX group at the second stage. Selection of the base employed in the second addition was dependent on the pKa of the RX group (Table 2.1). The reaction was carried out initially at low temperature (0 °C). Once the RXH and base were added, the reaction mixture was allowed to slowly reach room temperature. Intermediates **2a-p** were isolated from the reaction mixture after removing the solvent under reduced pressure and washing the crude material with distilled water to remove salts since, in most cases, the intermediates **2a-p** were not soluble in water. With few exceptions, these intermediates did not required further purification in order to proceed with the following steps.

The last substitution performed on the triazine ring was the addition of 2-hydrazinylpyridine in the presence of one equivalent of potassium carbonate in THF. Apart from two exceptions (the chloro- and iodo- derivatives), the reaction mixtures were refluxed for at least 6 hours in order to obtain intermediates **3a-p**. The addition of 2-hydrazinylpyridine to the chloro and iodo intermediates (**2g** and **2h**, respectively) could be carried out at room temperature. As with the intermediates **2a-p**, intermediates **3a-p** were

isolated by removing solvent under reduced pressure and washing the crude material with deionized water. Intermediates **3a-p** were employed in the next step without further purification.

Hydrazines **3a-p** were oxidized in the presence of (diacetoxyiodo)benzene to obtain the desired final products **4a-p**. The (diacetoxyiodo)benzene oxidation can be performed under mild conditions in good yields using a variety of solvent systems, which is an advantage over many other oxidants.^{35,36} In total, there were 16 derivatives synthesized of general structure **4** (Table 2.1).

The characterization of each of the intermediates and final products is located in the Synthetic Methods section at the end of this chapter (Section 2.5.2). The UV-Vis absorption spectra of **4a-p** are described in Chapter 3 wherein the photochemical properties and effects on aggregation are discussed.

Table 2.1 Reactants, yields of intermediates **2a-p** and overall yields of photoswitchable self-complementary hydrogen bond arrays **4a-p**.

Derivative	RXH	Base ^a	Intermediate 2 Yield (%)	Product 4 Overall Yield (%) ^b
4a	Piperidine	(CH ₃ CH ₂) ₃ N	57	13
4b	methanol ^c	NaOCH ₃	81	40
4c	<i>n</i> -butanol	NaH	99	36
4d	<i>n</i> -octanol	NaH	36	8
4e	propargyl alcohol	K ₂ CO ₃	94	19
4f	Hexanethiol	NaOH	76	14
4g^d	-	-	-	74
4h	hydroiodic acid	NaHCO ₃ ^e	42	10
4i	Phenol	NaOH	99	20
4j	4'-nitrophenol	NaOH	97	37
4k	4'- <i>tert</i> -butylphenol	K ₂ CO ₃	59	6
4l	3-(trifluoromethyl)phenol	K ₂ CO ₃	87	15
4m	3,5-bis(trifluoromethyl)phenol	K ₂ CO ₃	96	31
4n	Perfluorophenol	K ₂ CO ₃	92	23
4o	benzyl alcohol	NaH	99	14
4p	4-tritylphenol	K ₂ CO ₃	71	8

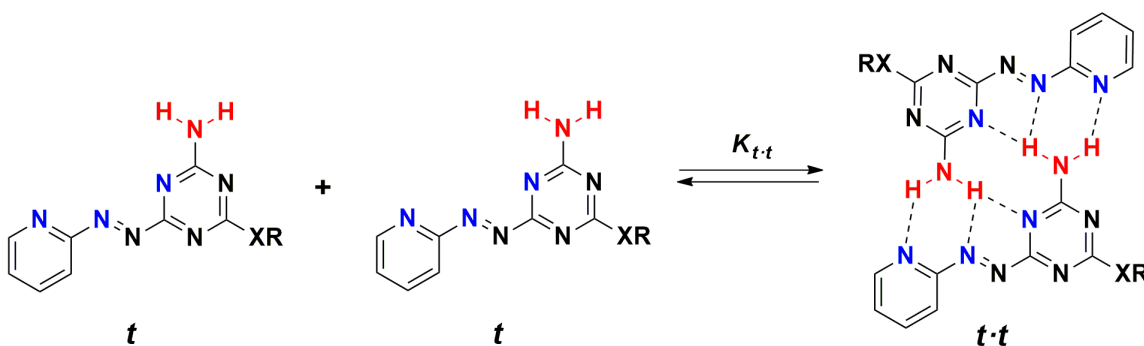
^a One equivalent added at 0 °C. ^b Percent yield over 3 synthetic steps starting from intermediate **1**. ^c Excess (Solvent system). ^d Chloro is already in place in intermediate **1**.

^e Base added until acid was neutralized.

2.3.2 ^1H NMR Dilution Experiments: Stability of *trans-trans* dimers.

Once the syntheses of our proposed hydrogen bond arrays were achieved, we proceeded to the study of their dimerization in solution.

Dimerization is a dynamic process represented by Scheme 2.4, wherein the dimerization constant ($K_{t \cdot t}$) is calculated from *trans* monomer ($[t]$) and *trans* dimer ($[t \cdot t]$) concentrations at equilibrium and described by Equation 1.



Scheme 2.4 Dimerization equilibrium of **4a-p**.

$$K_{t \cdot t} = \frac{[t \cdot t]}{[t]^2} \quad \text{Equation 1}$$

Experimentally, dimerization constants are calculated based on the change of an observed physical property.³⁷ In the present case, the physical property observed was the chemical shift of the proton signals from the amino group. As a dimer is formed, hydrogen bond interactions decrease the electron density of these protons, which leads to a deshielding effect detected in the ^1H NMR spectrum.³⁸

The observed chemical shift (δ_{obs}), is a weighted average of the chemical shift of monomer (δ_m) and dimer (δ_d) in solution (Equation 2)³⁹ when complexation is fast on the NMR timescale.

$$\delta_{obs} = \delta_m \cdot \frac{[t]}{[t]_0} + \delta_d \cdot \frac{2 \cdot [t \cdot t]}{[t]_0} \quad \text{Equation 2}$$

$$[t]_0 = [t] + 2 \cdot [t \cdot t] \quad \text{Equation 3}$$

In this way, it is possible to monitor changes in the observed chemical shift while increasing the total monomer concentration, $[t]_0$. The dependency of the observed chemical shift on monomer total concentration allows the use of an iterative fitting procedure to calculate monomer shift, dimer shift and dimerization constant.³⁹ The method consists in fitting the relationship between experimental data δ_{obs} versus $[t]_0$ (also known as dimerization isotherm, Figures 2.9, 2.10, 2.14 and 2.15) to a dimerization model (Equation 4).

$$\delta_{obs} = \delta_m + (\delta_d - \delta_m) \cdot \frac{[1 + 8 \cdot K_{tt} \cdot [t]_0]^{1/2} - 1}{[1 + 8 \cdot K_{tt} \cdot [t]_0]^{1/2} + 1} \quad \text{Equation 4}$$

In addition to precisely measured experimental data, there are other elements to consider before the experiment:⁴⁰

- (i) Reliability of the method. ¹H NMR determinations of association and dimerization constants are typically reliable in the range $1 - 10^5 \text{ M}^{-1}$. Small association and dimerization constants (lower than 10 M^{-1}) often involve large $\Delta\delta_{max}$ extrapolation errors. On the other hand, supramolecular complexes with

large association constants ($>10^5 \text{ M}^{-1}$) show little curvature at detectable concentrations which makes it difficult to fit to an isotherm.

- (ii) The difference between monomer and dimer chemical shifts needs to be as large as possible to be considered significantly different; i.e. total $\Delta\delta \geq 0.5 \text{ ppm}$ (the accuracy of the method depends on the spectrometer resolution; e.g. in a 400 MHz ^1H NMR spectrum a sharp singlet can be measured with an accuracy of $\approx \pm 0.005 \text{ ppm}$).
- (iii) Concentration increments. The range of data obtained in a dilution experiment should provide good coverage of the isotherm. In this sense, it has been demonstrated that it is advisable to collect a minimum of 10 data points within a range of 20% to 80% of the complex concentration in a dilution experiment.⁴¹

In the present case, dilution experiments with **4a-p** were performed in CDCl_3 , with the exception of **4b**, **4e**, **4g**, **4h** and **4j** due to insolubility (Table 2.2). Additionally, dilution experiments with **4c**, **4f**, **4k** and **4n** were also performed in toluene- d_8 since they were soluble in this solvent (Table 2.3). The general experiment consisted of adding aliquots of a highly concentrated solution of **4** to an NMR tube filled with 500 μL of pure solvent. Thus, as the concentration of **4** increased, the chemical shifts of the amino protons increased (i.e. moved downfield, Figure 2.6 and 2.7).

Table 2.2 Dimerization constants, free energies of dimerization, calculated chemical shifts of monomer (δ_m) and dimer (δ_d) species studied, and the total change in chemical shift ($\Delta\delta_{max}$) in $CDCl_3$ at 298 K.

Derivative	RX	K_{t-t} in $CDCl_3$ (M^{-1}) ^a	ΔG_{t-t} ($kJ\ mol^{-1}$) ^a	δ_m (ppm) ^a	δ_d (ppm) ^a	$\Delta\delta_{max}$ (ppm)
4a	-NC ₅ H ₁₀	8.4 ± 2	-5.27 ± 0.66	5.14 (2H)	6.92 (2H)	1.78 ^b
4c	-O(<i>n</i> -C ₄ H ₉)	32 ± 7	-8.61 ± 0.57	5.49 (2H)	6.80	1.31
					8.76	3.27 ^b
4d	-O(<i>n</i> -C ₈ H ₁₇)	36 ± 5	-8.87 ± 0.36	5.50	6.78	1.28
				5.54	8.78	3.24 ^b
4f	-S(<i>n</i> -C ₆ H ₁₃)	32 ± 3	-8.62 ± 0.22	5.38	6.80	1.42
				5.48	8.67	3.19 ^b
4i	-OC ₆ H ₅	59 ± 11	-10.10 ± 0.48	5.55	6.77	1.22
				5.63	8.05	2.42 ^b
4k	-OC ₆ H ₄ -4'-C(CH ₃) ₃	50 ± 7	-9.68 ± 0.36	5.53	6.70	1.17
				5.56	8.04	2.48 ^b
4l	-OC ₆ H ₄ -3'-CF ₃	62 ± 1	-10.24 ± 0.05	5.57	6.80	1.23
				5.68	8.67	2.99 ^b
4m	-OC ₆ H ₃ -3',5'-bis(CF ₃)	96 ± 6	-11.31 ± 0.16	5.63	6.57	0.95
				5.79	7.45	1.66 ^b
4n	-OC ₆ F ₅	180 ± 14	-12.92 ± 0.19	5.67	6.48	0.80
				5.81	7.82	2.00 ^b
4o	-OCH ₂ C ₆ H ₅	49 ± 8	-9.63 ± 0.39	5.54	7.08	1.54
				5.56	8.85	3.29 ^b
4p	-OC ₆ H ₄ -4'-(C(C ₆ H ₅) ₃)	64 ± 25	-10.28 ± 0.94	5.56	6.68	1.12
				5.64	8.01	2.37 ^b
5c	-O(<i>n</i> -C ₄ H ₉)	5.5 ± 0.3	-4.43 ± 0.14	5.53	6.87	1.34
				5.67	7.92	2.25 ^b
5f	-S(<i>n</i> -C ₆ H ₁₃)	4.8 ± 0.9	-3.90 ± 0.45	5.50	5.70	0.20
				5.49	7.98	2.49 ^b
5k	-OC ₆ H ₄ -4'-C(CH ₃) ₃	11 ± 3	-5.85 ± 0.73	5.53	6.80	1.27
				5.65	7.41	1.76 ^b

^a Average values obtained using Equation 5 and three separate dilution experiments. Errors calculated from twice the standard deviation to give a 95% confidence interval

^b Resonance used in fitting process assigned to the H_a proton in Figure 2.8.

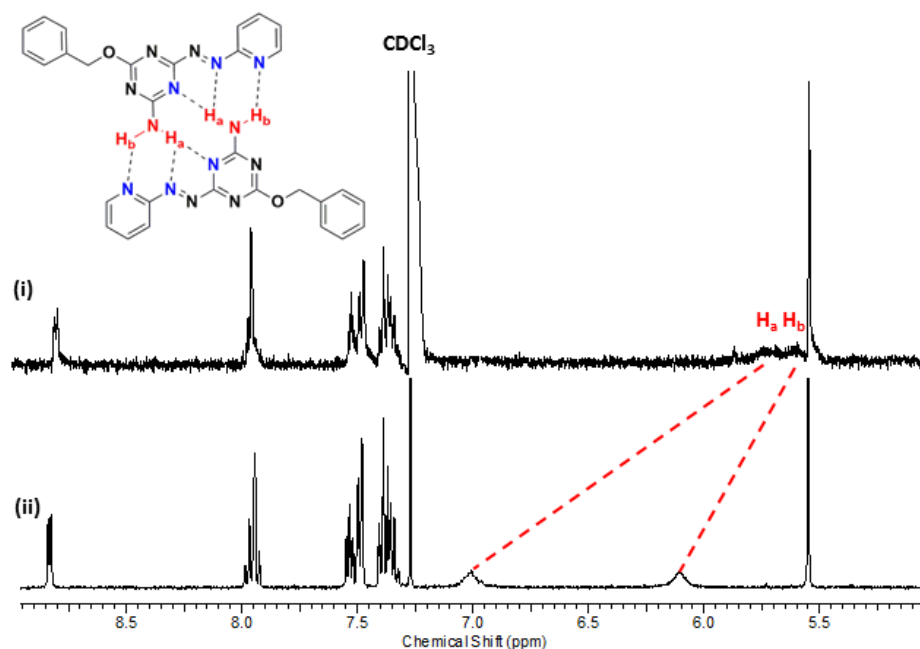


Figure 2.6 ^1H NMR spectra displaying the concentration-dependent behavior of **4o** in CDCl_3 at 298 K. (i) 5.59×10^{-4} M, and (ii) 1.61×10^{-2} M.

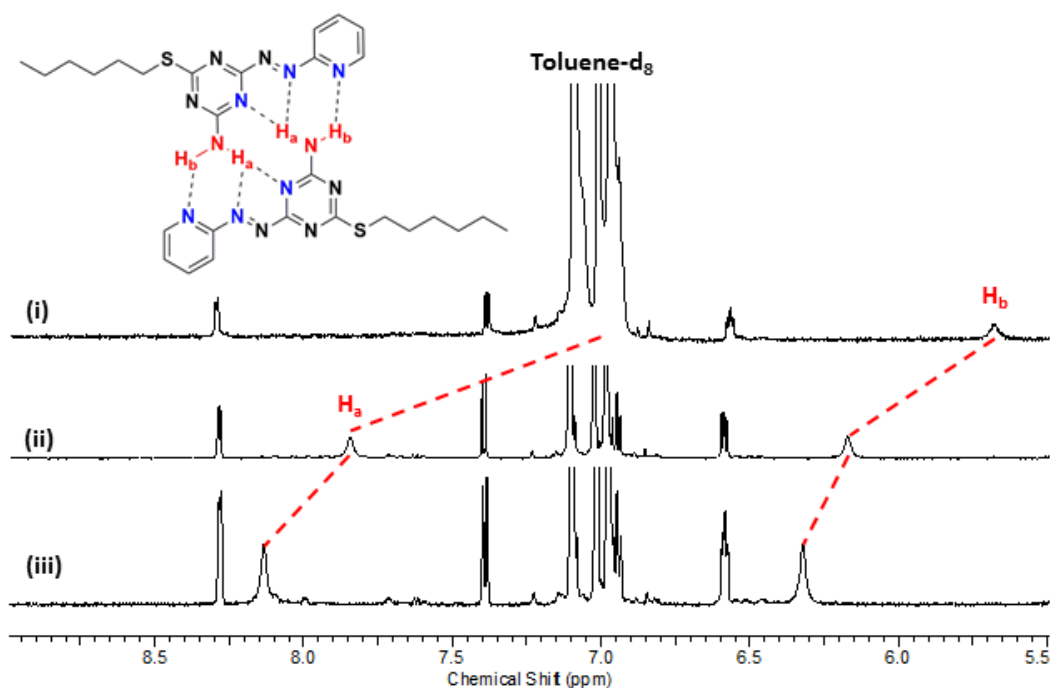


Figure 2.7 ^1H NMR spectra displaying the concentration-dependent behavior of **4f** in $\text{Toluene-}d_8$ at 298 K. (i) 2.45×10^{-3} M (H_a signal covered by the toluene reference signal), (ii) 8.56×10^{-3} M, and (iii) 1.61×10^{-2} M.

Once experimental data for a dilution experiment was collected, an iterative fitting process of the dimerization isotherm was performed on the chemical shift observations. Generally, the proton signal chosen to fit the isotherm was that showing the largest change during the dilution experiment and the one that was not occluded by solvent signals during the dilution. This signal was tentatively assigned as proton **H_a** since it was expected to interact with two acceptor sites forming a donating bifurcated hydrogen bond (Figure 2.8); and therefore, the deshielding effect on that proton would be anticipated to be larger than **H_b** as the solution becomes more and more concentrated. Compound **4a** was the only exception since it showed only one signal which integrated for both amino protons over the entire dilution. It is important to note that ¹H NOESY experiments were carried out in order to corroborate the proximity of the **H_b** proton with the proton *ortho*- to the pyridyl nitrogen. However, no correlation peak between these protons was observed in these experiments for derivatives **4a**, **4c**, **4f**, **4k** and **4n**.

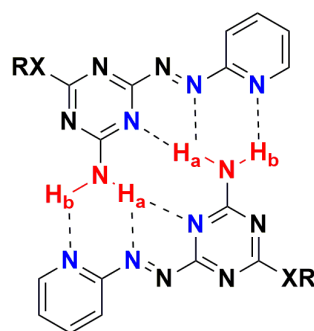


Figure 2.8 Amino's proton assignment based on chemical shift in compounds **4a-p**.

As can be observed in Table 2.2, dimerization constants in CDCl₃ ranged from 8.4 to 180 M⁻¹; wherein the weakest dimerization isotherm calculated corresponded to the piperidin-1-yl derivative **4a** (Figure 2.9) and the strongest corresponded to the

perfluorophenoxy derivative **4n** (Figure 2.10). From the range of results obtained, we generally observed that as stronger electron withdrawing moieties were added as substituent RX, dimerization constants increased. For example, phenoxy derivative **4i** showed a dimerization constant of 59 M^{-1} ; meanwhile, the inclusion of two *meta*-trifluoromethyl groups to the phenyl ring increased the $K_{t,t}$ value to 96 M^{-1} for derivative **4m**. Thus, the perfluorophenoxy derivative **4n** had the highest dimerization constant of those studied ($K_{t,t} = 180 \text{ M}^{-1}$).

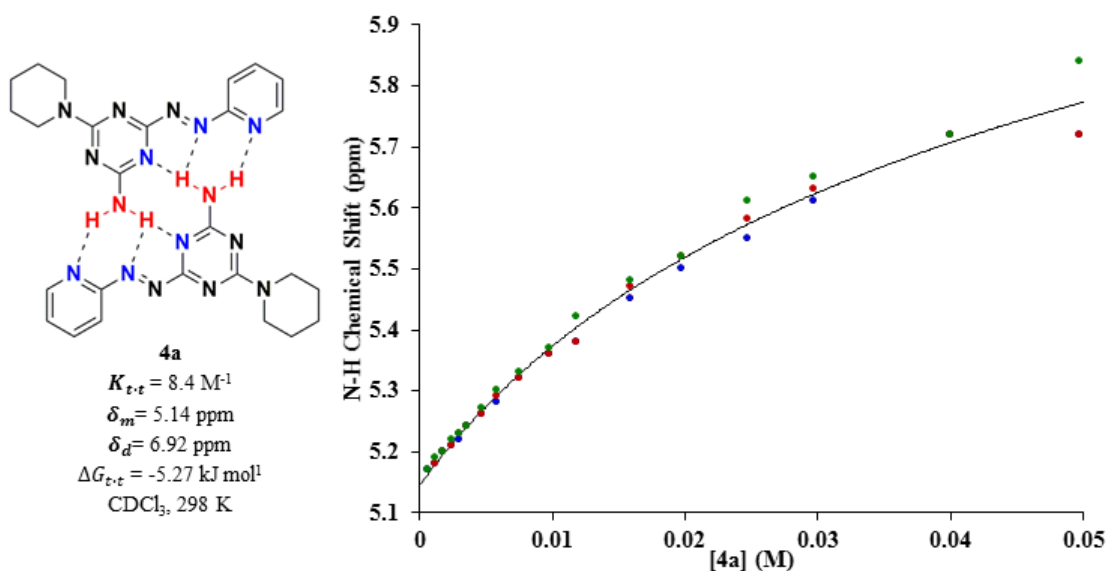


Figure 2.9 Dimerization isotherm of **4a** with $K_{t,t}$ value and free energy calculated from fitting of the data to a 1:1 dimerization model. Blue, green and red dots correspond to first, second and third separate dilution experiments, respectively. Solid line corresponds to the theoretical dilution curve obtained from the average $K_{t,t}$ of three separate dilution experiments.

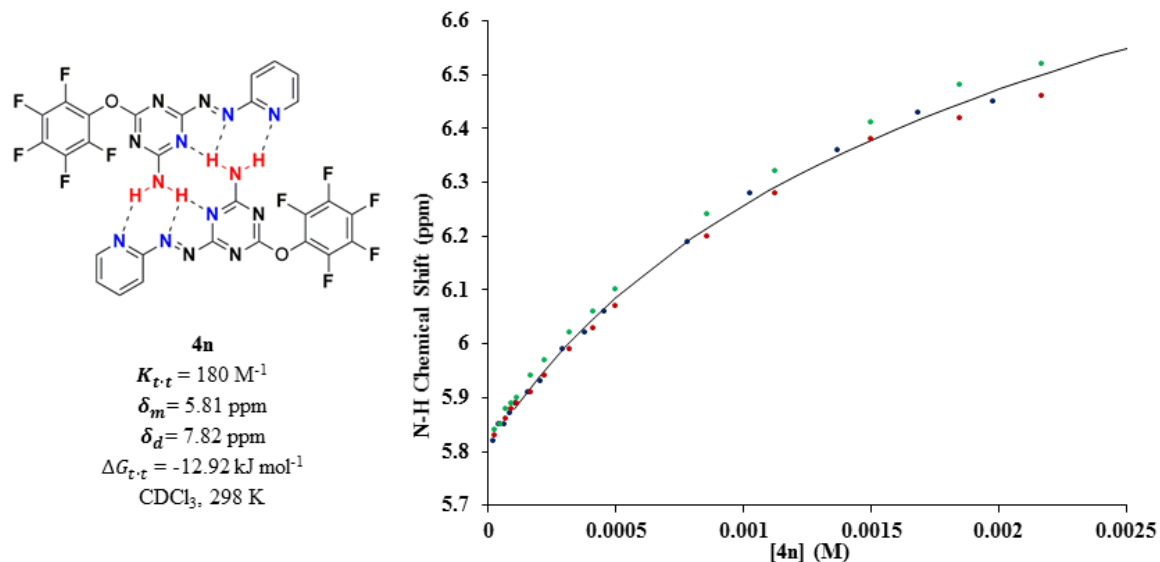


Figure 2.10 Dimerization isotherm of **4n** with $K_{t,t}$ value and free energy calculated from fitting of the data to a 1:1 dimerization model. Blue, green and red dots correspond to first, second and third separate dilution experiments, respectively. Solid line corresponds to the theoretical dilution curve obtained from the average $K_{t,t}$ of three separate dilution experiments.

Given the range of data gathered for the dimerizations in solution, we were interested in whether the characters of the substituents in derivatives **4a-p** could be correlated with our results. To this end, the maximum change in the chemical shift of all the derivatives **4a-p** in CDCl_3 was plotted against $\Delta G_{t,t}$ (Figure 2.11). From this plot, it was observed that there is a roughly linear correlation between these two values ($r = 0.81396$); i.e. as the difference between monomer and dimer chemical shift increases, the $\Delta G_{t,t}$ also increases. Interestingly, the derivative with the lowest dimerization constant (the piperidine derivative **4a**) was an obvious outlier from this trend.

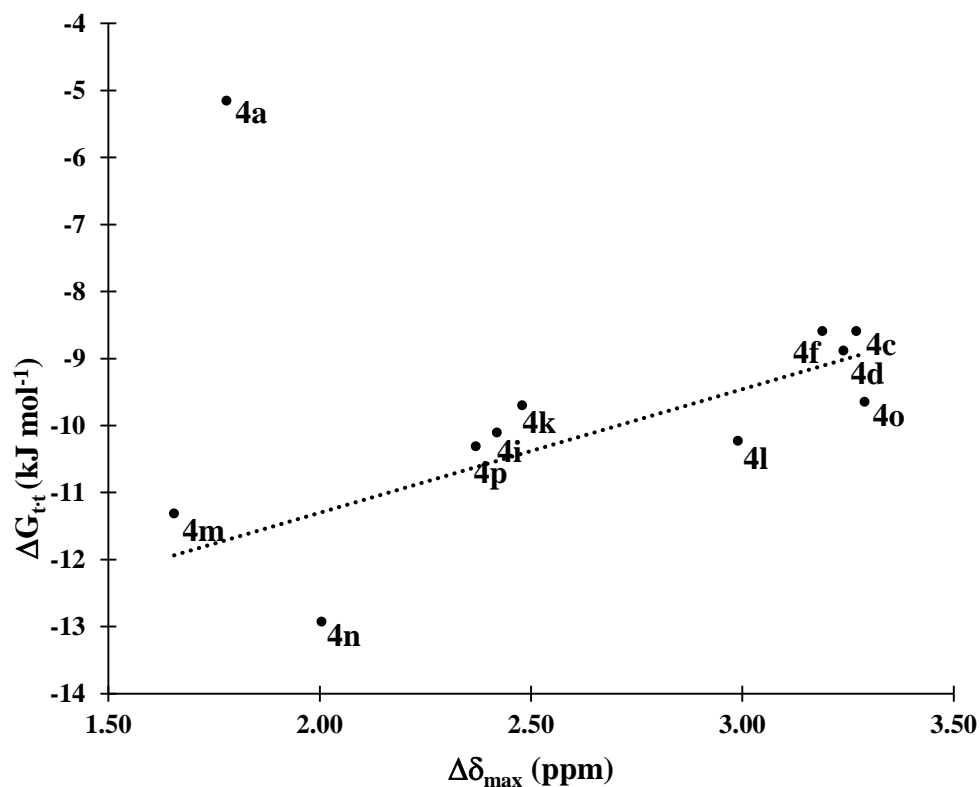


Figure 2.11 Plot of ΔG_{t-t} vs $\Delta\delta_{\max}$ for derivatives **4a-p** in CDCl_3 at 298 K. Dotted line corresponds to the linear least squares correlation for derivatives **4a-p** excluding **4a** ($r = 0.81396$).

Another correlation explored corresponded to the σ_m values of the RX moieties in derivatives **4c** and **4i** and the approximation to the σ_m values of the RX moieties in derivatives **4a**, **4d**, **4f**, **4k** and **4n** with the free energy of dimerization ΔG_{t-t} ($r = -0.9725$, Figure 2.12).⁴² In this sense, it was noted that as the σ_m value increases, the ΔG_{t-t} value decreases. Since σ_m is the major contributor to the inductive parameter (I),⁴³ a very similar relationship is observed between I and ΔG_{t-t} ($r = -0.9699$, Figure 2.13). This observation is in agreement with the influence of the inductive withdrawing effect ($-I$) of the RX substituents evaluated. The inductive withdrawing effect polarizes the amino N-H bonds increasing their donor strength, which contributes to the stability of the dimer structure.

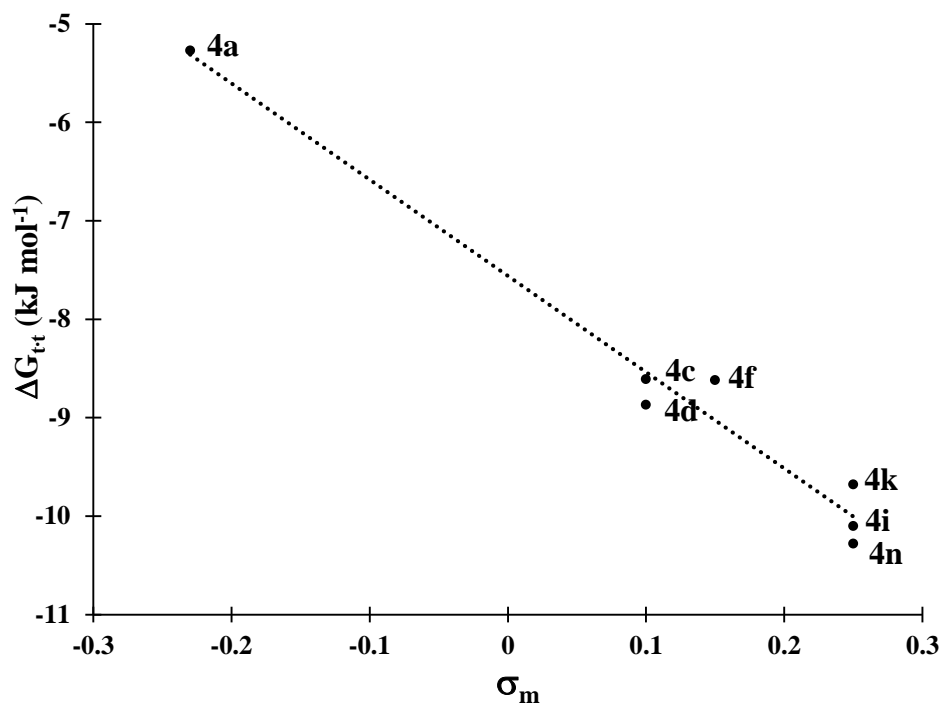


Figure 2.12 Plot of ΔG_{t-t} vs σ_m of derivatives **4a**, **4c**, **4d**, **4f**, **4i**, **4k** and **4n** in CDCl_3 at 298 K. Dotted line corresponds to the least squares correlation line ($r = -0.9861$).

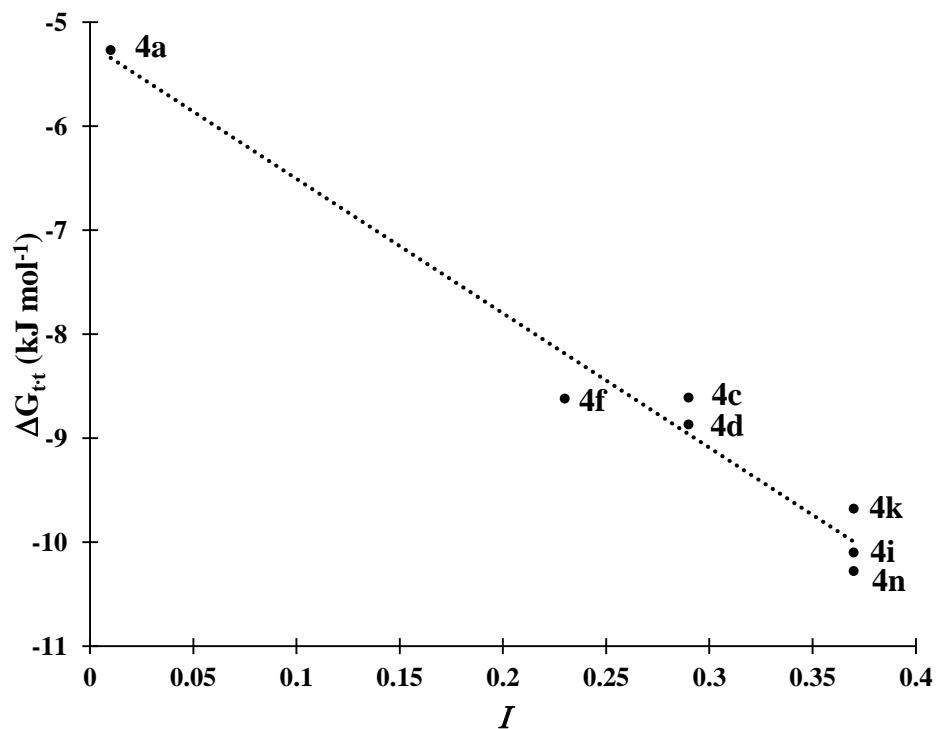
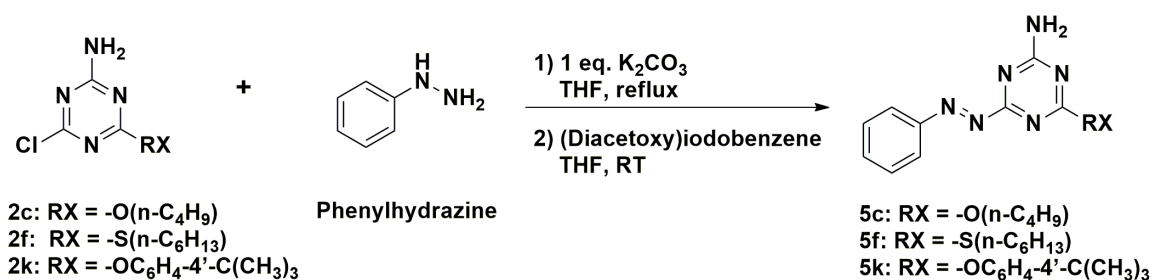


Figure 2.13 Plot of ΔG_{t-t} vs I of derivatives **4a**, **4c**, **4d**, **4f**, **4i**, **4k** and **4n** in CDCl_3 at 298 K. Dotted line corresponds to the least squares correlation line ($r = -0.9848$).

Considering the design of the system and based on the number of hydrogen bond interactions expected in the array, it was disappointing to observe dimerization constants lower than 10^2 M^{-1} in CDCl_3 . In this sense, it raised the issue of whether the pyridine ring was participating as an acceptor in the complexation. To probe this interaction, phenyl analogues **5c**, **5f** and **5k** were synthesized in order to eliminate the interaction of the pyridine acceptor in the dimerization equilibrium (Scheme 2.5).



Scheme 2.5 Synthesis of (*E*)-6-(phenyldiazenyl)-1,3,5-triazin-2-amine, derivatives **5c**, **5f** and **5k**.

Compounds **5c**, **5f** and **5k** exhibited dimerization constants of 6, 5 and 11 M^{-1} respectively, which are comparable with the weakest constant obtained for array **4a**. Likewise, comparing **5c**, **5f** and **5k** with derivatives **4c**, **4f** and **4k**, it is observed that derivatives **4** have dimerization constants at least fourfold larger than **5** (Table 2.2). In this sense, it is important to outline that the main difference between derivatives **4** and **5** is the absence of an extra hydrogen bond acceptor in the latter. This can be translated as an energetic contribution of approximately 4 kJ mol^{-1} in CDCl_3 ($\Delta\Delta G_{\text{Butoxy}} = -4.18 \text{ kJ mol}^{-1}$, $\Delta\Delta G_{\text{Hexylthiol}} = -4.72 \text{ kJ mol}^{-1}$, and $\Delta\Delta G_{4'\text{-tert-butylphenoxy}} = -3.83 \text{ kJ mol}^{-1}$) from both pyridine moieties (or 2 kJ mol^{-1} per pyridine moiety) to the dimerization event in this case.

Table 2.3 Dimerization constants, free energies of dimerization, calculated chemical shifts of monomer (δ_m) and dimer (δ_d) species studied, and the total change in chemical shift ($\Delta\delta_{max}$) in Toluene- d_8 at 298 K.

Derivative	RX	K_{t-t} in Toluene- d_8 (M^{-1}) ^a	ΔG_{t-t} (kJ mol ⁻¹)	δ_m (ppm) ^a	δ_d (ppm) ^a	$\Delta\delta_{max}$ (ppm)
4c	-O(<i>n</i> -C ₄ H ₉)	900 ± 70	-16.80 ± 0.20	4.33	7.13	2.80 ^b
				4.42	9.47	5.05
4f	-S(<i>n</i> -C ₆ H ₁₃)	590 ± 90	-15.80 ± 0.38	4.11	6.89	2.78 ^b
				4.14	9.20	5.06
4k	-OC ₆ H ₄ -4'-C(CH ₃) ₃	1200 ± 600	-17.70 ± 1.15	4.12	6.97	2.85 ^b
				4.23	8.94	4.71
4n	-OC ₆ F ₅	3700 ± 280	-20.35 ± 0.19	4.02	6.25	2.23 ^b
				4.61	8.72	4.11
5c	-O(<i>n</i> -C ₄ H ₉)	18 ± 1	-7.16 ± 0.04	4.29	7.15	2.86 ^b
				4.34	8.46	4.12
5f	-S(<i>n</i> -C ₆ H ₁₃)	26 ± 2	-8.13 ± 0.19	4.18	6.21	2.03
				4.16	7.94	3.78 ^b
5k	-OC ₆ H ₄ -4'-C(CH ₃) ₃	46 ± 7	-9.46 ± 0.42	4.11	6.39	2.28
				4.23	7.37	3.14 ^b

^a Average values obtained using Equation 5 and three separate dilution experiments. Errors calculated from two times the standard deviation to give a 95% of confidence interval ^b Resonance used in fitting process assigned to H_b in Figure 2.8.

Dimerization constants obtained for **4c**, **4f**, **4k** and **4n** in toluene- d_8 were significantly higher than the values obtained in CDCl₃ (Table 2.3). The range of dimerization constant values was from 600 to 3700 M⁻¹. These results can be rationalized based on the hydrogen bond donor character of the solvent system wherein the intermolecular interactions take place. Comparing chloroform and toluene as solvents for complexation, chloroform is known as a better hydrogen bond donor ($\alpha_{CHCl_3} = 2.2$, $\alpha_{Benzene} = 1.0$).⁴⁴ Since compounds **4a-p** have more acceptors than donors, chloroform likely forms stronger solute-solvent complexes than toluene. Therefore, the energetic cost to break these strong solute-solvent interactions would be reflected by lower dimer stability in CDCl₃. This is in agreement with the dimerization values obtained in CDCl₃ and toluene- d_8 .

An effect of the RX group character was also observed in differences between $K_{t,t}$ values of derivatives **4**. For example, perfluorophenoxy derivative **4n** displayed the highest dimerization constants in CDCl_3 and toluene- d_8 due to the electron withdrawing effect of the five fluorine substituents. On the other hand, the derivatives **4c** and **4f** showed nearly identical $K_{t,t}$ values in CDCl_3 . However, in toluene- d_8 $K_{t,t}$ for **4c** was higher (900 M^{-1}) than that for **4f** (590 M^{-1}). This difference is also in agreement with the electron withdrawing nature of the alkoxy group compared with the thiol group. Both substituents have as heteroatom an element of the same group; i.e. oxygen and sulfur. Since oxygen is the more electronegative element, it has a higher electron withdrawing inductive effect ($-I$)⁴² on the amino group polarizing the N-H bond. Conversely, both elements hold lone pairs of electrons that can provide an electron donating resonance effect ($+R$) to the nitrogen acceptor in the triazine ring. In this case, oxygen also provides a greater resonance effect due to a better orbital overlap with the π -bonds of the heteroaromatic ring (all elements of the second row) compared with sulfur (element of the third row). Hence; both effect favor the oxygen substituent as having the higher $K_{t,t}$.

Lastly, Table 2.3 can be used to estimate the effect of the hydrogen bond acceptor site located on the pyridine ring in toluene- d_8 . Compounds **5c**, **5f** and **5k** displayed dimerization constants of 18, 26 and 46 M^{-1} , respectively (e.g. dimerization isotherm of **5c**, Figure 2.14); meanwhile, **4c**, **4f** and **4k** had values of 900, 590 and 1200 M^{-1} (e.g. dimerization isotherm of **4c**, Figure 2.15). That is, the energetic contribution of the extra acceptor can be estimated to be approximately 8 kJ mol^{-1} in toluene- d_8 ($\Delta\Delta G_{\text{Butoxy}} = -9.64 \text{ kJ mol}^{-1}$, $\Delta\Delta G_{\text{Hexylthiol}} = -7.67 \text{ kJ mol}^{-1}$, and $\Delta\Delta G_{4\text{-tert-butylphenoxy}} = -8.24 \text{ kJ mol}^{-1}$); or 4 kJ mol^{-1} .

mol^{-1} per pyridine ring. The higher value in this solvent is again likely reflective of the reduced solvent competition for the acceptor sites.

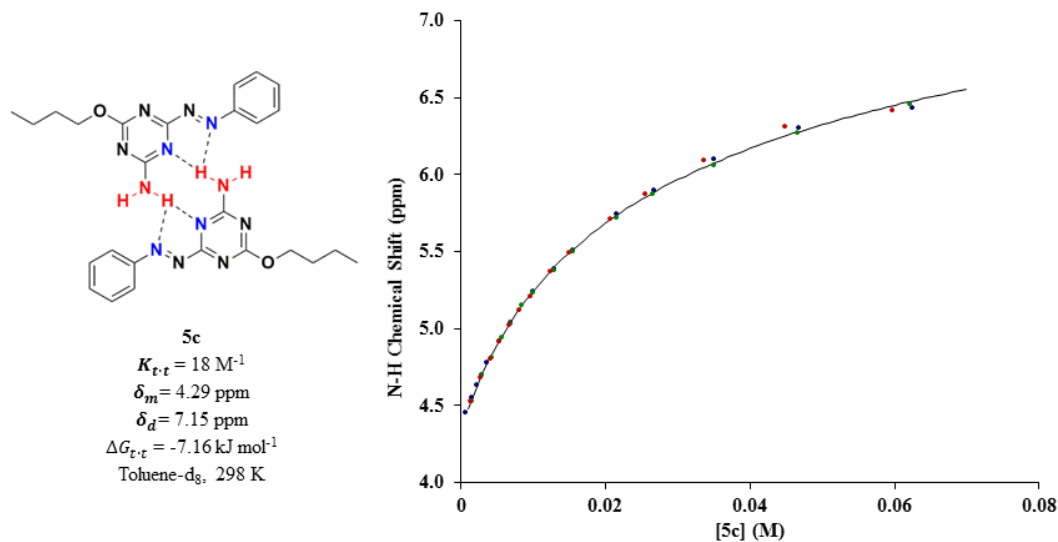


Figure 2.14 Dimerization isotherm of **5c** with $K_{t,t}$ value and free energy calculated from fitting of the data to a 1:1 dimerization model. Blue, green and red dots correspond to first, second and third separate dilution experiments, respectively. Solid line corresponds to the theoretical dilution curve obtained from the average $K_{t,t}$ of three separate dilution experiments.

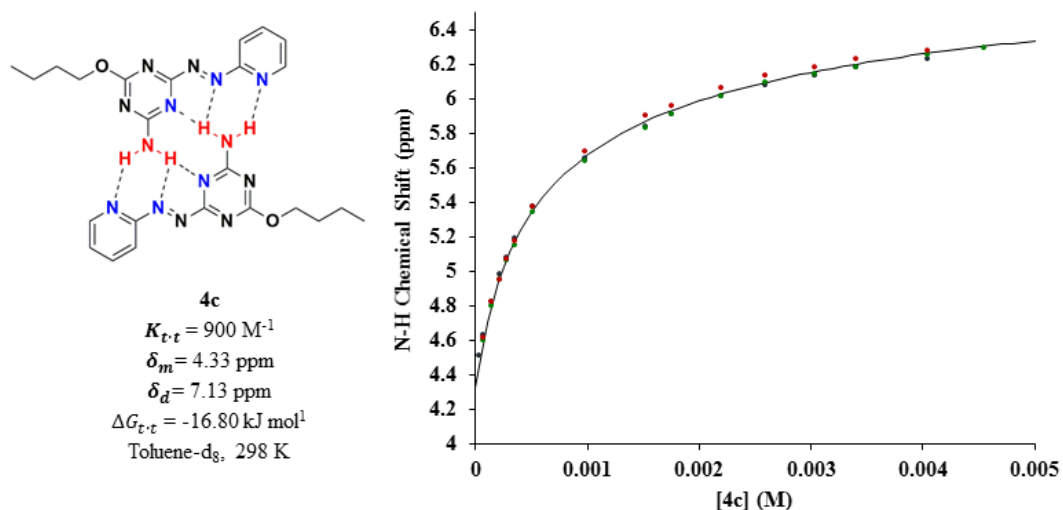


Figure 2.15 Dimerization isotherm of **4c** with $K_{t,t}$ value and free energy calculated from fitting of the data to a 1:1 dimerization model. Blue, green and red dots correspond to first, second and third separate dilution experiments, respectively. Solid line corresponds to the theoretical dilution curve obtained from the average $K_{t,t}$ of three separate dilution experiments.

2.3.3 X-Ray Analysis of Self-Complementary Arrays.

Single crystal X-ray diffraction is potentially useful to corroborate our proposed dimer structure in the solid state. In this case, we were able to obtain X-ray crystal structures of **4a**, **4d**, **4f** and **4k** (Table 2.4). Crystal growth was carried out by slow evaporation or slow diffusion using various dry solvents or solvent mixtures. The solvent selection was based on solubility; i.e. most of **4a-p** were highly soluble in CHCl_3 , CH_2Cl_2 , ethyl acetate and acetone, and poorly soluble or not soluble in toluene, hexanes and diisopropyl ether. In a typical crystal growing experiment 20 mg of **4** was dissolved in approximately 5 mL of a chosen solvent. The resulting solution was divided into four small vials. One of them was loosely capped for slow solvent evaporation. Each of the remaining vials was placed into a larger vial surrounded by either hexanes, toluene or diisopropyl ether, and tightly capped for slow diffusion. Vials were monitored regularly for the appearance of X-ray quality single crystals.

Table 2.4 Crystallographic parameters for **4a**, **4d**, **4f** and **4k** crystals.

	4a	4d	4f	4k
Chemical Formula	C ₁₃ H ₁₆ N ₈	C ₁₆ H ₂₃ N ₇ O	C ₁₄ H ₁₉ N ₇ S	C ₁₉ H ₂₀ Cl ₃ N ₇ O
Molecular Weight (g·mol ⁻¹)	284.34	329.41	317.42	468.77
Crystal System	Triclinic	Triclinic	Triclinic	Monoclinic
Space Group	<i>P</i> $\bar{1}$	<i>P</i> $\bar{1}$	<i>P</i> $\bar{1}$	<i>P</i> 2 ₁ / <i>n</i>
<i>a</i> (Å)	8.157 (3)	13.101 (3)	7.5968 (9)	13.7969 (17)
<i>b</i> (Å)	8.489 (2)	13.726 (4)	10.8490 (10)	17.697 (3)
<i>c</i> (Å)	10.736 (3)	15.153 (5)	13.2133 (17)	18.179 (3)
α (°)	67.693 (12)	83.268 (10)	66.494 (7)	90
β (°)	79.709 (11)	82.181 (11)	83.486 (6)	100.985 (7)
γ (°)	89.079 (10)	74.493 (10)	71.772 (5)	90
<i>V</i> (Å ³)	675.6 (4)	2591.9 (12)	948.44 (19)	4357.4
<i>Z</i>	2	6	2	8
F(000)	300	1056	336	1936
<i>T</i> (K)	110	110	173	110
λ (Å)	0.71073	0.71073	1.54178	1.54178
ρ_{calc} (g·cm ⁻³)	1.398	1.266	1.111	1.429
μ (mm ⁻¹)	0.094	0.085	1.571	4.031
Reflections Collected	35366	129610	14138	52827
Unique Reflections	5981	19753	3179	7640
Absorption Correction	multi-scan	multi-scan	multi-scan	multi-scan
Refinement on	<i>F</i> ²	<i>F</i> ²	<i>F</i> ²	<i>F</i> ²
Parameters Refined	198	925	275	586
<i>R</i> (<i>F</i> _o)(<i>I</i> > 2σ(<i>I</i>))	0.0614	0.0576	0.0304	0.0514
<i>R</i> _w (<i>F</i> _o ²)(<i>I</i> > 2σ(<i>I</i>))	0.1623	0.1456	0.0847	0.1363
<i>R</i> (<i>F</i> _o)(all data)	0.1126	0.1044	0.0334	0.0640
<i>R</i> _w (<i>F</i> _o ²)(all data)	0.1867	0.1735	0.0886	0.1482
GOF on <i>F</i> ²	1.063	1.016	1.058	1.031

Piperidine derivative **4a** was crystallized by the slow evaporation of a chloroform solution to yield deep red plates that were suitable for single crystal X-ray diffraction analysis. The collected data was modeled in space group $P\bar{1}$ and yielded a structure with two symmetry-related molecules per unit cell. The two molecules take up the anticipated dimer configuration in which the self-complementary arrays pair up in an antiparallel manner through hydrogen bonds (Table 2.5) to stabilize a complex with inversion symmetry. The least squares planes of the aminotriazine rings in the complex are offset from each other by 0.79 Å and participate in a symmetry related pair of hydrogen bonds ($\text{N6-H6B}\cdots\text{N7}' = 3.16 \text{ \AA}$; $\angle\text{N-H}\cdots\text{N} = 168^\circ$). The dimer is further stabilized by more oblique hydrogen bond interactions between the amino N-H donors and the azo ($\text{N6-H6B}\cdots\text{N2}' = 3.01 \text{ \AA}$; $\angle\text{N-H}\cdots\text{N} = 118^\circ$) and pyridyl ($\text{N6-H6A}\cdots\text{N1}' = 3.55 \text{ \AA}$; $\angle\text{N-H}\cdots\text{N} = 135^\circ$) nitrogen acceptors. It is also notable that the distance from H6A to the nearest opposing pyridyl proton (H5') is 4.15 Å, likely outside or at the distance limit for detection by a ^1H NMR NOESY experiment. This is supported by the absence of such a contact when this dimer was subjected to NOESY analysis (see Section 2.3.2). The dimer takes up the expected disposition of complementary hydrogen bonds but is distorted from a (presumably) ideal planar arrangement of the two molecules. Deviations from coplanarity of the azo group and the adjacent heterocyclic rings (11° and 27° for pyridine and triazine, respectively) result in interplanar angles between the two rings of 44° both in an intramolecular and intermolecular sense in the dimer due to the symmetry of the space group. There are no other notable non-covalent interactions observed in the extended lattice structure between dimers.

Table 2.5 Hydrogen bond distances and angles of complex **4a**·**4a** X-ray crystal structure data.

D...A	d <u>NH</u> ... <u>N</u> (Å)	d <u>NH</u> ... <u>N</u> (Å)	∠ <u>NH</u> ... <u>N</u> (°)
N6-H6B...N7'	3.1551 (8)	2.3071 (6)	167.677 (34)
N6-H6B...N2'	3.0115 (7)	2.5070 (7)	118.145 (25)
N6-H6A...N1'	3.5477 (10)	2.8770 (8)	134.659 (20)

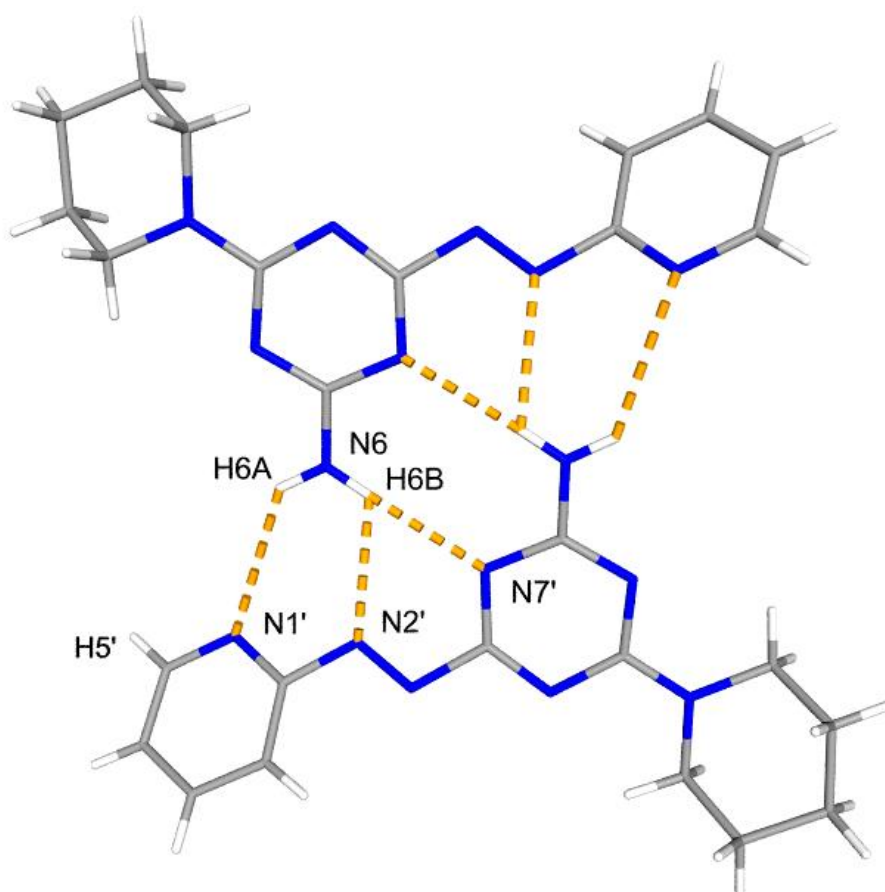


Figure 2.16 Stick representation of the X-ray crystal structure of **4a** dimer with intermolecular hydrogen bonds indicated (dashed orange lines). Blue, grey and white correspond to nitrogen, carbon and hydrogen atoms, respectively.

X-ray quality crystals of octyloxy derivative **4d** were obtained by slow diffusion of hexanes into a chloroform solution of the array. **4d** crystallized as red prisms in space group $P\bar{1}$ with six molecules per unit cell designated as three molecules: A, B and C. These three molecules are organized into two dimer structures: 1) two molecules of A form a dimer with inversion symmetry; 2) molecules B and C form a non-centrosymmetric dimer (Figure 2.17). The **4d** dimer structures both display similar hydrogen bond interactions to those observed in the preceding **4a** dimer in the solid state. However, the intermolecular distances between hydrogen bond donor-acceptor sites in both **4d** dimers are generally shorter than the ones reported for the **4a** dimer (Table 2.6). Based on this observation it can be presumed that **4d** dimers are stabilized by stronger hydrogen bond interactions than the **4a** dimer. This is in agreement with the higher dimerization constant in CDCl_3 for **4d** (32 M^{-1}) compared with **4a** (8.4 M^{-1}). In spite of the proximity of **4d** dimers, the distances between H5X2 ($X = \text{A, B/C}$) and the nearest opposing pyridyl proton $\text{H1X}'$ ($X' = \text{A}', \text{C/B}$) are still at or outside the limit for detection by a ^1H NMR NOESY experiment ($\text{H5A2}\cdots\text{H1A}' = 3.78 \text{ \AA}$, $\text{H5B2}\cdots\text{H1C} = 3.57 \text{ \AA}$ and $\text{H5C2}\cdots\text{H1B} = 3.67 \text{ \AA}$). The dimer formed by two **A** molecules can be considered planar since there is no heavy atom deviating from the least squares plane of all the heavy atoms in the dimer more than 0.30 \AA . Conversely, molecules **B** and **C** form a dimer more distorted from planarity. The least squares planes of all the heavy atoms in the azoheteroaromatic cores (i.e. without taking into account the octyloxy and amino groups) in **B** and **C** form an angle of 157° with respect to each other. Individually, molecules A, B and C in the **4d** crystal structure show small deviations from coplanarity along the azoheterocyclic backbone (greatest heavy atom deviation from least squares planes of 0.13 \AA for molecule A, 0.10 \AA for molecule B and 0.21 \AA for molecule

C). In addition to the expected hydrogen bond interactions in **4d**, molecules A, B and C exhibit C3(A/B/C)-H3(A/B/C)···N7(A/C/B) hydrogen bonds at the opposing edges of the **DDAAA** array (Figure 2.18, Table 2.6). In the course of the three dilution experiments of **4d** in CDCl₃ there were no observable changes in the chemical shift corresponding to the H3 proton; therefore, it is concluded that these hydrogen bond interactions are a result of crystal packing.

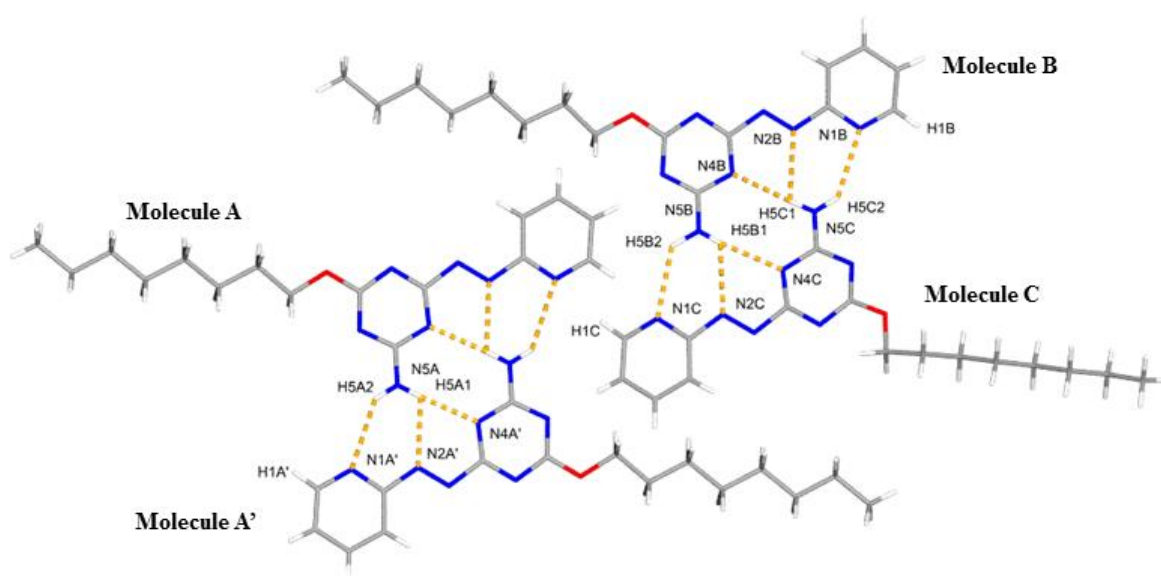


Figure 2.17 Stick representation of the X-ray crystal structure of **4d** dimers with intermolecular hydrogen bonds indicated (dashed orange lines). Blue, grey, white and red correspond to nitrogen, carbon, hydrogen and oxygen atoms, respectively.

Table 2.6 Hydrogen bond distances and angles of complex **4d·4d** X-ray from the crystal structure data.

Dimer	D...A	d XH...N (Å)	d XH...N (Å)	∠ XH...N (°)
A·A' Dimer	N5A-H5A1...N4A'	3.0436 (8)	2.1531 (6)	176.147 (46)
	N5A-H5A1...N2A'	2.9228 (6)	2.4367 (5)	114.601 (41)
	N5A-H5A2...N1A'	3.3159 (8)	2.5775 (6)	140.401 (40)
	C3A-H3A...N7A'	3.3815 (7)	2.4578 (5)	169.583 (41)
B·C Dimer	N5B-H5B1...N4C	3.1785 (8)	2.3379 (6)	173.118 (52)
	N5B-H5B1...N2C	3.0158 (5)	2.4981 (5)	120.456 (42)
	N5B-H5B2...N1C	3.3145 (7)	2.5311 (6)	130.407 (37)
	C3B-H3B...N7C	3.6602 (7)	2.6886 (5)	168.170 (38)
	N5C-H5C1...N4B	3.1199 (8)	2.2146 (6)	169.261 (52)
	N5C-H5C1...N2B	2.9262 (6)	2.4805 (5)	110.191 (40)
	N5C-H5C2...N1B	3.2669 (7)	2.4955 (6)	138.273 (40)
	C3C-H3C...N7B	3.3215 (7)	2.4140 (5)	157.109 (40)

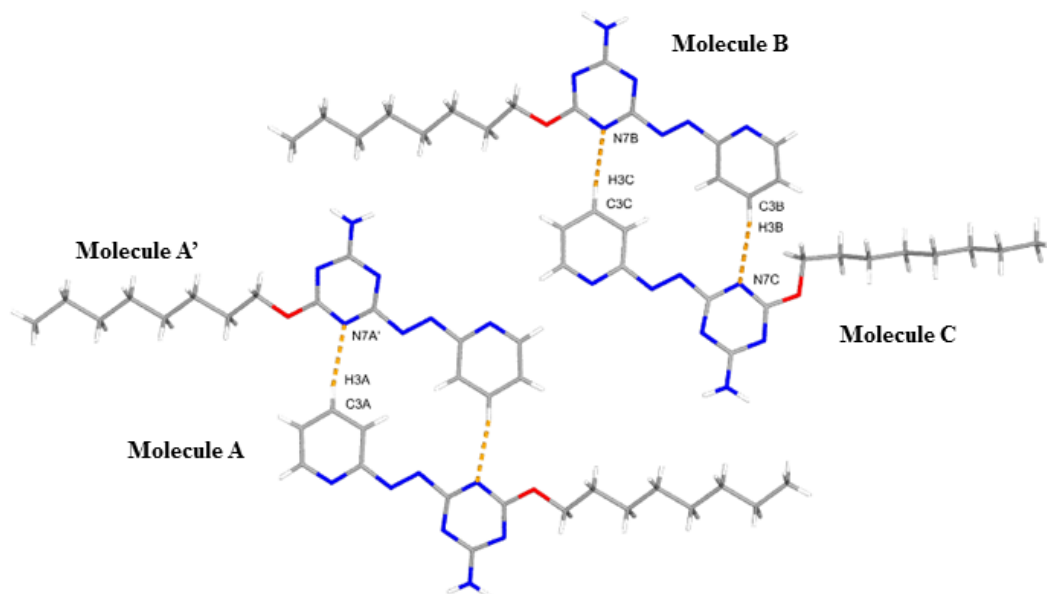


Figure 2.18 Stick representation of the X-ray crystal structure of **4d** with C-H...N interactions indicated (dashed orange lines). Blue, grey, white and red correspond to nitrogen, carbon, hydrogen and oxygen atoms, respectively.

Examining array **4f**, single crystals of this derivative were obtained by slow evaporation from a solution in toluene-*d*₈. The gold prismatic crystals obtained were solved in triclinic space group $P\bar{1}$, where each unit cell comprised two symmetry related molecules. As observed in the preceding crystal structures, dimers of **4f** are present in the crystal lattice with a similar hydrogen bond array displayed by the dimers of **4d** (Figure 2.19 and Table 2.7) in the solid state. The intermolecular least squares planes of the two symmetry related heterocyclic backbones are offset from each other by 0.25 Å with six hydrogen bond interactions stabilizing the dimer. There is a symmetry related pair of hydrogen bonds between an amino proton and a triazine nitrogen atom ($\text{N7-H7A}\cdots\text{N6}' = 3.15 \text{ \AA}$; $\angle\text{N-H}\cdots\text{N} = 178^\circ$), and two pairs of less linear hydrogen bonds between the amino protons and the azo ($\text{N7-H7A}\cdots\text{N2}' = 2.95 \text{ \AA}$; $\angle\text{N-H}\cdots\text{N} = 115^\circ$) and pyridyl (N7-

$\text{H7B}\cdots\text{N1}' = 3.28 \text{ \AA}$; $\angle\text{N-H}\cdots\text{N} = 137^\circ$) nitrogen acceptors. The intermolecular distances displayed in the **4f** dimer are similar in character to **4d** dimers and generally shorter in length than the **4a** dimer. This similarity between **4f** and **4d** dimers is consistent with the similar dimerization constants in CDCl_3 of both derivatives (32 M^{-1} and 36 M^{-1} for **4d** and **4f**, respectively). Likewise, the lack of a cross-relaxation peak between H7B and H1' in a ^1H NOESY experiment is again sustained by the distance between these two protons in the dimer ($\text{H7B}\cdots\text{H1}' = 3.8 \text{ \AA}$). The dimer is planar with no heavy atom deviating from the least squares plane described by all the non-hydrogen atoms in the molecule by more than 0.16 \AA . Other intermolecular interactions appear in the crystal lattice such as C-H \cdots N interactions at the opposite edges of the **DDAAA** hydrogen bond arrays (Figure 2.20 and Table 2.7) and π - π interactions between stacked aromatic planes of adjacent dimers (triazine ring centroid to least squares plane of adjacent molecule distance = 3.54 \AA ; pyridine ring centroid to least squares plane of adjacent molecule distance = 3.61 \AA).⁴⁵ Both interactions are attributed to crystal packing since dilution experiments did not show the expected changes in the chemical shift of protons likely to be affected by these interactions (i.e. pyridyl ring protons).

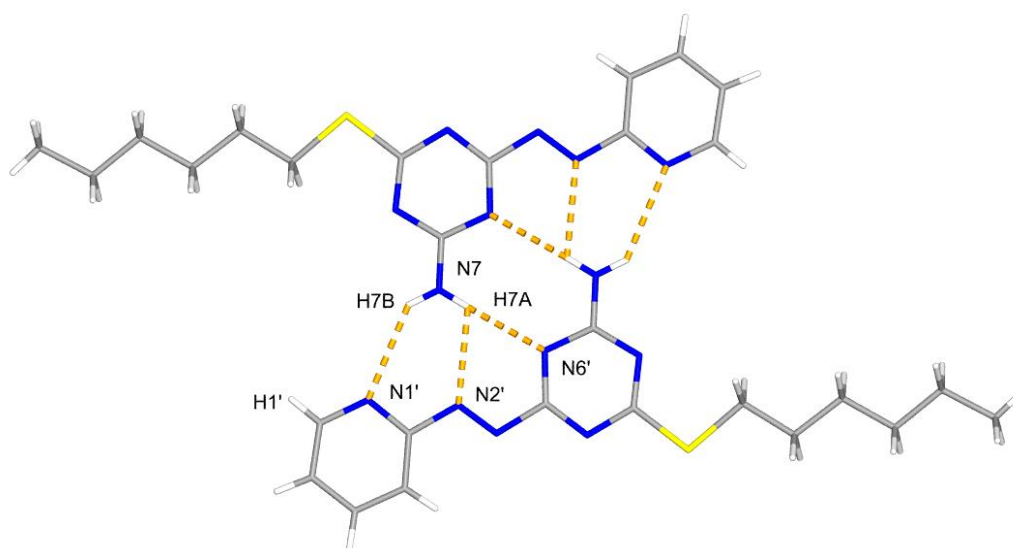


Figure 2.19 Stick representation of the X-ray crystal structure of **4f** dimer with intermolecular hydrogen bonds indicated (dashed orange lines). Blue, grey, white and yellow correspond to nitrogen, carbon, hydrogen and sulfur atoms, respectively.

Table 2.7 Hydrogen bond distances and angles of complex **4f·4f** X-ray from the crystal structure data.

D...A	d NH...N (Å)	d NH...N (Å)	∠ NH...N (°)
N7-H7A...N6'	3.1500 (3)	2.2848 (2)	177.961 (10)
N7-H7A...N2'	2.9500 (4)	2.4723 (3)	115.468 (6)
N7-H7B...N1'	3.2831 (3)	2.5905 (3)	137.388 (8)
C3-H3...N4'	3.4354 (4)	2.5038 (3)	170.492 (6)

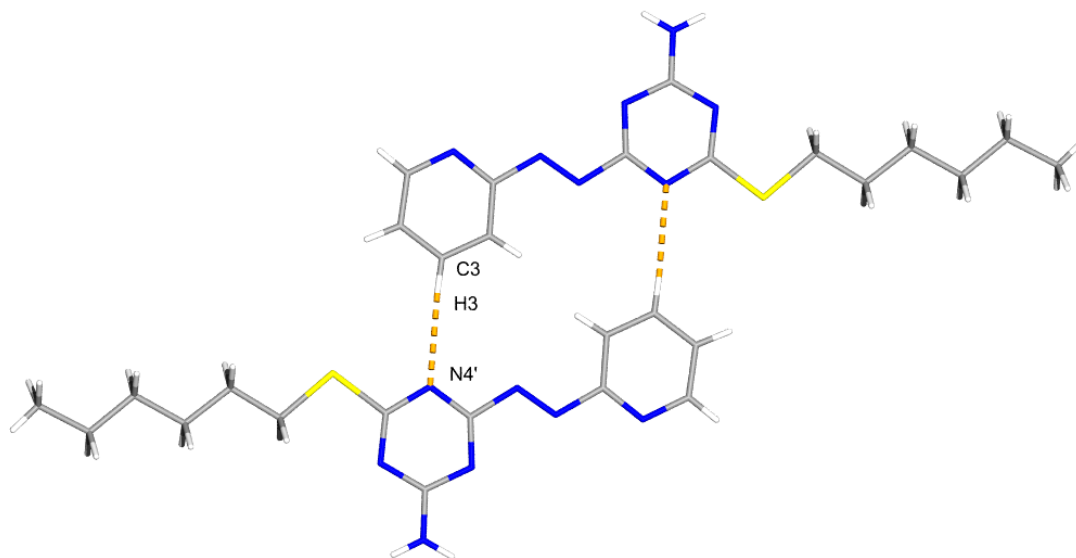


Figure 2.20 Stick representation of the X-ray crystal structure of **4f** with indicating C-H \cdots N interactions (dashed orange lines). Blue, grey, white and yellow correspond to nitrogen, carbon, hydrogen and sulfur atoms, respectively.

Finally, single crystals of **4k** were obtained by slow evaporation from a chloroform solution to yield orange plates. The diffraction data from **4k** was solved in space group $P2_1/n$ with eight molecules per unit cell arranged as four symmetry related pairs of two molecules: A and B. Solution of the crystal structure of **4k** included the presence of chloroform solvent molecules occluded, as indicated in the chemical formula obtained (Table 2.4). Molecules A and B form a dimer in accordance with the previous crystal structures obtained (Figure 2.21). The intermolecular hydrogen bond distances observed in the **4k** dimer are slightly shorter than to those observed in the **4d** and **4f** dimers (Table 2.8), which implies a stronger dimerization for derivative **4k** compared with **4d** and **4f**. This observation is again consistent with their dimerization constants in CDCl_3 (36 M^{-1} , 32 M^{-1} and 50 M^{-1} for **4d**, **4f** and **4k**, respectively). The intermolecular distances of the amino protons H1X4 (X = A or B) with the closest pyridyl proton from the opposing molecule

(H18X) also fall outside the ^1H NOESY experiment detection distance (H1A4 \cdots H18B = 3.75 Å and H1B4 \cdots H18A = 3.70 Å). Though the azoheterocyclic backbones in molecules A and B can each be considered planar (no heavy atom more than 0.44 Å from least squares planes described by azoheterocyclic cores), the dimer formed by the two molecules deviates from overall coplanarity since their azoheterocyclic backbones converge at an angle of 156° between the least squares planes. In contrast, in both molecules the 4'-*tert*-butylphenoxy group is twisted nearly perpendicular to the triazine ring (63° and 88° for molecules A and B respectively). It is likely that because of this 4'-*tert*-butylphenoxy arrangement that C-H \cdots N interactions similar to the preceding two structures are not observed in the solid state for 4k. However, the 4'-*tert*-butylphenoxy groups participate in C-H \cdots π interactions involving H17X and H3X (X = A or B) protons (Figure 2.22, Table 2.8). Lastly, there are π - π interactions stacked along the crystal lattice's *b* direction. Molecules A and B are arranged above one another in an antiparallel manner with distances from ring centroids to azoheterocyclic core least squares planes of 3.27 Å and 3.30 Å for A and B molecules respectively.⁴⁵

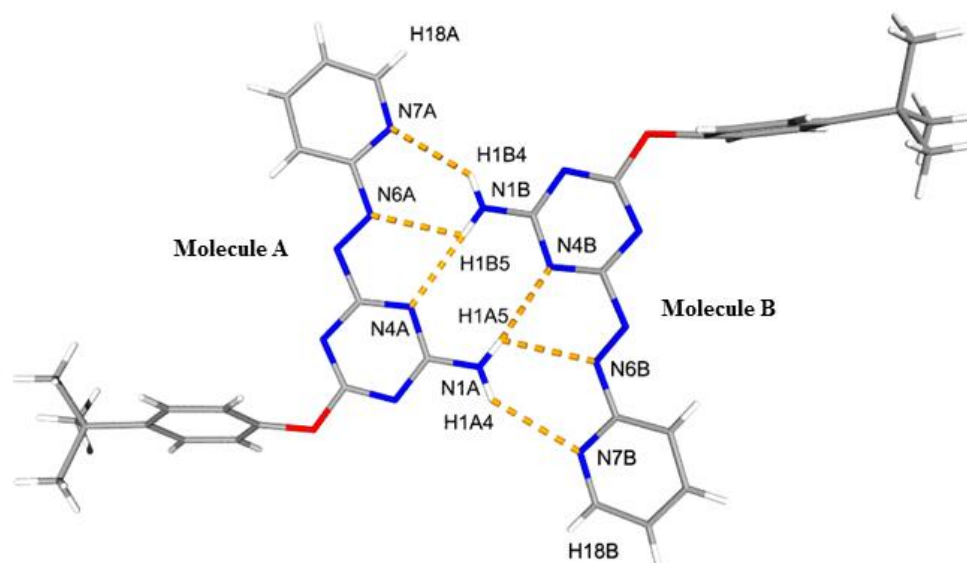


Figure 2.21 Stick representation of the X-ray crystal structure of **4k** dimers with intermolecular hydrogen bonds indicated (dashed orange lines). Blue, grey, white and red correspond to nitrogen, carbon, hydrogen and oxygen atoms, respectively.

Table 2.8 Hydrogen bond distances and angles of complex **4k·4k** X-ray from the crystal structure data.

D...A	d XH...Y (Å)	d XH...Y (Å)	∠ XH...Y (°)
N1A-H15A...N4B	3.1270 (4)	2.2624 (3)	167.324 (21)
N1A-H15A...N6B	2.9725 (4)	2.4707 (3)	116.745 (19)
N1A-H14A...N7B	3.2790 (4)	2.5618 (3)	139.222 (20)
C3A-H3A...π _B	3.6757 (2)	2.8396 (2)	58.554 (4)
C17A-H17A...π _B	3.6741 (2)	2.7363 (2)	80.817 (9)
N1B-H15B...N4A	3.0813 (4)	2.2218 (3)	165.374 (23)
N1B-H15B...N6A	2.9223 (4)	2.4405 (3)	114.912 (20)
N1B-H14B...N7A	3.2270 (4)	2.4895 (3)	141.760 (21)
C3B-H3B...π _A	3.6362 (2)	2.7270 (2)	68.090 (6)
C17B-H17B...π _A	3.7234 (2)	2.8697 (2)	63.976 (10)

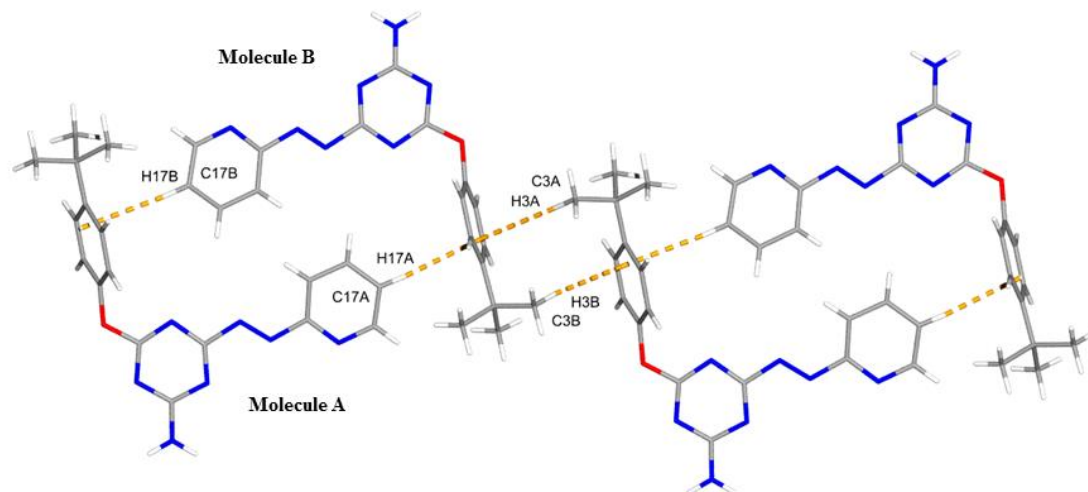


Figure 2.22 Stick representation of the X-ray crystal structure of **4k** with indicating C-H \cdots π interactions (dashed orange lines). Blue, grey, white and red correspond to nitrogen, carbon, hydrogen and oxygen atoms, respectively.

A comparison of the intermolecular distances and heterocyclic ring planes angles of all the dimer arrays described in the preceding X-ray crystal structures are listed in Table 2.9. It is worth outlining the correlation between the hydrogen bond distances and dimer's planarity in the crystal structure with the dimerization strength estimated in the dilution experiments. In this sense, the compound with the largest intermolecular distances shows the lowest dimerization constant, **4a**. Dimer structures from derivatives **4d** and **4f** have similar intermolecular distances with small deviations from coplanarity between heterocyclic rings. Hence, it is not unexpected to note that their dimerization constants in CDCl₃ fall within the same range (36 and 32 M⁻¹ for **4d** and **4f**, respectively). Finally, **4k** dimer has intermolecular distances slightly lower than those observed for **4d** and **4f** dimers. Particularly **4k** dimer has the lowest N-Hb \cdots Nc distance (3.2 Å, Table 2.9) which implies a stronger participation of the pyridyl nitrogen acceptor compared with **4a**, **4d** and **4f**. This

might rationalize that from all compounds studied through X-Ray crystallography **4k** has the highest dimerization constant in solution

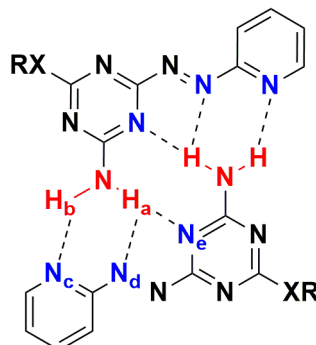


Figure 2.23 Donor and acceptor sites assignment of **4a**, **4d**, **4f** and **4k** dimers.

Table 2.9 Summary of hydrogen bond distances, intramolecular and intermolecular ring's planes angles of **4a**, **4d**, **4f** and **4k** from their crystal structure data.

Derivative	$\underline{\text{N-H}_a \cdots \text{N}_e}$ (Å)	$\underline{\text{N-H}_a \cdots \text{N}_d}$ (Å)	$\underline{\text{N-H}_b \cdots \text{N}_c}$ (Å)	Intramolecular Ring Plane Angles (°) ^a	Intermolecular Ring Plane Angles (°) ^a
4a	3.1551 (8)	3.0115 (7)	3.5477 (10)	44.576	44.576
4d	3.0436 (8)	2.9228 (6)	3.3159 (8)	11.357	11.357
	3.1785 (8)	3.0158 (5)	3.3145 (7)	3.830	20.285
	3.1199 (8)	2.9262 (6)	3.2669 (7)	7.637	26.896
	3.1140 ^b	2.9549 ^b	3.2991 ^b	7.608 ^b	19.513 ^b
4f	3.1500 (3)	2.9500 (4)	3.2831 (3)	0.912	0.912
4k	3.1270 (4)	2.9725 (4)	3.2790 (4)	9.096	21.076
	3.0813 (4)	2.9223 (4)	3.2270 (4)	4.468	24.592
	3.1042 ^b	2.9474 ^b	3.2530 ^b	6.782 ^b	22.834 ^b

^a Angle between least squares triazine and pyridine ring planes, ^b Average values from all dimers present in the crystal structure

2.4 Summary and Conclusion

A range of self-complementary hydrogen bond **DDAAA** arrays (**4a-p**) were designed, synthesized and characterized. The novelty of the system proposed lies in the inclusion of a photochromic group in the binding site's array; utilizing an azo group as a hydrogen bond acceptor. Dimerization constants of derivatives **4a-p** were obtained employing two different solvent systems: CDCl_3 and Toluene- d_8 . In deuterated chloroform, dimerization constants varied from 8.4 to 180 M^{-1} . In deuterated toluene, dimerization constants ranged from 600 to 3700 M^{-1} . The difference in K_{t-t} values in different solvents is consistent with a stronger interaction between chloroform and the monomers which competes with dimerization. Nevertheless, in both solvent systems, derivatives **4a-p** with stronger electron withdrawing RX groups achieved larger dimerization constants (e.g. perfluorophenoxy derivative **4n** displayed the highest dimerization constants). The dimer structures in the solid state were confirmed by single crystal X-ray diffraction of four derivatives: **4a**, **4d**, **4f**, and **4k**. The structures supported the existence of hydrogen bond interactions between amino group and triazine, azo and pyridine moieties as anticipated from the original design. Of all these interactions, the strongest one appeared to be between the amino group and triazine ring since in all dimer structures observed, it displayed $\text{N-H}\cdots\text{N}$ angles closest to 180° . Differences between intermolecular distances of derivatives **4a**, **4d**, **4f** and **4k** are in accordance with the dimerization strength observed for each derivative (e.g. derivative **4a** has the smallest dimerization constant and showed the largest intermolecular distances).

Finally, the impact of the pyridine acceptor was examined through a comparison between **4c**, **4f** and **4k** with compounds **5c**, **5f** and **5k**. The energetic contribution of the pyridine acceptors in each solvent system was estimated at 4 and 8 kJ mol⁻¹ in chloroform and toluene respectively. According to literature, primary and secondary hydrogen bonds have energetic contributions in chloroform of 7.9 and 2.9 kJmol⁻¹, respectively ⁴⁶. In this sense, and based on the dimer structures obtained by X-ray diffraction, the pyridine acceptor site is located far enough away from the amino group that the hydrogen bond between these moieties falls somewhere between a primary and a secondary interaction. These observations leave room for improvement on the design proposed in this chapter. A design wherein the pyridine rings are replaced by another aromatic system with an acceptor site bonded *ortho*- to the azo group and closer to the amino group in a dimer structure will be considered in Chapter 4.

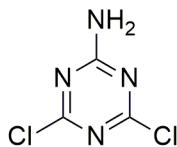
2.5 Experimental Methodology

2.5.1 Generalities

All experiments were performed in ambient atmospheric conditions unless otherwise indicated. Chemicals were purchased from Alfa Aesar, Sigma-Aldrich, and Oakwood Products and used as received. Solvents (acetone, acetonitrile, butanol, chloroform, dichloromethane, diethyl ether, diisopropyl ether, dimethyl formamide, ethyl acetate, hexanes, methanol, tetrahydrofuran, and toluene) were obtained from Caledon Laboratories, Fisher Chemicals, Sigma-Aldrich and VWR Analytical. In the case of inert

atmosphere conditions, solvents were dried using an Innovative Technology Inc. Controlled Atmospheres Solvent Purification System that utilizes dual alumina columns (SPS-400-5), or purchased from Sigma-Aldrich and used as received. Reactions were monitored by thin-layer chromatography (TLC) on pre-coated TLC-sheets POLYGRAM®SIL G/UV₂₅₄. Column chromatography was performed with SiliCycle®SiliaFlash® F60, 40-63 μm 60 Å. Nuclear Magnetic Resonance spectra were recorded on Mercury 400 MHz, INOVA 400 MHz and INOVA 600 MHz spectrometers (¹H = 400.08 MHz, 399.77 MHz and 599.32 MHz; ¹³C {¹H} = 100.52 MHz and 150.78 MHz respectively). ¹H and ¹³C spectra were referenced relative to Me₄Si using the residual non-deuterated NMR solvent signal (¹H: CHCl₃, δ = 7.26 ppm, (CHD₂)₂SO, δ = 2.50 ppm, (CHD₂)C₆D₅, δ = 2.09 ppm, ; ¹³C {¹H}: CHCl₃, δ = 77.0 ppm, (CHD₂)₂SO, δ = 39.5 ppm). Solvents for NMR spectroscopy (Chloroform-d, DMSO-d₆, and Toluene-d₈) were purchased from Cambridge Isotope Laboratories and Sigma-Aldrich. Mass spectra were recorded using an electron ionization Finnigan MAT 8200 spectrometer at an ionizing voltage of 70 eV. X-Ray diffraction data were collected on Bruker Apex II and Nonius Kappa CCD X-Ray diffractometers using graphite monochromatic Mo-Kα radiation (γ = 0.71073 Å) and Cu-Kα radiation (γ = 1.54178 Å), respectively.

2.5.2 Synthetic Methods



Synthesis of 4,6-dichlorotriazin-2-amine (1). Synthetic procedure as reported by Baliani and coworkers.³⁴ In a round bottom flask with a stir bar, cyanuric chloride (20.0 g, 0.11 mol, 1 eq.) was dissolved in acetone (100 mL) and then a 1:1 ice and distilled water mixture (100 mL) was poured into the solution to make a thick slurry. The slurry was cooled down to a temperature below 5 °C and 2 eq. of aqueous ammonia 29% (30 mL, 0.22 mol, 2 eq.) was added dropwise without letting the reaction mixture exceed 5°C. The reaction mixture was stirred 30 minutes at a temperature below 5°C and then 30 minutes coming to room temperature. The product was filtered and dried by vacuum filtration. Yield = 14 g, 78%. EI-HRMS: Calc. for C₃H₂Cl₂N₄:163.9657, Found: 163.9658. ¹H NMR (400 MHz, DMSO-d₆): δ(ppm) 8.57 (bs, 2H). ¹³C NMR (100 MHz, DMSO-d₆): δ(ppm) 166.9, 169.1.

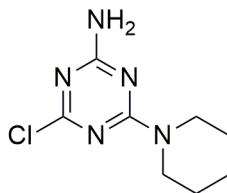
General procedures for synthesis of 4-chloro-1,3,5-triazin-2-amine derivatives (2a-p).

Method A: 2-amino-4,6-dichlorotriazine (5.0 g, 30.3 mmol, 1 eq.) was dissolved in THF. The solution was cooled down to -78°C and then K₂CO₃ (4.19 g, 30.3 mmol, 1 eq.) and reactant RXH (30.3 mmol, 1 eq.) were added sequentially. The reaction mixture was stirred overnight and allowed to slowly reach room temperature. The solvent was removed under reduced pressure and the crude was washed with distilled water and filtered by vacuum filtration. If necessary, further purification was performed by flash chromatography using 1: 1 hexanes / diethyl ether as eluent.

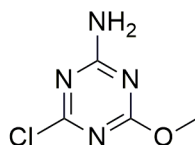
Method B: Under an N₂ atmosphere, a round bottom flask, provided with a stir bar, was filled with 100 mL of dry THF and chilled to 0°C in an ice-water bath. NaH (60% dispersion in mineral oil, 1.45 g, 36.4 mmol, 1.2 eq.) was poured into the dry THF and stirred to generate a fine suspension. Fifteen minutes later reactant RXH (36.4 mmol, 1.2 eq.) was added dropwise over 30 minutes to the fine suspension and the reaction mixture was stirred 30 minutes (in the ice-water bath). Then the reaction mixture was gradually warmed to reflux for 4 hours and finally cooled down to room temperature. In a separated flask under N₂, 4,6-dichlorotriazin-2-amine (5.86 g, 35.5 mmol, 1 eq.) was dissolved in 100 mL of dry THF and cooled to -78°C. Once the alkoxide reaction mixture had reached room temperature, it was added drop-wise to the 4,6-dichlorotriazin-2-amine solution. The resulting reaction mixture was stirred overnight and allowed to reach room temperature. The solvent was removed under reduced pressure and the crude was washed with distilled water and filtered. If necessary, further purification was performed by flash chromatography using 1:1 hexanes / diethyl ether as eluent.

Method C: In a round bottom flask provided with a stir bar, 4,6-dichlorotriazin-2-amine (5.00 g, 30.3 mmol, 1 eq.) was dissolved in 100 mL of acetone and then 100 mL of distilled water was poured into the solution to form a slurry. The reaction mixture was cooled down to 0°C. In a separate flask 50 mL of distilled water, reactant RXH (30.31 mmol, 1 eq.) and sodium hydroxide (1.21g, 30.30 mmol, 1 eq.) were dissolved. To the 4,6-dichlorotriazin-2-amine suspension prepared before, the reactant RXH and sodium hydroxide solution was added dropwise keeping the temperature below 5°C. The product reaction mixture was stirred overnight allowing it to reach room temperature. The reaction mixture was filtered

and washed with distilled water. If necessary, further purification was performed by flash chromatography using 1:1 hexanes / diethyl ether as eluent.

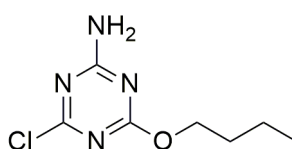


Synthesis of 4-chloro-6-(piperidin-1-yl)-1,3,5-triazin-2-amine (2a). 4,6-dichlorotriazin-2-amine (5.00 g, 30.3 mmol, 1 eq.) was dissolved in 100 mL of THF in a round bottom flask provided with a stir bar; the solution was cooled to -78°C . In a separated flask piperidine (3.0 mL, 30.3 mmol, 1 eq.) and triethylamine (4.2 mL, 30.3 mmol, 1 eq.) were dissolved in 100 mL of THF and the resulting solution slowly added to the 4,6-dichlorotriazin-2-amine solution. The reaction mixture was stirred overnight allowing it to reach room temperature. The solvent was removed at reduced pressure and the crude was washed with distilled water and filtered. Yield = 3.70 g, 57% EI-HRMS: Calc. for $\text{C}_8\text{H}_{12}\text{ClN}_5$: 213.0781, Found: 213.0786. ^1H NMR (600 MHz, CDCl_3): δ (ppm) 5.19 (b, 2H), 3.74 (m, 4H), 1.62 (m, 6H). ^{13}C NMR (100 MHz, CDCl_3) δ (ppm) 169.6, 166.7, 164.2, 44.5, 25.8, 24.5.

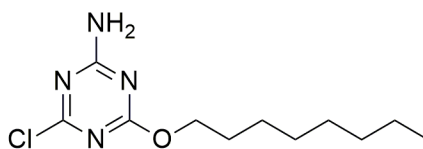


Synthesis of 4-chloro-6-methoxy-1,3,5-triazin-2-amine (2b). In a round bottom flask 4,6-dichlorotriazin-2-amine (5.00 g, 30.3 mmol, 1 eq.) was dissolved in 100 mL of methanol. The solution was cooled down to -78°C and later added sodium methoxide salt

(1.64 g, 30.3 mmol, 1 eq.). The reaction mixture was stirred over 6 hours allowing it to reach room temperature. Later, the reaction mixture was poured into an ice-water mixture and the product was filtered and dried by vacuum filtration. Yield = 4.87 g, 81%. EI-HRMS: Calc. for C₄H₅ClN₄O: 160.0152, Found: 160.0154. ¹H NMR (400 MHz, DMSO-d₆) δ(ppm) 7.99 (bs, 2H), 3.85 (s, 3H). ¹³C NMR (100 MHz, DMSO-d₆) δ(ppm) 170.8, 169.8, 168.0, 54.9.

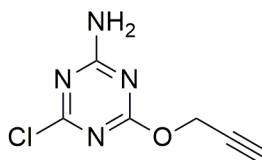


Synthesis of 4-butoxy-6-chloro-1,3,5-triazin-2-amine (2c). Synthesis performed according to **Method B**; wherein reactant RXH corresponds to 1-butanol. Yield = 6.10 g, 99%. EI-HRMS: Calc. for C₇H₁₁ClN₄O: 202.0621, Found: 203.0703. ¹H NMR (400 MHz, CDCl₃) δ(ppm) 5.83 (b, 1H), 5.56 (b, 1H), 4.34 (t, 2H, *J* = 6.6 Hz), 1.74 (m, 2H, *J* = 7.8, 6.6 Hz), 1.46 (m, 2H, *J* = 7.8, 7.4 Hz), 0.95 (t, 3H, *J* = 7.4 Hz). ¹³C NMR (100 MHz, CDCl₃) δ(ppm) 171.4, 171.1, 168.1, 68.4, 30.6, 18.9, 13.7.

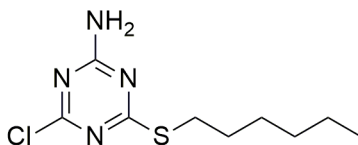


Synthesis of 4-chloro-6-(octyloxy)-1,3,5-triazin-2-amine (2d). Synthesis performed according to **Method B**; wherein reactant RXH corresponds to 1-octanol. The product was isolated by flash chromatographic column with a mixture 2:1 hexanes : diethyl Ether as eluent. Yield = 3.31g, 36%. EI-HRMS: Calc. for C₁₁H₁₉ClN₄O: 258.1247, Found:

259.1321. ^1H NMR (400 MHz, DMSO- d_6) = δ (ppm) 7.97 (bs, 1H), 7.92 (bs, 1H), 4.23 (t, 2H, J = 6.6 Hz), 1.65 (q, 2H, J = 6.6 Hz), 1.48-1.22 (m, 10H), 0.85 (t, 3H, J = 6.6 Hz). ^{13}C NMR (100 MHz, DMSO- d_6) δ (ppm) 170.3, 169.8, 168.0, 67.4, 32.5, 31.2, 28.6, 25.2, 22.0, 13.8.

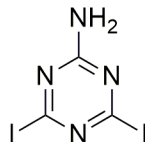


Synthesis of 4-chloro-6-(prop-2-ynoxy)-1,3,5-triazin-2-amine (2e). Synthesis performed according to **Method A**; wherein reactant RXH is propargyl alcohol. The product was purified by flash chromatography with a mixture of 1:1 hexanes : diethyl ether as eluent. Yield = 5.26 g, 94%. EI-HRMS: Calc. for $\text{C}_6\text{H}_5\text{ClN}_4\text{O}$: 184.0152, Found: 185.0231. ^1H NMR (400 MHz, DMSO- d_6) δ (ppm) 8.12 (bs, 2H), 4.95 (d, 2H, J = 2.3 Hz), 3.64 (t, 1H, J = 2.3 Hz). ^{13}C NMR (100 MHz, DMSO- d_6) δ (ppm) 169.9, 169.6, 167.9, 78.4, 78.2, 54.9.

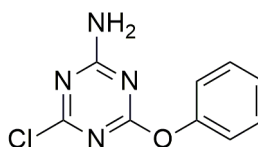


Synthesis of 4-chloro-6-(hexylthio)-1,3,5-triazin-2-amine (2f). Synthesis performed according to **Method C**; wherein reactant RXH is 1-hexanethiol. Yield = 5.70 g, 76%. EI-HRMS: Calc. for $\text{C}_9\text{H}_{15}\text{ClN}_4\text{S}$: 246.0706, Found: 246.0707. ^1H NMR (400 MHz, CDCl_3) δ (ppm) 5.40 (bs, 2H), 3.09 (t, 2H, J = 7.4 Hz), 1.70 (q, 2H, J = 7.8, 7.0 Hz), 1.47-1.39 (m,

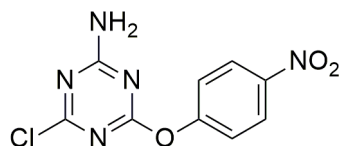
2H), 1.33-1.29 (m, 4H), 0.90 (t, 3H, $J = 7.0$ Hz). ^{13}C NMR (100 MHz, CDCl_3) δ (ppm) 184.0, 169.0, 165.4, 31.2, 30.4, 28.8, 28.4, 22.5, 14.0.



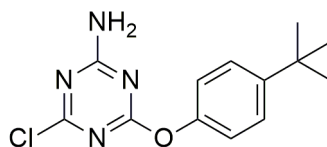
Synthesis of 4,6-diiodotriazin-2-amine (2h). Synthetic procedure based on procedure reported by Smith and coworkers⁴⁷. In a round bottom flask provided with a stir bar, 1 eq. of 4,6-dichlorotriazin-2-amine (5.00 g, 30.31 mmol) dissolved in CH_2Cl_2 and 2 eq. of hydroiodic acid 67% (12.73 mL, 60.67 mmol) were stirred overnight at room temperature. The reaction mixture was treated with a saturated aqueous solution of NaHCO_3 until $\text{pH} = 7$. The product was filtered from the reaction mixture and washed with water. Yield = 4.38 g, 42%. EI-HRMS: Calc. for $\text{C}_3\text{H}_2\text{I}_2\text{N}_4$: 347.8369, Found: 347.8370. ^1H NMR (400 MHz, DMSO-d_6) δ (ppm) 8.20.



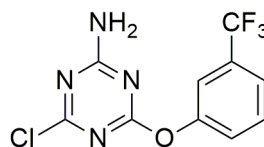
Synthesis of 4-chloro-6-phenoxy-1,3,5-triazin-2-amine (2i). Synthesis performed according to **Method C**; wherein reactant RXH is phenol. Yield = 6.70 g, 99% EI-HRMS: Calc. for $\text{C}_9\text{H}_7\text{ClN}_4\text{O}$: 222.0308, Found: 222.0305. ^1H NMR (400 MHz, CDCl_3) δ (ppm) 7.43 (m, 2H), 7.30 (m, 1H), 7.16 (m, 2H), 5.68 (bs, 1H), 5.51 (bs, 1H). ^{13}C NMR (100 MHz, CDCl_3) δ (ppm) 172.0, 171.2, 168.3, 151.5, 129.6, 126.2, 121.5.



Synthesis of 4-chloro-6-(4-nitrophenoxy)-1,3,5-triazin-2-amine (2j). Synthesis performed according to **Method C**; wherein reactant RXH is 4-nitrophenol. Yield = 7.26 g, 97%. EI-HRMS: Calc. for C₉H₆ClN₅O₃: 267.0159, Found: 267.0152. ¹H NMR (400 MHz, DMSO-d₆) δ(ppm) 8.32 (m, 2H), 8.17 (bs, 1H), 8.24 (bs, 1H), 7.56 (m, 2H). ¹³C NMR (100 MHz, DMSO-d₆) δ(ppm) 170.2, 169.9, 168.1, 156.4, 145.0, 125.4, 123.2.

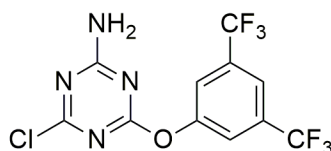


Synthesis of 4-(4-tert-butylphenoxy)-6-chloro-1,3,5-triazin-2-amine (2k). Synthesis performed according to **Method A**; wherein reactant RXH is 4-*tert*-butylphenol. Yield = 4.98 g, 59%. EI-HRMS: Calc. for C₁₃H₁₅ClN₄O: 278.0934, Found: 278.0931. ¹H NMR (400 MHz, CDCl₃) δ(ppm) 7.42 (m, 2H), 7.07 (m, 2H), 5.91 (bs, 1H), 5.72 (bs, 1H), 1.34 (s, 9H). ¹³C NMR (100 MHz, DMSO-d₆) δ(ppm) 170.1, 168.2, 149.3, 148.0, 126.3, 121.0, 114.6, 34.2, 31.2.

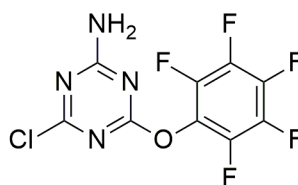


Synthesis of 4-chloro-6-(3-(trifluoromethyl)phenoxy)-1,3,5-triazin-2-amine (2l). Synthesis performed according to **Method A**; wherein reactant RXH is 3-

(trifluoromethyl)phenol. Yield = 7.70 g, 87%. EI-HRMS: Calc. for $C_{10}H_6ClF_3N_4O$: 290.0182, Found: 290.0177. 1H NMR (600 MHz, DMSO- d_6) δ (ppm) 8.16 (bs, 1H), 8.12 (bs, 1H), 7.70-7.65 (m, 3H), 7.59 (m, 1H). ^{13}C NMR (100 MHz, DMSO- d_6) δ (ppm) 170.3, 170.1, 168.1, 151.9, 131.0, 130.2, 126.3, 122.7, 122.3, 119.0. ^{19}F NMR (376 MHz, DMSO- d_6) δ (ppm) -60.99.

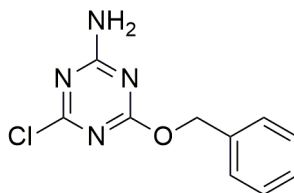


Synthesis of 4-(3,5-bis(trifluoromethyl)phenoxy)-6-chloro-1,3,5-triazin-2-amine (2m). Synthesis performed according to **Method A**; wherein reactant RXH is 3,5-bis(trifluoromethyl)phenol. Yield = 10.72 g, 96%. EI-HRMS: Calc. for $C_{11}H_5ClF_6N_4O$: 358.0056, Found: 358.0053. 1H NMR (400 MHz, DMSO- d_6) δ (ppm) 8.24 (bs, 1H), 8.16 (s, 1H), 7.97 (s, 2H), 7.93 (bs, 1H). ^{13}C NMR (100 MHz, DMSO- d_6) δ (ppm) 171.2, 170.2, 168.1, 167.1, 152.6, 131.5, 131.4, 124.1, 123.6, 121.4, 109.6. ^{19}F NMR (376 MHz, DMSO- d_6) δ (ppm) -61.31, -61.55.

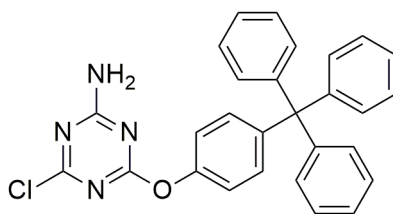


Synthesis of 4-chloro-6-(perfluorophenoxy)-1,3,5-triazin-2-amine (2n). Synthesis performed according to **Method A**; wherein reactant RXH is perfluorophenol. Yield = 8.72 g, 92%. EI-HRMS: Calc. for $C_9H_2ClF_5N_4O$: 311.9837, Found: 311.9847. 1H NMR (400 MHz, $CDCl_3$) δ (ppm) 6.07 (bs, 1H), 5.76 (bs, 1H). ^{13}C NMR (100 MHz, DMSO- d_6)

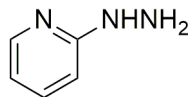
$\delta(\text{ppm})$ 173.7, 170.3, 169.3, 165.8, 158.5, 154.2, 148.0. ^{19}F NMR (376 MHz, CDCl_3)
 $\delta(\text{ppm})$ -152.55 (d, 2H, $J = 17.2$ Hz), -157.48 (t, 1H, $J = 22.4$ Hz), -162.01 (dd, 2H, $J =$
 22.4, 17.2).



Synthesis of 4-(benzyloxy)-6-chloro-1,3,5-triazin-2-amine (2o). Synthesis performed according to **Method B**; wherein reactant RXH corresponds to benzyl alcohol. Yield = 7.10 g, 99%. EI-HRMS: Calc. for $\text{C}_{10}\text{H}_9\text{N}_4\text{O}$: 236.0465, Found: 236.0463. ^1H NMR (400 MHz, DMSO-d_6) $\delta(\text{ppm})$ 8.03 (bs, 1H), 8.00 (bs, 1H), 7.45-7.35 (m, 5H), 5.33 (s, 2H). ^{13}C NMR (100 MHz, DMSO-d_6) $\delta(\text{ppm})$ 170.2, 170.0, 168.1, 135.7, 128.5, 128.3, 68.8.



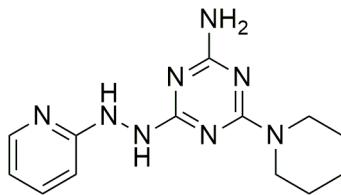
Synthesis of 4-chloro-6-(4-tritylphenoxy)-1,3,5-triazin-2-amine (2p). Synthesis performed according to **Method A**; wherein reactant RXH is 4-tritylphenol. Yield = 10.0 g, 71%. EI-HRMS: Calc. for $\text{C}_{28}\text{H}_{21}\text{N}_4\text{O}$: 461.1546, Found: 461.1408. ^1H NMR (400 MHz, DMSO-d_6) $\delta(\text{ppm})$ 8.20 (bs, 2H), 7.34-7.16 (m, 19H). ^{13}C NMR (100 MHz, DMSO-d_6) $\delta(\text{ppm})$ 168.1, 146.3, 131.6, 130.4, 127.8, 126.1, 120.7, 64.1.



Synthesis of 2-hydrazinylpyridine. Synthetic procedure as based on the procedure reported by Klingele and coworkers⁴⁸. A mixture of 2-fluoropyridine (8.86 mL, 103 mmol, 1 eq.) and hydrazine monohydrate (50.20 mL, 1030 mmol, 10 eq.) was refluxed for 6 hours. After cooling down the reaction mixture to room temperature 100 mL of NaOH 1M aqueous solution was added and the crude was extracted with dichloromethane (3 x 50 mL). The combined organic extracts were dried with MgSO₄ and the solvent was removed under reduced pressure to get pure product. Yield = 10.5 g, 94%. EI-HRMS; Calc. for C₅H₇N₃: 109.0640, Found: 109.0637. ¹H NMR (400MHz, CDCl₃): δ(ppm) 8.12 (dd, 1H, 5.1, 0.8 Hz), 7.48 (ddd, 1H, 8.6, 7.0, 1.5 Hz), 6.69 (d, 1H, J=8.6 Hz), 6.67 (ddd, 1H, J=7.0, 5.1, 0.8 Hz), 5.82 (bs, 1H), 3.77 (bs, 2H). ¹³C NMR (100 MHz, CDCl₃): δ(ppm) 161.1, 147.3, 137.1, 113.8, 106.6.

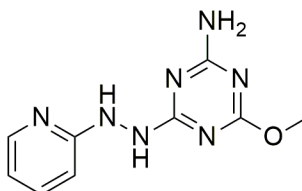
General procedure for synthesis of 6-(2-(pyridine-2-yl)hydrazinyl)-1,3,5-triazin-2-amine derivatives (3a-p)

In a round bottom flask 4-chloro-1,3,5-triazin-2-amine derivative (**2**) (1 eq.), potassium carbonate (1 eq.) and 2-hydrazinopyridine (1 eq.) were dissolved in THF and the reaction mixture was refluxed overnight. The solvent was removed via reduced pressure and the crude was washed with distilled water to then filter the crude by vacuum filtration. The product was purified by flash chromatography using diethyl ether as eluent.



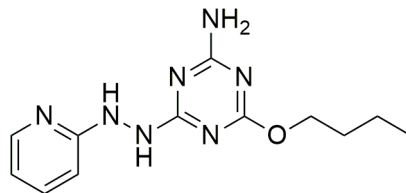
Synthesis of 4-(piperidin-1-yl)-6-(2-(pyridine-2-yl)hydrazinyl)-1,3,5-triazin-2-amine

(3a). Synthesis performed according to general procedure for intermediate **3**; wherein the 4-chloro-1,3,5-triazin-2-amine derivative is **2a**. Yield = 1.60 g, 32%. EI-HRMS: Calc. for $C_{13}H_{18}N_8$: 286.1654, Found: 286.1650. 1H NMR (400 MHz, $CDCl_3$) δ (ppm) 8.14 (d, 1H, $J= 4.7$ Hz), 7.49 (dd, 1H, $J= 8.2, 8.2$ Hz), 6.89 (bs, 1H), 6.79 (d, 1H, $J = 8.2$ Hz), 6.74 (dd, 1H, $J = 5.9, 5.9$ Hz), 5.01 (bs, 2H), 3.60 (m, 4H), 1.91 (bs, 1H), 1.57-1.45 (m, 6H). ^{13}C NMR (100 MHz, $CDCl_3$) δ (ppm) 167.1, 164.8, 147.7, 137.9, 115.9, 110.0, 107.3, 44.1, 25.7, 24.8.



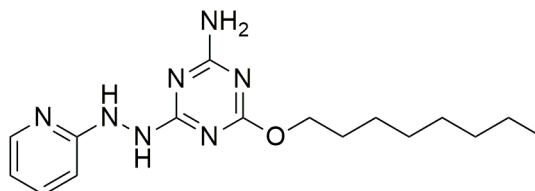
Synthesis of 4-methoxy-6-(2-(pyridine-2-yl)hydrazinyl)-1,3,5-triazin-2-amine (3b).

Synthesis performed according to general procedure for intermediate **3**; wherein the 4-chloro-1,3,5-triazin-2-amine derivative is **2b**. Yield = 3.20 g, 55%. EI-HRMS: Calc. for $C_9H_{11}N_7O$: 233.1025, Found: 233.1022. 1H NMR (400 MHz, $DMSO-d_6$) δ (ppm) 8.90 (bs, 1H), 8.28 (bs, 1H), 8.01 (d, 1H, $J = 4.3$ Hz), 7.47 (dd, 1H, $J = 7.8, 7.8$ Hz), 6.85 (bs, 2H), 6.64 (dd, 1H, $J = 6.0, 6.0$ Hz), 6.50 (d, 1H, $J = 7.8$ Hz), 3.77 (s, 3H). ^{13}C NMR (100 MHz, $DMSO-d_6$) δ (ppm) 147.5, 137.3, 113.9, 105.7, 53.4.



Synthesis of 4-butoxy-6-(2-(pyridine-2-yl)hydrazinyl)-1,3,5-triazin-2-amine (3c).

Synthesis performed according to general procedure for intermediate **3**; wherein the 4-chloro-1,3,5-triazin-2-amine derivative is **2c**. Yield = 7.87 g, 95%. EI-HRMS: Calc. for $C_{12}H_{17}N_7O$: 275.1495, Found: 275.1487. 1H NMR (400 MHz, $CDCl_3$) δ (ppm) 8.19 (bs, 2H), 7.98 (d, 1H, $J = 3.9$ Hz), 7.50 (dd, 1H, $J = 8.2, 7.4$ Hz), 6.78 (d, 1H, $J = 8.2$ Hz), 6.70 (dd, 1H, $J = 6.2, 6.2$ Hz), 6.29 (bs, 2H), 4.10 (t, 2H, $J = 6.6$ Hz), 1.53 (m, 2H), 1.29 (m, 2H), 0.84 (t, 3H, $J = 7.0$ Hz). ^{13}C NMR (100 MHz, $DMSO-d_6$) δ (ppm) 170.4, 169.3, 168.5, 160.0, 147.5, 137.3, 113.9, 105.7, 65.3, 30.4, 18.6, 13.6.

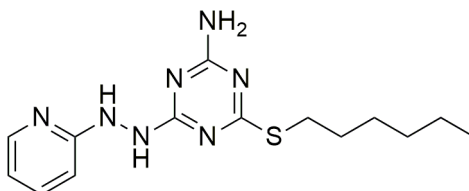


Synthesis of 4-(octyloxy)-6-(2-(pyridine-2-yl)hydrazinyl)-1,3,5-triazin-2-amine (3d).

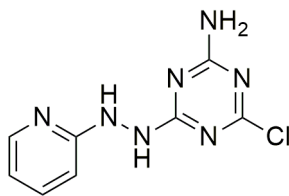
Synthesis performed according to general procedure for intermediate **3**; wherein the 4-chloro-1,3,5-triazin-2-amine derivative is **2d**. Yield = 6.77 g, 58%. EI-HRMS: Calc. for $C_{16}H_{25}N_7O$: 331.2121, Found: 331.2122. 1H NMR (400 MHz, $CDCl_3$) δ (ppm) 8.02 (d, 1H, $J = 4.7$ Hz), 7.48 (dd, 1H, $J = 7.0, 7.0$ Hz), 6.69-6.74 (m, 2H), 5.89 (bs, 2H), 4.11 (t, 2H), 1.56 (m, 2H), 1.29 (m, 10H), 0.86 (t, 3H, $J = 7.0$ Hz). ^{13}C NMR (100 MHz, $CDCl_3$) δ (ppm) 176.0, 169.0, 159.6, 159.4, 138.7, 115.5, 115.4, 107.0, 67.3, 31.8, 29.2, 29.1, 28.6, 25.8, 22.6, 14.0.



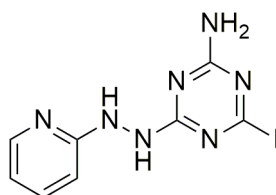
Synthesis of 4-(prop-2-ynoxy)-6-(2-(pyridine-2-yl)hydrazinyl)-1,3,5-triazin-2-amine (3e). Synthesis performed according to general procedure for intermediate **3**; wherein the 4-chloro-1,3,5-triazin-2-amine derivative is **2e**. Yield = 6.38 g, 87 %. EI-HRMS: Calc. for $C_{11}H_{11}N_7O$: 257.1025, Found: 257.1033. 1H NMR (400 MHz, DMSO- d_6) δ (ppm) 9.00 (bs, 1H), 8.32 (bs, 1H), 8.02 (d, 1H, $J = 4.7$ Hz), 7.48 (dd, 1H, $J = 8.2, 8.2$ Hz), 6.96 (bs, 2H), 6.64 (d, 1H, $J = 5.9$ Hz), 6.49 (d, 1H, $J = 8.2$ Hz), 4.88 (s, 2H), 4.75 (s, 1H). ^{13}C NMR (100 MHz, DMSO- d_6) δ (ppm) 169.3, 168.5, 159.8, 147.4, 137.4, 114.0, 105.8, 79.8, 77.3, 53.2.



Synthesis of 4-(hexylthio)-6-(2-(pyridine-2-yl)hydrazinyl)-1,3,5-triazin-2-amine (3f). Synthesis performed according to general procedure for intermediate **3**; wherein the 4-chloro-1,3,5-triazin-2-amine derivative is **2f**. Yield = 1.77 g, 24%. EI-HRMS: Calc. for $C_{14}H_{21}N_7S$: 319.1579, Found: 319.1578. 1H NMR (400 MHz, DMSO- d_6) δ (ppm) 8.01 (bs, 1H), 7.96 (m, 1H), 7.42 (m, 1H), 7.35 (bs, 1H), 6.68 (m, 1H), 6.52 (m, 2H), 4.07 (t, 2H, $J = 7.4$ Hz), 1.64 (m, 2H), 1.37 (m, 2H), 1.27 (m, 4H), 0.86 (t, 3H, $J = 7.0$ Hz). ^{13}C NMR (100 MHz, DMSO- d_6) δ (ppm) 178.6, 169.3, 166.6, 159.8, 147.4, 137.4, 114.0, 105.8, 36.8, 30.9, 29.2, 27.9, 22.1, 13.9.

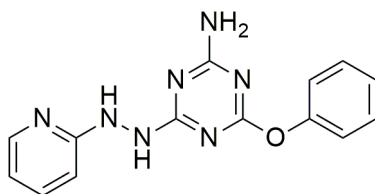


Synthesis of 4-chloro-6-(2-(pyridine-2-yl)hydrazinyl)-1,3,5-triazin-2-amine (3g). In a round bottom flask, 4,6-dichlorotriazin-2-amine (**1**) (5.00 g, 30.3 mmol, 1 eq.) was dissolved in THF. The solution was cooled down to -78°C and potassium carbonate (4.19 g, 30.3 mmol, 1 eq.) and 2-hydrazinopyridine (3.30 g, 30.3 mmol, 1 eq.) were added. The reaction mixture was stirred overnight allowing it to reach room temperature. The solvent was removed from the reaction mixture under reduced pressure and washed with distilled water. The product was filtered and dried by vacuum filtration. Yield = 7.13 g, 99%. EI-HRMS: Calc. for $\text{C}_8\text{H}_8\text{ClN}_7$: 237.0530, Found: 237.0526. ^1H NMR (400 MHz, DMSO-d_6) δ (ppm) 9.00 (bs, 1H), 8.60 (bs, 1H), 8.07 (dd, 1H, $J = 7.8, 7.8$ Hz), 7.99 (d, 1H, $J = 5.6$ Hz), 7.73 (bs, 2H), 7.29 (d, 1H, $J = 8.6$ Hz), 7.05 (t, 1H, $J = 6.6$ Hz). ^{13}C NMR (100 MHz, DMSO-d_6) δ (ppm) 174.4, 169.2, 168.0, 153.9, 147.4, 139.7, 127.9, 115.5.



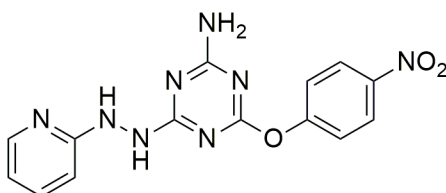
Synthesis of 4-iodo-6-(2-(pyridine-2-yl)hydrazinyl)-1,3,5-triazin-2-amine (3h). 4,6-diiodotriazin-2-amine (**2h**) (4.38 g, 12.6 mmol, 1 eq.) was dissolved in THF. The solution was cooled down to -78°C and 2-hydrazinopyridine (1.37 g, 12.6 mmol, 1 eq.) and potassium carbonate (1.74 g, 12.6 mmol, 1 eq.) were added. The reaction mixture was stirred overnight allowing it to reach room temperature. The solvent was removed under

reduced pressure and the crude was washed with distilled water. The product was finally filtered and dried by vacuum filtration. Yield = 3.81 g, 92%. Intermediate **3h** was not characterized since it was immediately taken into the oxidation step.



Synthesis of 4-phenoxy-6-(2-(pyridine-2-yl)hydrazinyl)-1,3,5-triazin-2-amine (3i).

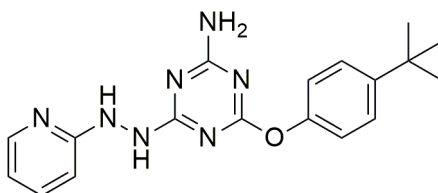
Synthesis performed according to general procedure for intermediate **3**; wherein the 4-chloro-1,3,5-triazin-2-amine derivative is **2i**. Yield = 5.19 g, 58 %. EI-HRMS: Calc. for $C_{14}H_{13}N_7O$: 295.1182 Found: 295.1181. 1H NMR (400 MHz, DMSO- d_6) δ (ppm) 9.06 (bs, 1H), 8.32 (bs, 1H), 8.02 (m, 1H), 7.00 – 7.50 (m, 9H), 6.64 (m, 1H), 6.52 (m, 1H). ^{13}C NMR (100 MHz, DMSO- d_6) δ (ppm) 170.4, 169.4, 168.7, 152.4, 147.5, 137.4, 129.4, 125.0, 122.0, 121.6, 114.0, 105.8.



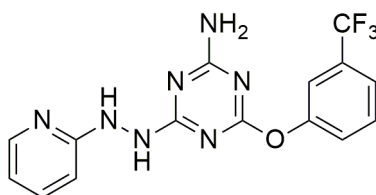
Synthesis of 4-(4-nitrophenoxy)-6-(2-(pyridin-2-yl)hydrazinyl)-1,3,5-triazin-2-amine (3j).

Synthesis performed according to general procedure for intermediate **3**; wherein the 4-chloro-1,3,5-triazin-2-amine derivative is **2j**. Yield = 2.70 g, 42%. EI-HRMS: Calc. for $C_{14}H_{12}N_8O_3$: 340.1032 Found: 340.1028. 1H NMR (400 MHz, DMSO- d_6) δ (ppm) 9.18 (bs, 1H), 8.29 (m, 2H), 8.09 (d, 1H, J = 9.0 Hz), 8.02 (1H, d, J = 4.7 Hz), 7.49 (m, 2H), 7.22

(d, 1H, $J = 9.0$ Hz), 7.13 (bs, 2H), 6.68 (m, 1H), 6.51 (d, 1H, $J = 8.6$ Hz). ^{13}C NMR (400 MHz, DMSO- d_6) δ (ppm) 169.3, 168.6, 159.6, 157.6, 147.6, 144.3, 137.4, 125.2, 123.0, 114.0, 105.8.

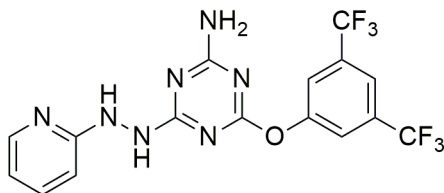


Synthesis of 4-(4-tert-butylphenoxy)-6-(2-(pyridine-2-yl)hydrazinyl)-1,3,5-triazin-2-amine (3k). Synthesis performed according to general procedure for intermediate **3**; wherein the 4-chloro-1,3,5-triazin-2-amine derivative is **2k**. Yield = 4.99 g, 99%. EI-HRMS: Calc. for $\text{C}_{19}\text{H}_{22}\text{N}_7\text{O}$: 351.1808 Found: 351.1808. ^1H NMR (400 MHz, DMSO- d_6) δ (ppm) 9.04 (bs, 1H), 8.33 (bs, 1H), 8.02 (m, 1H), 7.49 (m, 1H), 7.41 (m, 2H, $J = 8.2$ Hz), 7.08 (m, 2H), 6.99 (bs, 2H), 6.72-6.62 (m, 1H), 6.51 (m, 1H), 1.29 (s, 9H). ^{13}C NMR (100 MHz, DMSO- d_6) δ (ppm) 170.6, 169.4, 168.0, 159.8, 150.0, 147.4, 137.4, 126.1, 125.8, 121.2, 120.8, 114.0, 113.9, 105.9, 105.8, 34.1, 31.2.

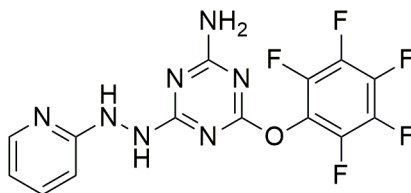


Synthesis of 4-(2-(pyridine-2-yl)hydrazinyl)-6-(3-(trifluoromethyl)phenoxy)-1,3,5-triazin-2-amine (3l). Synthesis performed according to general procedure for intermediate **3**; wherein the 4-chloro-1,3,5-triazin-2-amine derivative is **2l**. Yield = 5.00 g, 80%. EI-HRMS: Calc. for $\text{C}_{15}\text{H}_{12}\text{F}_3\text{N}_7\text{O}$: 363.1055 Found: 363.1056. ^1H NMR (400 MHz, DMSO-

d_6) δ (ppm) 9.14 (bs, 1H), 8.34 (bs, 1H), 8.02 (d, 1H, $J = 3.9$ Hz), 7.45 – 7.66 (m, 5H), 7.08 (bs, 2H), 6.66 (m, 1H), 6.52 (d, 1H, $J = 8.2$ Hz). ^{13}C NMR (100 MHz, DMSO- d_6) δ (ppm) 168.7, 159.8, 158.1, 152.7, 147.6, 146.4, 137.4, 130.8, 126.6, 121.9, 119.0, 114.0, 106.1. ^{19}F NMR (376 MHz, DMSO- d_6) δ (ppm) -60.99.

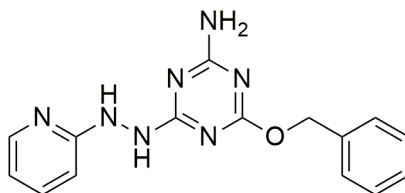


Synthesis of 4-(3,5-bis(trifluoromethyl)phenoxy)-6-(2-(pyridine-2-yl)hydrazinyl)-1,3,5-triazin-2-amine (3m). Synthesis performed according to general procedure for intermediate **3**; wherein the 4-chloro-1,3,5-triazin-2-amine derivative is **2m**. Yield = 3.13 g, 52%. EI-HRMS: Calc. for $\text{C}_{16}\text{H}_{11}\text{F}_6\text{N}_7\text{O}$: 431.0929 Found: 431.0931. ^1H NMR (400 MHz, DMSO- d_6) δ (ppm) 9.16 (bs, 1H), 8.37 (bs, 1H), 7.89-8.05 (m, 4H), 7.49 (dd, 1H, $J = 7.8, 7.8$ Hz), 7.25 (bs, 1H), 7.11 (bs, 1H), 6.64 (ddd, 1H, $J=7.0, 5.1, 0.8$ Hz) 6.50 (d, 1H, $J=8.2$ Hz). ^{13}C NMR (100 MHz, DMSO- d_6) δ (ppm) 170.7, 169.3, 159.7, 153.4, 147.6, 137.4, 131.6, 123.9, 121.6, 118.9, 114.0, 105.8. ^{19}F NMR (376 MHz, DMSO- d_6) δ (ppm) -61.18.



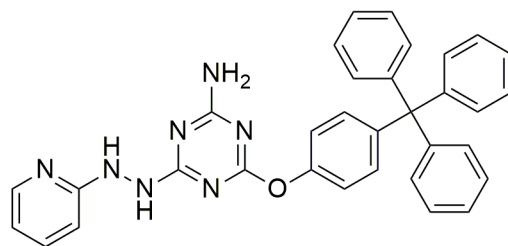
Synthesis of 4-(perfluorophenoxy)-6-(2-(pyridine-2-yl)hydrazinyl)-1,3,5-triazin-2-amine (3n). Synthesis performed according to general procedure for intermediate **3**;

wherein the 4-chloro-1,3,5-triazin-2-amine derivative is **2n**. The product was filtered by vacuum filtration and isolated via flash chromatography starting from mixture of hexanes : diethyl ether 1:1 to 100% diethyl ether as eluent. Yield = 2.46 g, 40%. EI-HRMS: Calc. for $C_{14}H_8F_5N_7O$: 385.0710 Found: 385.0721. 1H NMR (400 MHz, DMSO- d_6) δ (ppm) 9.32 (bs, 1H), 9.24 (bs, 1H), 8.39 (bs, 1H), 8.11 (bs, 1H), 8.02 (d, 1H, $J = 4.0$ Hz), 7.92 (d, 1H, $J = 4.0$ Hz), 7.41-7.51 (m, 3H), 7.20-7.30 (m, 3H), 6.64 (q, 2H, $J = 12.1, 5.5$ Hz), 6.50 (d, 1H, $J = 8.2$ Hz), 6.38 (d, 1H, $J = 8.2$ Hz). ^{19}F NMR (376 MHz, DMSO- d_6) δ (ppm) -153.94 (d, 1F, $J = 20.6$ Hz), -154.42 (d, 1F, $J = 20.6$ Hz), -160.03 (t, 1/2F, $J = 22.4, 20.6$ Hz), -160.72 (t, 1/2F, $J = 22.4, 20.6$ Hz), -163.38 (t, 2F, $J = 22.4$ Hz).



Synthesis of 4-(benzyloxy)-6-(2-(pyridin-2-yl)hydrazinyl)-1,3,5-triazin-2-amine (**3o**).

Synthesis performed according to general procedure for intermediate **3**; wherein the 4-chloro-1,3,5-triazin-2-amine derivative is **2o**. The product was filtered by vacuum filtration and purified via flash chromatography using a mixture of ethyl acetate and 10% methanol as eluent. Yield = 5.20 g, 56%. EI-HRMS: Calc. for $C_{15}H_{15}N_7O$: 309.1338 Found: 309.1337. 1H NMR (400 MHz, DMSO- d_6) δ (ppm) 8.94(bs, 1H), 8.28 (m, 1H), 8.03 (m, 1H), 7.48-7.26 (m, 5H), 6.87 (m, 1H), 6.65 (bs, 1H), 5.32 (s, 2H), 5.29 (bs, 1H), 5.14 (bs, 1H). ^{13}C NMR (100 MHz, DMSO- d_6) δ (ppm) 171.5, 169.3, 168.5, 147.5, 137.3, 136.4, 128.4, 128.0, 127.8, 113.9, 105.7, 66.9.

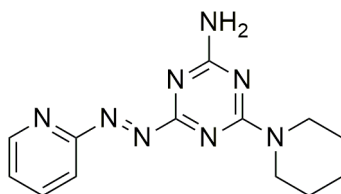


Synthesis of 4-(2-(pyridin-2-yl)hydrazinyl)-6-(4-tritylphenoxy)-1,3,5-triazin-2-amine (3p). Synthesis performed according to general procedure for intermediate **3**; wherein the 4-chloro-1,3,5-triazin-2-amine derivative is (**2p**). The product was filtered by vacuum filtration and purified via flash chromatography using a mixture of ethyl acetate and 10% methanol as eluent. Yield = 4.93g, 38%. EI-HRMS: Calc. for $C_{33}H_{27}N_7O$: 537.2277 Found: 537.2266. 1H NMR (400 MHz, DMSO- d_6) δ (ppm) 9.05(bs, 1H), 8.31 (m, 1H), 8.02 (m, 1H), 6.45-7.49 (m, 24H). ^{13}C NMR (100 MHz, DMSO- d_6) δ (ppm) 170.3, 169.4, 168.7, 168.2, 147.5, 146.4, 137.3, 131.4, 130.5, 127.8, 126.0, 120.9, 120.2, 113.9, 106.2, 105.8, 64.1.

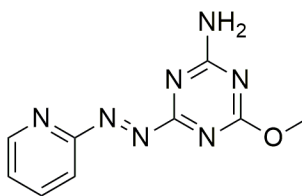
General procedure for synthesis of (*E*)-4-(pyridin-2-yl diazenyl)-1,3,5-triazin-2-amine derivatives (4a-p)

Synthetic procedure based on a report by Iranpoor and coworkers⁴⁹. In a round bottom flask, intermediate **3** (1 eq.) was dissolved in 50 mL of THF and stirred at room temperature. Iodobenzene diacetate (1 eq.) was added at once and the solution was stirred for 6 hours at room temperature. The solvent was removed under reduced pressure and the crude was washed with 50 mL of distilled water. The product was purified by flash chromatography starting with diethyl ether and ending with ethyl acetate as eluents. Note: The chemical shift of the amino protons of derivatives **4a-p** are concentration sensitive.

The amino protons chemical shift reported below correspond to the average values of the monomer shift, dimer shift obtained from three separate dilution experiments obtained using an iterative fitting procedure.



Synthesis of (*E*)-4-(piperidin-1-yl)-6-(pyridin-2-yl)diazenyl-1,3,5-triazin-2-amine (4a). Synthesis performed according to the general procedure for product **4**; wherein the 6-(2-(pyridine-2-yl)hydrazinyl)-1,3,5-triazin-2-amine derivative is **3a**. Yield = 1.36 g, 73%. EI-HRMS: Calc. for C₁₃H₁₈N₈ (M+2H): 286.1654 Found: 286.1645. ¹H NMR (400 MHz, CDCl₃) = δ (ppm) 8.78 (dd, 1H, *J* = 4.7, 1.6 Hz), 7.87-7.94 (m, 2H), 7.47 (ddd, 1H, *J* = 6.6, 4.7, 2.0 Hz), 6.92 (bs, 2H)**, 5.14 (bs, 2H)*, 3.88-3.82 (m, 4H), 1.70-1.60 (m, 6H) *NH₂ of free monomer, **NH₂ of dimer. ¹³C NMR (100 MHz, CDCl₃) = δ (ppm) 174.0, 168.0, 165.5, 162.6, 149.7, 138.3, 126.5, 116.0, 44.6, 25.8, 24.7. Melting Point = 206.9 - 209.1 C.



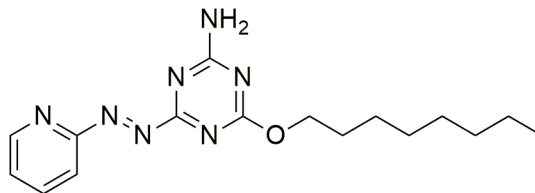
Synthesis of (*E*)-4-methoxy-6-(pyridin-2-yl)diazenyl-1,3,5-triazin-2-amine (4b). Synthesis performed according to general procedure for product **4**; wherein the 6-(2-(pyridine-2-yl)hydrazinyl)-1,3,5-triazin-2-amine derivative is **3b**. Yield = 2.88 g, 90%. EI-

HRMS: Calc. for C₉H₁₀N₇O (M+1H): 232.0947 Found: 232.0952. ¹H NMR (400 MHz, DMSO-d₆) = δ (ppm) 8.12 (ddd, 1H, *J* = 7.8, 7.4, 2.0 Hz), 7.99 (bs, 1H), 8.02 (bs, 1H), 7.78 (d, 1H, *J* = 7.8 Hz), 7.68 (ddd, 1H, *J* = 7.4, 4.7, 1.2 Hz), 3.92 (s, 1H). ¹³C NMR (100 MHz, DMSO-d₆) = δ (ppm) 175.9, 171.9, 169.0, 162.1, 149.8, 139.4, 127.3, 114.8, 54.7. Melting Point = 210.6 - 211.1 C.



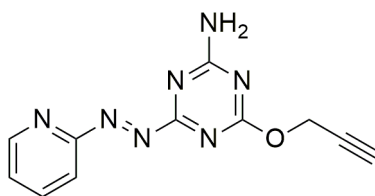
Synthesis of (E)-4-butoxy-6-(pyridin-2-yl)hydrazinyl-1,3,5-triazin-2-amine (4c).

Synthesis performed according to general procedure for product **4**; wherein the 6-(2-(pyridine-2-yl)hydrazinyl)-1,3,5-triazin-2-amine derivative is **3c**. Yield = 1.88 g, 38%. EI-HRMS: Calc. for C₁₂H₁₇N₇O (M+2H): 275.1495 Found: 275.1489. ¹H NMR (400 MHz, CDCl₃) = δ (ppm) 8.82 (dd, 1H, *J* = 4.7, 1.6 Hz), 8.76 (bs, 1H)***, 7.89-7.97 (m, 2H), 7.52 (ddd, 1H, *J* = 7.0, 4.7, 1.6 Hz), 6.80 (bs, 1H)***, 5.49 (bs, 2H)*, 4.47 (t, 2H, *J* = 6.6 Hz), 1.79 (m, 2H, *J* = 6.6 Hz), 1.50 (m, 2H, *J* = 7.4 Hz), 0.97 (t, 3H, *J* = 7.4 Hz) *NH of free monomer, **NH of dimer. ¹³C NMR (100 MHz, CDCl₃) = δ (ppm) 175.1, 172.5, 169.3, 162.3, 149.9, 138.5, 127.0, 115.3, 68.2, 30.7, 19.0, 13.7. Melting Point = 131.4 - 134.7 C.



Synthesis of (*E*)-4-(octyloxy)-6-(pyridin-2-yl-diazenyl)-1,3,5-triazin-2-amine (4d).

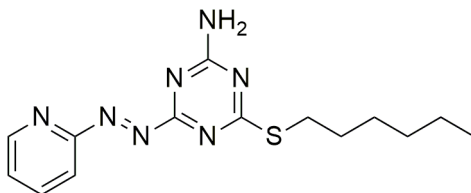
Synthesis performed according to general procedure for product **4**; wherein the 6-(2-(pyridine-2-yl)hydrazinyl)-1,3,5-triazin-2-amine derivative is **3d**. Yield = 2.57 g, 38%. EI- HRMS: Calc. for C₁₆H₂₅N₇O (M+2H): 331.2121 Found: 331.2111. ¹H NMR (600 MHz, CDCl₃) = δ (ppm) 8.80 (dd, 1H, *J* = 4.7, 1.8 Hz), 8.78 (bs, 1H)**, 7.97-7.92 (m, 2H), 7.50 (ddd, 1H, *J* = 6.4, 4.7, 1.8 Hz), 6.78 (bs, 1H)**, 5.54 (bs, 1H)*, 5.50 (bs, 1H)*, 1.80 (dd, 2H, *J* = 7.6, 6.4 Hz), 1.45 (m, 2H, *J* = 7.6 Hz), 1.35-1.25 (m, 8H), 0.88 (t, 3H, *J* = 7.6 Hz) * NH of free monomer ** NH of dimer. ¹³C NMR (100 MHz, CDCl₃) = δ (ppm) 174.5, 172.4, 169.2, 162.2, 149.9, 138.4, 127.0, 114.1, 68.3, 31.7, 29.2, 29.1, 28.6, 25.8, 22.6, 14.0. Melting Point = 121.6 - 123.2 C.



Synthesis of (*E*)-4-(prop-2-ynoxy)-6-(pyridin-2-yl-diazenyl)-1,3,5-triazin-2-amine (4e).

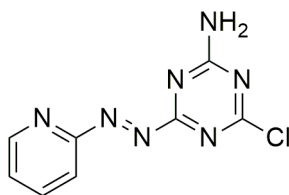
Synthesis performed according to general procedure for product **4**; wherein the 6-(2-(pyridine-2-yl)hydrazinyl)-1,3,5-triazin-2-amine derivative is **3e**. Yield = 0.23 g, 23%. EI- HRMS: Calc. for C₁₁H₉N₇O: 255.0869 Found: 255.0862. ¹H NMR (400 MHz, DMSO-d₆) = δ (ppm) 8.78 (dd, 1H, *J* = 4.7, 2.0 Hz), 8.13 (ddd, 1H, *J* = 7.8, 7.4, 2.0 Hz), 8.11 (bs, 1H), 8.06 (bs, 1H), 7.79 (dd, 1H, *J* = 7.8, 1.2 Hz), 7.70 (ddd, 1H, *J* = 7.4, 4.7, 1.2 Hz), 5.04 (d,

2H, $J = 2.3$ Hz), 3.62 (t, 1H, $J = 2.3$ Hz). ^{13}C NMR (100 MHz, DMSO- d_6) = δ (ppm) 175.9, 170.7, 169.0, 162.0, 149.8, 139.4, 127.4, 115.0, 78.2, 54.7.



Synthesis of (*E*)-4-(hexylthio)-6-(pyridin-2-ylidiazenyl)-1,3,5-triazin-2-amine (4f).

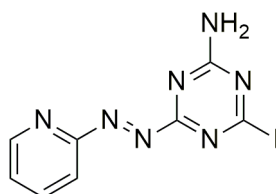
Synthesis performed according to general procedure for product **4**; wherein the 6-(2-(pyridine-2-yl)hydrazinyl)-1,3,5-triazin-2-amine derivative is **3f**. Yield = 1.36 g, 77 %. EI- HRMS: Calc. for $\text{C}_{14}\text{H}_{19}\text{N}_7\text{S}$: 317.1423 Found: 317.1414. ^1H NMR (600 MHz, CDCl_3) = δ (ppm) 8.80 (d, 1H, $J = 4.7$ Hz), 8.67 (bs, 1H)**, 7.96-7.91 (m, 2H), 7.51 (dd, 1H, $J = 7.0$, 4.7 Hz), 6.80 (bs, 1H)**, 5.48 (bs, 1H)*, 5.38 (bs, 1H)*, 3.20 (t, 2H, $J = 7.6$ Hz), 1.74 (m, 2H, $J = 7.6$ Hz), 1.45 (m, 2H, $J = 7.0$), 1.33-1.30 (m, 4H), 0.89 (t, 3H, $J = 7.0$ Hz) *NH of free monomer, **NH of dimer. ^{13}C NMR (100 MHz, CDCl_3) = δ (ppm) 184.5, 171.7, 166.5, 162.3, 149.9, 138.5, 127.1, 114.6, 31.3, 30.4, 28.9, 28.4, 22.5. Melting Point = 131.1 - 132.5 C



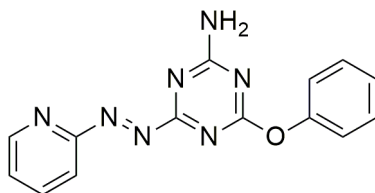
Synthesis of (*E*)-4-chloro-6-(pyridin-2-ylidiazenyl)-1,3,5-triazin-2-amine (4g).

Synthesis performed according to general procedure for product **4**; wherein the 6-(2-(pyridine-2-yl)hydrazinyl)-1,3,5-triazin-2-amine derivative is **3g**. Yield = 1.22 g, 24 %. EI-

HRMS: Calc. for C₈H₇ClN₇ (M+1H): 236.0451 Found: 236.0460. ¹H NMR (400 MHz, DMSO-d₆) = δ (ppm) 8.80 (d, 1H, *J* = 4.7 Hz), 8.62 (bs, 1H), 8.60 (bs, 1H), 8.14 (m, 1H, *J* = 7.8, 2.0 Hz), 7.82 (d, 1H, *J* = 8.2 Hz), 7.72 (ddd, 1H, *J* = 7.4, 4.7, 1.2 Hz). ¹³C NMR (100 MHz, DMSO-d₆) = δ (ppm) 174.4, 170.5, 168.0, 161.9, 149.9, 139.5, 127.7, 115.4.

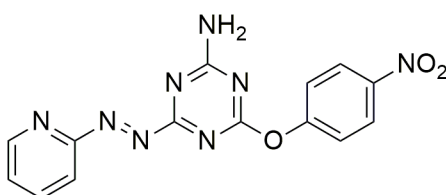


Synthesis of (*E*)-4-iodo-6-(pyridin-2-yl)diazenyl-1,3,5-triazin-2-amine (4h). Synthesis performed according to general procedure for product **4**; wherein the 6-(2-(pyridine-2-yl)hydrazinyl)-1,3,5-triazin-2-amine derivative is **3h**. Yield = 0.74 g, 25%. EI-HRMS: Calc. for C₈H₈IN₇ (M+2H): 328.9886 Found: 328.9887. ¹H NMR (400 MHz, DMSO-d₆) = δ (ppm) 8.79 (dd, 1H, *J* = 4.7, 1.6 Hz), 8.46 (bs, 1H), 8.37 (bs, 1H), 8.14 (ddd, 1H, *J* = 7.8, 7.4, 1.6 Hz), 7.80 (d, 1H, *J* = 8.2 Hz), 7.71 (ddd, 1H, *J* = 7.4, 4.7, 1.2 Hz). ¹³C NMR (100 MHz, DMSO-d₆) = δ (ppm) 165.7, 161.9, 154.9, 149.9, 142.9, 139.4, 127.6, 115.1. Melting Point = >300 C.

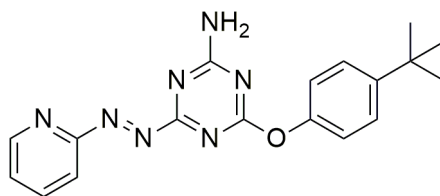


Synthesis of (*E*)-4-phenoxy-6-(pyridin-2-yl)diazenyl-1,3,5-triazin-2-amine (4i). Synthesis performed according to general procedure for product **4**; wherein the 6-(2-(pyridine-2-yl)hydrazinyl)-1,3,5-triazin-2-amine derivative is **3i**. Yield = 4.20 g, 81%. EI-

HRMS: Calc. for C₁₄H₁₃N₇O (M+2H): 295.1182 Found: 295.1184. ¹H NMR (400 MHz, CDCl₃) = δ (ppm) 8.78 (d, 1H, *J* = 4,7 Hz), 8.05 (bs, 1H)**, 7.97-7.90 (m, 2H), 7.5 (ddd, 1H, *J* = 5.1, 4.7, 2.0 Hz), 7.45-7.41 (m, 2H), 7.30-7.23 (m, 3H), 6.77 (bs, 1H)**, 5.63 (bs, 1H)*, 5.55 (bs, 1H)* *NH of free monomer, **NH of dimer. ¹³C NMR (100 MHz, DMSO-d₆) = δ (ppm) 176.1, 171.7, 169.2, 162.0, 151.8, 149.8, 139.4, 129.7, 127.4, 125.7, 121.8, 115.1. Melting Point = 208 - 212 C.



Synthesis of (*E*)-4-(4-nitrophenoxy)-6-(pyridin-2-yl)diazenyl-1,3,5-triazin-2-amine (4j). Synthesis performed according to general procedure for product **4**; wherein the 6-(2-(pyridine-2-yl)hydrazinyl)-1,3,5-triazin-2-amine derivative is **3j**. Yield = 2.38 g, 89%. EI-HRMS: Calc. for C₁₄H₁₂N₈O₃ (M+2H): 340.1032 Found: 340.0991. ¹H NMR (600 MHz, DMSO-d₆) = δ (ppm) 8.77 (dd, 1H, *J* = 4.7, 1.2 Hz) 8.33 (m, 2H), 8.26 (bs, 1H), 8.17 (bs, 1H), 8.12 (m, 1H, *J* = 7.6, 1.8 Hz), 7.62 (m, 2H), 7.78 (d, 1H, *J* = 7.6 Hz), 7.69 (ddd, 1H, *J* = 7.6, 4.7, 1.2 Hz). ¹³C NMR (100 MHz, DMSO-d₆) = δ (ppm) 178.5, 171.1, 169.1, 161.9, 156.7, 149.8, 144.9, 139.4, 125.4, 123.2, 115.2, 109.5.

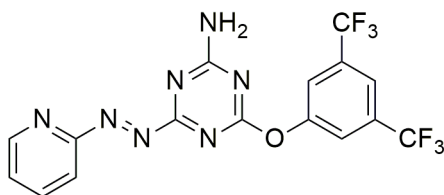


Synthesis of (E)-4-(4-tert-butylphenoxy)-6-(pyridin-2-yl)diazenyl-1,3,5-triazin-2-amine (4k). Synthesis performed according to general procedure for product **4**; wherein the 6-(2-(pyridine-2-yl)hydrazinyl)-1,3,5-triazin-2-amine derivative is **3k**. Yield = 0.44 g, 11%. EI-HRMS: Calc. for $C_{18}H_{21}N_7O$ ($M+2H$): 351.1808, Found: 351.1818. 1H NMR (600 MHz, $CDCl_3$) = δ (ppm) 8.78 (d, 1H, $J = 4.1$ Hz), 8.04 (bs, 1H)**, 7.94-7.89 (m, 2H), 7.50 (dd, 1H, $J = 5.9, 5.3$ Hz), 7.42 (m, 2H), 7.16 (m, 2H), 6.70 (bs, 1H)**, 5.56 (bs, 1H)*, 5.53 (bs, 1H)*, 1.34 (s, 9H), *NH of free monomer, **NH of dimer. ^{13}C NMR (100 MHz, $CDCl_3$) = δ (ppm) 175.2, 172.6, 169.3, 162.2, 149.9, 149.5, 148.7, 138.5, 127.1, 126.4, 121.0, 115.1, 34.5, 31.4. Melting Point = 171.3 - 173.1 C.

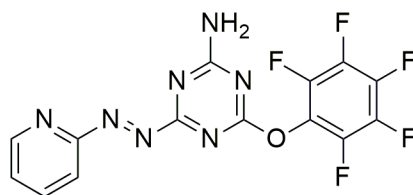


Synthesis of (E)-4-(3-(trifluoromethyl)phenoxy)-6-(pyridin-2-yl)diazenyl-1,3,5-triazin-2-amine (4l). Synthesis performed according to general procedure for product **4**; wherein the 6-(2-(pyridine-2-yl)hydrazinyl)-1,3,5-triazin-2-amine derivative is **3l**. Yield = 1.10 g, 22%. EI-HRMS: Calc. for $C_{15}H_{12}F_3N_7O$ ($M+2H$): 363.1055, Found: 363.1049. 1H NMR (600 MHz, $CDCl_3$) = δ (ppm) 8.67 (bs, 1H)**, 8.79 (d, 1H, $J = 4.7$ Hz), 7.98-7.90 (m, 2H), 7.56-7.50 (m, 4H), 7.46-7.42 (m, 1H), 6.80 (bs, 1H)**, 5.57 (bs, 1H)*, 5.68 (bs, 1H)*, * NH of free monomer, ** NH of dimer. ^{13}C NMR (100 MHz, $CDCl_3$) = δ (ppm)

175.4, 172.2, 169.4, 162.1, 151.9, 150.0, 138.6, 132.2, 131.9, 130.1, 127.3, 125.4, 122.7, 119.1, 115.5. ^{19}F NMR (376.42 MHz, CDCl_3) = δ (ppm) -62.6. Melting Point = 170.2 - 172.4 C.



Synthesis of (*E*)-4-(3,5-bis(trifluoromethyl)phenoxy)-6-(pyridin-2-yl)diazenyl-1,3,5-triazin-2-amine (4m). Synthesis performed according to general procedure for product **4**; wherein the 6-(2-(pyridine-2-yl)hydrazinyl)-1,3,5-triazin-2-amine derivative is **3m**. Yield = 1.94 g, 62%. EI-HRMS: Calc. for $\text{C}_{16}\text{H}_{11}\text{F}_6\text{N}_7\text{O}$ ($\text{M}+2\text{H}$): 431.0929, Found: 431.0877. ^1H NMR (600 MHz, DMSO-d_6) = δ (ppm) 8.78 (d, 1H, $J = 4.7$ Hz), 8.26 (bs, 1H), 8.22 (s, 2H), 8.18 (bs, 1H), 8.13 (ddd, 1H, $J = 7.8, 7.4, 1.9$), 8.06 (s, 1H), 7.80 (d, 1H, $J = 7.8$ Hz), 7.70 (ddd, 1H, $J = 7.4, 4.7, 1.2$ Hz), * NH of free monomer, ** NH of dimer. ^{13}C NMR (100 MHz, DMSO-d_6) = δ (ppm) 176.0, 171.3, 169.1, 162.0, 152.8, 149.8, 139.4, 131.6, 127.5, 124.0, 121.5, 119.6, 115.3. ^{19}F NMR (376 MHz, DMSO-d_6) = δ (ppm) -61.22. Melting Point = 193.2 - 196.2 C



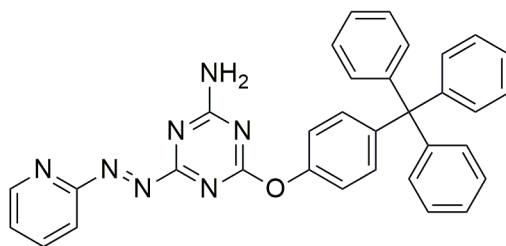
Synthesis of (*E*)-4-(perfluorophenoxy)-6-(pyridin-2-yl)diazenyl-1,3,5-triazin-2-amine (4n). Synthesis performed according to general procedure for product **4**; wherein the 6-(2-(pyridine-2-yl)hydrazinyl)-1,3,5-triazin-2-amine derivative is **3n**. Yield = 1.54 g, 62%. EI-

HRMS: Calc. for $C_{14}H_8F_5N_7O$ (M+2H): 385.0710 Found: 385.0710. 1H NMR (400 MHz, DMSO- d_6) = δ (ppm) 8.78 (ddd, 1H, $J = 4.7, 2.0, 0.8$ Hz), 8.57 (bs, 1H), 8.40 (bs, 1H), 8.14 (ddd, 1H, $J = 8.2, 7.4, 2.0$ Hz), 7.82 (d, 1H, $J = 8.2$ Hz), 7.70 (ddd, 1H, $J = 7.4, 4.7, 0.8$ Hz). ^{13}C NMR (100 MHz, DMSO- d_6) = δ (ppm) 176.2, 170.0, 169.2, 161.8, 159.4, 149.9, 139.5, 127.7, 115.7, 109.5. ^{19}F NMR (376 MHz, DMSO- d_6) = δ (ppm) -153.6 (d, 2H, $J = 19.9$ Hz), -158.3 (dd, 1H, $J = 23.9, 19.9$ Hz), -162.6 (t, 2H, $J = 23.9$ Hz).



Synthesis of (*E*)-4-(benzyloxy)-6-(pyridin-2-yl)hydrazinyl-1,3,5-triazin-2-amine (4o).

Synthesis performed according to general procedure for product **4**; wherein the 6-(2-(pyridine-2-yl)hydrazinyl)-1,3,5-triazin-2-amine derivative is **3o**. Yield = 1.35 g, 26%. EI-HRMS: Calc. for $C_{15}H_{15}N_7O$ (M+2H): 309.1338 Found: 309.1335. 1H NMR (400 MHz, $CDCl_3$) = δ (ppm) 8.85 (bs, 1H)**, 8.82 (d, 1H, $J = 4.3$ Hz), 7.97-7.90 (m, 2H), 7.52 (ddd, 1H, $J = 6.6, 4.7, 1.6$ Hz), 7.48 (m, 2H), 7.39-7.31 (m, 3H), 7.08 (bs, 1H)**, 5.56 (bs, 1H)*, 5.54 (s, 2H), 5.54 (bs, 1H)*, *NH Free monomer, **NH dimer. ^{13}C NMR (100 MHz, $CDCl_3$) = δ (ppm) 174.9, 172.3, 169.3, 162.3, 150.0, 138.5, 135.5, 128.5, 128.2, 128.1, 127.1, 114.9, 69.6.

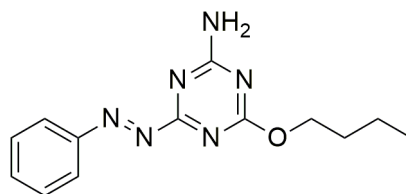


Synthesis of (*E*)-4-(pyridin-2-ylhydrazinyl)-6-(4-tritylphenoxy)-1,3,5-triazin-2-amine (4p). Synthesis performed according to general procedure for product **4**; wherein the 6-(2-(pyridine-2-yl)hydrazinyl)-1,3,5-triazin-2-amine derivative is **3p**. Yield = 1.38 g, 28%. EI-¹H NMR (400 MHz, CDCl₃) = δ (ppm) 8.80 (d, 1H, *J* = 5.1 Hz), 8.01 (bs, 1H)**, 7.99-7.92 (m, 2H), 7.53 (ddd, 1H, *J* = 7.0, 5.1, 2.0 Hz), 7.30-7.19 (m, 17H), 7.15 (m, 2H), 6.68 (bs, 1H)**, 5.64 (bs, 1H)*, 5.56 (bs, 1H)*, *NH free monomer, **NH dimer. ¹³C NMR (100 MHz, CDCl₃) = δ (ppm) 175.4, 172.4, 169.4, 162.2, 149.9, 146.6, 144.4, 138.6, 132.2, 131.1, 127.5, 127.2, 126.0, 120.4, 115.6, 110.0, 64.6.

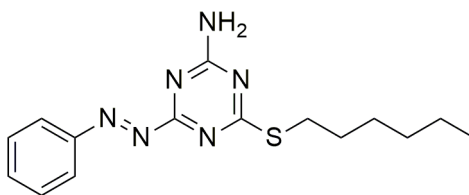
General procedure for synthesis of (*E*)-6-(phenyldiazenyl)-1,3,5-triazin-2-amine derivatives (5)

In a clean, dry round bottom flask 4-chloro-1,3,5-triazin-2-amine derivative (**2**) (1 eq.), phenylhydrazine (1 eq.) and potassium carbonate (1 eq.) were mixed with 100 mL of THF. The reaction mixture was refluxed for 5 hours, cooled and the solvent removed under reduced pressure. The crude material was poured into 50 mL of distilled water and the intermediate was extracted with 3 x 50 mL of dichloromethane. The organic phase was dried over sodium sulfate and the drying agent was removed by gravity filtration. One equivalent of (diacetoxy)iodobenzene was added to the intermediate solution and stirred

overnight at room temperature. Solvent was removed under reduced pressure and the product was purified by flash chromatography using a solvent mixture 1:1 hexanes : diethyl ether as eluent.

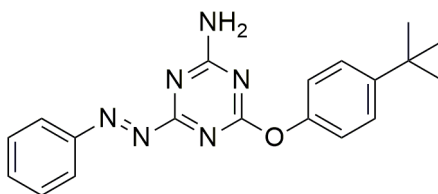


Synthesis of (*E*)-4-butoxy-6-(phenyldiazenyl)-1,3,5-triazin-2-amine, 5c. Synthesis performed according to general procedure for product **5**; wherein the 4-chloro-1,3,5-triazin-2-amine derivative is **2c**. Yield = 1.00 g 21%. EI-HRMS: Calc. for C₁₃H₁₈N₆O (M+2H): 274.1542 Found: 274.1548. ¹H NMR (400 MHz, CDCl₃) = δ (ppm) 8.02 (m, 2H), 7.92 (bs, 1H)**, 7.59-7.52 (m, 3H), 6.89 (bs, 1H)**, 5.67 (bs, 1H)*, 5.52 (bs, 1H)*, 4.44 (t, 2H, *J* = 6.4 Hz), 1.78 (m, 2H, *J* = 7.6, 6.4 Hz), 1.48 (m, 2H, *J* = 7.6 Hz), 0.95 (t, 3H, *J* = 7.6 Hz), *NH free monomer, **NH dimer. ¹³C NMR (100 MHz, CDCl₃) = δ (ppm) 175.2, 172.3, 169.2, 152.1, 133.5, 129.2, 124.0, 68.1, 30.6, 19.0, 13.7.



Synthesis of (*E*)-4-(hexylthio)-6-(phenyldiazenyl)-1,3,5-triazin-2-amine, 5f. Synthesis performed according to general procedure for product **5**; wherein the 4-chloro-1,3,5-triazin-2-amine derivative is **2f**. Yield = 0.25 g 15%. EI-HRMS: Calc. for C₁₅H₂₂N₆S (M+2H): 318.1627 Found: 318.1629. ¹H NMR (400 MHz, CDCl₃) = δ (ppm) 8.05 (m, 2H),

7.97 (bs, 1H)**, 7.61-7.52 (m, 3H), 5.70 (bs, 1H)**, 5.50 (bs, 1H)*, 5.49 (bs, 1H)*, 3.18 (t, 2H, $J = 7.4$ Hz), 1.73 (m, 2H), 1.45 (m, 2H), 1.32 (m, 4H), 0.89 (t, 3H, $J = 7.0$ Hz), *NH free monomer, **NH dimer. ^{13}C NMR (100 MHz, CDCl_3) = δ (ppm) 184.5, 172.1, 166.6, 152.2, 133.5, 129.2, 124.0, 31.2, 30.0, 28.9, 28.4, 22.4, 14.0.



Synthesis of (*E*)-4-(4-(*tert*-butyl)phenoxy)-6-(phenyldiazenyl)-1,3,5-triazin-2-amine, **5k.** Synthesis performed according to general procedure for product **5**; wherein the 4-chloro-1,3,5-triazin-2-amine derivative is **2k**. Yield = 0.35 g 22%. EI-HRMS: Calc. for $\text{C}_{19}\text{H}_{22}\text{N}_6\text{O}$ ($\text{M}+2\text{H}$): 350.1855 Found: 350.1857. ^1H NMR (400 MHz, CDCl_3) = δ (ppm) 8.06 (m, 2H), 7.59-7.53 (m, 3H), 7.43 (m, 2H), 7.40 (bs, 1H)**, 7.14 (m, 2H), 6.80 (bs, 1H)**, 5.65 (bs, 1H)*, 5.53 (bs, 1H)*, 1.34 (s, 9H), *NH free monomer, **NH dimer. ^{13}C NMR (100 MHz, CDCl_3) = δ (ppm) 175.4, 172.5, 169.3, 152.0, 149.5, 148.8, 133.6, 129.2, 126.4, 124.0, 121.0, 34.4, 31.4.

2.5.3 ^1H NMR Dilution Experiments

General Procedure for a Dilution Experiment.

Preparation of saturated solutions of (*E*)-4-(pyridin-2-ylidiazanyl)-1,3,5-triazin-2-amine derivative (4). At least one day before the dilution experiment, a volume of 8 mL of saturated solution of the (*E*)-4-(pyridin-2-ylidiazanyl)-1,3,5-triazin-2-amine derivative (4) in the selected solvent (CHCl_3 or Toluene) was prepared in a clean and dry vial. Separately, three clean and dry vials were labeled and weighed on a Sartorius Analytical Balance CPA124S. To each of the three vials, 2.0 mL of a previously prepared saturated solution of 4 was added, to later take them into a desiccator and remove the solvent under reduced pressure. Once all solvent was removed, the vials were weighed again to record the exact mass of 4 in each vial. Right before a dilution procedure, 2.0 mL of deuterated solvent (CDCl_3 or Toluene- d_8 , consistent with the selected solvent) were added to each vial in order to dissolve 4.

Dilution Procedure. In a clean and dry eight inches NMR tube, 0.5 mL of the selected deuterated solvent (CDCl_3 or Toluene- d_8) was injected via syringe. A ^1H NMR spectrum was recorded in order to ensure the purity of the same. Aliquots of the prepared saturated solution were added successively to the NMR tube with the selected deuterated solvent (4 μL x 5, 10 μL x 2, 20 μL x 3, 50 μL x 2, 100 μL , 200 μL , 500 μL x 2). The NMR tube was shaken between each addition and a ^1H NMR spectrum was recorded right after. The chemical shifts of the N-H protons from 4 were identified and tracked during the experiment. The correlation between the concentration of 4 and the chemical shift of an N-H proton was fitted satisfactorily to the dimerization model using Origin Data Analysis

Software. Dilution procedure was repeated twice more to ensure the reliability and reproducibility of the obtained values.

2.6 References

- (1) Lehn, J.-M. *Polym. Int.*, **2002**, 51 (10), 825.
- (2) Bouteiller, L. *Adv Polym Sci.*, **2007**, 207, 79.
- (3) Binder, W. H.; Zirbs, R. *Adv. Polym. Sci.*, **2007**, 207, 1.
- (4) Folmer, B.; Sijbesma, R. *Adv. Mater.*, **2000**, 12 (12), 874.
- (5) Bosman, A. W.; Sijbesma, R. P.; Meijer, E. *Mater. Today*, **2004**, 7 (4), 34.
- (6) Han, J. T.; Lee, D. H.; Ryu, C. Y.; Cho, K. *J. Am. Chem. Soc.*, **2004**, 126, 4796.
- (7) Dankers, P. Y. W.; Harmsen, M. C.; Brouwer, L. A.; Van Luyn, M. J. A.; Meijer, E. W. *Nat. Mater.*, **2005**, 4 (7), 568.
- (8) Dankers, P. Y. W.; Boomker, J. M.; Huizinga-van der Vlag, A.; Wisse, E.; Appel, W. P. J.; Smedts, F. M. M.; Harmsen, M. C.; Bosman, A. W.; Meijer, W.; van Luyn, M. J. A. *Biomaterials*, **2011**, 32 (3), 723.
- (9) Hentschel, J.; Kushner, A. M.; Ziller, J.; Guan, Z. *Angew. Chemie Int. Ed. Engl.*, **2012**, 51 (42), 10561.
- (10) Dong, R.; Zhou, Y.; Huang, X.; Zhu, X.; Lu, Y.; Shen, J. *Adv. Mater.*, **2015**, 27 (3), 498.
- (11) Zhu, X. *ACS Macro Lett*, **2012**, 1, 1208.
- (12) Yu, B.; Wang, B.; Guo, S.; Zhang, Q.; Zheng, X.; Lei, H.; Liu, W.; Bu, W.; Zhang, Y.; Chen, X. *Chem. Eur. J.*, **2013**, 19, 4922.
- (13) Li, Y.; Chen, Y.; Dong, H.; Dong, C. *Med. Chem. Commun.*, **2015**, 6 (10), 1874.
- (14) Yagai, S.; Karatsu, T.; Kitamura, A. *Chem. Eur. J.*, **2005**, 11 (14), 4054.
- (15) Ball, P.; Nicholls, C. H. *Dye. Pigment.*, **1982**, 3 (1), 5.
- (16) Rwe, P. *Tetrahedron Lett.*, **1973**, 37, 3559.
- (17) Bandara, H. M. D.; Friss, T. R.; Enriquez, M. M.; Isley, W.; Incarvito, C.; Frank, H.

- A.; Gascon, J.; Burdette, S. C. *J. Org. Chem.*, **2010**, 75 (14), 4817.
- (18) Mudraboyina, B. P.; Wang, H.-B.; Newbury, R.; Wisner, J. A. *Acta Crystallogr. Sect. E. Struct. Rep. Online*, **2011**, 67 (Pt 5), o1222.
- (19) Mayer, M. F.; Nakashima, S.; Zimmerman, S. C. *Org. Lett.*, **2005**, 7 (14), 3005.
- (20) Li, X.-Q.; Jia, M.-X.; Wang, X.-Z.; Jiang, X.-K.; Li, Z.-T.; Chen, G.-J.; Yu, Y.-H. *Tetrahedron*, **2005**, 61 (40), 9600.
- (21) Brown, E. V.; Granneman, G. R. *J. Am. Chem. Soc.*, **1975**, 97 (3), 621.
- (22) Bullock, D. J. W.; Cumper, C. W. N.; Vogel, A. I. *J. Chem. Soc.*, **1965**, 5316.
- (23) Campbell, N.; Henderson, A. W.; Taylor, D. *J. Chem. Soc.*, **1953**, 1281.
- (24) Hunter, C. A. *Angew. Chem. Int. Ed. Engl.*, **2004**, 43 (40), 5310.
- (25) Gilli, G.; Bellucci, F.; Ferretti, V.; Bertolasi, V. *J. Am. Chem. Soc.*, **1989**, 111 (3), 1023.
- (26) Bertolasi, V.; Gilli, P.; Ferretti, V.; Gilli, G. *Acta Crystallogr. Sect. B Struct. Sci.*, **1998**, 54 (1), 50.
- (27) Jeffrey, G. A. *J. Mol. Struct.*, **1999**, 293, 485.
- (28) Seto, C. T.; Mathias, J. P.; Whitesides, G. M. *J. Am. Chem. Soc.*, **1993**, 115 (4), 1321.
- (29) Seto, C. T.; Whitesides, G. M. *J. Am. Chem. Soc.*, **1993**, 115 (4), 1330.
- (30) Mathias, J. P.; Simanek, E. E.; Zerkowski, J. A.; Seto, C. T.; Whitesides, G. M. *J. Am. Chem. Soc.* **1994**, 116 (10), 4316.
- (31) Simanek, E. E.; Isaacs, L.; Li, X.; Wang, C. C. C.; Whitesides, G. M. *J. Org. Chem.*, **1997**, 62 (26), 8994.
- (32) Choi, I. S.; Li, X.; Simanek, E. E.; Akaba, R.; Whitesides, G. M. *Chem. Mater.*, **1999**, 11 (3), 684.
- (33) de Hoog, P.; Gamez, P.; Driessen, W. L.; Reedijk, J. *Tetrahedron Lett.*, **2002**, 43 (38), 6783.
- (34) Baliani, A.; Bueno, G. J.; Stewart, M. L.; Yardley, V.; Brun, R.; Barrett, M. P.; Gilbert, I. H. *J. Med. Chem.*, **2005**, 48 (17), 5570.
- (35) Ma, H.; Li, W.; Wang, J.; Xiao, G.; Gong, Y.; Qi, C.; Feng, Y.; Li, X.; Bao, Z.; Cao, W.; Sun, Q.; Veaceslav, C.; Wang, F.; Lei, Z. *Tetrahedron*, **2012**, 68 (39), 8358.

- (36) Bez, G. *Bull. Chem. Soc. Jpn.*, **2010**, 83 (8) 923.
- (37) Thordarson, P. *Chem. Soc. Rev.*, **2011**, 40 (3), 1305.
- (38) Arunan, E.; Desiraju, G. R.; Klein, R. A.; Sadlej, J.; Scheiner, S.; Alkorta, I.; Clary, D. C.; Crabtree, R. H.; Dannenberg, J. J.; Hobza, P.; Kjaergaard, H. G.; Legon, A. C.; Mennucci, B.; Nesbitt, D. J. *Pure Appl. Chem.*, **2011**, 83 (8), 1637.
- (39) Chen, J. S.; Shirts, R. B. *J. Phys. Chem.*, **1985**, 89 (9), 1643.
- (40) Fielding, L. *Tetrahedron*, **2000**, 56 (34), 6151.
- (41) Beer, P. D. *Adv. Mater.*, **1991**, 3 (10), 517.
- (42) Hansch, C.; Leo, A.; Taft, R. W. *Chem. Rev.*, **1991**, 91 (2), 165.
- (43) Hansch, C.; Leo, A.; Unger, S. H.; Kim, K. H.; Xikaitani, D.; Lien, E. J. *J. Med. Chem.*, **1973**, 16 (11), 1207.
- (44) Hunter, C. a. *Angew. Chem. Int. Ed. Engl.*, **2004**, 43 (40), 5310.
- (45) Salonen, L. M.; Ellermann, M.; Diederich, F. *Angew. Chem. Int. Ed. Engl.*, **2011**, 50 (21), 4808.
- (46) Sartorius, J.; Schneider, H.-J. *Chem. Eur. J.*, **1996**, 2 (11), 1446.
- (47) Smith, A. L.; D'Angelo, N. D.; Bo, Y. Y.; Booker, S. K.; Cee, V. J.; Herberich, B.; Hong, F.-T.; Jackson, C. L. M.; Lanman, B. A.; Liu, L.; Nishimura, N.; Pettus, L. H.; Reed, A. B.; Tadesse, S.; Tamayo, N. A.; Wurz, R. P.; Yang, K.; Andrews, K. L.; Whittington, D. A.; McCarter, J. D.; Miguel, T. S.; Zalameda, L.; Jiang, J.; Subramanian, R.; Mullady, E. L.; Caenepeel, S.; Freeman, D. J.; Wang, L.; Zhang, N.; Wu, T.; Hughes, P. E.; Norman, M. H. *J. Med. Chem.*, **2012**, 55 (11), 5188.
- (48) Klingele, J.; Kaase, D.; Hilgert, J.; Steinfeld, G.; Klingele, M. H.; Lach, J. *Dalton Trans.*, **2010**, 39 (19), 4495.
- (49) Iranpoor, N.; Firouzabadi, H.; Khalili, D. *Bull. Chem. Soc. Jpn.*, **2010**, 83 (8), 923.

Chapter 3

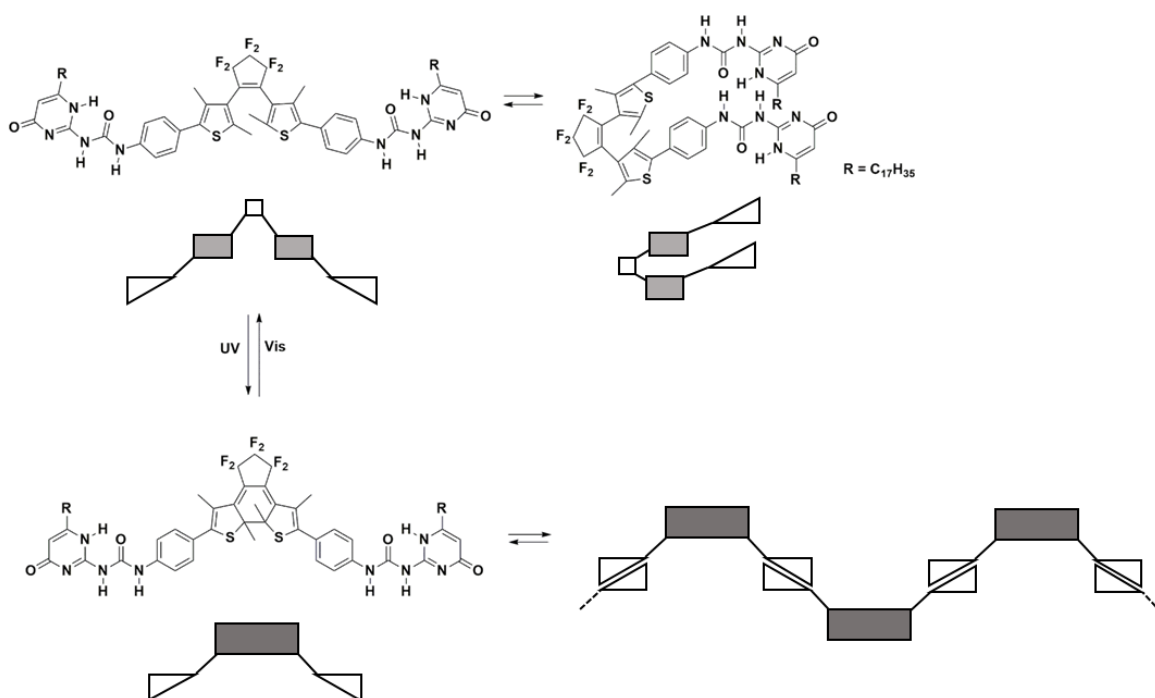
3 Photochemistry of Photoswitchable Self-Complementary DDAAA Hydrogen Bond Arrays

3.1 Introduction

The development of smart materials has encouraged the design and synthesis of novel and sophisticated molecules that are responsive to their environment. In this regard, photoswitches are some of the most attractive examples. Interest in these systems is often due to the fact that there is no extra chemical additive required in order to induce a change in the system, in contrast to stimuli such as pH, ions and solvent system.¹⁻³ The only requirement is the irradiation of a specific wavelength which offers an effective and specific method of controlling the property one is interested in modifying.⁴ A common application of photoswitches in smart materials is control over their patterns of aggregation. The strategic inclusion of a photoswitch can generally either: (1) turn ON/OFF the formation of a supramolecular entity; or (2) increase/reduce the complexation strength between monomers forming aggregates (e.g. dimers or higher order complexes).

The first scenario is exemplified by Takeshita and co-workers' report of a photoreversible supramolecular polymer.^{5,6} In this work, the supramolecular polymer binding sites were two quadruple hydrogen bond units (Meijer's ureidopyrimidones) linked to a diarylethene moiety by phenyl groups (Scheme 3.1).⁶ The authors reported a significant increase in particle size once chloroform and tetrahydrofuran solutions were irradiated with

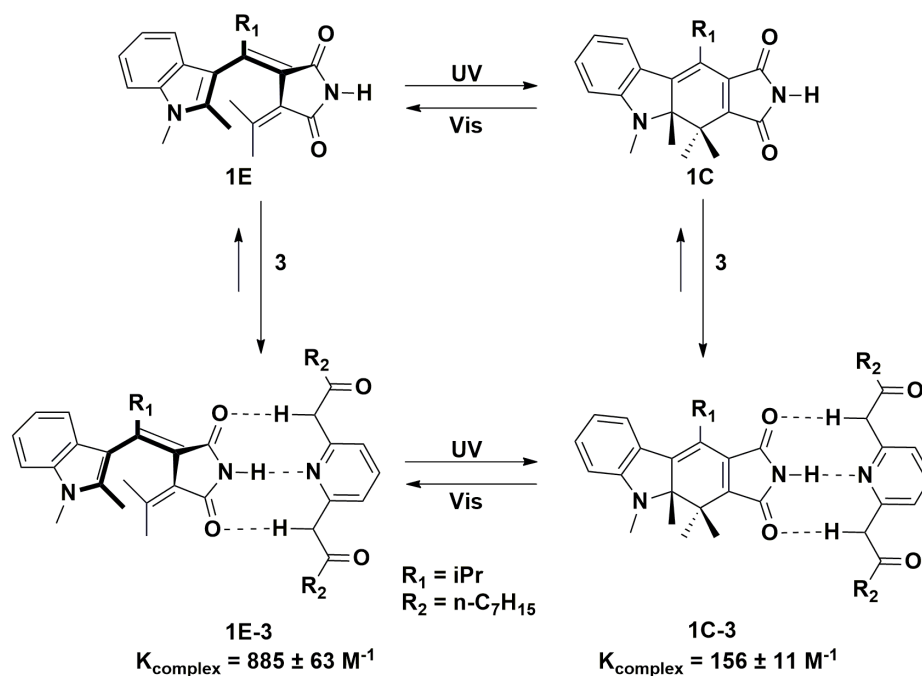
UV light. The reasoning behind this change is that the closed form of the diarylethene moiety fixes the two quadruple hydrogen bond units on opposing sides of the molecule. This configuration promotes intermolecular hydrogen bond interactions that lead to the formation of a supramolecular polymer. Once the system is exposed to visible light, the average particle size in solution decreased in value. This is due to the flexibility of the open form that allows weak intramolecular hydrogen bonding. When chloroform was employed as the solvent, besides visible light irradiation, heating was required in order to return the particle size to its initial value. On the other hand, when tetrahydrofuran was used, the particle size returned to its beginning value without further assistance. These results are in accordance with the effect of the solvent polarity on the hydrogen bond strength: the more polar the solvent, the weaker the hydrogen bond interactions.



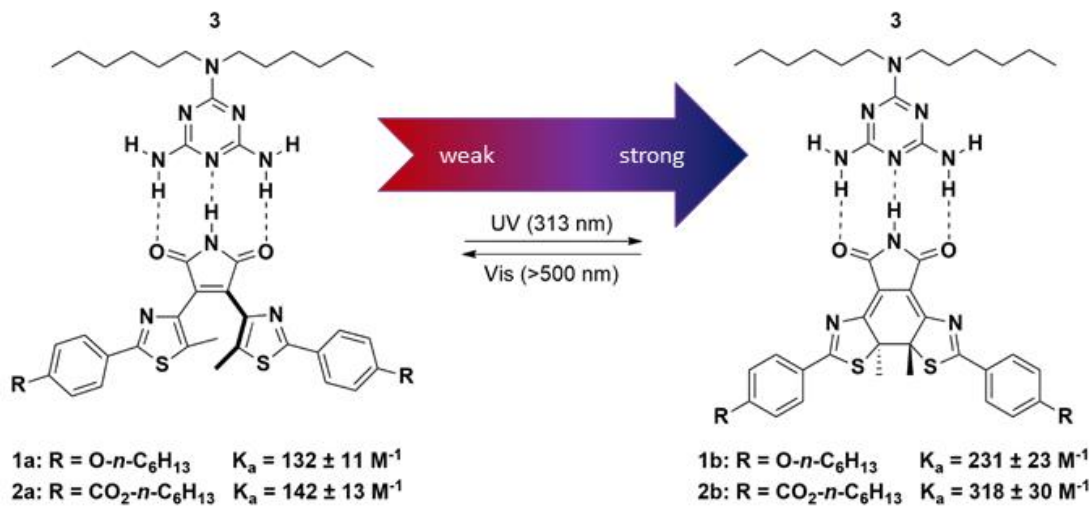
Scheme 3.1 Takeshita's photoreversible supramolecular polymer.

On the other hand, photoswitches can also control the strength of non-covalent interactions between participating entities. In 2001, Yokoyama and coworkers reported an indolylfulgimide – bis(acylamino)pyridine **ADA-DAD** complex whose association constant can be controlled upon irradiation of a particular wavelength (Scheme 3.2).⁷ As outlined in Scheme 3.2, the complexation constant of **1E-3** (photoswitch open form) is significantly higher than the complexation constant of **1C-3** (photoswitch closed form); i.e. $885 \pm 63 \text{ M}^{-1}$ and $156 \pm 11 \text{ M}^{-1}$ respectively. The authors explained the drop in the complexation constant as due to a loss of planarity of the **1E-3** complex once switched to the **1C-3** complex. In the former complex, the bismethylenesuccinimide moiety in **1E** is flexible, and therefore, it can rearrange to interact with **3** in a planar fashion. In the latter complex, the maleimide moiety in **1C** is fixed which does not allow reorganization and reduces recognition between interacting sites.

Another example that outlines how the stability of a supramolecular complex can be modulated by a photochromic system is that reported by Hecht and coworkers (Scheme 3.3).⁸ In this example, the enhanced or diminished stability of the bis(thiazol-4-yl)maleimides – melamine complexes depends on changes in the electron-density of the maleimide moiety. The π conjugation in the closed forms (**1b/2b**) reduces the electron-density on the maleimide ring and polarizes the imide N-H bond turning it into a better donor compared with the imide N-H bond of the open form (**1a/2a**).



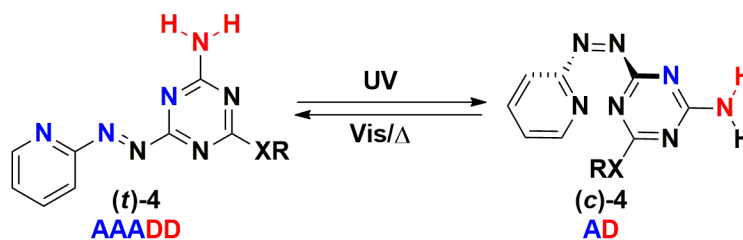
Scheme 3.2 Yokoyama's indolylfulgimide – bis(acylamino)pyridine complex.



Scheme 3.3 Photoswitchable triple hydrogen bond motif studied by Hecht and coworkers.

In these examples, the control over complexation via photoswitching is based on the premise that one of the isomers is particularly designed to be part of a supramolecular array. Meanwhile, the other isomer is expected either to be unable to interact or to form a weaker complex due to structural changes *peripheral* to the array itself. In this sense, the photoswitchable self-complementary **DDAAA** hydrogen bond arrays reported in Chapter 2 differ significantly. Here, the array's structure itself is changed by photoisomerization to an inherently less complementary arrangement.

Compounds **4a-p** were designed to dimerize as *trans* isomers, now referred as (*t*)-**4a-p**. In these compounds, the location of the acceptor sites in the pyridine moiety and the azo group were tailored to match the donor sites from the amino group. Likewise, the planarity of these isomers contributes to the alignment between binding sites. Once (*t*)-**4a-p** are transformed into the *cis*-isomeric form (referred to as (*c*)-**4a-p**) the change in the geometric disposition of the aromatic rings and the concurrent loss of molecular planarity^{9,10} cause a reduction in the number of sites available to interact in a putative dimer; i.e. **4a-p** change from **DDAAA** arrays to **DA** arrays (Scheme 3.4).



Scheme 3.4 Photoisomerization of derivatives **4a-p**.

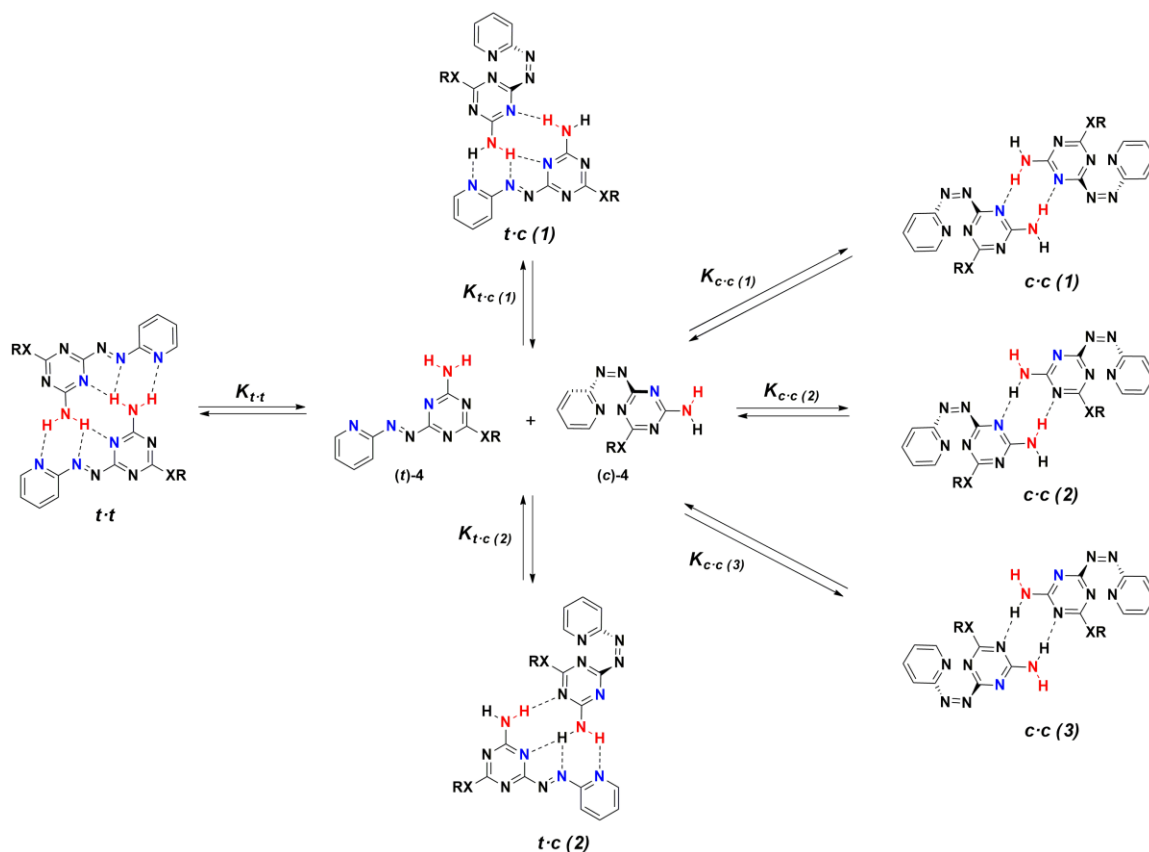
Assuming a 100% interconversion from *trans* to *cis* (and *vice versa*), the equilibria would be simplified to a comparison between the dimerization strengths of each isomeric

form (as exemplified in Yokoyama's complexes). Conversely, if both isomeric forms are present at the photostationary state (PSS), the study of the distribution of all species present would be represented by the different equilibria taking place at the same time (Scheme 3.5).

Scheme 3.5 illustrates how a *trans* to *cis* interconversion with a yield less than 100% results in the presence of several (*t*)-**4a-p** and (*c*)-**4a-p** species in solution. The *trans*-isomer would be able to dimerize (*t*·*t*) as reported in Chapter 2 (Section 2.3.2). On the other hand, the existence of *cis*-isomer in solution allows for two further complexation options: the dimerization of (*c*)-**4a-p** (*c*·*c* in Scheme 3.5); and, the complexation of (*c*)-**4a-p** with (*t*)-**4a-p** (*t*·*c* in Scheme 3.5).

As noted in Chapter 2 (and Scheme 3.5) the design of (*t*)-**4a-p** provides an effective molecular recognition in the sense that only one spatial arrangement of the monomeric units results in the desired stable dimer structure. Conversely, (*c*)-**4a-p** is able to form *t*·*c* complexes with two different relative geometries. This is due to the isomerization that discards two hydrogen bond acceptors (the nitrogen atoms on the azo and pyridyl moieties). This change results in two edges of the triazine ring with the same hydrogen bond array (**AD**) where molecular recognition can take place. For the same reason, there are three potential *c*·*c* dimer structures (*c*·*c* (1), *c*·*c* (2) and *c*·*c* (3) in Scheme 3.5). As a result, the observed (*c*)-**4a-p** dimerization constant ($K_{c\cdot c}$) will be the sum of all *c*·*c* dimer equilibria present. Similarly the observed complexation constant of (*c*)-**4a-p** with (*t*)-**4a-p** ($K_{t\cdot c}$) will be the summation of the two complexation processes in solution. Therefore, the real microscopic $K_{c\cdot c}$ and $K_{t\cdot c}$ values for each complex will be lower than those calculated. However, since all *c*·*c* dimer structures and *t*·*c* complex structures contribute to the

equilibria in solution, the composite K_{c-c} and K_{t-c} , are most useful to describe the response of our derivatives **4a-p**. Regardless, it is likely impossible to deconvolute the contributions from the different individual $c-c$ and $t-c$ equilibria anyway. This is similar to the contribution of Watson-Crick and non-Watson-Crick base pairing in solution.^{50,51,52}



Scheme 3.5 Hypothetical complexation equilibria present in mixed *cis/trans* solutions of derivatives **4a-p** in non-polar solvents.

The aim of this chapter is to discuss the photochemical properties of derivatives **4a-p** since the intended functionality of them depends on these properties. Likewise, it is our intention to elucidate the stabilities of the supramolecular species present in solution after photoisomerization where possible. The study of the stability of these complexes

compared with the *trans-trans* dimerization is desirable in order to understand the impact (and control) of the external stimulus (light) over the solution equilibria. Finally, an analysis of the thermal stability of the *cis* isomer of derivatives **4c**, **4f** and **4k** in toluene-*d*₈ solution is presented.

3.2 Results and Discussion

3.2.1 UV-Vis Characterization

The absorption spectra of all derivatives **4a-p** in their thermally stable *trans*-isomeric form (i.e. (*t*)-**4a-p**) were obtained from 10⁻⁵ to 10⁻⁴ M acetonitrile solutions at room temperature (Figure 3.1).

As expected for aromatic azo derivatives, (*t*)-**4a-p** displayed two characteristic absorption bands corresponding to n→π* and π→π* transitions (Table 3.1), where the latter transition showed higher absorption coefficients. The UV-Vis absorption spectra of (*t*)-**4a-p** showed a hypsochromic shift of the π→π* band in comparison with azobenzene and 2,2'-azopyridine (π→π* maximum of 313 and 306 nm respectively).^{11,12} This effect can be attributed to the triazine ring and its lower electron density that increases the π→π* energy gap. Regarding the n→π* band, all derivatives (*t*)-**4a-p** showed maximum absorptions similar to those observed in azobenzene and 2,2'-azopyridine (n→π* maximum of 436 and 466 nm respectively)^{11,12}.

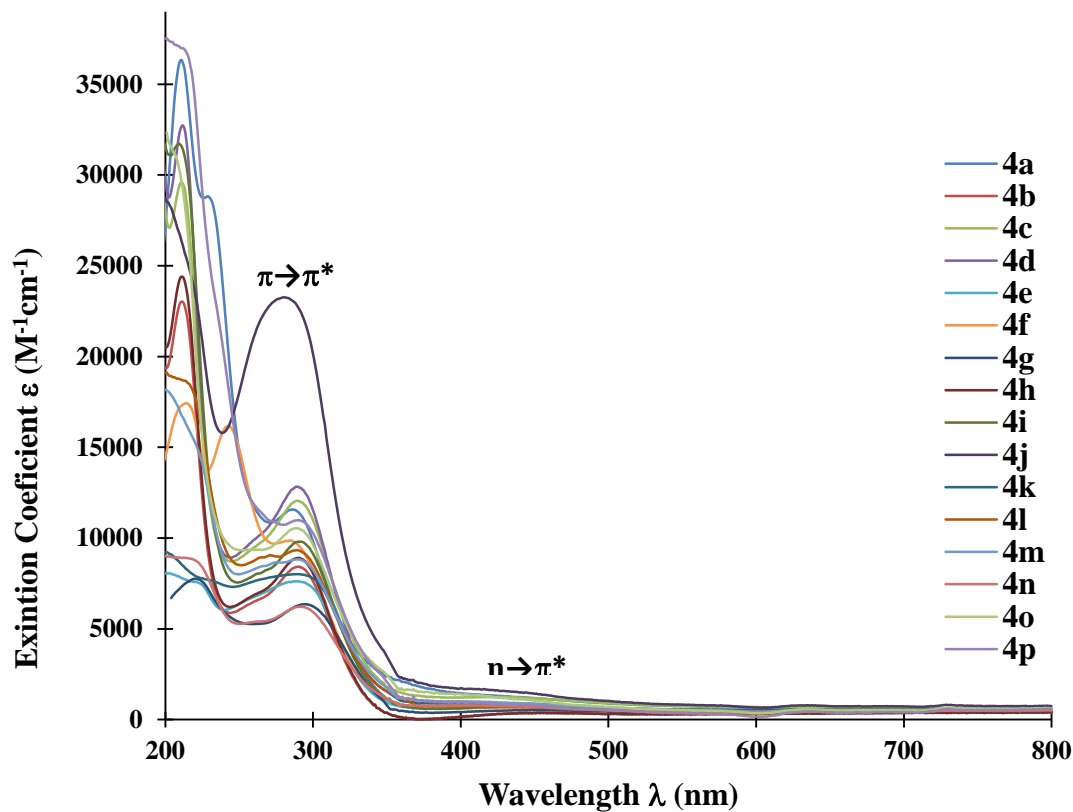


Figure 3.1 Normalized UV-Vis absorption spectra of (*t*)-**4a-p** in acetonitrile at 298 K.

Attempts to perform dilution experiments using UV-Vis absorption spectroscopy with chloroform and toluene as solvent systems were carried out. However, these efforts revealed no useful measurable changes.

Table 3.1 Characteristic $n \rightarrow \pi^*$ and $\pi \rightarrow \pi^*$ transition bands of derivatives (**t**)-**4a-p** from UV-Vis spectroscopy in acetonitrile at 298 K.

Derivative	RX	$n \rightarrow \pi^*$ Transition		$\pi \rightarrow \pi^*$ Transition	
		λ_{\max} (nm)	ϵ ($M^{-1} \text{ cm}^{-1}$)	λ_{\max} (nm)	ϵ ($M^{-1} \text{ cm}^{-1}$)
(t)- 4a	piperidin-1-yl	449	702	286	11100
(t)- 4b	methoxy	451	125	290	7930
(t)- 4c	<i>n</i> -butoxy	428	761	290	11600
(t)- 4d	<i>n</i> -octyloxy	438	402	289	12400
(t)- 4e	prop-2-ynyloxy	435	253	290	7140
(t)- 4f	hexylthio	435	175	284	9380
(t)- 4g	chloro	448	41	295	5870
(t)- 4h	iodo	452	107	290	8420
(t)- 4i	phenoxy	441	245	290	9320
(t)- 4j	4'-nitrophenoxy	444	1009	280	22800
(t)- 4k	4'- <i>tert</i> -butylphenoxy	426	403	289	7530
(t)- 4l	3-(trifluoromethyl)phenoxy	426	236	289	8850
(t)- 4m	3,5-bis(trifluoromethyl)phenoxy	430	458	289	8340
(t)- 4n	perfluorophenoxy	407	292	291	5730
(t)- 4o	benzyloxy	440	636	288	10000
(t)- 4p	4-tritylphenoxy	413	459	290	10500

On the other hand, UV-Vis absorption spectra of (**c**)-**4c**, (**c**)-**4f**, and (**c**)-**4k** and were obtained from 10^{-4} M acetonitrile solutions (Figures 3.2 to 3.4). Details of the experimental procedure followed to obtain *cis*-isomer are outlined in the Experimental section at the end

of this chapter. The absorption spectra of derivatives (c)-4c, (c)-4f and (c)-4k displayed more intense $n \rightarrow \pi^*$ bands; conversely, the $\pi \rightarrow \pi^*$ band decreased in intensity compared to the *trans*-isomeric derivatives (Table 3.2).

Table 3.2 Characteristic $n \rightarrow \pi^*$ and $\pi \rightarrow \pi^*$ transition bands of derivatives (c)-4 from UV-Vis spectroscopy in acetonitrile at 298 K.

Compound	RX	$n \rightarrow \pi^*$ Transition		$\pi \rightarrow \pi^*$ Transition		Isosbestic Point	
		λ_{\max} (nm)	ϵ ($M^{-1} cm^{-1}$)	λ_{\max} (nm)	ϵ ($M^{-1} cm^{-1}$)	λ (nm)	ϵ ($M^{-1} cm^{-1}$)
(c)-4c	<i>n</i> -butoxy	432	853	283	7210	375	85
						242	8270
(c)-4f	Hexylthio	436	538	284	4790	391	143
(c)-4k	4'- <i>tert</i> -butylphenoxy	433	919	287	5930	370	210

It is important to outline that the *cis*-isomers obtained from 4a-p were stable in the solid state at low temperature (< 0 °C) and protected from visible light. In all cases, *cis* to *trans* thermal reversion was observed to take place immediately after dissolution at room temperature. The gradual transition from *cis* to *trans* is observed in the changes in the absorption spectra: the $n \rightarrow \pi^*$ band decreases while the $\pi \rightarrow \pi^*$ band increases in intensity (Figures 3.2 to 3.4). Likewise, isosbestic points are observed during the course of each thermal reversion. The presence of these points in the UV-Vis spectra confirm the presence of only two species during these reversions: *cis* and *trans*. It is important to point out that since acetonitrile was the solvent system used during these UV-Vis absorption characterizations, no complexation is possible due to hydrogen bond competition by the solvent.

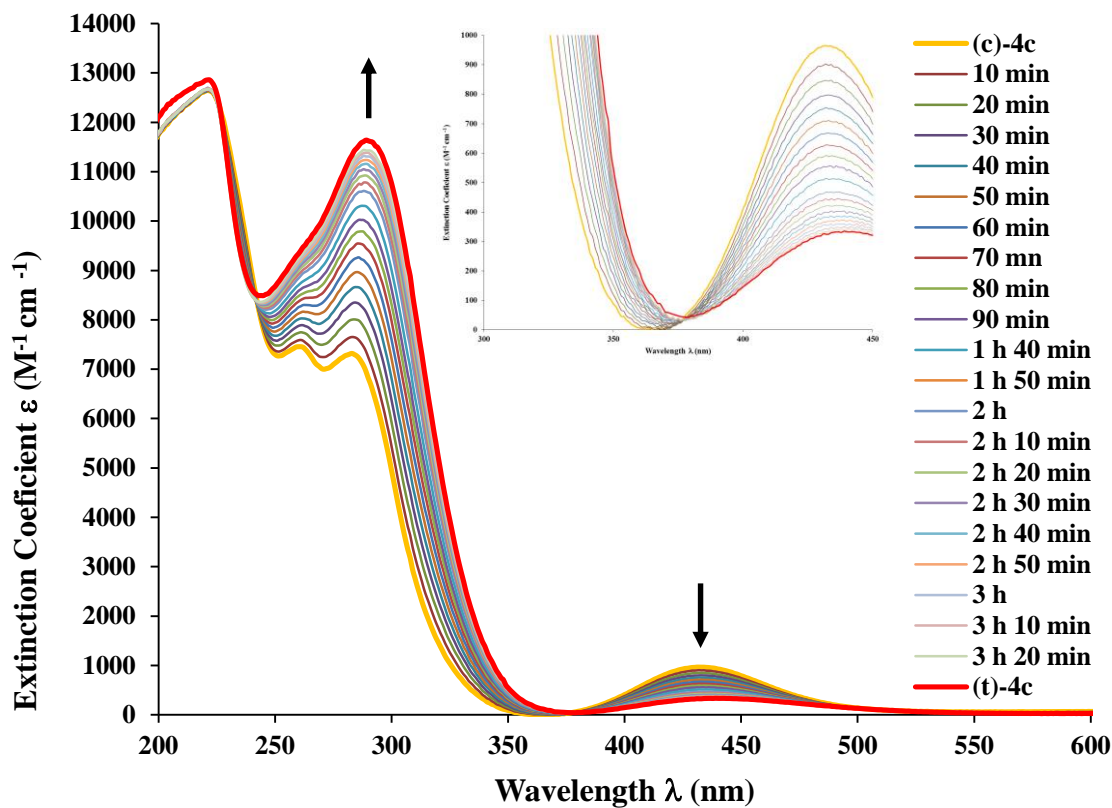


Figure 3.2 UV-Vis absorption spectra of (c)-4c and its thermal reversion to (t)-4c in acetonitrile at 298 K (4c total concentration = 1.71×10^{-4} M). Inset figure: isosbestic point at 375 nm.

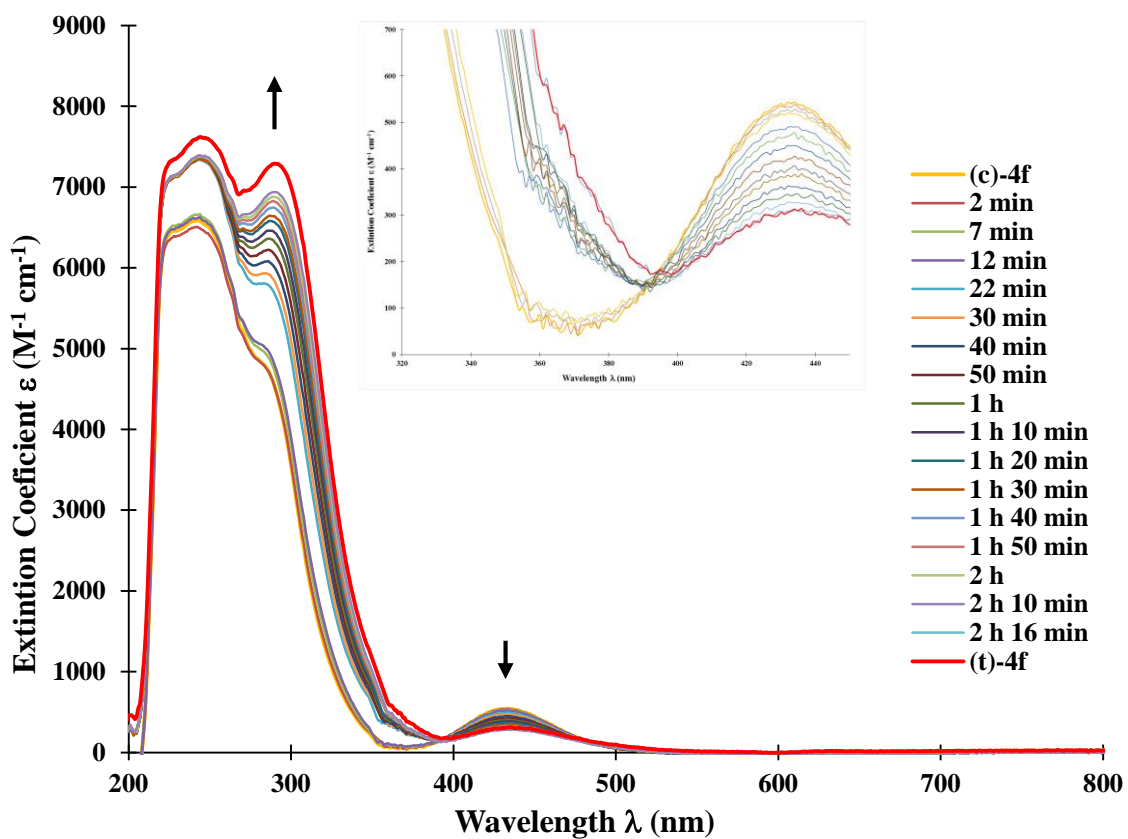


Figure 3.3 UV-Vis absorption spectra of *(c)*-**4f** and its thermal reversion to *(t)*-**4f** in acetonitrile at 298 K (**4f** total concentration = 1.67×10^{-4} M). Inset figure: isosbestic point at 391 nm.

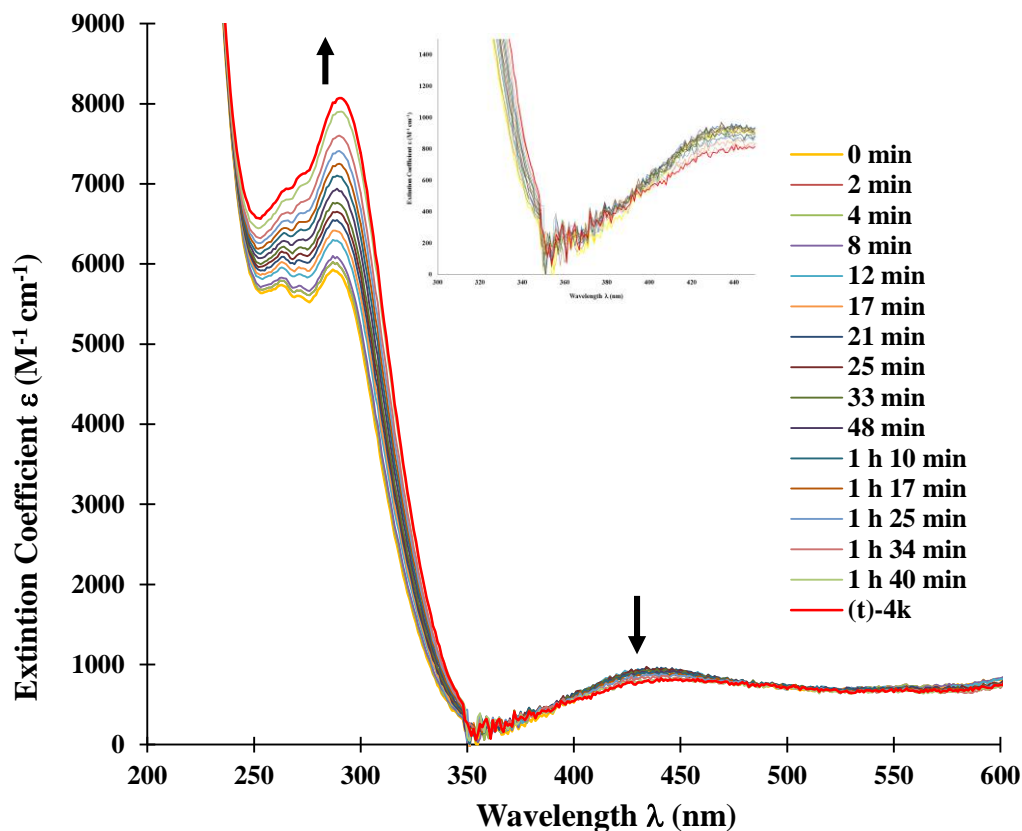


Figure 3.4 UV-Vis absorption spectra of **(c)-4k** and its thermal reversion to **(t)-4k** in acetonitrile at 298 K (**4k** total concentration = 3.72×10^{-5} M). Inset figure: isosbestic point at 370 nm.

3.2.2 Photoisomerization *Trans* to *Cis*.

Photoisomerization experiments were carried out irradiating solutions of derivatives **(t)-4a-p** with UV light centered at 360 nm. These experiments were performed employing three different solvent systems: CDCl_3 , toluene- d_8 , and CD_3CN . The selection of the first two solvents was made in order to replicate the dilution experiments of derivatives **4a-p** in Chapter 2 (Section 2.3.2). On the other hand, photoisomerization experiments in CD_3CN were carried out in order to observe whether or not there is a

difference using a polar solvent that prevents self-complexation. Deuterated solvents were used in order to verify the photoisomerization through ^1H NMR spectroscopy.

The presence of the *cis*-isomer after UV irradiation was corroborated by the presence of a new set of signals in the ^1H NMR spectrum. These signals were generally located upfield in reference to the *trans*-isomer (Figure 3.5 and 3.6). The changes in the chemical shift are in agreement with the disposition of the *cis* isomer wherein the proximity of the heteroaromatic rings locates most of the pyridyl hydrogen atoms in the shielding cone of the facing triazine heterocycle. The *trans*- to *cis*- interconversion yield was calculated from the *cis/trans* integration ratio of two signals that represent the same proton in (*t*)-**4a-p** and (*c*)-**4a-p** isomers. Table 3.3 shows the *trans*- to *cis*- interconversion yields of all derivatives **4a-p** tested at their PSS.

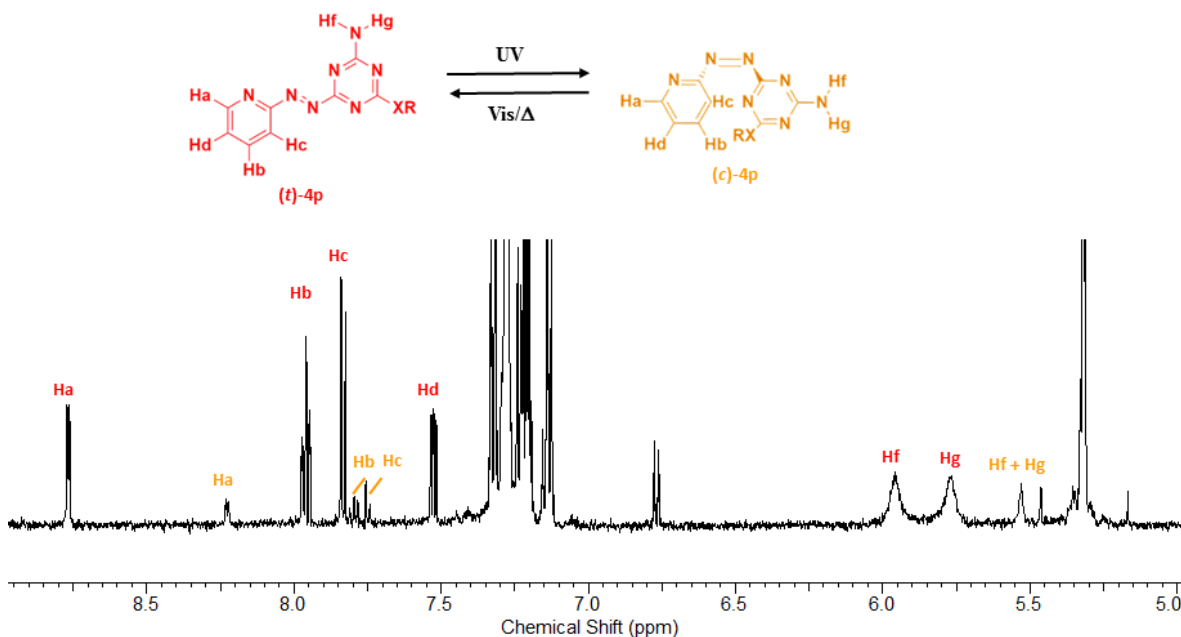


Figure 3.5 ^1H NMR spectra displaying derivative **4p** at PSS in CDCl_3 at 298 K. RX = 4'-tritylphenoxy.

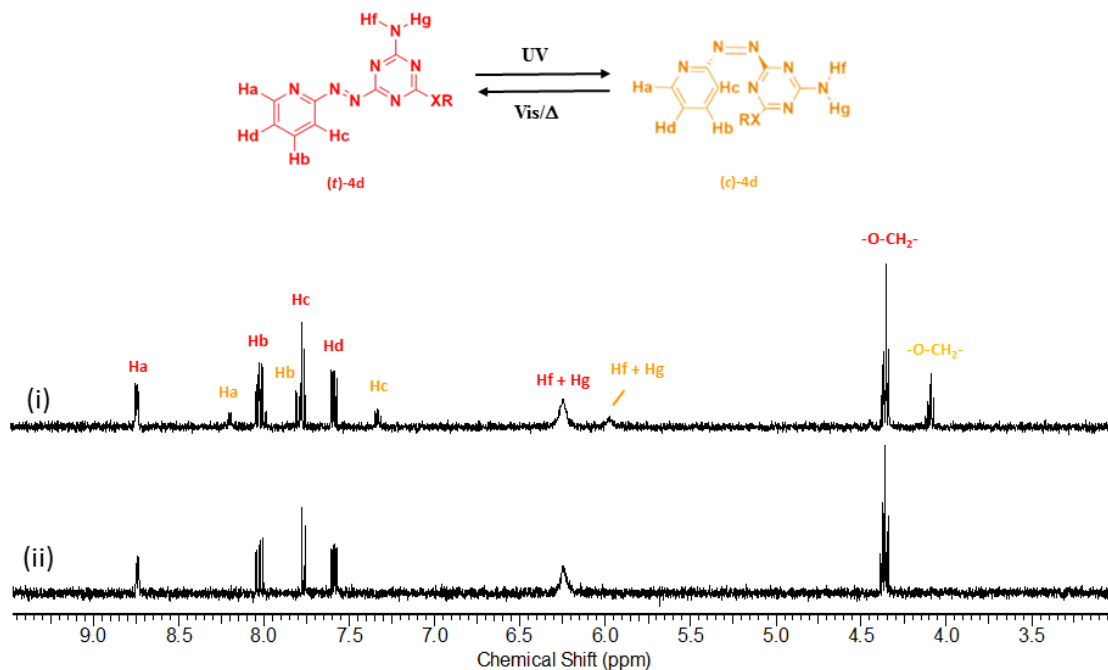


Figure 3.6 ¹H NMR spectra displaying derivative **4d** at (i) PSS, and (ii) after complete *cis*- to *trans*- thermal reversion in CD₃CN at 298 K. RX = *n*-octyloxy.

Table 3.3 *Trans* to *cis* interconversion yields at PSS after irradiation with UV Light (360 nm) at 298 K.

Derivative	RX	<i>trans</i> to <i>cis</i> conversion in CDCl ₃ (%)	<i>trans</i> to <i>cis</i> conversion in Toluene- <i>d</i> ₈ (%)	<i>trans</i> to <i>cis</i> conversion in CD ₃ CN (%)
4a	piperidin-1'-yl	22	-	18
4b	Methoxy	-	-	22
4c	<i>n</i> -butoxy	12	22	24
4d	<i>n</i> -octyloxy	9	-	26
4f	Hexylthio	18	20	19
4g	Chloro	-	-	14
4h	Iodo	-	-	16
4i	phenoxy	28	-	35
4k	4'- <i>tert</i> -butylphenoxy	15	0	32
4l	3'-(trifluoromethyl)phenoxy	17	-	27
4m	3',5'-bis(trifluoromethyl)phenoxy	16	-	23
4n	perfluorophenoxy	17	0	15
4o	benzyloxy	9	-	21
4p	4'-tritylphenoxy	24	-	33

- Compound non soluble in the solvent system used.

The *trans*- to *cis*- interconversion yields for derivatives **4a-p** at their PSS in CDCl₃ range from 9 to 28 percent. The lowest yield corresponded to the *n*-octyloxy **4d** and the benzyloxy **4o**; meanwhile the highest yield was achieved by the phenoxy derivative **4i**. When toluene-*d*₈ was employed as solvent system, of the four derivatives tested (**4c**, **4f**, **4k** and **4n**) the only ones that contained *cis*-isomer in solution after UV irradiation were the

derivatives **4c** (*n*-butoxy) and the **4f** (hexylthio) with 22 and 20 percent yields, respectively. Finally, the photoisomerization of derivatives **4a-p** dissolved in CD₃CN provided interconversions from 14 to 35 percent. In this case, the highest yield corresponded to the phenoxy derivative **4i** again and the lowest yield to the derivative **4g** (chloro). Comparing the results obtained from the different solvent systems examined it can be observed that photoisomerization yields were generally slightly higher in CD₃CN than in CDCl₃. One important thing to point out from the use of CD₃CN as solvent is the repercussion in the dimerization of the derivatives **4a-p**; i.e. due to the polar nature of this solvent, derivatives **4a-p** do not dimerize. This is supported by the observed concentration independence of the amino proton chemical shifts upon thermal relaxation to the *trans*-starting material (Figure 3.6).

Another important feature to evaluate in our systems was the fatigue or photodegradation after the repetitive use of their photochromic properties. In this sense, a toluene-*d*₈ solution of **4c** ([**4c**] = 9.10 × 10⁻⁴ M) was submitted to 5 cycles of alternate irradiation of UV light (centered at 360 nm for 1h) and visible light (λ > 400 nm for 10 minutes) in order to observe the consistency in the system response (Figure 3.7). The response observed was the chemical shift of an amino proton of the *trans*-isomer in the ¹H NMR spectra after each UV/Vis light irradiation. The average response after UV light irradiation of the **4c** solution corresponded to an N-H chemical shift of 5.45 ppm; meanwhile the average response after visible light irradiation corresponded to 5.55 ppm. In both cases, the larger deviation from the average value corresponds to 0.03 ppm. It is remarkable that after irradiation of visible light, the system did not recover to its *trans*-isomeric form in 100%; and therefore, it was not observed the initial chemical shift prior

trans- to *cis*- photoisomerization. Likewise, once the alternate irradiation was stopped and the system was allowed to *cis*- to *trans*- thermal reversion, it was noted that the N-H amino proton chemical shift was lower than the observed before UV/Vis irradiation without traces of *cis*-isomer or other side product observed at the ^1H NMR spectrum. This final chemical shift corresponds to a solution with a concentration 6% lower than at the beginning of the experiment (i.e. 6×10^{-5} M); which might not be detected by the NMR spectrometer resolution at the range of concentrations employed.

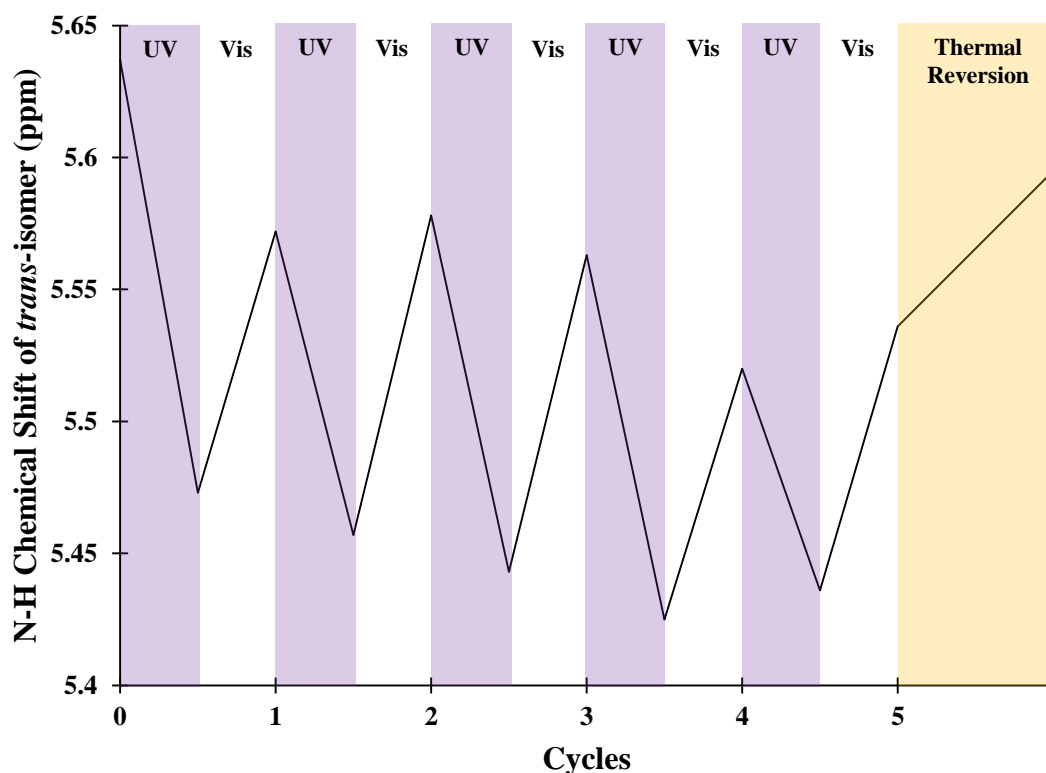


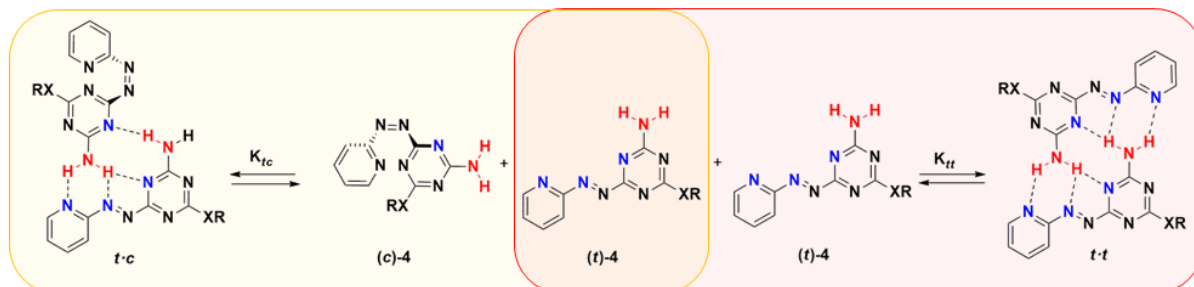
Figure 3.7 Cyclization plot of **4c** ($[\mathbf{4c}] = 9.1 \times 10^{-4}$ M). Purple areas correspond to the N-H chemical shift change after UV light irradiation (centered at 360 nm for 1h). White areas correspond to the N-H chemical shift change after visible light irradiation ($\lambda > 400$ nm for 10 minutes). Yellow area correspond to the N-H chemical shift observed after thermal reversion of the solution over 72h.

Since the *trans*- to *cis*- interconversions of the derivatives **4a-p** are lower than 100%, the model that describes the distribution of species after photoisomerization involves multiple complexation equilibria taking place at the same time in solution (Scheme 3.5). In addition, since thermal reversion to the *trans*-isomer takes place immediately after UV light irradiation is stopped, the distribution of species changes as the *cis/trans* ratio does. The following sections describe the approach we followed to mitigate these difficulties and evaluate the effect of the light induced isomerization on the distribution of species in solution.

3.2.3 Complexation Constants in Solution After Photoisomerization

The main challenge in determining the distribution of monomeric and dimeric species for mixed solutions of *cis*- and *trans*-**4a-p** is the determination of complexation constants involving the *cis*-isomer. Since (*c*)-**4a-p** are not thermally stable in solution, the determination of K_{c-c} and K_{t-c} are not possible by standard procedures such as dilution and titration.^{11,12} Therefore, it was necessary to take a different approach in order to determine or estimate these unknown constants.

In a mixed solution of *cis*- and *trans*- **4a-p**, the *trans*-isomer in solution participates in the two equilibria illustrated in Scheme 3.6.



Scheme 3.6 Complexation equilibria involving the **4a-p** *trans*-isomer.

Based on Scheme 3.6, the total concentration of *trans*-isomer in solution ($[t]_0$) can be expressed as:

$$[t]_0 = [t] + 2 \cdot [t \cdot t] + [t \cdot c] \quad \text{Equation 1}$$

Wherein

$[t]$ is the concentration of free *trans*-isomer;

$[t \cdot t]$ is the concentration of the *trans*-isomer dimer; and

$[t \cdot c]$ is the concentration of *trans-cis* complex.

The dimerization constant K_{t-t} and complexation constant K_{t-c} that characterize the equilibria illustrated in Scheme 3.5 are outlined in Equations 2 and 3.

$$K_{t-t} = \frac{[t \cdot t]}{[t]^2} \quad \text{Equation 2}$$

$$K_{t-c} = \frac{[t \cdot c]}{[t] \cdot [c]} \quad \text{Equation 3}$$

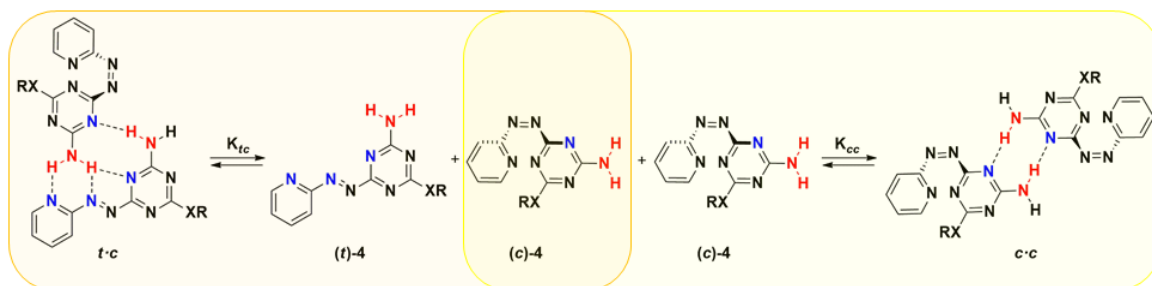
Where

$[c]$ is the concentration of free *cis*-isomer;

Solving Equations 2 and 3 for $[t \cdot t]$ and $[t \cdot c]$ allow us to express Equation 1 in terms of $[t]$ and $[c]$:

$$[t]_0 = [t] + 2 \cdot K_{t-t} \cdot [t]^2 + K_{t-c} \cdot [t] \cdot [c] \quad \text{Equation 4}$$

In a similar manner to the *trans*-isomer, the total concentration of *cis*-isomer in solution ($[c]_0$) that participates in the complexation equilibria illustrated in Scheme 3.7 is expressed in Equation 5 as a solution of free *trans*-isomer ($[t]$) and *cis*-isomer ($[c]$).



Scheme 3.7 Complexation equilibria involving the **4a-p** *cis*-isomer.

$$[c]_0 = [c] + 2 \cdot K_{c-c} \cdot [c]^2 + K_{t-c} \cdot [t] \cdot [c] \quad \text{Equation 5}$$

Where

$[c]$ is the concentration of free *cis*-isomer;

K_{c-c} is the dimerization constant that describes the equilibrium between free *cis*-isomer and the dimer of *cis*-isomer; and,

K_{t-c} is the complexation constant as described in Equation 3.

To sum up, all derivatives **4a-p** in solution can be present in five different forms: free *trans* ($[t]$), free *cis* ($[c]$), *trans-trans* dimer ($[t \cdot t]$), *cis-cis* dimer ($[c \cdot c]$) and a *trans-cis* complex ($[t \cdot c]$). The distribution of these species is dependent on three dimerization/association constants: K_{t-t} , K_{c-c} , and K_{t-c} . K_{t-t} has already been determined for each of the soluble (**t**)-**4a-p** in Chapter 2 (Section 2.3.2). In contrast, estimation of K_{c-c} had as a limitation that once in solution, pure *cis*-isomer immediately begins reverting thermally to the *trans*-isomer which makes difficult the execution of a dilution experiment.

An important thing to note is the effect of the solvent system where all the species previously described are present. That is, how significant is the change in the physical property going to be studied in different solvents. In our case, the physical property studied is the drop in the stability of derivatives **4a-p** as dimers by reducing the number of binding sites available, which is observed in the differences between K_{t-t} with K_{c-c} and K_{t-c} . Since K_{t-t} represents the dimerization constant of the most stable complex, K_{c-c} , and K_{t-c} values are within the range from 0 to K_{t-t} . The larger the K_{t-t} the more significant is going to be the difference observed with the other constants. Therefore, we decided to study the distribution of monomer, dimer and complex structures in toluene- d_8 since, as reported in Chapter 2 (Section 2.3.2), K_{t-t} values in toluene- d_8 were much higher than those in $CDCl_3$.

In order to have an approximation of the expected values for K_{c-c} , we looked back at the dimerization of **5c**, **5f** and **5k**. Since the hydrogen bond array for these systems does not include the nitrogen acceptor located on the pyridine ring, it is reasonable to infer that the K_{c-c} values for (**c**)-**4c**, (**c**)-**4f** and (**c**)-**4k** will be equal to or lower than the dimerization constants of **5c**, **5f** and **5k**, respectively. Moreover, **5c**, **5f** and **5k** are likely overestimations

of the real K_{c-c} since dilution experiments of intermediates **1** and **2b** (Figure 3.8) in toluene- d_8 presented maximum changes in the chemical shift of 0.12 and 0.04 ppm which are below the minimum $\Delta\delta$ to consider the ^1H NMR dilution method employed reliable ($\Delta\delta_{\text{max}} = 0.5$ ppm, Chapter 2, Section 2.3.2). Plots of the chemical shift of the amino protons vs. concentration implied dimerization constant values less than 1 M^{-1} and could not be fitted to the dimerization model due to lack of curvature.

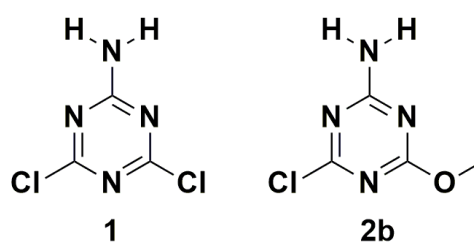


Figure 3.8 Chemical structures of intermediates **1** and **2b**.

Based on this hypothesis K_{t-t} would be at least 20 times larger than K_{c-c} (Table 2.3) in toluene- d_8 . For this reason, the K_{c-c} contribution can be eliminated without significant consequences in the calculation of the complexation distribution (*vide infra*). Equation 5 is thus reduced to Equation 6:

$$[c]_0 = [c] + K_{t-c} \cdot [t] \cdot [c] \quad \text{Equation 6}$$

Solving Equation 6 for $[c]$, and substituting $[c]$ in Equation 4:

$$[t]_0 = [t] + 2 \cdot K_{t-t} \cdot [t]^2 + \frac{K_{t-c} \cdot [t] \cdot [c]_0}{1 + K_{t-c} \cdot [t]} \quad \text{Equation 7}$$

Equation 7 is important due to the fact that $[t]_0$ is described in terms of only one variable ($[t]$) and the only constant to be determined is $K_{t \cdot c}$. Regarding the total concentration of *trans* and *cis*-isomers in solution ($[t]_0$ and $[c]_0$), these concentrations can be calculated through the integration of their signals in the ^1H NMR spectra (in the same way as the determination of the PSS in Section 3.3).

Besides the calculation of the total amount of each isomer in solution using integration, ^1H NMR spectroscopy provides an observable property whose change is proportional to the concentration of each specie in solution; e.g. the chemical shift of the amino protons of the *trans*-isomer. In this case, the chemical shift observed for an amino proton (δ_{obs}) is the weighted average of all the chemical species wherein this isomer is participating (Equation 8).

$$\delta_{obs} = \delta_m \cdot \frac{[t]}{[t]_0} + \delta_d \cdot \frac{2 \cdot [t \cdot t]}{[t]_0} + \delta_{tc} \cdot \frac{[t \cdot c]}{[t]_0} \quad \text{Equation 8}$$

Where

δ_m and δ_d are the chemical shifts of the *trans*-isomer as a monomer and dimer, respectively (Chapter 2, Section 2.3.2); and

δ_{tc} corresponds to the chemical shift of the *trans*-isomer in the $[t \cdot c]$ complex.

Similarly to the solution of Equation 1 into Equation 7, Equation 8 can be transformed in order to be expressed in terms of $[t]$ (Equation 9).

$$\delta_{obs} = 2 \cdot K_{t \cdot t} \cdot (\delta_d - \delta_{tc}) \cdot \frac{[t]^2}{[t]_0} + (\delta_m - \delta_{tc}) \cdot \frac{[t]}{[t]_0} + \delta_{tc} \quad \text{Equation 9}$$

Since Equations 7 and 9 share the same variable ($[t]$), it is possible to establish a relationship between $K_{t,c}$ and δ_{tc} once the value of $[t]$ is known. This relationship provided a strategy where through the assignment of a range of values to δ_{tc} a set of $K_{t,c}$ values are obtained for a δ_{obs} in a ^1H NMR spectrum at a specific *cis/trans* ratio. For this purpose Equation 9 was rearranged as a second order polynomial (Equation 10) and Equation 7 was rearranged to solve $K_{t,c}$ (Equation 11). The relationship between δ_{tc} and $K_{t,c}$ is illustrated in Figure 3.9 at a specific total concentration of **4a-p** (**[4]**) and ratio of *cis/trans* isomer.

$$2 \cdot K_{t,t} \cdot (\delta_d - \delta_{tc}) \cdot [t]^2 + (\delta_m - \delta_{tc}) \cdot [t] + (\delta_{tc} - \delta_{obs}) \cdot [t]_0 = 0 \quad \text{Equation 10}$$

Where

$$[t] = \frac{-(\delta_m - \delta_{tc}) \pm \sqrt{(\delta_m - \delta_{tc})^2 - 8 \cdot K_{t,t} \cdot (\delta_d - \delta_{tc}) \cdot (\delta_{tc} - \delta_{obs}) \cdot [t]_0}}{4 \cdot K_{t,t} \cdot (\delta_d - \delta_{tc})}$$

$$K_{t,c} = \frac{[t]_0 - [t] - 2 \cdot K_{t,t} \cdot [t]^2}{2 \cdot K_{t,t} \cdot [t]^3 + [t]^2 + ([c]_0 - [t]_0) \cdot [t]} \quad \text{Equation 11}$$

And we assume the boundary conditions:

$$\delta_m < \delta_{tc} < \delta_d$$

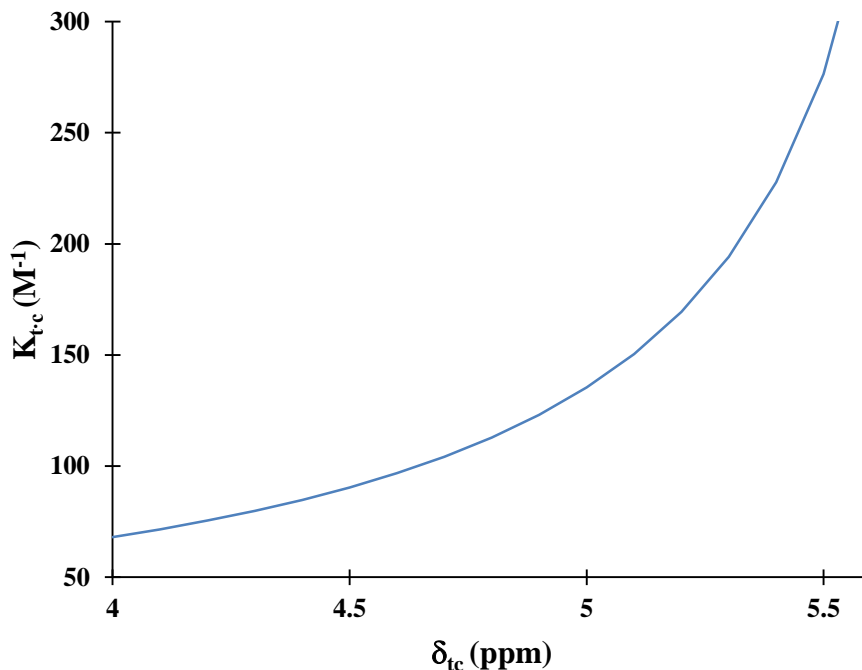


Figure 3.9 Relationship between K_{t-c} and δ_{tc} , when $\delta_{obs} = 5.61$ ppm at a *cis/trans* ratio = 1.85 for a total $[4c] = 3.42 \times 10^{-3}$ M.

The solution of the real K_{t-c} and δ_{tc} values comes after applying this strategy to a set of δ_{obs} at different *cis/trans* ratios when the total concentration of a derivative **4a-p** is held constant. These data were obtained from a reversion experiment which consisted in following the chemical shift of an amino proton of the *trans*-isomer while the *cis* to *trans* thermal reversion takes place (Figure 3.10). The experiment was carried out from mixed *cis/trans* isomeric solutions in toluene- d_8 at known total concentrations of each of the derivatives **4c**, **4f** and **4k**. An example of the change in the chemical shift observed (δ_{obs}) as total *trans*-isomer concentration increases in a reversion experiment ($[t]_0$) is illustrated in Figure 3.11. It is important to note that as the reversion experiment was carried out, the amino protons of the *cis*-isomer shift downfield significantly as the concentration of $[t]_0$

increases. This behavior supports the assumption that K_{t-c} is significantly higher than K_{c-c} .

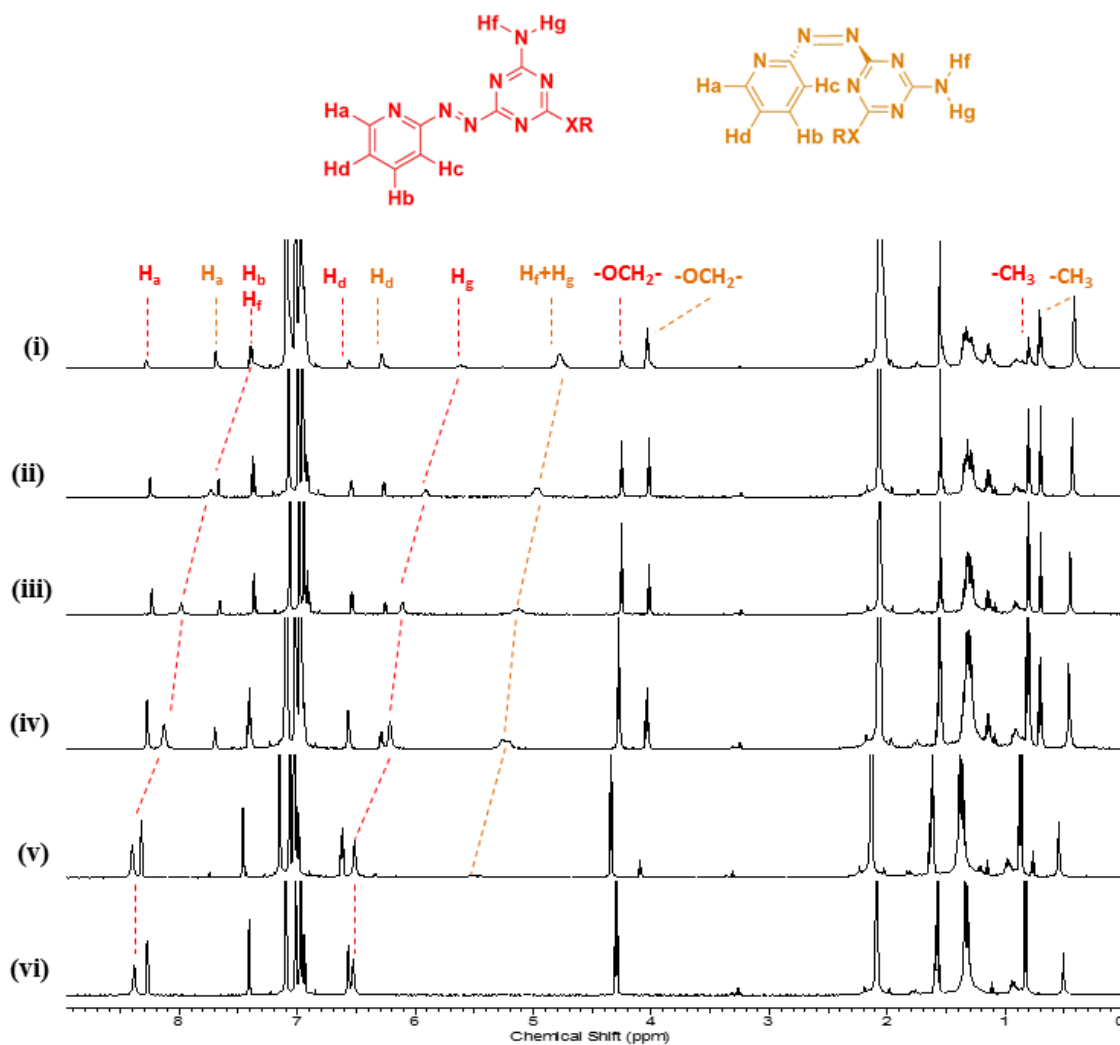


Figure 3.10 ^1H NMR spectra displaying the concentration-dependent behavior of **4c** in toluene- d_8 at 298 K. Total concentration $[\mathbf{4c}] = 3.27 \times 10^{-3}$ M, (i) $[\mathbf{c}]_0/[\mathbf{t}]_0 = 1.73$ (ii) $[\mathbf{c}]_0/[\mathbf{t}]_0 = 0.93$, (iii) $[\mathbf{c}]_0/[\mathbf{t}]_0 = 0.59$, (iv) $[\mathbf{c}]_0/[\mathbf{t}]_0 = 0.33$, (v) $[\mathbf{c}]_0/[\mathbf{t}]_0 = 0.22$, and (vi) $[\mathbf{c}]_0/[\mathbf{t}]_0 = 0$.

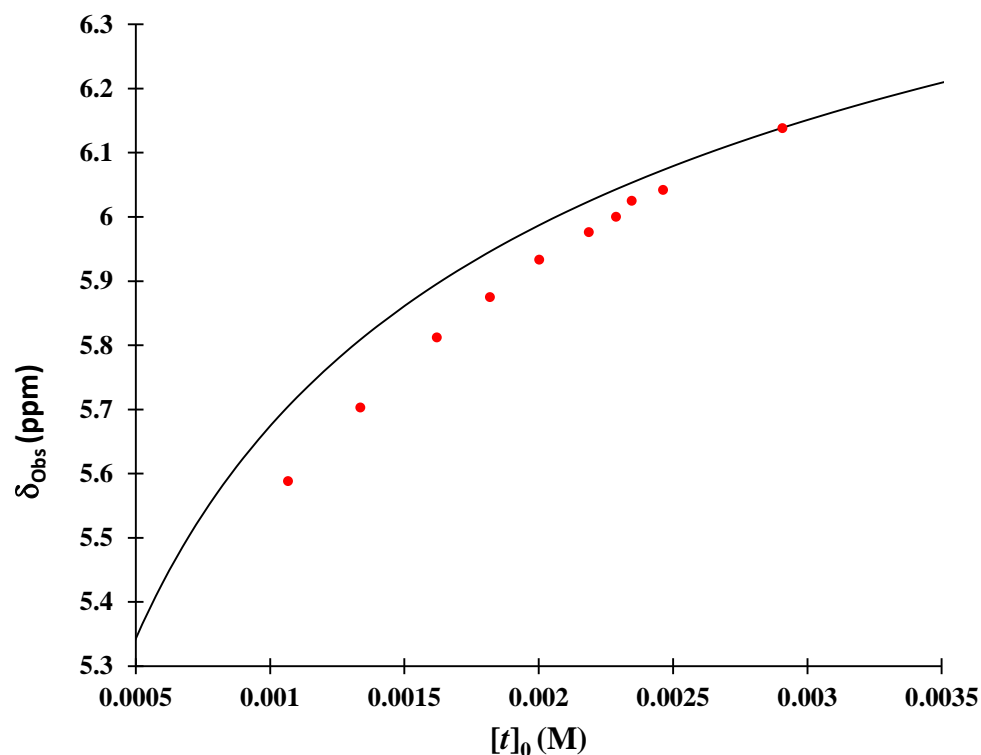


Figure 3.11. Relationship between δ_{Obs} vs $[t]_0$ during a thermal reversion experiment of derivative **4c**. Red corresponds to a reversion experiment ($[4c] = 2.90 \times 10^{-3}$ M). Solid line corresponds to the theoretical dilution curve obtained from the average of three separate dilution experiments with **(t)-4c**.

From each chemical shift observed at a specific *cis/trans* ratio evaluated in a reversion experiment, a relationship curve of K_{t-c} vs δ_{tc} (as observed in Figure 3.9) is obtained. Since it is impossible to observe the same K_{t-c} vs. δ_{tc} relationship (curve) for each δ_{Obs} in a reversion experiment, the point where all these curves converge represents the real pair of values for K_{t-c} and δ_{tc} (Figure 3.12). In our case, errors in the real data render the plot less visually accurate and required a method of determining the point of best fit to the data (Figure 3.13). Hence, we used a statistical procedure to determine these values.

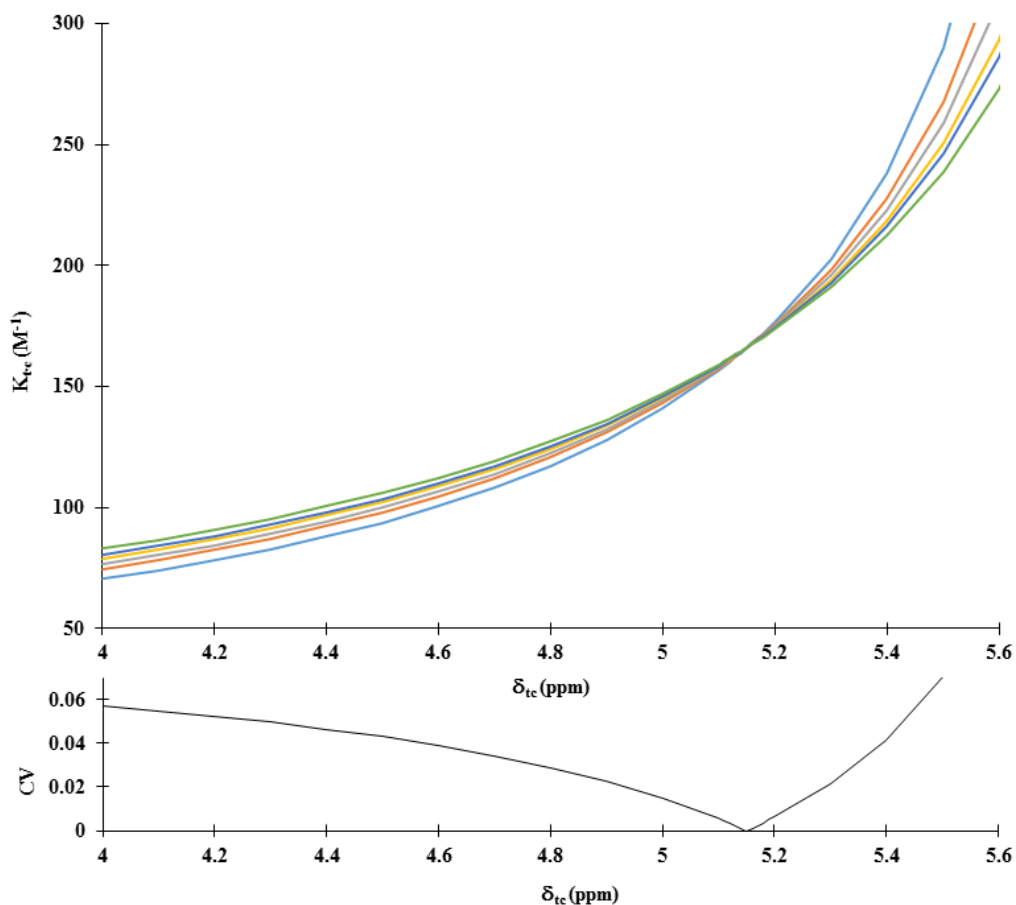


Figure 3.12 Top Plot: Theoretical K_{t-c} vs δ_{t-c} curves for the set of δ_{obs} from the least squares line that describes third reversion experiment of derivative **4c** (green dots at Figure 3.14, $[4c] = 3.42 \times 10^{-3}$ M). Bottom Plot: Theoretical CV vs δ_{t-c} curve for the set of K_{t-c} calculated from the third reversion experiment of derivative **4c** (Green dots at Figure 3.8, $[4c] = 3.42 \times 10^{-3}$ M).

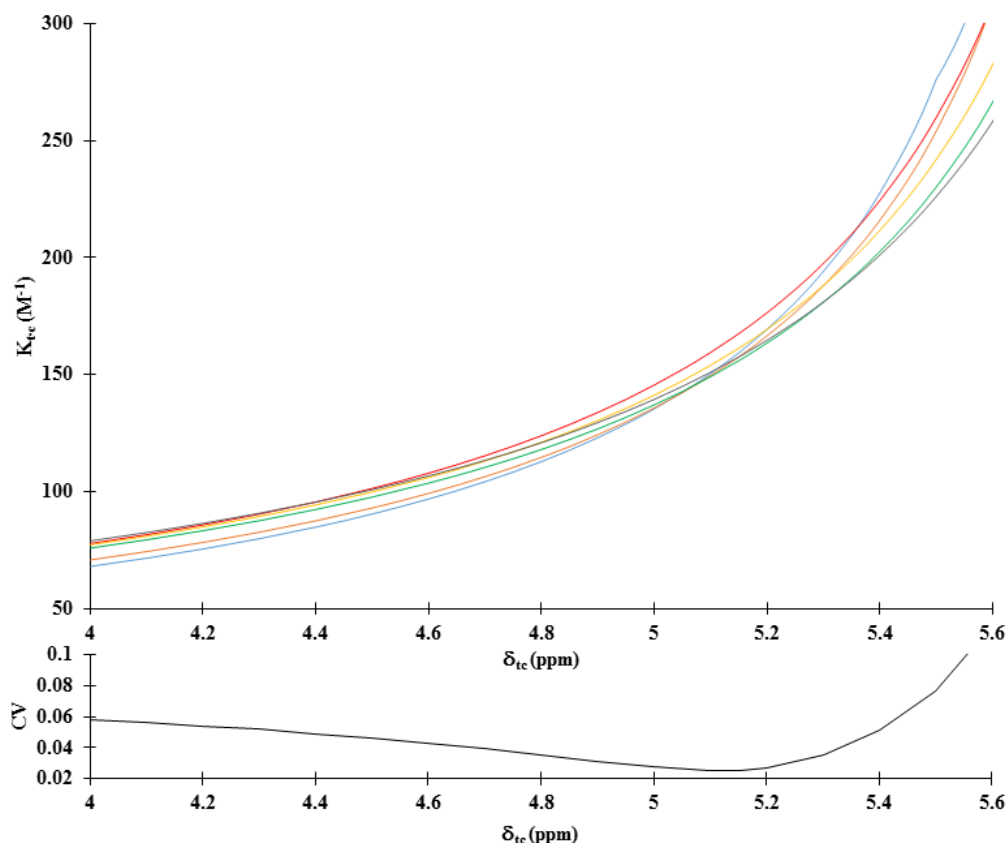


Figure 3.13 Top Plot: K_{t-c} vs δ_{tc} curves for the set of δ_{Obs} from the third reversion experiment of derivative **4c** (green dots at Figure 3.14, $[4c] = 3.42 \times 10^{-3}$ M). Bottom Plot: CV vs δ_{tc} curve for the set of K_{t-c} calculated from the third reversion experiment of derivative **4c** (Green dots at Figure 3.8, $[4c] = 3.42 \times 10^{-3}$ M).

The convergence point of each set of K_{t-c} vs δ_{tc} curves was determined through the coefficient of variation ($CV_{\delta_{tc}}$) from all K_{t-c} obtained at a constant δ_{tc} (i.e. a vertical slice in Figure 3.13 plot, Equations 12 to 14). The coefficient of variation is defined as a standardized measure of the dispersion of a distribution.¹³ In the present case, each set of K_{t-c} values (at a constant δ_{tc} value) is a distribution. Hence, the distribution that shows the value of minimum dispersion (i.e. minimum $CV_{\delta_{tc}}$ value) over a range of δ_{tc} represents the point where all curves converge closest to one another.

$$\bar{K}_{t,c} = \frac{1}{n} \sum_{i=1}^n K_{t,c}(i) \quad \text{Equation 12}$$

$$S_{t,c} = \sqrt{\frac{1}{n-1} \sum_{i=1}^n (K_{t,c}(i) - \bar{K}_{t,c})^2} \quad \text{Equation 13}$$

$$CV_{\delta_{t,c}} = \frac{S_{t,c}}{\bar{K}_{t,c}} \quad \text{Equation 14}$$

Where

$K_{t,c}(i)$ is the $K_{t,c}$ calculated at a specific $\delta_{t,c}$;

$\bar{K}_{t,c}$ is the average value from all $K_{t,c}(i)$ at a constant $\delta_{t,c}$ value;

n is the number of δ_{obs} values in a reversion experiment;

$S_{K_{t,c}}$ is the sample standard deviation at constant $\delta_{t,c}$ value; and,

$CV_{\delta_{t,c}}$ is the coefficient of variation at constant $\delta_{t,c}$ value.

This way, from each reversion experiment $\bar{K}_{t,c}$ and $\delta_{t,c}$ were obtained at the convergence point. In total, three reversion experiments at different total concentrations ([4]) were carried out for each derivative **4** studied under this model. The $\bar{K}_{t,c}$, $\Delta G_{t,c}$ and $\delta_{t,c}$ values obtained for derivatives **4c**, **4f** and **4k** are listed in Table 3.4. Likewise, Figures 3.14 - 3.16 illustrate the predicted δ_{obs} vs $[t]_0$ plots compared with the experimental data obtained for all reversion experiments carried out for derivatives **4c**, **4f** and **4k**.

Table 3.4 Complexation constants, free energies of complexation and chemical shifts of the *trans*-isomer in the complex δ_{tc} studied in Toluene- d_8 (at 298 K).

Derivative	RX	\bar{K}_{tc} (M ⁻¹) ^a	ΔG_{tc} (kJ mol ⁻¹)	δ_{tc} (ppm)
4c	<i>n</i> -butoxy	160 ± 15	-12.57 ± 0.24	5.14 ± 0.11
4f	Hexylthio	172 ± 8	-12.76 ± 0.12	5.38 ± 0.13
4k	4'- <i>tert</i> -butylphenoxy	931 ± 123	-16.94 ± 0.33	5.01 ± 0.39

^a Average values obtained using Equation 12 and three separate reversion experiments. Errors calculated from twice the standard deviation to give a 95% confidence interval.

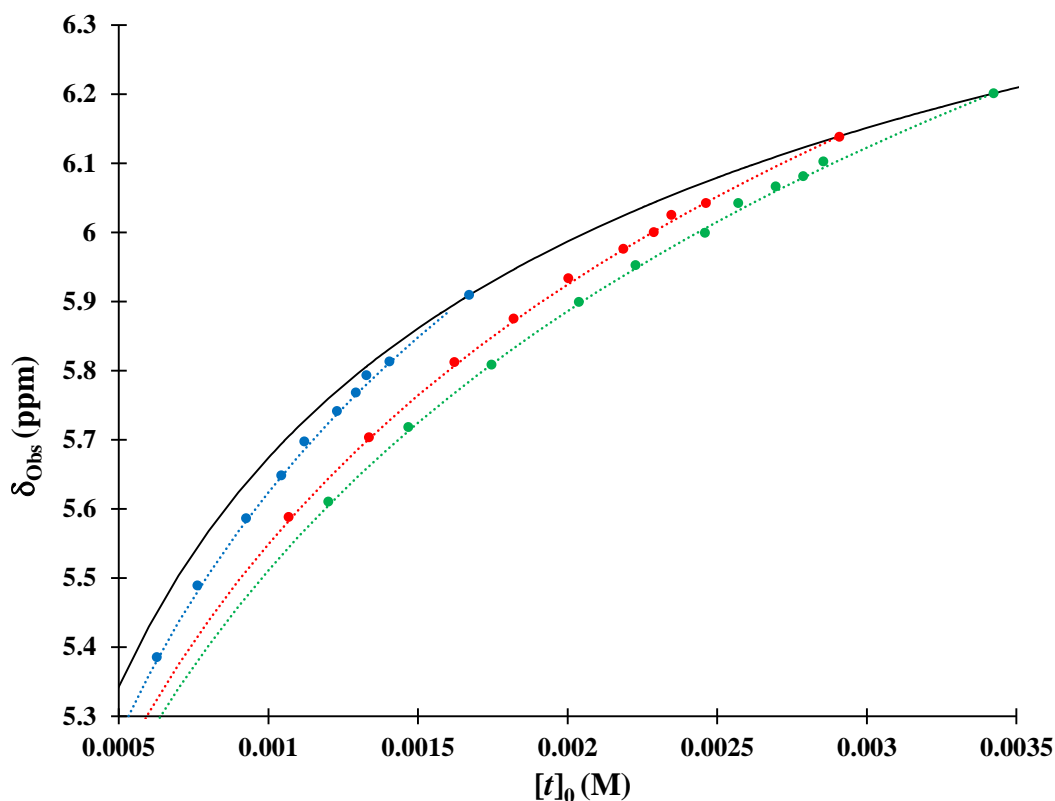


Figure 3.14 Relationship between δ_{obs} vs $[t]_0$ for three reversion experiments of derivative **4c**. Blue, red and green dots correspond to first, second and third separate reversion experiments, respectively. Blue, red and green dashed lines correspond to the calculated δ_{obs} vs $[t]_0$ plots for the first, second and third reversion experiments with the \bar{K}_{tc} and δ_{tc} values with minimum *CV* (sample standard deviations of 0.003, 0.003 and 0.008 ppm, respectively). Solid line corresponds to the dilution curve obtained for (*t*)-**4c** from the average of three separate dilution experiments.

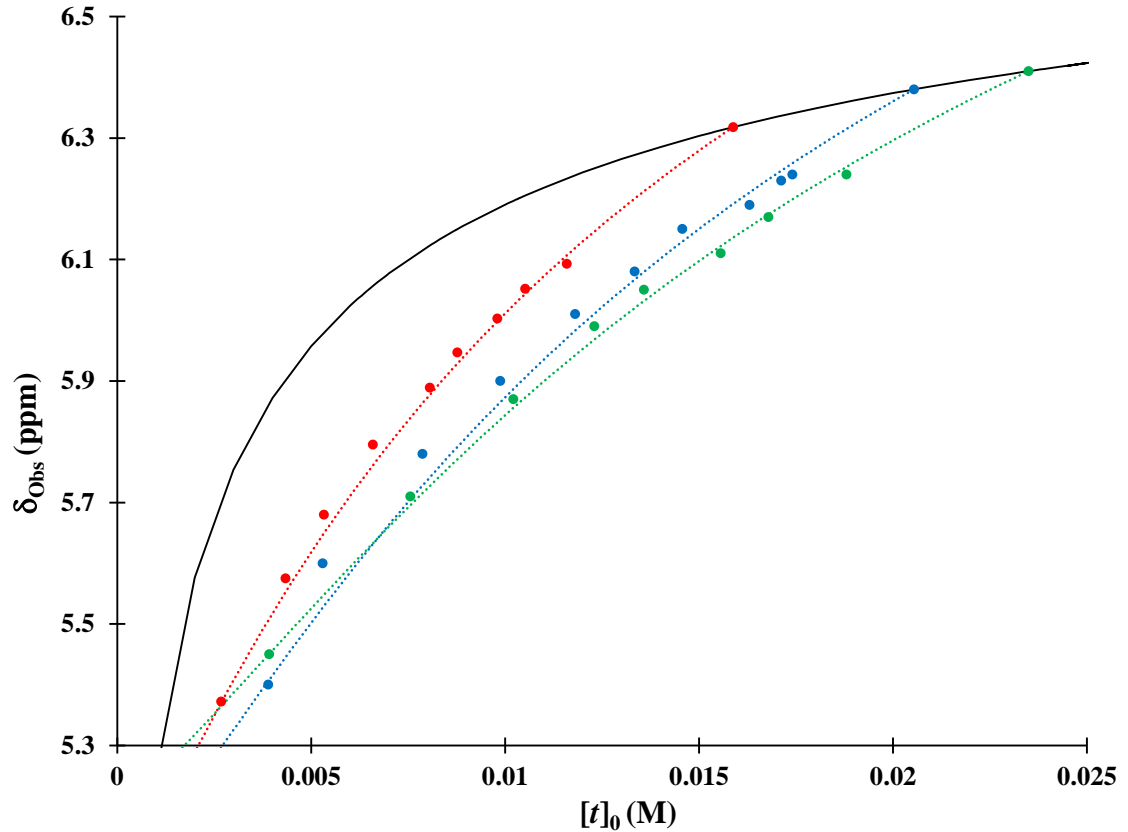


Figure 3.15 Relationship between δ_{obs} vs $[t]_0$ for three reversion experiments of derivative **4f**. Blue, red and green dots correspond to first, second and third separate reversion experiments, respectively. Blue, red and green dashed lines correspond to the calculated δ_{obs} vs $[t]_0$ plots for the first, second and third reversion experiments with the \bar{K}_{t-c} and δ_{tc} values with minimum CV (sample standard deviations of 0.01, 0.005 and 0.02 ppm, respectively). Solid line corresponds to the dilution curve obtained for **(t)-4f** from the average of three separate dilution experiments.

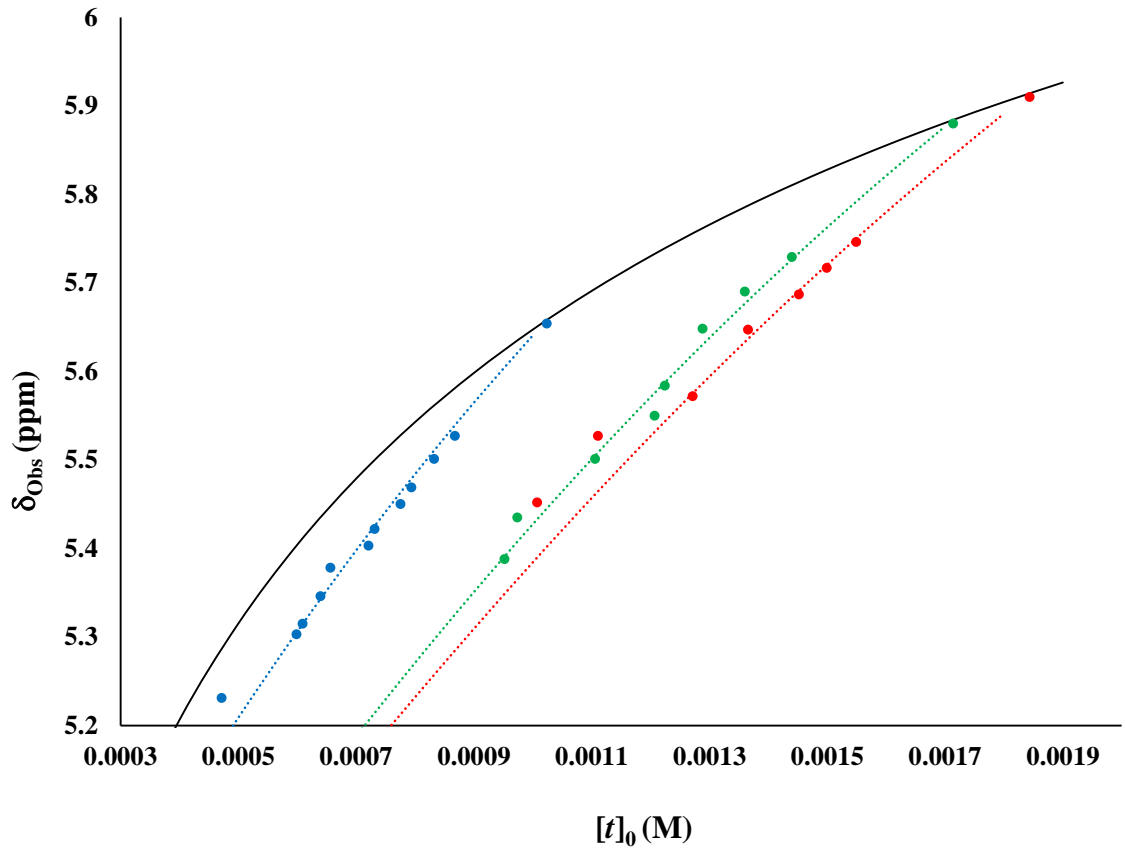


Figure 3.16 Relationship between δ_{Obs} vs $[t]_0$ for three reversion experiments of derivative **4k**. Blue, red and green dots correspond to first, second and third separate reversion experiments, respectively. Blue, red and green dashed lines correspond to the calculated δ_{Obs} vs $[t]_0$ plots for the first, second and third reversion experiments with the \bar{K}_{t-c} and δ_{t-c} values with minimum CV (sample standard deviations of 0.03, 0.02 and 0.04 ppm, respectively). Solid line corresponds to the dilution curve obtained for **(t)-4k** from the average of three separate dilution experiments.

The *trans-cis* complexation constants obtained through this method for **4c**, **4f** and **4k** were 160, 172 and 931 M⁻¹, respectively. Comparing *trans-trans* dimerization with *trans-cis* complexation, the energy differences between the two arrays for **4c**, **4f** and **4k** are 4.46, 3.05 and 0.68 kJ mol⁻¹. Regarding derivatives **4c** and **4f**, \bar{K}_{t-c} and ΔG_{t-c} values are in agreement with the expectancy that the *trans-cis* complex stability should likely be an average of the *trans-trans* and *cis-cis* dimer stabilities. The reasoning behind this expectation is that in a *trans-cis* complex the *trans*-isomer donors participate as the *cis*-isomer donors do in a *cis-cis* complex; the *cis* donors interact similarly as the *trans* donors do in a *trans-trans* complex (Figure 3.17). In other words, the *trans-trans* dimer has six hydrogen bond interactions, *cis-cis* dimer would exhibit two and the *trans-cis* complex would thus contain four hydrogen bonds; i.e. the average number of interactions of the two dimer structures.

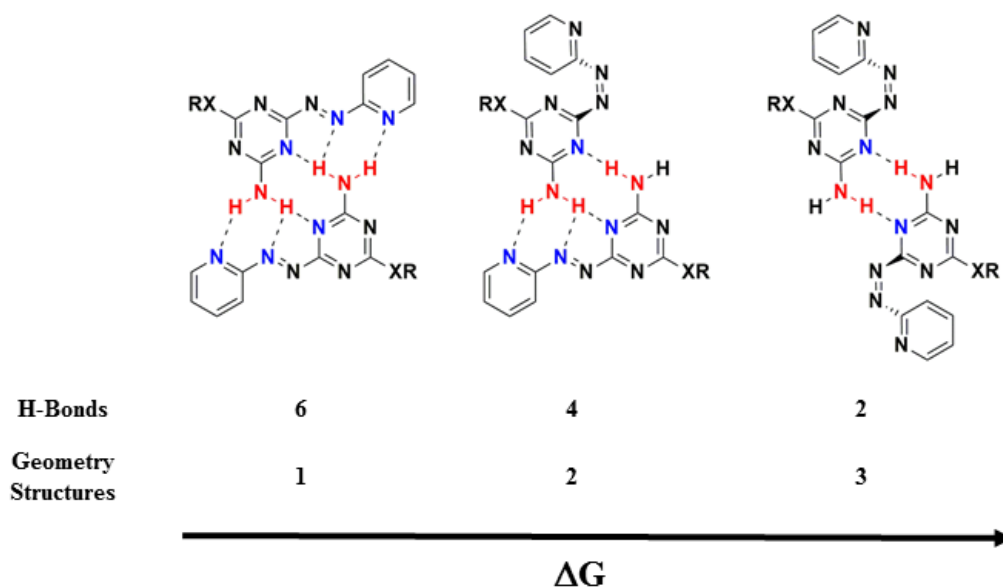


Figure 3.17 Structural similarities between *trans-trans*, *cis-cis* dimers and the *trans-cis* complex in mixed solution of **4a-p**.

If the ΔG_{t-t} values of butoxy **5c** and hexylthiol **5f** (-7.16 and -8.13 kJ mol⁻¹, respectively) were taken as ΔG_{c-c} approximations for butoxy **4c** and hexylthiol **4f**, the average $\overline{\Delta G}$ for **4c** and **4f** are -12.00 and -11.97 kJ mol⁻¹, respectively. These values differ from the calculated ΔG_{t-c} values by less than 1 kJ mol⁻¹ (0.57 and 0.79 kJ mol⁻¹ for **4c** and **4f**, respectively); therefore, *trans-cis* complexations for these systems are in accordance with the predicted model.

On the other hand, 4'-*tert*-butylphenoxy derivative **4k** deviates from the expected complexation values since the average $\overline{\Delta G}$ is -13.54 kJ mol⁻¹; i.e. 3.4 kJ mol⁻¹ higher than the calculated ΔG_{t-c} . This difference from the predicted $\overline{\Delta G}$ and the estimated ΔG_{t-c} is obvious visually when comparing the expected δ_{obs} vs $[t]_0$ plots from the reversion experiments with the experimental data obtained (Figure 3.18).

The explanation of why the derivative **4k** deviates from the model proposed is not clear from our data. It could be that either there are more complex structures in solution than those proposed at the beginning; or, there are other factors we are not aware of that enhance *trans-cis* complexation stability. In this sense, after a careful observation of the particularities of compound **4k**, we noticed that a *trans-cis* complex might provide an N-H/ π interaction that could increase the stability of the complex in comparison to complexes **4c** and **4f** complexes (Figure 3.19 (A)).

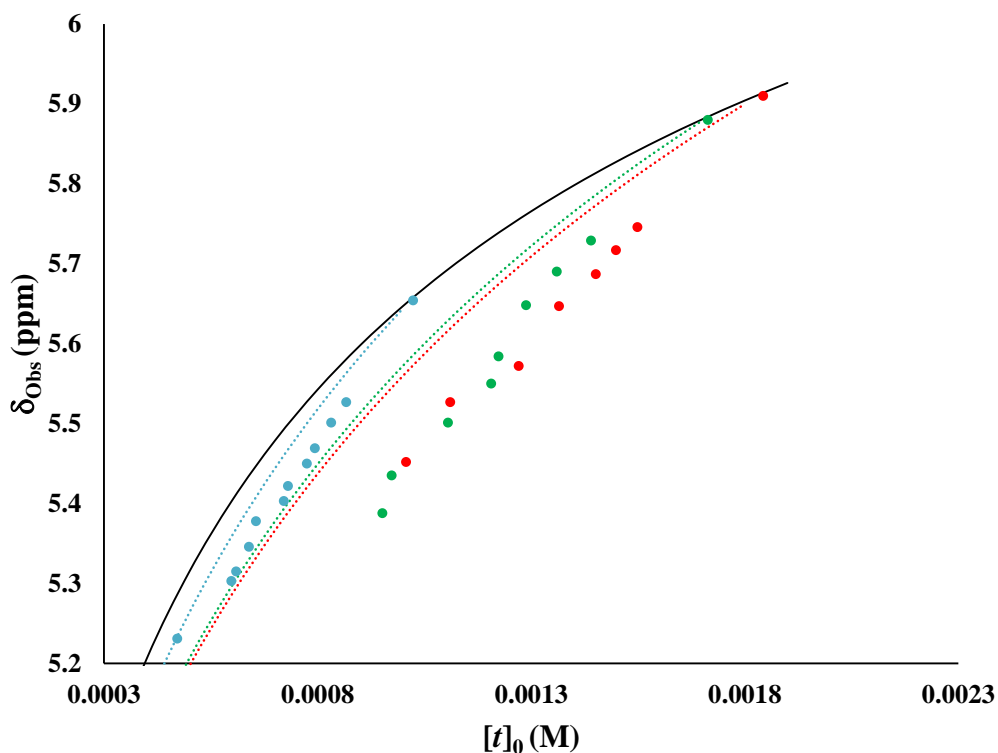


Figure 3.18 Relationship between δ_{Obs} vs $[t]_0$ through three reversion experiments of the derivative **4k**. Blue, red and green dots correspond to first, second and third separated reversion experiments, respectively. Blue, red and green dashed lines correspond to the predicted δ_{Obs} vs $[t]_0$ plots for the first, second and third reversion experiments with the expected $\overline{\Delta G}$ values (sample standard deviations of 0.05, 0.12, 0.11 ppm, respectively). Solid line corresponds to the dilution curve obtained from the average of three separated dilution experiments.

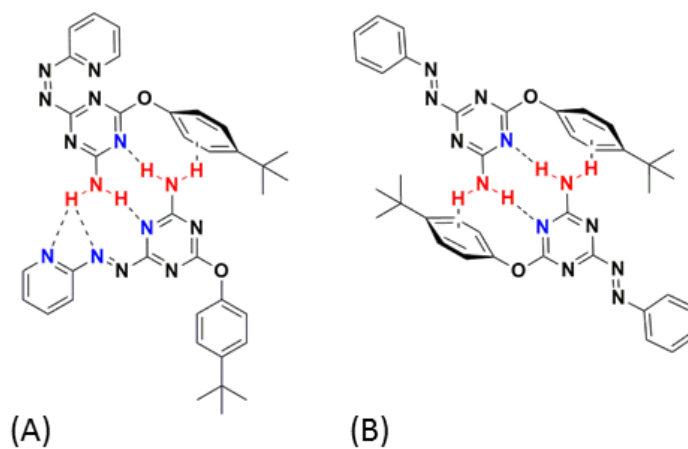


Figure 3.19 Potential N-H/ π intermolecular interactions in (A) **4k** *trans-cis* complex structure; and (B) **5k** dimer structure.

The N-H/ π interaction is well known and reported in the literature.¹⁴⁻¹⁵ One of the main characteristics of this interaction is its effect over the chemical shift of the proton involved. That is, since the participating proton is shielded by the magnetic anisotropy of the aryl ring there is generally an observed upfield shift;¹⁶ contrary to a conventional hydrogen bond interaction. If this interaction were playing a significant energetic contribution in the *trans-cis* complexation, an upfield shift should have been observed at higher concentrations of *cis* isomer; which was not observed. Likewise; similar behavior should have been observed in the dilution of the derivative **5k**, since **5k** monomers can be arranged to allow N-H/ π interactions (Figure 3.19 (B)). Therefore, due to the lack of evidence that supports the possible contribution of an N-H/ π interaction, the reasoning behind the strength of the **4k** *trans-cis* complex remains unclear.

Finally, the calculation of K_{t-c} allow us to obtain a complete representation of the distribution of all species in solution at different *cis/trans* ratios at a specific concentration; i.e. a speciation diagram. Calculated speciation diagrams for **4c**, **4f** and **4k** taking two scenarios into account: 1) when *cis* dimerization is not present in solution ($K_{c-c} = 0$); and, 2) when *cis* dimerization is present in solution ($K_{c-c} > 0$). The K_{c-c} values employed for the second scenario corresponded to the dimerization constants of **5c**, **5f** and **5k**. The purpose behind the comparison between these two scenarios is to estimate the impact that *cis-cis* dimerization has over the distribution of the species when both (c)-**4** and (t)-**4** are present (Figures 3.20 - 3.22).

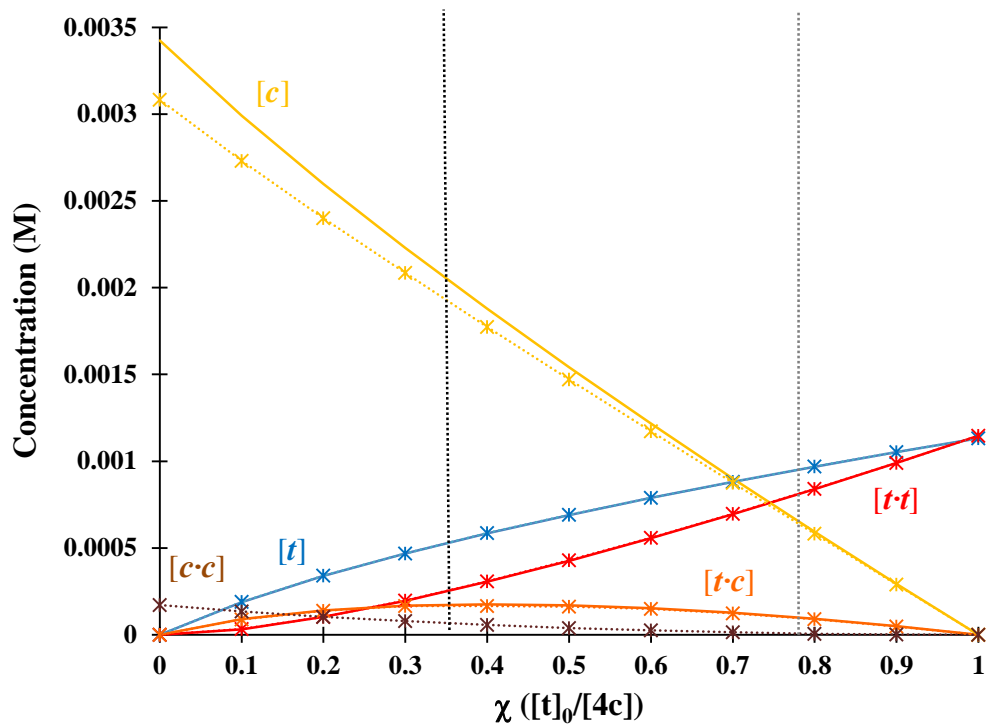


Figure 3.20 Theoretical speciation diagram of derivative **4c** at the third reversion experiment (green dots at Figure 3.14, $[4c] = 3.42 \times 10^{-3} \text{ M}$) at 298 K. Solid lines correspond to the first scenario ($K_{c-c} = 0$) and dotted-star marked lines correspond to the second scenario ($K_{c-c} = 18 \text{ M}^{-1}$) respectively. Blue, red, orange, yellow and brown colors correspond to $[t]$, $[t \cdot t]$, $[t \cdot c]$, $[c]$, and $[c \cdot c]$, respectively. Black dotted line corresponds to maximum *cis/trans* ratio in reversion experiment. Grey dotted line corresponds to *cis/trans* ratio at PSS.

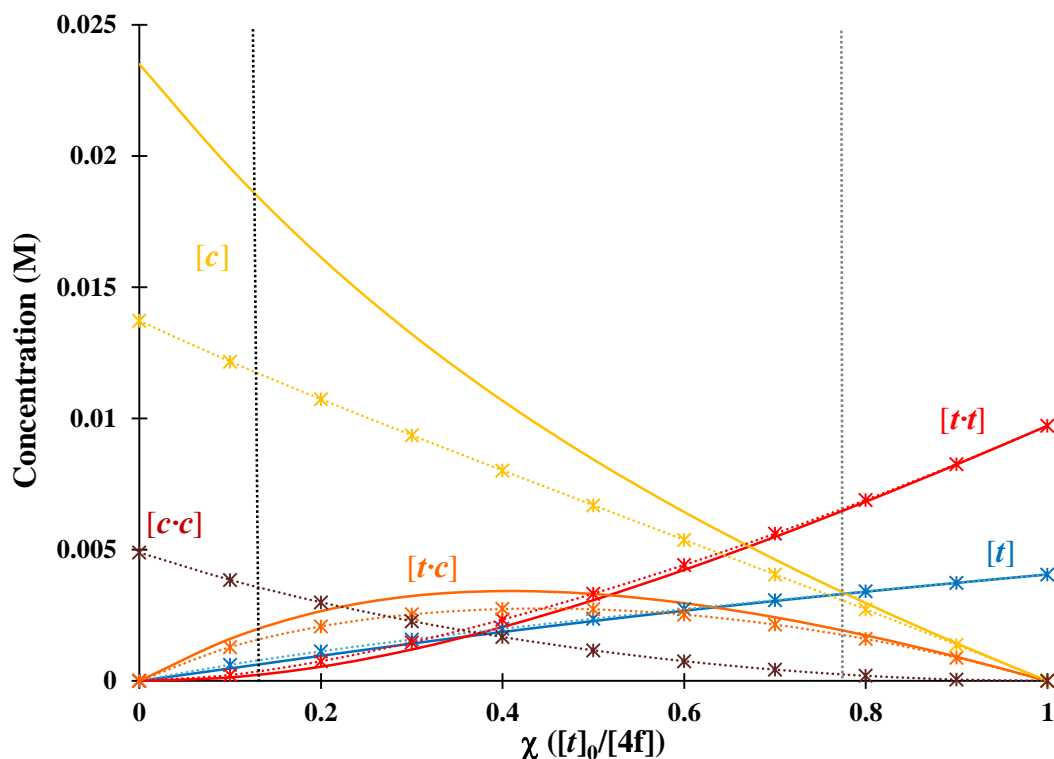


Figure 3.21 Theoretical speciation diagram of derivative **4f** at the third reversion experiment (green dots at Figure 3.15, $[4f] = 2.35 \times 10^{-3} \text{ M}$) at 298 K. Solid lines correspond to the first scenario ($K_{c-c} = 0$) and dotted-star marked lines correspond to the second scenario ($K_{c-c} = 26 \text{ M}^{-1}$) respectively. Blue, red, orange, yellow and brown colors correspond to $[t]$, $[t \cdot t]$, $[t \cdot c]$, $[c]$, and $[c \cdot c]$, respectively. Black dotted line corresponds to maximum *cis/trans* ratio in reversion experiment. Grey dotted line corresponds to *cis/trans* ratio at PSS.

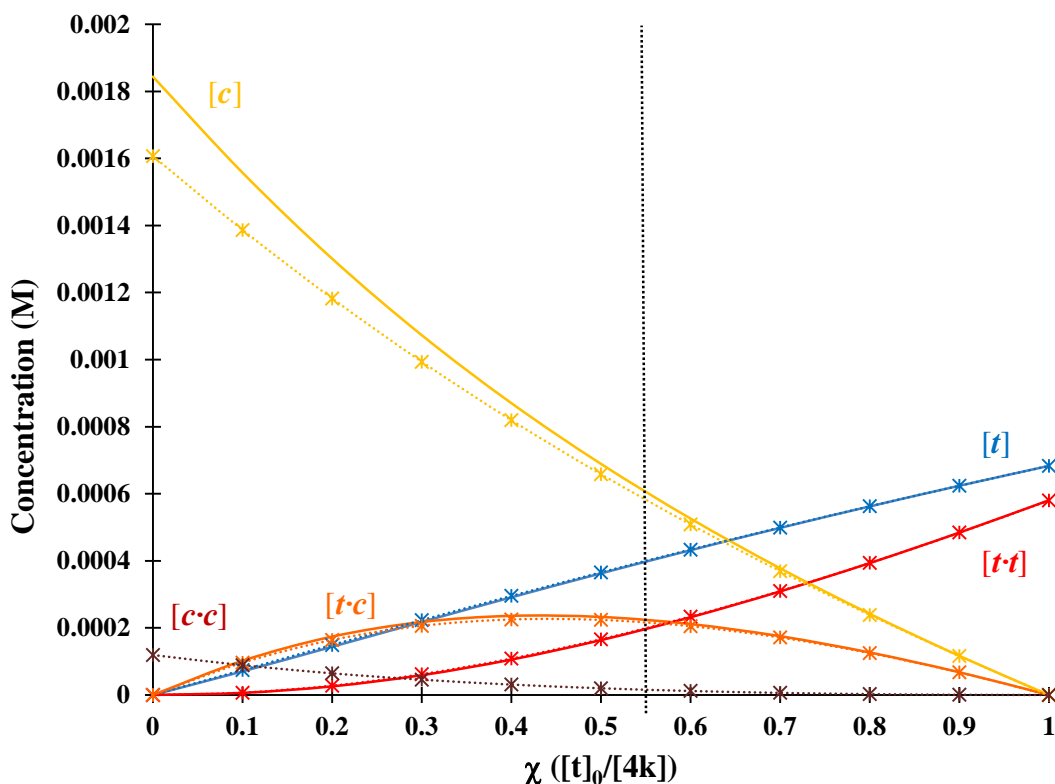


Figure 3.22 Theoretical speciation diagram of derivative **4k** at the third reversion experiment (green dots at Figure 3.16, $[4\mathbf{k}] = 1.84 \times 10^{-3} \text{ M}$) at 298 K. Solid lines correspond to the first scenario ($K_{c \cdot c} = 0$) and dotted-star marked lines correspond to the second scenario ($K_{c \cdot c} = 46 \text{ M}^{-1}$) respectively. Blue, red, orange, yellow and brown colors correspond to $[t]$, $[t \cdot t]$, $[t \cdot c]$, $[c]$, and $[c \cdot c]$, respectively. Black dotted line corresponds to maximum *cis/trans* ratio in reversion experiment.

Figures 3.20 to 3.22 illustrate the differences in concentration of all the species when *cis-cis* dimerization is assumed as nonexistent (solid lines) or present (dotted-star marked lines). From all the systems studied, derivative **4f** showed the highest difference in concentration between both scenarios ($K_{c \cdot c} = 0$ and $K_{c \cdot c} = 26 \text{ M}^{-1}$). This is, approximately 13% in *trans-cis* complex concentration ($[t \cdot c]$) between both scenarios over the total amount of *trans*-isomer ($[t]_0$). This difference is observed in a solution with an excess of *cis*-isomer (i.e. 90% of **(c)-4f**, or $\chi = 0.1$ in Figure 3.20), and decreases as the total concentration of *cis*-isomer also decreases; e.g. at 50% of **(c)-4f**, or $\chi = 0.5$ in Figure 3.20

the difference in $[t \cdot c]$ between the two cases is 5%. Since nearly all the reversion experiments started at a *cis/trans* ratio ≤ 1 (i.e. 50% of (c)-4, or $\chi = 0.5$), the differences in $[t \cdot c]$ did not surpass the 5% over the total concentration of *trans*-isomer. Therefore, it can be said that the mathematical model used to calculate the *trans-cis* complexation constant (K_{t-c}) is reliable since it provides a good description of the species distribution at the observed concentrations.

3.2.4 *Cis to Trans* Reversion Kinetics

One of the major difficulties during the study of the photochemistry of derivatives **4a-p** was the *cis to trans* reversion that takes place immediately once the *cis* isomer is in solution at room temperature. We also observed during the reversion experiments that the rate of *cis to trans* reversion was different for each derivative. Therefore, parallel to the *trans-cis* complexation study, the *cis/trans* ratios obtained from each reversion experiment at specific times were useful to estimate the kinetics of the *cis to trans* thermal reversion. The thermal *cis to trans* reversions of derivatives **4c**, **4f** and **4k** in toluene- d_8 at room temperature corresponded to a first order reaction model (Equations 15 and 16). This is in agreement with the *cis to trans* thermal reversion of azobenzene documented by Cammenga and coworkers.¹⁷ The rate constants for each derivative tested are displayed in Table 3.5; and, the decay profiles of the *cis*-isomer of derivatives **4c**, **4f** and **4k** are presented in Figures 3.23 to 3.25, respectively.

$$\text{Rate} = -\frac{d[A]}{dt} = k[A] \quad \text{Equation 15}$$

$$\ln[A] - \ln[A]_0 = -kt$$

$$\text{Equation 16}$$

Table 3.5 Rate constants calculated for *cis* to *trans* thermal reversion of **4c**, **4f** and **4k** studied in Toluene-*d*₈ at 298 K.

Derivative	RX	$k \times 10^{-4} \text{ (s}^{-1}\text{)}^a$
4c	<i>n</i> -butoxy	3.36 ± 0.43
4f	Hexylthio	2.74 ± 0.40
4k	4'- <i>tert</i> -butylphenoxy	6.02 ± 1.12

^a Average values obtained using the first order reaction model and three separate reversion experiments. Errors calculated from twice the standard deviation to give a 95% confidence interval.

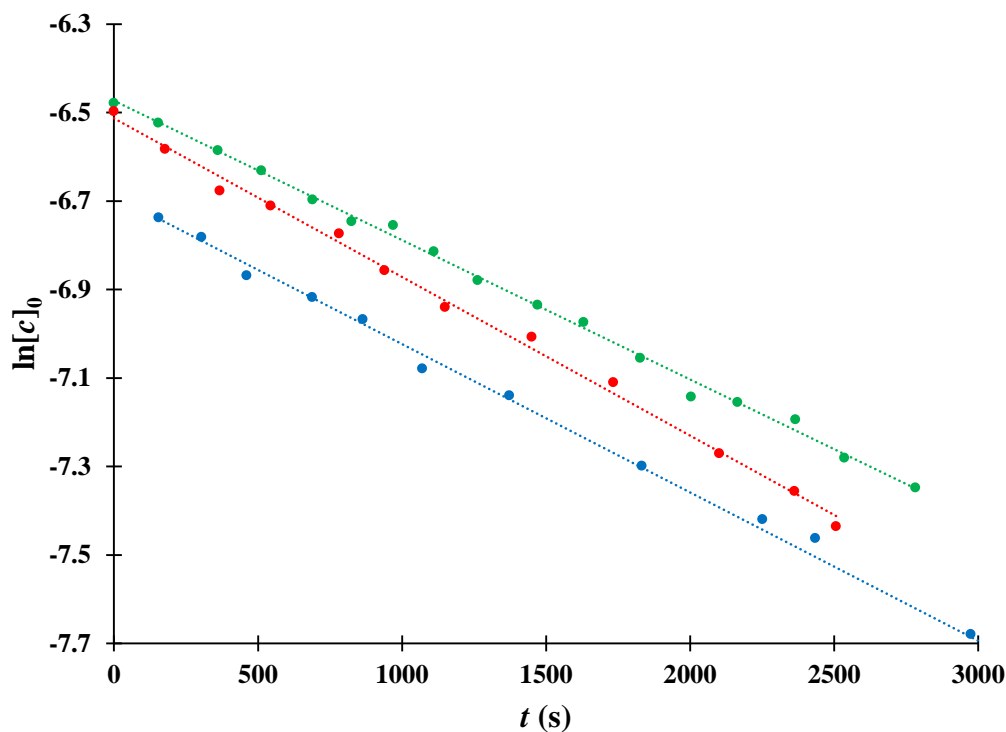


Figure 3.23 Decay profiles of (c)-**4c** isomer in toluene-*d*₈ at 298 K. Blue, red and green dots correspond to first, second and third separate reversion experiments ($r = -0.9973$, -0.9982 and -0.9981) respectively. Blue, red and green dashed lines correspond to the calculated values obtained by linear least squares regression of the first, second and third separate reversion experiments, respectively.

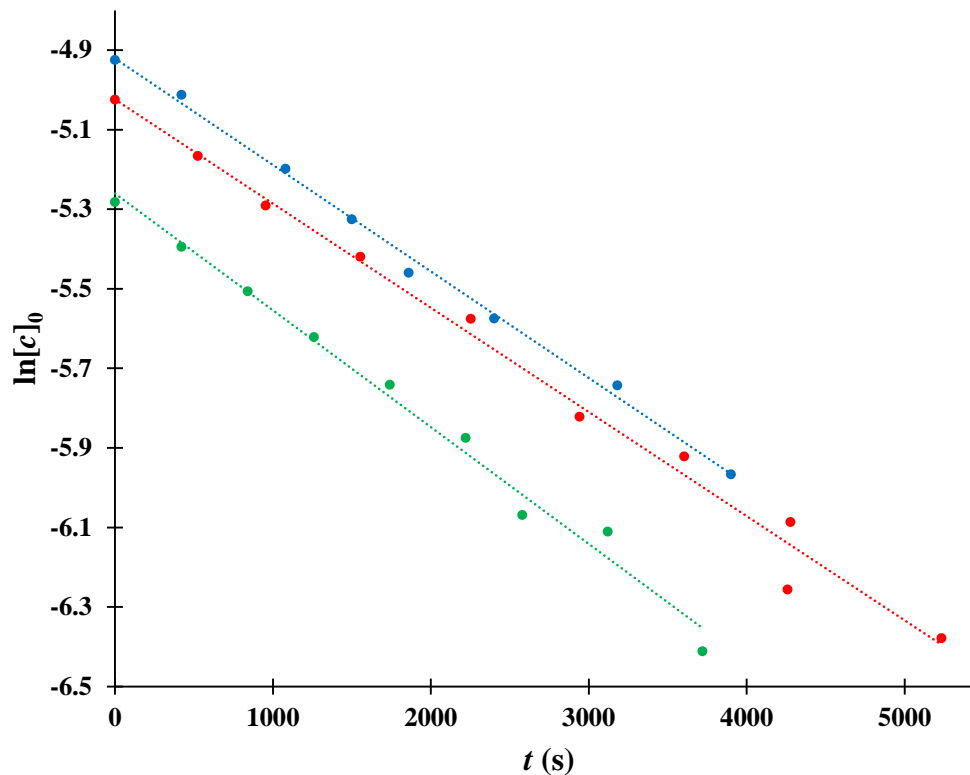


Figure 3.24 Decay profiles of (c)-4f isomer in toluene- d_8 at 298 K. Blue, red and green dots correspond to first, second and third separate reversion experiments ($r = -0.9995$, -0.9981 and -0.9987) respectively. Blue, red and green dashed lines correspond to the calculated values obtained by linear least squares regression of the first, second and third separate reversion experiments, respectively.

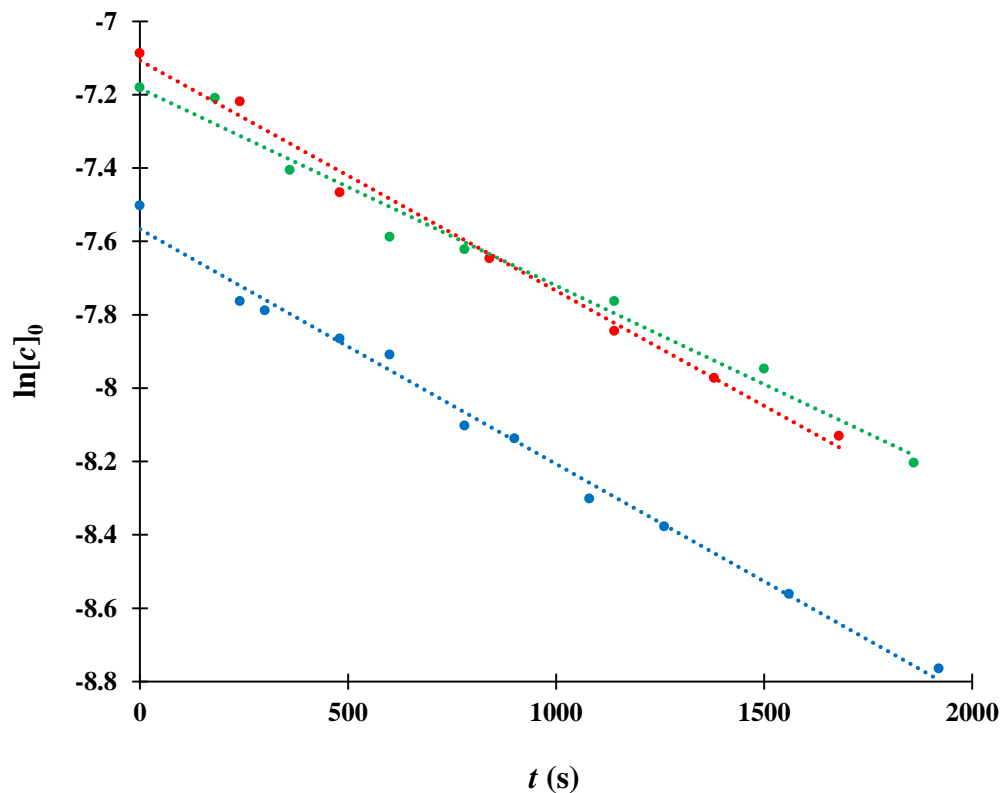


Figure 3.25 Decay profiles of (*c*)-**4k** isomer in toluene-*d*₈ at 298 K. Blue, red and green dots correspond to first, second and third separate reversion experiments ($r = -0.9954$, -0.9907 and -0.9962) respectively. Blue, red and green dashed lines correspond to the calculated values obtained by linear least squares regression of the first, second and third separate reversion experiments, respectively.

An interesting observation from the thermal reversion rates observed is how the derivative with the lowest K_{t-t} value has the lowest *cis*- to *trans*- reversion rate (i.e. hexylthiol **4f**); meanwhile, the system with the highest K_{t-t} has the highest thermal reversion rate (i.e. *tert*-butylphenoxy **4k**). The unimolecular nature of the kinetics in **4c**, **4f** and **4k** indicates that the complexation equilibria have no impacted the reversion. Hence, there is no template effect accelerating the reversion as observed in complementary designs (Wisner and Pleizier unpublished results).

3.3 Summary and Conclusions

The photophysical properties of derivatives **4a-p** were evaluated. The UV-Vis absorption spectra of all derivatives **4a-p** in their *trans*-isomeric form are similar to azobenzene and 2,2'-azopyridine UV-Vis absorption spectra. This is, the maximum absorptions for the $n \rightarrow \pi^*$ band are approximately 440 nm, and for the $\pi \rightarrow \pi^*$ band are approximately 290 nm (hypsochromic shift). On the other hand, the *cis*-isomers of derivatives **4c**, **4f** and **4k** have UV-Vis absorption spectra wherein the $n \rightarrow \pi^*$ band showed higher absorptivity and the $\pi \rightarrow \pi^*$ band showed lower absorptivity compared with the *trans*-isomers. The presence of an isosbestic point during the *cis* to *trans* thermal reversion of **4c**, **4f** and **4k** confirms that during this transition there are only two species involved: the *cis* and *trans*-isomers. The percentages of interconversion from *trans* to *cis* at the photostationary state for all derivatives **4a-p** ranged from 9 - 28, 20 - 22 and 14 - 35 percent in CDCl_3 , toluene- d_8 and CD_3CN , respectively. Since the photoisomerization yields obtained were lower than 100%, the presence of two more complexation equilibria in solution was assumed; i.e. the *cis-cis* dimerization and *trans-cis* complexation. The *cis-cis* dimerization strength was assumed to be equal to or lower than the dimerization constant values obtained for derivatives **5c**, **5f** and **5k**. Therefore, since these constants are at least 20 times lower than their derivatives **4** counterparts in toluene- d_8 , the effect of these complexes in the distribution of the total amount *cis*-isomer was disregarded. The *trans-cis* complexes of derivatives **4c**, **4f** and **4k** stabilities were examined. The calculated K_{t-c} complexation constants for **4c** and **4f** are 160 and 172 M^{-1} ; which are in accordance with expected values. On the other hand, the derivative **4k** shows a complexation constant

higher than the anticipated value. The reasoning behind the enhanced stability of the **4k** *trans-cis* complex is unclear. The speciation diagrams of **4c**, **4f** and **4k** at different *trans*-isomer molar fractions corroborate the minimal impact that *cis* dimer has over the species distribution in solution after photoisomerization. Finally, the stability of the **4c**, **4f** and **4k** *cis*-isomers in solution were studied. In this sense, thermal reversions back to the *trans*-isomer proceeded as first order reactions wherein the rate constants for derivatives **4c**, **4f** and **4k** are 3.36×10^{-4} , 2.74×10^{-4} and $6.02 \times 10^{-4} \text{ s}^{-1}$, respectively.

3.4 Experimental Methodology

3.4.1 Generalities

All experiments were performed in ambient atmospheric conditions unless otherwise indicated. Solvents (dichloromethane, diethyl ether and hexanes) were obtained from Caledon Laboratories, Fisher Chemicals, Sigma-Aldrich and VWR Analytical. In the case of inert atmosphere conditions, solvents were dried using an Innovative Technology Inc. Controlled Atmospheres Solvent Purification System that utilizes dual alumina columns (SPS-400-5), or purchased from Sigma-Aldrich and used as received. Reactions were monitored by thin-layer chromatography (TLC) on pre-coated TLC-sheets POLYGRAM®SIL G/UV₂₅₄. Flash chromatography was performed with SiliCycle®SiliaFlash® F60, 40-63 μm 60 Å. Nuclear Magnetic Resonance spectra were recorded on INOVA 400 MHz spectrometer ($^1\text{H} = 399.77 \text{ MHz}$; $^{13}\text{C} \{^1\text{H}\} = 100.52 \text{ MHz}$). ^1H spectra were referenced relative to Me_4Si using the residual non-deuterated NMR

solvent signal (^1H : CHCl_3 , $\delta = 7.26$ ppm, $(\text{CHD}_2)\text{C}_6\text{D}_5$, $\delta = 2.09$ ppm, CHD_2CN $\delta = 1.94$ ppm). Solvents for NMR spectroscopy (Chloroform-d, Acetonitrile-d₃ and Toluene-d₈) were purchased from Cambridge Isotope Laboratories and Sigma-Aldrich. All photoisomerization experiments were carried out at a photoreactor unit LZC 4V from Luzchem Research Inc. with a complete set of low-pressure blue lamps with a radiation centered at 360 nm. UV-Vis absorption spectra were obtained from a CARY 300 UV-Visible spectrometer employing quartz curvette (chamber volume 300 mL, pathlength 10 mm, limit 200 – 2500 nm spectral range).

3.4.2 Photostationary State Experiments

Photoisomerization experiments were carried out by irradiating UV light to solutions of derivatives (*t*)-**4a-p** in CDCl_3 , toluene-*d*₈ and CD_3CN . In a typical photostationary state experiment 2 mL of a derivative **4a-p** solution in the selected solvent system was prepared at concentrations of approximately 10^{-3} M. For each derivative, 1 mL of the prepared solution was poured into a Wilmar ® quartz NMR tube (Limit = 400 MHz, Cutoff wavelength = 265 nm). The solution was purged with N_2 in order to avoid side reactions with O_2 present in solution. The UV light source employed in all photoisomerizations was a photoreactor unit LZC 4V from Luzchem Research Inc. with a complete set of low-pressure blue lamps with a radiation peak at 360 nm. Each sample was irradiated for one hour at room temperature and immediately placed into an ice bath and taken to the NMR Spectrometer INOVA 400 MHz. The *cis/trans* ratio was calculated from

the integration of the signals corresponding to the *ortho*-pyridine proton of **(c)-4a-p** and **(t)-4a-p** in the ^1H NMR spectrum recorded immediately.

3.4.3 Synthesis of (*Z*)-4-(pyridin-2-yl diazenyl)-1,3,5-triazin-2-amine derivatives (**(c)-4c**, **(c)-4f** and **(c)-4k**).

Approximately 160 mL of a 10^{-2} M solution of a derivative **4** in dichloromethane was prepared and distributed between 16 test tubes. Each test tube containing the derivative **4** solution was purged with N_2 in order to avoid side reactions with O_2 present in solution. The 16 test tubes were placed in the photoreactor and irradiated using lamps with radiation centered at 360 nm for 3 hours. After irradiation, the solution was cooled down to -78° and the solvent was removed employing a constant air flow to yield a mixture of *cis* and *trans* isomers. The *cis*-isomer was isolated through flash chromatography with diethyl ether as eluent. Once the first fraction (*cis* isomer) was obtained, it was cooled down to -78° to remove the diethyl ether with the aid of a constant air flow. In all cases, the *cis*-isomer was a yellow powder that was stored in a vial wrapped with black tape in the freezer to prevent thermal and photochemical reversion.

3.4.4 ^1H NMR Reversion Experiments

In a clean and dry eight inches NMR tube, 0.5 mL of toluene- d_8 was injected via syringe. Locking and shimming of pure toluene- d_8 was carried out in order to speed up the acquisition of the first ^1H NMR spectrum of the *cis/trans* mixture in solution. Apart, a freshly prepared toluene- d_8 solution of the *cis*-isomer was filtered and poured into a

separate empty NMR tube. A ^1H NMR spectrum was recorded immediately in order to obtain the maximum *cis/trans* ratio. Then, a ^1H NMR spectrum was recorded every 3 to 5 minutes until the signal to noise ratio of the *cis*-isomer signals were lower than 4. The *cis/trans* ratio and chemical shifts of the N-H protons of (*c*)-**4** and (*t*)-**4** were identified and tracked during the experiment. For each derivative **4** tested, the reversion procedure was repeated at least twice to ensure the reliability and reproducibility of the data. Data processing was performed off-line using the commercial software package MATLAB R2015b (The MathWorks Inc. 1984-2015).

3.5 References

- (1) Ma, L.; Kang, H.; Liu, R.; Huang, Y. *Langmuir*, **2010**, *26* (23), 18519.
- (2) Bai, T.; Han, Y.; Zhang, P.; Wang, W.; Liu, W. *Soft Matter*, **2012**, *8* (25), 6846.
- (3) Wang, J.-H.; Li, M.; Li, D. *Chem. Sci.*, **2013**, *4* (4), 1793.
- (4) Ercole, F.; Davis, T. P.; Evans, R. A. *Polym. Chem.*, **2010**, *1* (1), 37.
- (5) Takeshita, M.; Hayashi, M.; Miyazaki, T. *Chem. Lett.*, **2010**, *39* (2), 82.
- (6) Takeshita, M.; Hayashi, M.; Kadota, S.; Mohammed, K. H.; Yamato, T. *Chem. Commun.*, **2005**, *6*, 761.
- (7) Okuyama, T.; Yokoyama, Y.; Yokoyama, Y. *Bull. Chem. Soc. Jpn.*, **2001**, *74* (11), 2181.
- (8) Herder, M.; Pätzelt, M.; Grubert, L.; Hecht, S. *Chem. Commun.*, **2011**, *47* (1), 460.
- (9) Hampson, G. C.; Robertson, J. M. *J. Chem. Soc.*, **1941**, 409.
- (10) Vogel, A. I. *J. Chem. Soc.*, **1965**, 5316.
- (11) Fischer, E. *J. Am. Chem. Soc.*, **1960**, *82* (13), 3249.
- (12) Brown, E. V.; Granneman, G. R. *J. Am. Chem. Soc.*, **1975**, *97* (3), 621.

- (13) Patel, J. K.; Kapadia, C. H.; Owen, D. B. *Handbook of statistical distributions*; M. Dekker, 1976.
- (14) Worth, G. A.; Wade, R. C. *J. Phys. Chem.*, **1995**, 99 (48), 17473.
- (15) Parkinson, G.; Gunasekera, A.; Vojtechovsky, J.; Zhang, X.; Kunkel, T. A.; Berman, H.; Ebright, R. H. *Nat. Struct. Biol.*, **1996**, 3 (10), 837.
- (16) Sébastien, D.; Jacques, B.; Axelle, A.; Brigitte, J.-G. *Tetrahedron*, **2012**, 68 (23), 4362.
- (17) Eckardt, N.; Flammersheim, H. J.; Cammenga, H. K. *J. Therm. Anal. Calorim.* **1998**, 52 (1), 177.

Chapter 4

4 Synthesis and Characterization of Second Generation Photoswitchable Self-Complementary DDAAA Hydrogen Bond Arrays.

4.1 Introduction: Design of Second Generation Photoswitchable Self-Complementary Hydrogen Bond Arrays.

In the second and third chapters, the design, synthesis and analysis of a system which dimerizes thanks to the presence of amino, triazine, azo and pyridine moieties was presented; i.e. derivatives **4a-p**. Based on the number and the nature of hydrogen bond interactions present in those arrays, it was expected that dimerization constants higher than 10^2 M^{-1} would be observed in CDCl_3 . Unfortunately, this was not the case. This unexpected poor performance led us to consider what improvement might be made to the design in order to achieve higher complex stability in the *trans*-form of the arrays.

In this sense, the X-ray crystal structures were useful since they allowed us to observe the dimer structure in the solid state. More specifically, it let us measure the intermolecular distances and angles between interacting sites. From this analysis, we noted that the pyridine nitrogen atom lone pair is not colinear with the N-H bond of the amino group. The calculated average of the **N-H...N**(pyridine) angles measured in all dimers of **4**

in the solid state averaged 138° (Figure 4.1). Therefore, the dimerization constants obtained were in agreement with a system stabilized by only one strong (or primary) hydrogen bond interaction and two weaker (or secondary) hydrogen bond interactions.

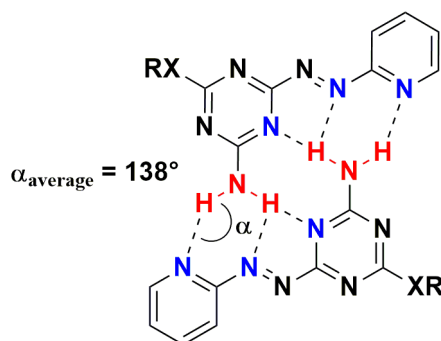


Figure 4.1 Average N-H \cdots N(pyridine) angle in dimer structures of **4** observed in the solid state.

From this observation and the results of molecular modeling, it was concluded that the pyridine ring could be replaced by a fragment containing an aromatic ring wherein the acceptor site would be *bonded ortho* to the azo group (instead of *located α* to the azo group). This way the lone pair participating in the hydrogen bond interaction would be lined up with the N-H bond and hopefully lead to an improved photoswitchable self-complementary **DDAAA** hydrogen bond array (Figure 4.2).

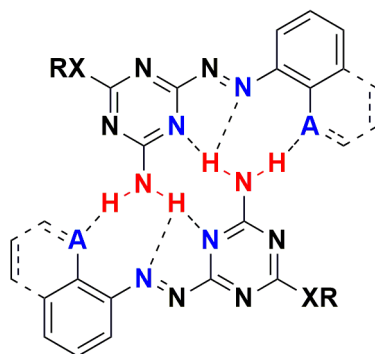
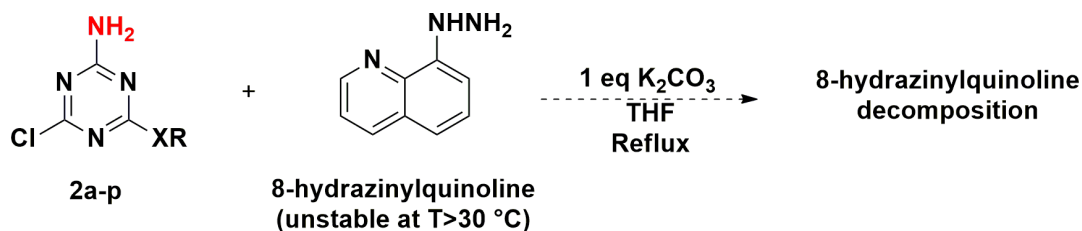


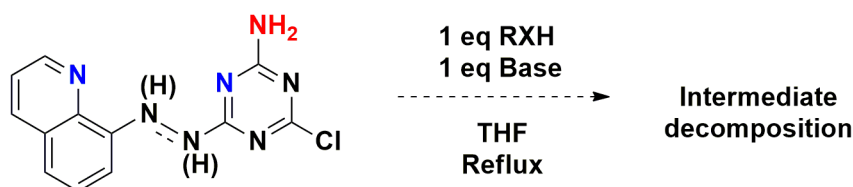
Figure 4.2 Proposed design for second generation photoswitchable self-complementary DDAAA hydrogen bond arrays.

In this sense, our first proposed change to the original design was to replace the pyridine ring by the quinoline group. The quinoline ring was a good option since it would provide an sp^2 nitrogen atom *ortho*- to the azo group to participate in a strong hydrogen bond interaction with an amino proton.^{1,2} Likewise, the planarity and aromaticity of this moiety could contribute to dimer stability through conjugation. Following the synthetic strategy employed for the synthesis of derivatives **4a-p**, the quinoline ring was planned to be inserted at the third step as 8-hydrazinylquinoline; i.e, similarly to the addition of 2-hydrazinylpyridine in the synthesis of derivatives **4a-p** (Scheme 4.1). However, the 8-hydrazinylquinoline is unstable at the temperatures needed to achieve the third addition to the triazine ring.



Scheme 4.1 Synthetic strategy to add quinoline ring as acceptor at the third step.

On the other hand, when the 8-hydrazinylquinoline is added at the second step, the addition of the RX group at the third step (or after oxidation of the hydrazinyl- derivative) attempted did not precede (Scheme 4.2). Therefore, the inclusion of a quinoline ring as a hydrogen bond acceptor was discarded.



Scheme 4.2 Synthetic strategy to add quinoline ring at the second step.

After a survey of alternative acceptor groups that could be incorporated into the aromatic ring, an alkoxy group was identified as a feasible alternative; i.e. an sp^3 oxygen atom as hydrogen bond acceptor. Jeffrey and coworkers reported an extensive analysis of the crystal structure of barbiturates, purines, pyrimidines, nucleosides and nucleotides (45 barbiturates, 214 purines and pyrimidines, and 119 nucleosides and nucleotides crystal structures, respectively).^{3,4} In these studies, there was a particular attention to the hydrogen bond lengths of different pairs of donor and acceptor groups. The data analyzed provide a guide to indicate the relative donor and acceptor strength. In this sense, the relative acceptor strength of an ether group is slightly lower compared with an sp^2 nitrogen atom, such as the acceptor site in the proposed quinoline ring (Table 4.1).⁵ However, the hydrogen bond distances reported for the alkoxy group as an acceptor are smaller in comparison with the hydrogen bond distances observed for the **4a**, **4d**, **4f** and **4k** dimer structures in the solid state reported in Chapter 2 (section 2.3.3). Therefore, it would be reasonable to expect an

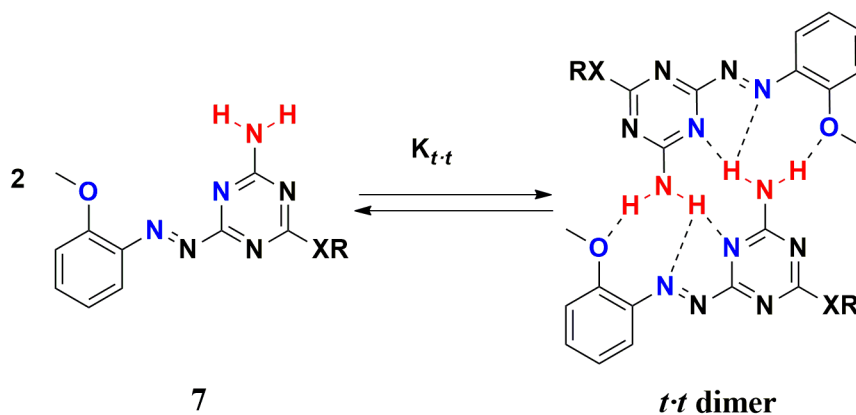
improvement in the strength of the hydrogen bond interaction between the amino N-H site and the alkoxy group for our photoswitchable self-complementary **DDAAA** arrays.

Table 4.1 Ranges and mean values of the lengths (Å) and angles (°) of hydrogen bonds in crystal structures of purines and pyrimidines, nucleosides, and nucleotides.^a

Donors	Acceptors					
	N		O		N ^b	
N-H	47		5			
	1.73	179	1.77	177		
	2.23	144	2.25	136		
	1.90	168	2.00	155		
-N(H)H	69		9		4	
	1.85	179	1.94	177	3.25	142
	2.76	119	2.60	117	3.55	130
	2.04	163	2.26	144	3.34	137

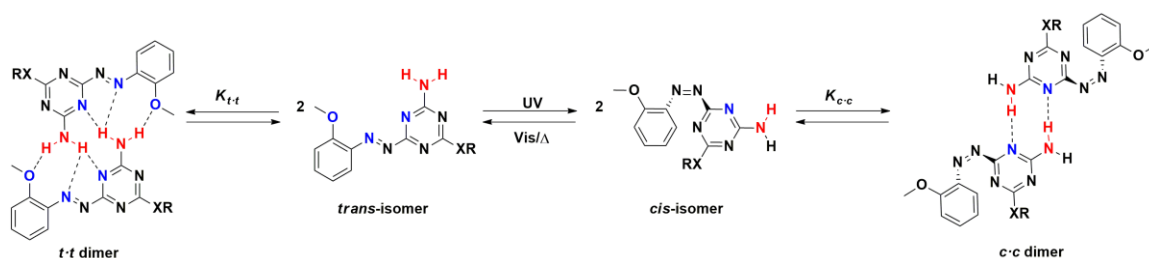
^a For each entry, row one is the number of data, row two is the minimum value, row three is the maximum value and row four the mean value; column one is the hydrogen bond length (Å) and column two is the two centered hydrogen bond angle (°). ^b Values obtained from crystal structures of derivatives **4a**, **4d**, **4f** and **4k** in Chapter 2 (Table 2.9)

Hence, we proposed the synthesis of (*E*)-4-((2-methoxyphenyl)diazenyl)-1,3,5-triazin-2-amine derivatives (**7**). These derivatives fulfill the main improvement proposed for our photoswitchable self-complementary array; i.e. the location of an acceptor group bonded *ortho*- to the azo group that would improve the *trans-trans* dimer stability (Scheme 4.3).



Scheme 4.3 Improved photoswitchable self-complementary **AAADD** hydrogen bond array.

Since the main purpose of the systems designed is to trigger a change in their molecular recognition through a light stimulus, it is important to note that, regardless of the alteration proposed, it is still expected that a *trans*- to *cis*- structural change should cause a reduction in the number of hydrogen bond interacting sites as assumed for derivatives **4a-p** (Scheme 4.4).



Scheme 4.4 Amended photoswitchable self-complementary **AAADD** hydrogen bond array and its idealized function.

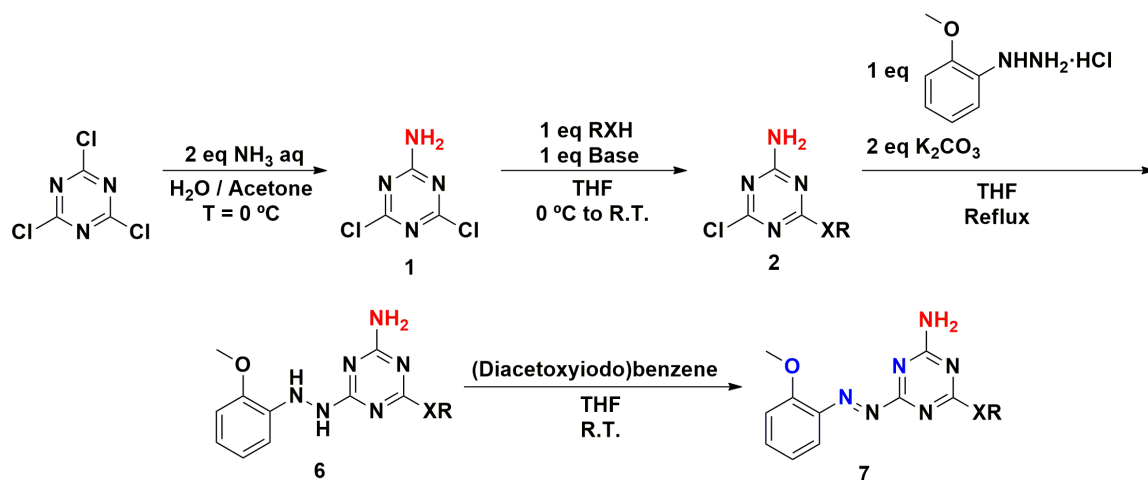
The remaining sections of this chapter present the synthesis and characterization of an amended photoswitchable self-complementary system. The dimer stability of the

proposed array in solution and the structure in the solid state will be discussed with a comparison to the derivatives **4a-p** reported in Chapter 2 and 3. Likewise, the photochemical properties and the complexation pattern before and after photoisomerization of these new derivatives will be presented.

4.2 Results and Discussion.

4.2.1 Synthesis of Second Generation Photoswitchable Self-Complementary Hydrogen Bond Arrays.

Since the main alteration to our proposed system replacing pyridine ring for an methoxyphenyl group, the syntheses of these systems followed the same synthetic pathway established for derivatives **4a-p** in Chapter 2 (Section 2.3.1). The only modification to the procedure corresponded to the use of the (2-methoxyphenyl)hydrazine hydrochloride salt instead of 2-hydrazinopyridine at the third stage of the triazine ring substitution (Scheme 4.5). Based on the results obtained from **4a-p**, the RX groups employed were those that provided the highest dimerization constants and where soluble in toluene (Table 4.2).



Scheme 4.5 Synthesis of second generation photoswitchable self-complementary DDAAA hydrogen bond arrays.

Table 4.2 Reactants and overall yields of photoswitchable self-complementary hydrogen bond arrays **7**.

Derivative	RXH	Base ^a	Yield (%) ^b
7c	<i>n</i> -butanol	NaH	12
7f	hexanethiol	NaOH	38
7g^c	-	NH ₄ OH ^d	12
7i	phenol	NaOH	78
7k	4'- <i>tert</i> -butylphenol	K ₂ CO ₃	8
7m	3,5-bis(trifluoromethyl)phenol	K ₂ CO ₃	20
7n	perfluorophenol	K ₂ CO ₃	46

^a One equivalent added at 0 °C. ^b Percent yield over 3 synthetic steps starting from intermediate **1**. ^c Chloro is already in place in intermediate **1**. ^d Two equivalents of base added.

The overall chemical yields obtained for derivatives **7** ranged from 8 to 78% starting from intermediate **1**. These yields are similar to the range of the chemical yields

obtained for derivatives **4a-p**. Based on those observations it can be concluded that the reactivity of (2-methoxyphenyl)hydrazine is similar to the 2-hydrazinopyridine.

4.2.2 ^1H NMR Dilution Experiments: Stability of *trans-trans* dimers.

Dilution experiments of all derivatives **7** were carried out in CDCl_3 . Table 4.3 displays the (most stable) *trans*-isomer dimerization constants ($K_{t,t}$) with the calculated chemical shifts of the amino protons when **7** are in solution as free monomers (δ_m) and in a dimer structure (δ_d).

Table 4.3 Dimerization constants, free energies of dimerization, chemical shifts of monomer (δ_m) and dimer (δ_d) species studied, and the total change in the chemical shift ($\Delta\delta_{max}$) in CDCl_3 at 298 K.

Derivative	RX	$K_{t,t}$ in CDCl_3 (M^{-1}) ^a	$\Delta G_{t,t}$ (kJ mol^{-1}) ^a	δ_m (ppm) ^a	δ_d (ppm) ^a	$\Delta\delta_{max}$ (ppm)
7c	-O(<i>n</i> -C ₄ H ₉)	36 ± 5	-8.86 ± 0.32	5.47	6.53	1.07
				5.66	9.19	3.53 ^b
7f	-S(<i>n</i> -C ₆ H ₁₃)	57 ± 1	-10.02 ± 0.03	5.46	6.56	1.11
				5.47	9.38	3.91 ^b
7g	-Cl	310 ± 140	-14.21 ± 1.09	5.72	6.46	0.74
				5.77	7.69	1.92 ^b
7i	-OC ₆ H ₅	210 ± 20	-13.29 ± 0.24	5.48	6.55	1.06
				5.69	8.56	2.87 ^b
7k	-OC ₆ H ₄ -4'-C(CH ₃) ₃	120 ± 30	-11.75 ± 0.74	5.49	6.55	1.06
				5.66	8.83	3.17 ^b
7m	-OC ₆ H ₃ -3',5'-bis(CF ₃)	130 ± 50	-12.03 ± 1.00	5.54	6.37	0.83
				5.74	8.37	2.63 ^b
7n	-OC ₆ F ₅	80 ± 1	-10.88 ± 0.04	5.56	6.44	0.88
				5.76	8.78	3.02 ^b

^a Average values obtained using Equation 5 (Chapter 2) and three separate dilution experiments. Errors calculated from twice the standard deviation to give a 95% confidence interval ^b Resonance used in fitting process assigned to H_a hydrogen atom in Figure 2.8.

In CDCl_3 , derivatives **7** showed dimerization constant values from 36 to 309 M^{-1} ; wherein the lowest constant corresponds to the butoxy derivative **7c** (Figure 4.3); and the highest constant corresponds to the chloro derivative **7g** (Figure 4.4).

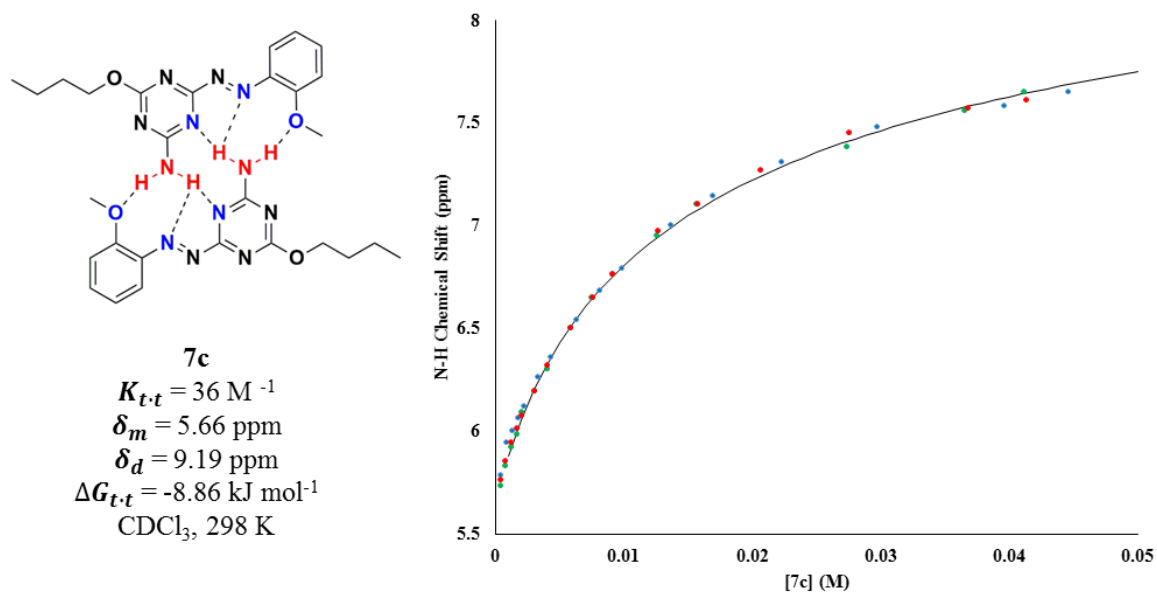


Figure 4.3 Dimerization isotherm of **7c** with $K_{t,t}$ value and free energy calculated from fitting of the data to a 1:1 dimerization model. Blue, green and red dots correspond to first, second and third separate dilution experiments, respectively. Solid line corresponds to the theoretical dilution curve obtained from the average $K_{t,t}$ of three separate dilution experiments.

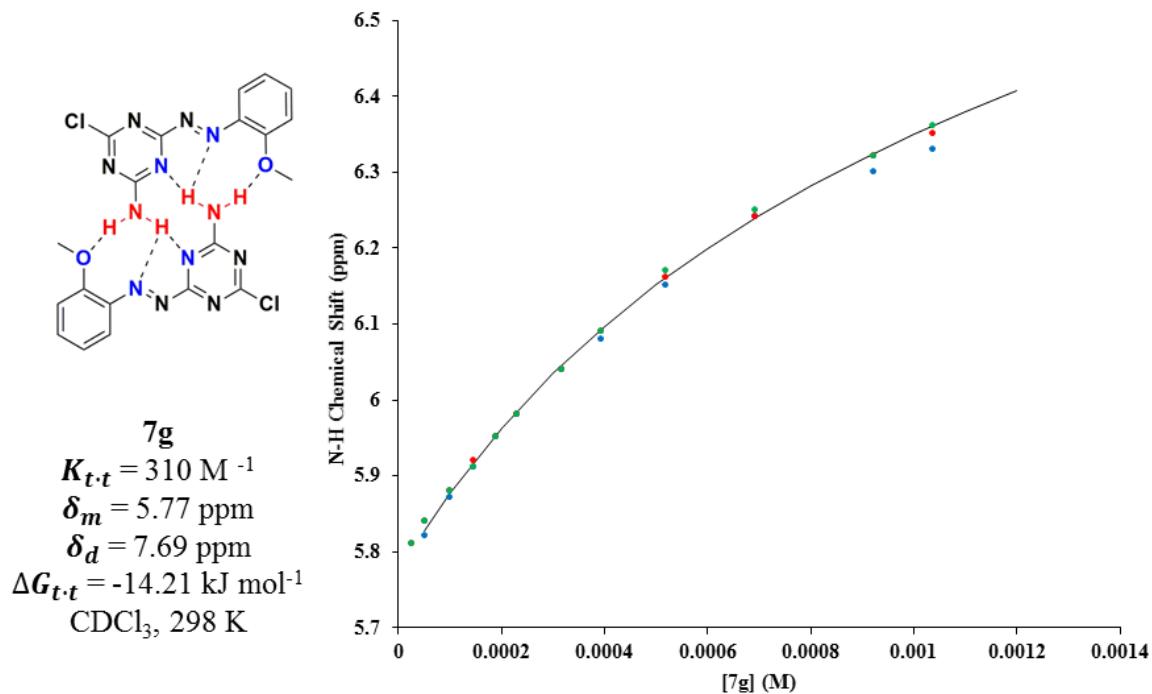


Figure 4.4 Dimerization isotherm of **7g** with $K_{t,t}$ value and free energy calculated from fitting of the data to a 1:1 dimerization model. Blue, green and red dots correspond to first, second and third separate dilution experiments, respectively. Solid line corresponds to the theoretical dilution curve obtained from the average $K_{t,t}$ of three separate dilution experiments.

When the free energy of dimerization ($\Delta G_{t,t}$) was associated with the difference between the monomer and dimer calculated chemical shift, it was observed a roughly linear relationship between these two values ($r = 0.8595$, Figure 4.5). That is, as the free energy of dimerization decreases, the difference in the chemical shift between dimer and monomer also decreases.

On the other hand, the free energies of dimerization in CDCl_3 ($\Delta G_{t,t}$) of the derivatives **7c**, **7g** and **7i** were plotted against the σ_m values for their RX moieties (Figure 4.6). To this plot it was also added the $\Delta G_{t,t}$ values of the **7f** and **7k** with approximations to the σ_m value for the hexylthiol and 4'-*tert*-butylphenoxy groups. Similarly to **4a-p**, there is a correlation ($r = -0.91784$) between these two values. Hence, as σ_m increases $\Delta G_{t,t}$

decreases. Likewise, a looser correlation between the ΔG_{t-t} values with the inductive effect contribution ($-I$) (Figure 4.7) is observed.

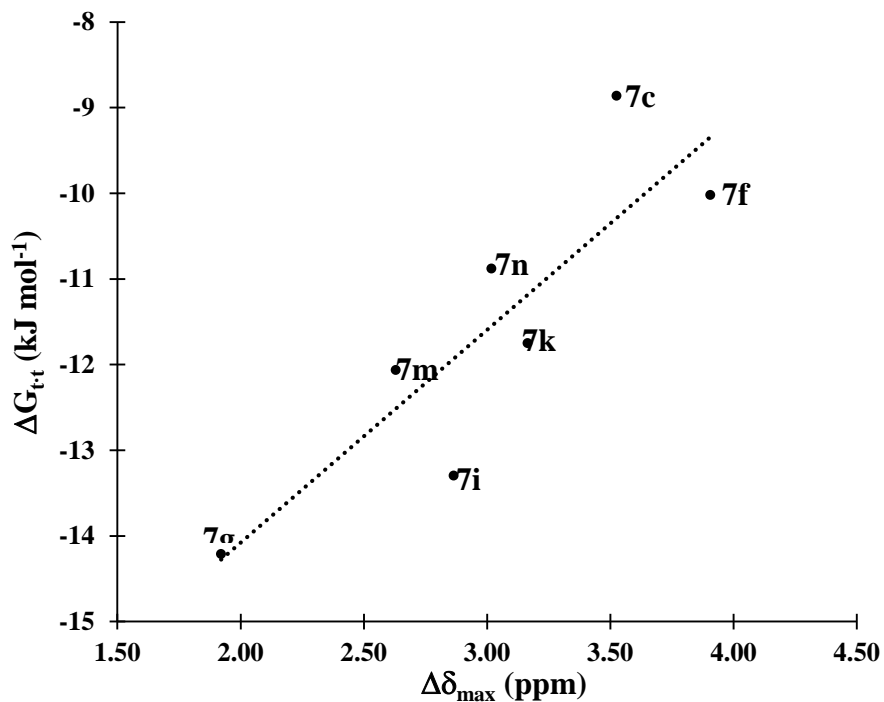


Figure 4.5 Correlation plot of $\ln(K_{t,t})$ vs $\Delta\delta_{max}$ for all derivatives **7** in $CDCl_3$ at 298 K ($r = 0.8595$).

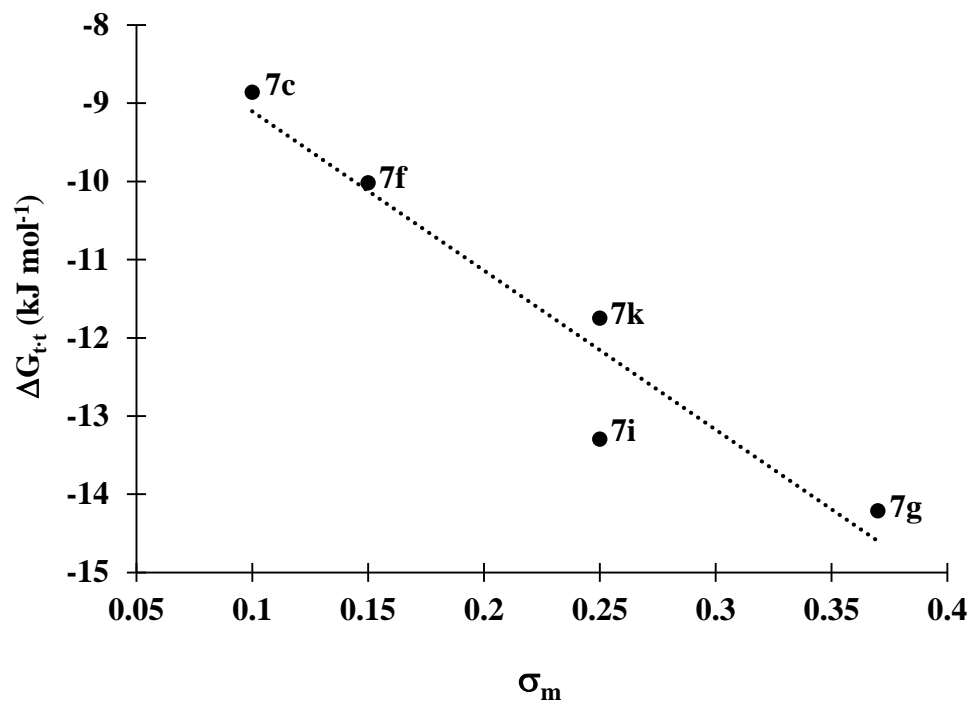


Figure 4.6 Correlation plot of $\Delta G_{t,t}$ vs σ_m of derivatives **7c**, **7f**, **7g**, **7i** and **7k** in toluene- d_8 at 298 K. Dotted line corresponds to the least squares correlation line ($r = -0.91784$).

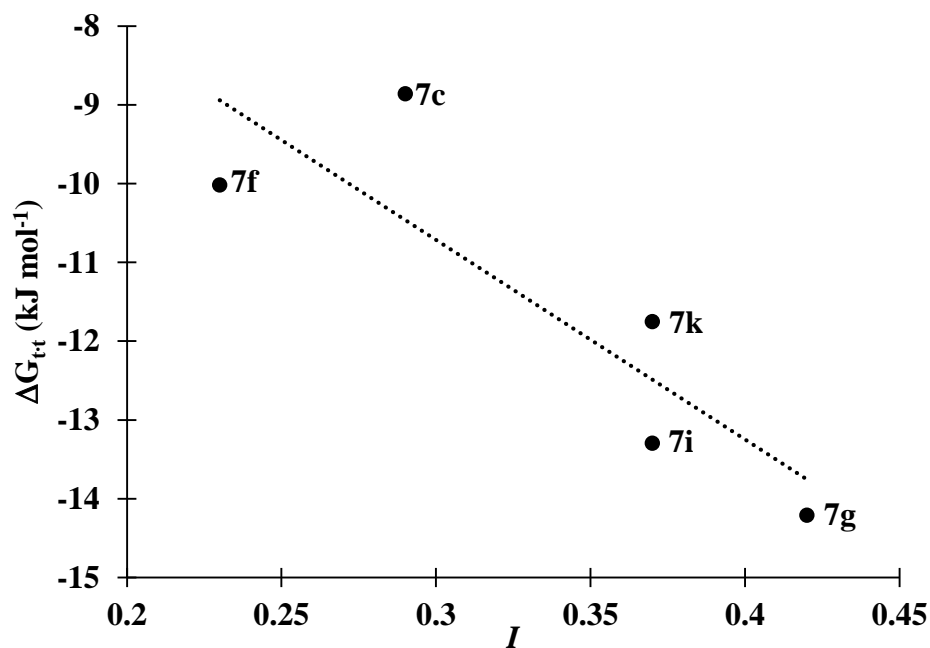


Figure 4.7 Correlation plot of $\Delta G_{t,t}$ vs I of derivatives **7c**, **7f**, **7g**, **7i**, and **7k** in $CDCl_3$ at 298 K. Dotted line corresponds to the least squares correlation line ($r = -0.86027$).

Regarding the effect of the *ortho*-methoxyphenyl acceptor, it can be observed that dimerization constants of the derivatives **7** are generally higher than those obtained for corresponding derivatives **4**. The only exception to this trend was the perfluorophenoxy derivative **7n**, whose dimerization constant is half that of perfluorophenoxy derivative **4n**. From those systems where derivatives **7** showed higher dimerization values than their derivatives **4** counterparts, dimerization free energy differences were from 0.25 kJmol⁻¹ to 3.19 kJmol⁻¹. In general, the total contribution of the *ortho*-methoxyphenyl group acceptor site to the dimer stability can be estimated through the comparison of derivatives **7c**, **7f** and **7k** with their counterparts derivatives **5** ($\Delta G_{t,t} = -4.43$ kJ mol⁻¹ for **5c**, $\Delta G_{t,t} = -3.90$ kJ mol⁻¹ for **5f**, and $\Delta G_{t,t} = -5.85$ kJ mol⁻¹ for **5k** in CDCl₃). The energetic contribution of both *ortho*-methoxyphenyl acceptor sites to the dimerization is approximately 5 kJ mol⁻¹ in CDCl₃ ($\Delta\Delta G_{\text{Butoxy}} = -4.43$ kJ mol⁻¹, $\Delta\Delta G_{\text{Hexylthiol}} = -6.12$ kJ mol⁻¹, and $\Delta\Delta G_{4\text{-tert-butylphenoxy}} = -5.90$ kJ mol⁻¹); or 2.5 kJ mol⁻¹ per *ortho*-methoxyphenyl moiety.

Alternatively, the dimerization constants obtained for derivatives **7c**, **7f** and **7n** in toluene-*d*₈ are summarized in Table 4.4. Surprisingly, the 4'-*tert*-butylphenoxy derivative **7k** was not soluble in toluene-*d*₈, contrary to its pyridyl counterpart; **4k**. As occurred for derivatives **4c**, **4f** and **4n**, **7c**, **7f** and **7n** displayed much higher dimerization constants in toluene-*d*₈ than those observed in CDCl₃. The highest dimerization constant corresponded to perfluorophenoxy derivative **7n** with a value of 5640 M⁻¹ (Figure 4.8); meanwhile, the butoxy **7c** and hexylthiol **7f** displayed dimerization constants of 2740 and 2420 M⁻¹, respectively (Figures 4.9 and 4.10).

Table 4.4 Dimerization constants, free energies of dimerization, chemical shifts of monomer (δ_m) and dimer (δ_d) species studied, and the total change in the chemical shift ($\Delta\delta_{max}$) in toluene- d_8 at 298 K.

Derivative	RX	K_{t-t} in Toluene- d_8 (M^{-1}) ^a	ΔG_{t-t} ($kJ\ mol^{-1}$)	δ_m (ppm) ^a	δ_d (ppm) ^a	$\Delta\delta_{max}$ (ppm)
7c	-O(<i>n</i> -C ₄ H ₉)	2740 ± 590	-19.62 ± 0.53	4.17	6.70	2.53 ^b
				4.10	9.64	5.54
7f	-S(<i>n</i> -C ₆ H ₁₃)	2420 ± 760	-19.30 ± 0.77	4.04	6.66	2.62 ^b
				3.86	9.71	5.85
7n	-OC ₆ F ₅	5640 ± 930	-21.40 ± 0.42	3.88	6.76	2.88 ^b
				3.75	9.69	5.94

^a Average values obtained using Equation 5 and three separate dilution experiments. Errors calculated from twice the standard deviation to give a 95% confidence interval

^b Resonance used in fitting process.

The dimerization constants obtained for derivatives **7** in toluene- d_8 at room temperature display a correlation with the electron withdrawing character of the RX substituent. Thus, the perfluorophenoxy derivative **7n** with the strongest electron withdrawing RX moiety exhibits the highest dimerization constant. Meanwhile, the hexylthiol derivative **7f** with the lowest electron withdrawing character had the lowest K_{t-t} .

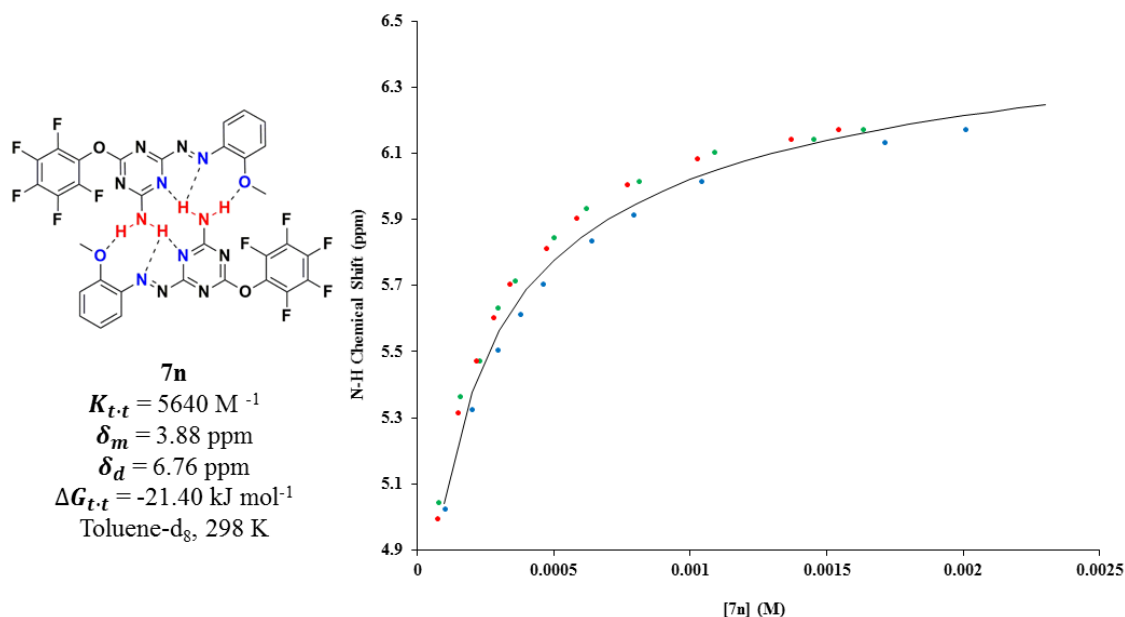


Figure 4.8 Dimerization isotherm of **7n** with $K_{t,t}$ value and free energy calculated from fitting of the data to a 1:1 dimerization model. Blue, green and red dots correspond to first, second and third separate dilution experiments, respectively. Solid line corresponds to the theoretical dilution curve obtained from the average $K_{t,t}$ of three separate dilution experiments.

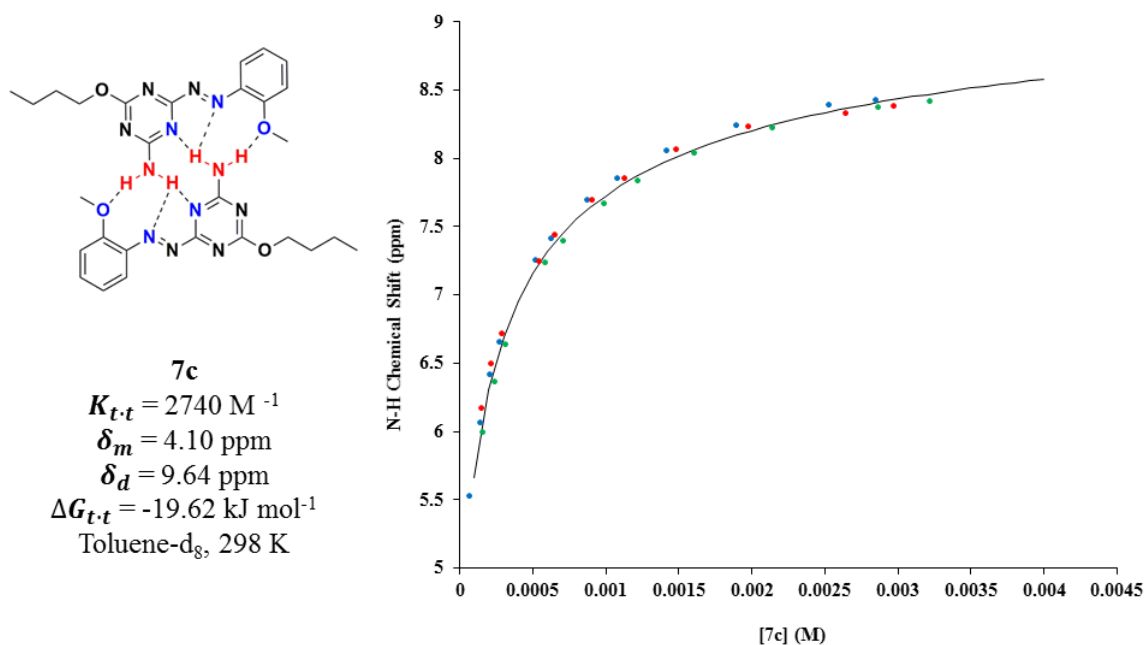


Figure 4.9 Dimerization isotherm of **7c** with $K_{t,t}$ value and free energy calculated from fitting of the data to a 1:1 dimerization model. Blue, green and red dots correspond to first, second and third separate dilution experiments, respectively. Solid line corresponds to the theoretical dilution curve obtained from the average $K_{t,t}$ of three separate dilution experiments.

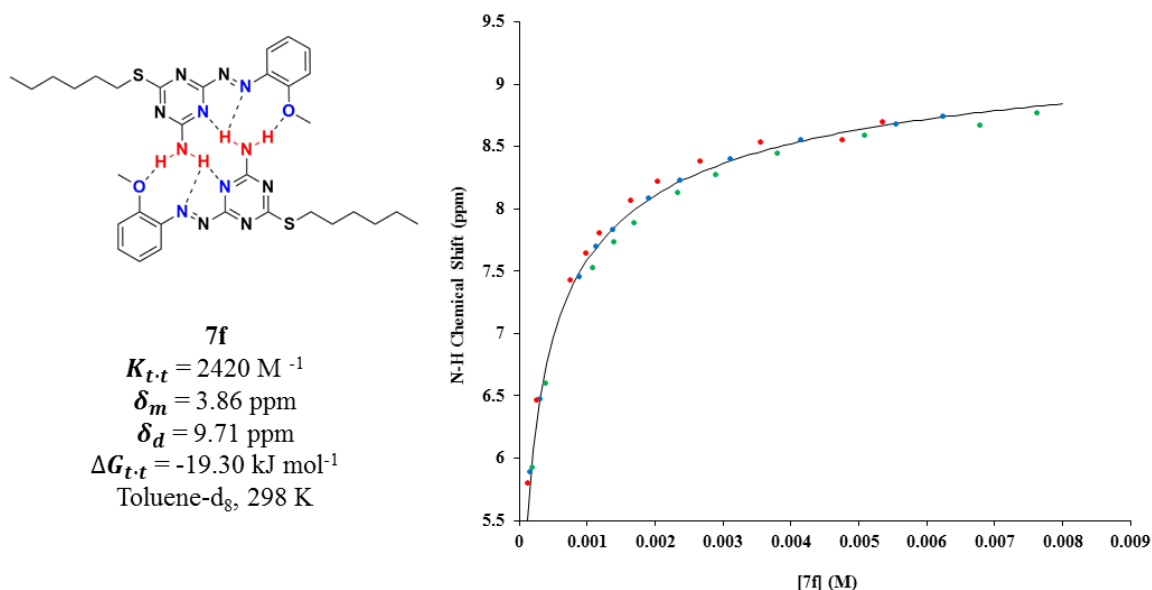


Figure 4.10 Dimerization isotherm of **7f** with K_{t-t} value and free energy calculated from fitting of the data to a 1:1 dimerization model. Blue, green and red dots correspond to first, second and third separate dilution experiments, respectively. Solid line corresponds to the theoretical dilution curve obtained from the average K_{t-t} of three separate dilution experiments.

Overall, the differences in the dimerization free energy between derivatives **7c**, **7f** and **7n** with their counterparts **4** ranged from 1.05 to 3.50 kJ mol⁻¹. Likewise, the differences in the dimerization free energy between **7c** and **7f** with the counterparts **5** ($\Delta G_{t-t} = -7.16$ kJ mol⁻¹ for **5c**, and $\Delta G_{t-t} = -8.13$ kJ mol⁻¹ for **5f** in toluene-*d*₈) are at least 11 kJ mol⁻¹ ($\Delta\Delta G_{\text{Butoxy}} = -12.46$ kJ mol⁻¹, and $\Delta\Delta G_{\text{Hexylthiol}} = -11.17$ kJ mol⁻¹). In other words, the energetic contribution to the dimer stability is approximately 11 kJ mol⁻¹ in toluene-*d*₈ when both *ortho*-methoxyphenyl moieties participate, or 5.5 kJ mol⁻¹ per acceptor site. In conclusion, the improvement over the dimer strength provided by changing the pyridine ring to an *ortho*-methoxyphenyl group is larger in toluene-*d*₈ than in CDCl₃. This is in agreement with the effect of the solvent system wherein the intermolecular interactions take place, as previously discussed (Chapter 2, Section 2.3.2).

4.2.3 X-Ray Analysis of Self-Complementary Arrays

As described in Chapter 2, single crystal X-ray diffraction was helpful to substantiate our proposed dimer structure for derivatives **7c**, **7f**, **7k** and **7n** (Table 4.5). Crystal growth was carried out by slow evaporation or slow diffusion; in a similar manner to the process outlined for derivatives **4** (Chapter 2, Section 2.3.3).

Table 4.5 Crystallographic parameters for **7c**, **7f**, **7k** and **7n** crystals.

	7c	7f	7k	7n
Chemical Formula	C ₁₄ H ₁₈ N ₆ O ₂	C ₁₆ H ₂₂ N ₆ OS	C ₂₀ H ₂₂ N ₆ O ₂	C ₁₆ H ₉ F ₅ N ₆ O ₂
Molecular Weight (g·mol ⁻¹)	302.34	346.45	378.43	412.29
Crystal System	Monoclinic	Triclinic	Monoclinic	Monoclinic
Space Group	<i>C</i> 2/ <i>c</i>	<i>P</i> $\bar{1}$	<i>P</i> 2/ <i>n</i>	<i>P</i> 2/ <i>n</i>
<i>a</i> (Å)	10.9333 (17)	8.7724 (18)	12.5420 (52)	8.6611 (16)
<i>b</i> (Å)	15.279 (2)	11.9917 (17)	11.1245 (36)	7.3759 (16)
<i>c</i> (Å)	18.203 (2)	18.233 (3)	14.175 (6)	25.874 (4)
α (°)	90	73.554 (5)	90	90
β (°)	107.366 (8)	76.971 (7)	101.2613 (15)	96.298 (11)
γ (°)	90	79.236 (7)	90	90
<i>V</i> (Å ³)	2902.1 (8)	1776.6 (5)	1939.66 (13)	1642.9 (5)
<i>Z</i>	8	4	4	4
F(000)	1280	736	800	832
<i>T</i> (K)	110	173	123	110
λ (Å)	1.54178	1.54178	0.71073	1.54178
ρ_{calc} (g·cm ⁻³)	1.384	1.295	1.296	1.667
μ (mm ⁻¹)	0.804	1.748	0.088	1.359
Reflections Collected	27839	40537	42708	33039
Unique Reflections	2529	6090	3403	2841
Absorption Correction	multi-scan	multi-scan	multi-scan	multi-scan
Refinement on	<i>F</i> ²	<i>F</i> ²	<i>F</i> ²	<i>F</i> ²
Parameters Refined	271	586	315	298
<i>R</i> (<i>F</i> _o)(<i>I</i> > 2σ(<i>I</i>))	0.0333	0.0520	0.0468	0.0471
<i>R</i> _w (<i>F</i> _o ²)(<i>I</i> > 2σ(<i>I</i>))	0.0865	0.1359	0.1180	0.1348
<i>R</i> (<i>F</i> _o)(all data)	0.0376	0.0617	0.0757	0.0536
<i>R</i> _w (<i>F</i> _o ²)(all data)	0.0902	0.1455	0.1375	0.1413
GOF on <i>F</i> ²	1.078	1.051	1.022	1.06

Butoxy derivative **7c** was crystallized by slow diffusion of dry pentane into a saturated toluene solution to yield red prisms suitable for single crystal X-ray diffraction analysis. The collected data from this analysis was solved in the $C 2/c$ space group with eight molecules per unit cell. Two symmetry related molecules take up the expected dimer configuration wherein the self-complementary array is arranged in an antiparallel manner through six hydrogen bonds (Table 4.6 and Figure 4.11). The aminotriazine rings of both monomers are coplanar and participate in a symmetry related pair of hydrogen bonds ($\text{N6-H6A}\cdots\text{N5}' = 2.93 \text{ \AA}$; $\angle\text{N-H}\cdots\text{N} = 175^\circ$) as observed for **4** in the solid state. Likewise, oblique hydrogen bond interactions between an amino N-H donor and the azo nitrogen acceptor are observed ($\text{N6-H6A}\cdots\text{N1}' = 3.12 \text{ \AA}$; $\angle\text{N-H}\cdots\text{N} = 110^\circ$). The last type of hydrogen bond present in the dimer structure corresponds to the interaction between the amino proton with the oxygen atom of the methoxy group. The intermolecular distance and angle between the interacting sites ($\text{N6-H6B}\cdots\text{O1}' = 2.88 \text{ \AA}$; $\angle\text{N-H}\cdots\text{O} = 164^\circ$) are in agreement with the anticipated improvement from the dimer structure obtained for **4** in the solid state; i.e. shorter distances and intermolecular angles closer to linearity. More specifically, in comparison with the octyloxy derivative **4d**, the intermolecular distances between the interacting sites in butoxy derivative **7c** are (generally) shorter; and, two of the three pairs of hydrogen bond interactions are less than 20° from linearity. The butoxy **7c** dimer deviates from planarity since there is an angle of 16° between the least squares planes of all heavy atoms in the triazine and phenyl rings. This angle is observed in an intramolecular and intermolecular sense since the dimer contains an inversion centre. Lastly, no other notable non-covalent interactions are observed in the extended lattice structure between dimers.

Table 4.6 Hydrogen bond distances and angles of complex **7c**·**7c** X-ray crystal structure data.

D...A	d NH...X (Å)	d NH...X (Å)	∠ NH...X (°)
N6-H6A...N5'	2.9282 (4)	2.0282 (3)	174.896 (17)
N6-H6A...N1'	3.1230 (4)	2.2836 (4)	110.043 (14)
N6-H6B...O1'	2.8792 (4)	2.0194 (3)	163.785 (16)

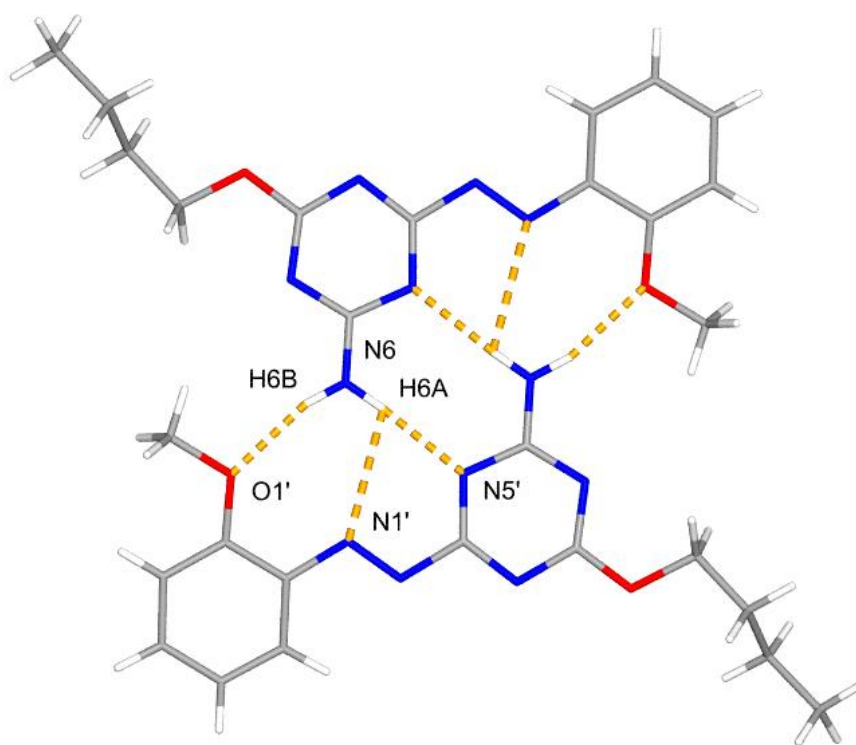


Figure 4.11 Stick representation of the X-ray crystal structure of **7c** dimer with intermolecular hydrogen bonds indicated (dashed orange lines). Blue, grey, white and red correspond to nitrogen, carbon, hydrogen and oxygen atoms, respectively.

X-ray quality crystals of hexylthiol derivative **7f** were obtained by slow diffusion of heptane into a saturated ethyl acetate solution. The crystals obtained were red prisms in space group $P\bar{1}$ with four molecules per unit cell displayed in the crystal lattice as two separate dimer structures: A-A' and B-B' (Figures 4.12 and 4.13). In each dimer structure, the monomers are related by symmetry (i.e. there is an inversion center). However, the dimers are differentiated by the dispositions of the hexylthiol groups. That is, the hexylthiol groups in dimer B-B' are disordered in comparison with dimer A-A'. The **7f** dimer structures display similar hydrogen bond interactions to those observed in the preceding **7c** dimer in the solid state; i.e. hydrogen bonds between amino N-H protons with the triazine, azo and methoxy heteroatoms (Table 4.7). Likewise, the hydrogen bond distances in **7f** dimers are alike to the hydrogen bond distances reported for the **7c** dimer in the solid state. This observation corroborates that the dimer strength of derivative **7f** is comparable to the dimer strength of **7c** as deduced from the dimerization constants obtained for the two derivatives (Section 4.2.2). Compared with the dimer structure of hexylthiol derivative **4f** in the solid state, **7f** dimers exhibit (generally) shorter intermolecular distances between donor and acceptor sites, and angles closer to linearity. The azoheteroaromatic core (i.e. without including the hexylthiol group) of both dimer structures can be considered planar since there are no deviations larger than 0.10 and 0.11 Å from the least squares planes of all the heavy atoms for dimers A-A' and B-B' respectively. In this sense, the coplanarity of both dimers is a result of the planarity of each monomer. The largest deviations from the least squares planes of all heavy atoms in the azoheteroaromatic cores are 0.09 and 0.07 Å for molecules A and B, respectively. In the extended crystal lattice, dimers are slip-stacked as layers through π - π interactions with their symmetry related dimers in the

adjacent unit cells. The angle between these layers of A-A' and B-B' dimers is 69° (Figure 4.14). In addition to the expected hydrogen bond interactions in **7f**, molecules A show C5A-H5A \cdots N3A' hydrogen bonds to the opposing edge to the **DDAAA** array, as observed in the crystal lattice of derivatives **4d** and **4f** (Figure 4.15, Table 4.7). Since in the course of the three dilution experiments of **7f** in CDCl_3 and toluene- d_8 there were no observable changes in the chemical shift corresponding to the H5A proton, it is concluded that these hydrogen bond interactions are a result of crystal packing.

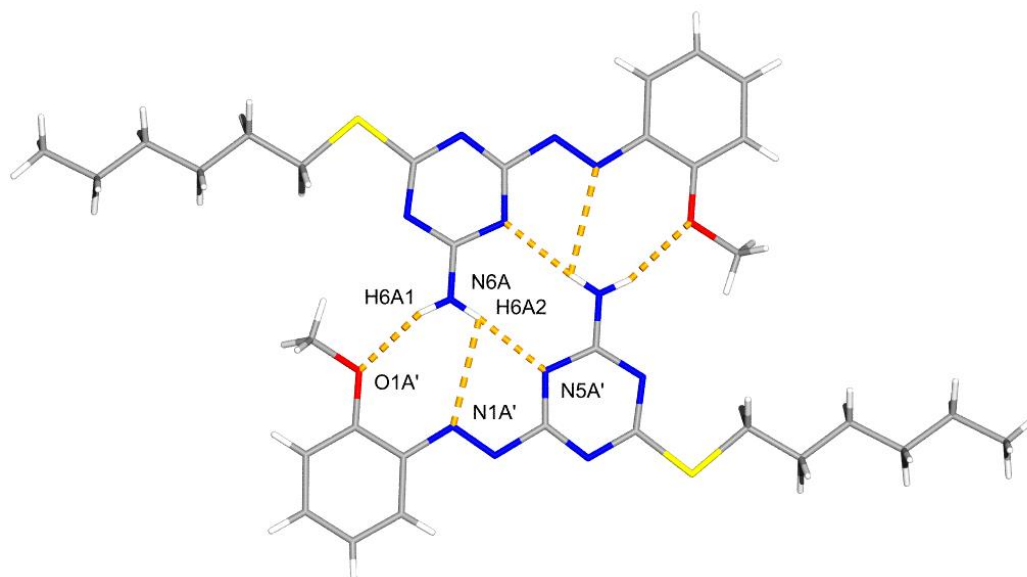


Figure 4.12 Stick representation of the X-ray crystal structure of **7f** dimer A-A' with intermolecular hydrogen bonds indicated (dashed orange lines). Blue, grey, white, red and yellow correspond to nitrogen, carbon, hydrogen, oxygen and sulfur atoms, respectively.

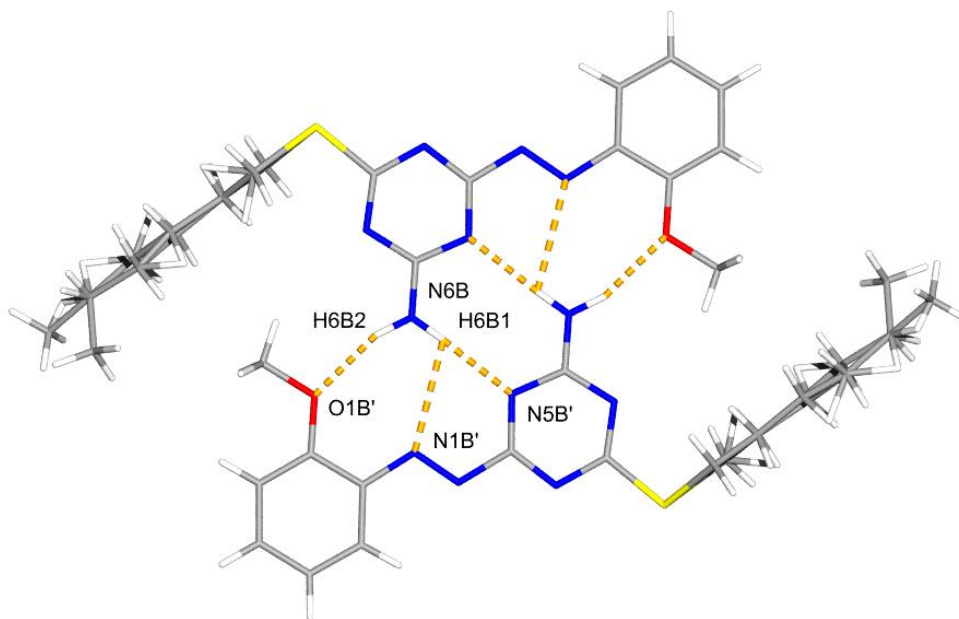


Figure 4.13 Stick representation of the X-ray crystal structure of **7f** dimer B-B' with intermolecular hydrogen bonds indicated (dashed orange lines). Blue, grey, white, red and yellow correspond to nitrogen, carbon, hydrogen, oxygen and sulfur atoms, respectively. Note: the alkyl chains are disordered.

Table 4.7 Hydrogen bond distances and angles of complex **7f·7f** X-ray from the crystal structure data.

Dimer	D...A	d YH...X (Å)	d YH...X (Å)	∠ YH...X (°)
Dimer A-A'	N6A-H6A2...N5A'	2.8966 (4)	2.0557 (3)	173.526 (17)
	N6A-H6A2...N1A'	3.0967 (4)	2.7139 (4)	109.236 (14)
	N6A-H6A1...O1A'	2.8728 (6)	2.0721 (4)	161.168 (27)
	C5A-H5A...N3A'	3.3715 (5)	2.4819 (3)	173.257 (15)
Dimer B-B'	N6B-H6B1...N5B'	2.9449 (3)	2.0431 (2)	176.753 (16)
	N6B-H6B1...N1B'	3.1489 (4)	2.7088 (4)	111.132 (13)
	N6B-H6B2...O1B'	2.9080 (5)	2.0128 (4)	158.980 (23)

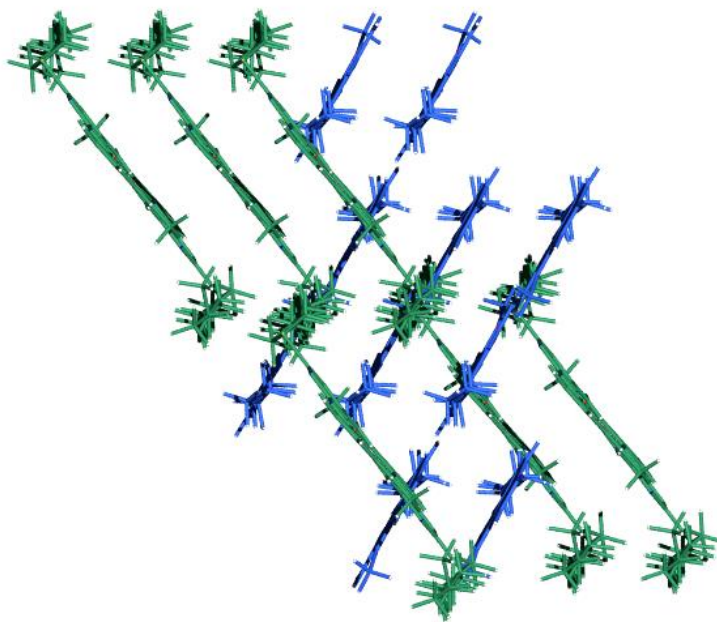


Figure 4.14 Selected molecules in the crystal lattice of **7f**. Green and blue structures correspond to dimer A-A' and dimer B-B', respectively.

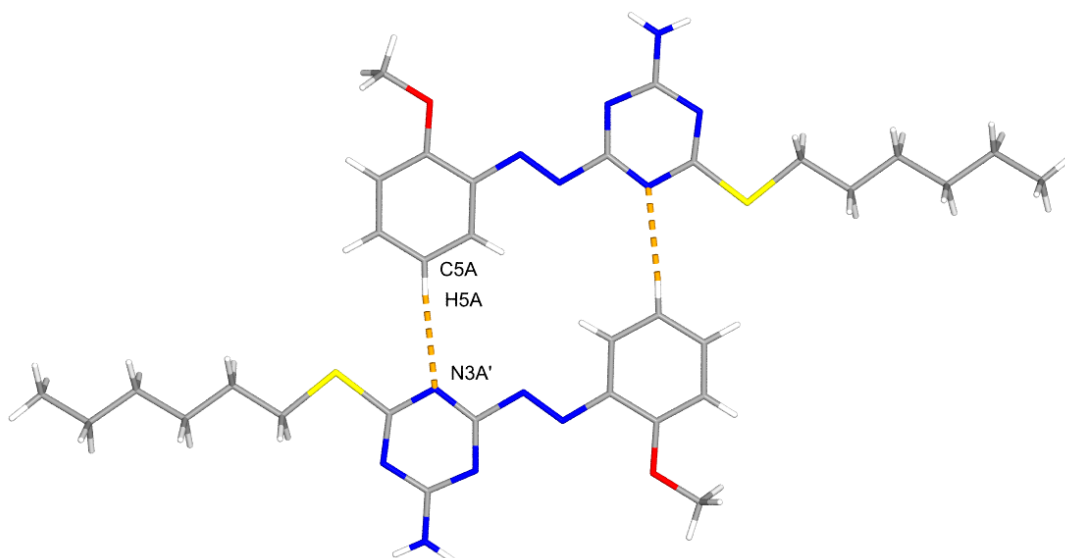


Figure 4.15 Stick representation of the X-ray crystal structure of **7f** with C-H...N interactions indicated (dashed orange lines). Blue, grey, white, red and yellow correspond to nitrogen, carbon, hydrogen, oxygen and sulfur atoms, respectively.

Single crystals from derivative **7k** were obtained by slow diffusion of heptane into a saturated solution of ethyl acetate. The red plates obtained were suitable for X-ray diffraction and were solved in the monoclinic space group $P 2/n$ with four molecules per unit cell. As observed in Figure 4.16, derivative **7k** in the solid state differs significantly from **7c** and **7f** in the sense that the molecular conformation of **7k** locates the amino group at the opposite side of the triazine ring from the methoxy group. This difference allows **7k** to form a head-to-tail infinite hydrogen bonded chains where the amino group participates in three hydrogen bond interactions with the triazine ($N6-H6B \cdots N3' = 3.00 \text{ \AA}$; $\angle N-H \cdots N = 164^\circ$), azo ($N6-H6B \cdots N1' = 3.08 \text{ \AA}$; $\angle N-H \cdots N = 109^\circ$) and methoxy ($N6-H6B \cdots O1' = 2.93 \text{ \AA}$; $\angle N-H \cdots O = 176^\circ$) acceptors from another molecule symmetry related by a screw operation. Compared with the 4'-*tert*-butylphenoxy derivative **4k**, the 4'-*tert*-butylphenoxy **7k** has (generally) shorter intermolecular distances between the heteroatoms participating in the hydrogen bond interactions. Another important characteristic of **7k** structure in the solid state is the lack of planarity of the molecule. The angle between the least squares planes of all heavy atoms in the triazine and *ortho*-methoxyphenyl rings is 44° . In addition, the least squares plane of the 4'-*tert*-butylphenyl ring is twisted 82° from the triazine ring plane. This particular twisted conformation of the **7k** molecules results in a zigzag layout in the extended lattice wherein layers are stacked through π - π interactions between the triazine and *ortho*-methoxyphenyl ring (Figure 4.17).

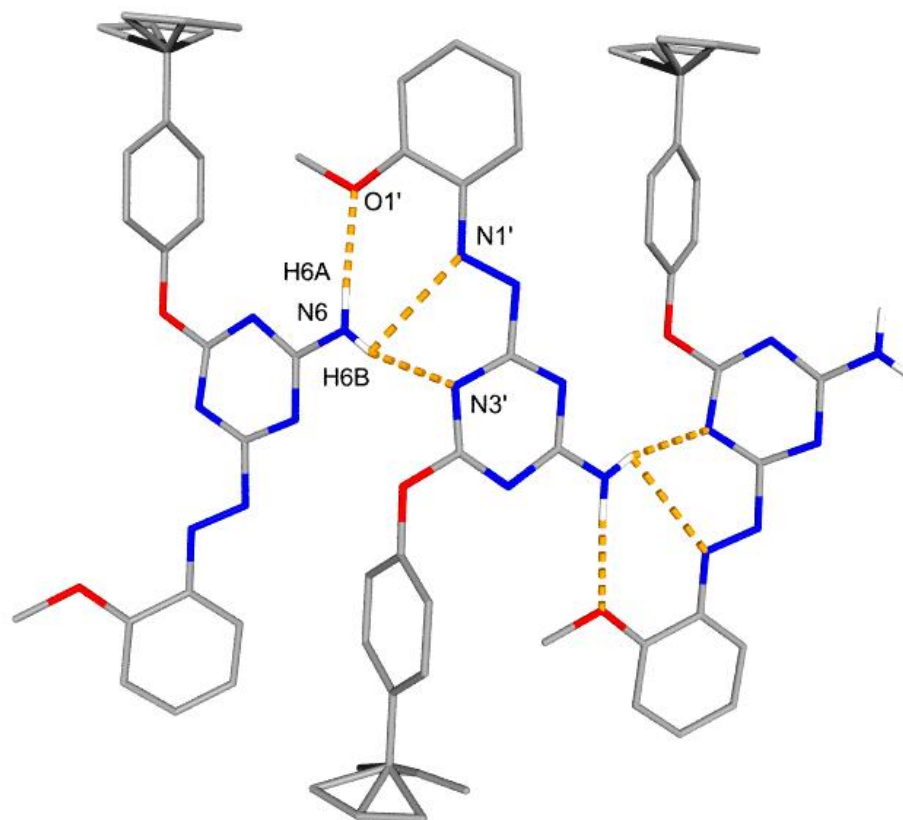


Figure 4.16 Stick representation of the X-ray crystal structure of **7k** array with intermolecular hydrogen bonds indicated (dashed orange lines). Blue, grey, white and red correspond to nitrogen, carbon, hydrogen and oxygen atoms, respectively. View perpendicular to *ab* plane. All C-H hydrogen atoms removed for clarity. Note: *tert*-butyl groups are disordered.

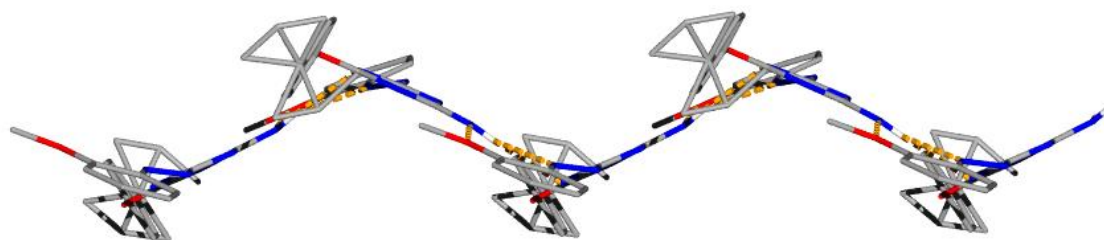


Figure 4.17 Stick representation of the X-ray crystal structure of **7k** layout with intermolecular hydrogen bonds indicated (dashed orange lines). Blue, grey, white and red correspond to nitrogen, carbon, hydrogen and oxygen atoms, respectively. View perpendicular to the *bc* plane. All C-H hydrogen atoms removed for clarity. Note: *tert*-butyl groups are disordered.

Table 4.8 Hydrogen bond distances and angles of the array **7k** X-ray from the crystal structure data.

D...A	d NH...X (Å)	d NH...X (Å)	∠ NH...X (°)
N6-H6B...N3	3.0049 (7)	2.1908 (5)	163.627 (21)
N6-H6A...N1	3.0811 (7)	2.6677 (7)	109.189 (19)
N6-H6A...O1	2.9339 (11)	2.0367 (7)	175.754 (45)

The infinite hydrogen bond chain exhibited by **7k** in the solid state raises the question of whether or not such structures are also present in solution. In this sense, it is improbable that this head-to-tail complex is present to any great extent in solution. Hydrogen bonded chains of this nature contain half of the interactions that stabilize the fully self-complementary dimer structure. Therefore, in solution such chains would be greatly out-competed by the formation of discrete dimers with all six hydrogen bonds interactions. The further association of a third molecule is thus even less likely statistically. Hence, the likelihood of an appreciable concentration of dimeric or even trimeric chain-like species can be ignored

Finally, single crystals of the perfluoro derivative **7n** were obtained by slow diffusion of diisopropyl ether into a saturated dichloromethane solution to produce red prisms suitable for X-ray analysis. The data obtained from such analysis was modeled in the monoclinic $P 2/n$ with four molecules per unit cell. Two molecules form a dimer structure with inversion symmetry, in a similar manner as described for **7c** and **7f** (Figure 4.18). The self-complementary arrays pair up in an antiparallel manner through hydrogen bonds between the amino N-H protons with the triazine (N6-H6A...N5' = 2.92 Å; ∠N-

H \cdots N = 176 $^\circ$), azo (N6-H6A \cdots N1' = 3.12 Å; \angle N-H \cdots N = 114 $^\circ$) and methoxy (N6-H6B \cdots O1' = 2.90 Å; \angle N-H \cdots O = 159 $^\circ$) acceptors. The intermolecular distances between donor and acceptor sites are within the range observed for **7c** and **7f** dimers in the solid state. The azoheterocyclic core of **7n** dimer can be considered planar since the larger deviation from least squares plane of all heavy atoms is no larger than 0.28 Å. In other words, the angle between the triazine and ortho-methoxyphenyl ring planes (least squares planes of all heavy atoms) is 7 $^\circ$ in an intramolecular and intermolecular sense. The perfluorophenoxy group of **7n** in the solid state is twisted from the triazine ring by 70 $^\circ$ (angle between least squares planes from all heavy atoms).

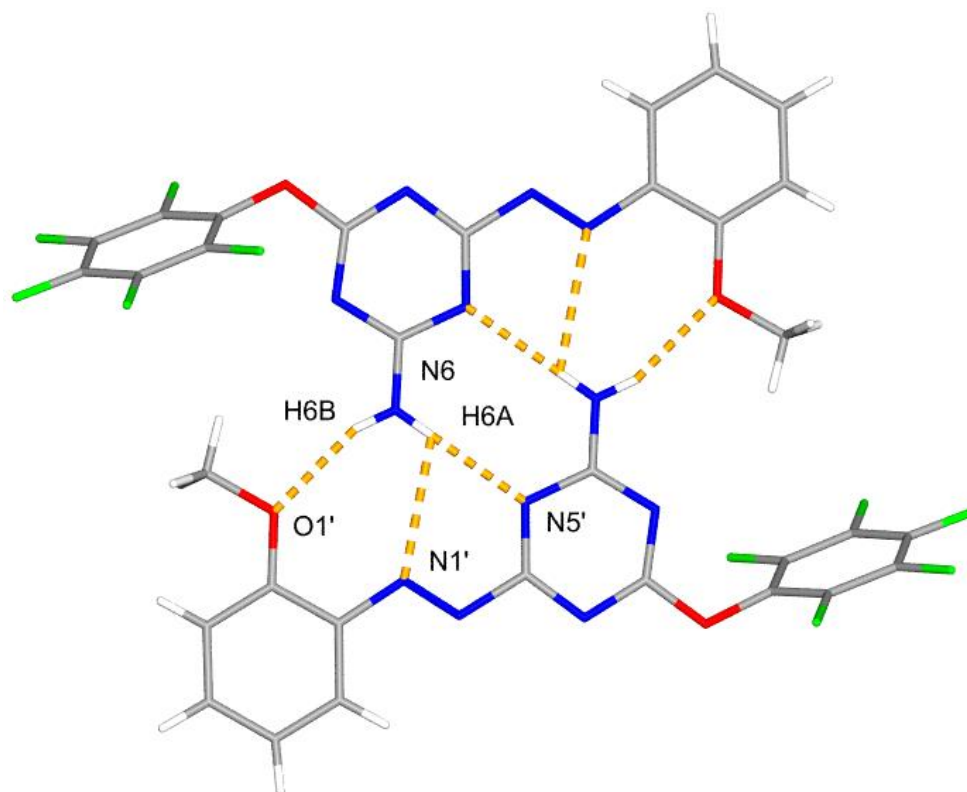


Figure 4.18 Stick representation of the X-ray crystal structure of **7n** dimer with intermolecular hydrogen bond indicated (dashed orange lines). Blue, grey, white, red and green correspond to nitrogen, carbon hydrogen oxygen and fluor atoms, respectively.

Table 4.9 Hydrogen bond distances and angles of complex **7n**·**7n** X-ray from the crystal structure data.

D...A	d <u>NH</u> ... <u>X</u> (Å)	d <u>NH</u> ... <u>X</u> (Å)	∠ NH...X (°)
N6-H6A ... N5'	2.9163 (4)	2.1058 (3)	175.540 (17)
N6-H6A ... N1'	3.1174 (5)	2.6940 (5)	114.297 (15)
N6-H6B ... O1'	2.8962 (4)	2.1236 (3)	158.768 (17)

In a summary, all the intermolecular distances and the angles between heterocyclic ring planes of derivatives **7c**, **7f**, **7k** and **7n** in the solid state are listed in Table 4.10. With the exception of **7k**, there is a correlation between the hydrogen bond distances with the dimerization constants obtained in the dilution experiments in CDCl₃; i.e. the shorter the intermolecular distances, the higher the dimerization constant in CDCl₃.

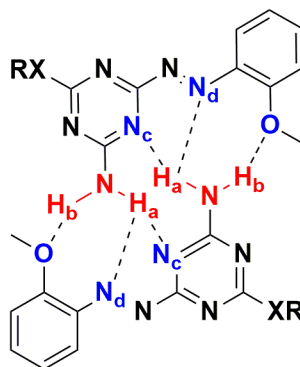


Figure 4.19 Donor and acceptor sites assignment of **7c**, **7f**, **7k** and **7n** dimers.

Table 4.10 Summary of hydrogen bond distances, intramolecular and intermolecular ring's planes angles of **7c**, **7f**, **7k** and **7n** from their crystal structure data.

Derivative	$\underline{\text{N-H}}_a \cdots \underline{\text{N}}_c$ (Å)	$\underline{\text{N-H}}_a \cdots \underline{\text{N}}_d$ (Å)	$\underline{\text{N-H}}_b \cdots \underline{\text{O}}$ (Å)	Intramolecular Ring's Planes Angle (°) ^a	Intermolecular Ring's Planes Angle (°) ^a
7c	2.9282 (4)	3.1230 (4)	2.8792 (4)	16.679	16.679
7f	2.8966 (4)	3.0967 (4)	2.8728 (6)	4.118	4.118
	2.9449 (3)	3.1489 (4)	2.9080 (5)	4.655	4.655
	2.9208 ^b	3.1228 ^b	2.8904 ^b	4.3865 ^b	4.3865 ^b
7k	3.0049 (7)	3.0811 (7)	2.9339 (11)	43.578 (12)	8.336 (16)
7n	2.9163 (4)	3.1174 (5)	2.8962 (4)	7.461	7.461

^a Angle between least squares triazine and pyridine ring planes, ^b Average values from all dimers present in the crystal structure

On the other hand, comparing derivatives **7** with **4** in the solid state, it can be noted that by changing the pyridine ring to *ortho*-methoxyphenyl the intermolecular distances between monomers were shortened. In this sense, intermolecular distances between the amino group and the methoxy acceptor site in derivatives **7** were at least 0.30 Å shorter than those observed between the amino group and the pyridine acceptor site in derivatives **4**. In addition, the position of the methoxy group was more closely aligned with the N-H bond of the amino group and the hydrogen bond interaction is closer to linearity. Besides the improvement in the proximity of these binding sites, the intermolecular distances of the amino group to the triazine acceptor site were reduced by at least 0.10 Å. A good example of all these observations can be seen comparing hexylthiol derivatives **4f** and **7f** (Table 4.11).

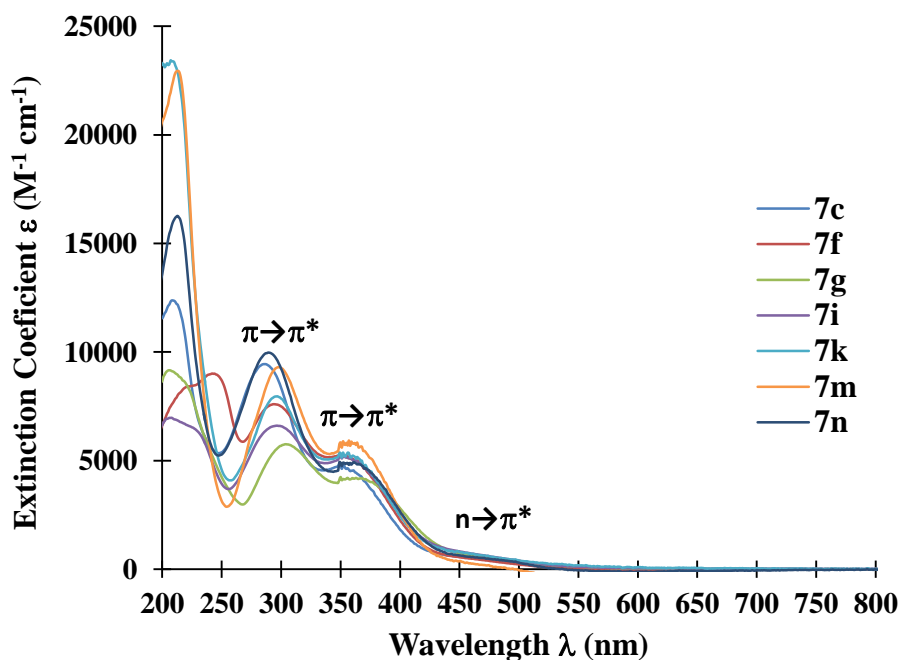
Table 4.11 Comparison of intermolecular distances in **4f** and **7f** dimer structures in the solid state.

D...A	d NH...X (Å)		d NH...X (Å)		∠ NH...X (°)	
	4f dimer	7f dimer ^b	4f dimer	7f dimer ^b	4f dimer	7f dimer ^b
N-H...N(triazine)	3.1500 (3)	2.9208	2.2848 (2)	2.0494	177.961 (10)	175.140
N-H...N(azo)	2.9500 (4)	3.1228	2.4723 (3)	2.7114	115.468 (6)	110.184
N-H...X ^a	3.2831 (3)	2.8904	2.5905 (3)	2.0424	137.388 (8)	160.074

^a **4f**: X = N(pyridine), **7b**: X = O (methoxy). ^b Average values from all dimers present in the crystal structure.

4.2.4 UV-Vis Characterization

The absorption spectra of **7** in their thermally stable *trans*-isomeric form (i.e. (*t*)-**7**) were obtained from 10⁻⁵ to 10⁻⁴ M acetonitrile solutions at room temperature (Figure 4.20).

**Figure 4.20** Normalized UV-Vis Absorption Spectra of derivatives (*t*)-**7** in acetonitrile at 298 K.

At first sight, the UV-Vis spectra of derivatives **7** is characterized by two prominent absorption bands, at wavelengths lower than 400 nm. This observation is in accordance with the literature that reports the 2,2'-dimethoxyazobenzene's UV-Vis spectrum has two $\pi \rightarrow \pi^*$ absorption bands at 310 and 366 nm.⁸ Similarly to derivatives **4a-p**, the $\pi \rightarrow \pi^*$ absorption bands of derivatives **7** are slightly shifted to lower wavelengths (hypsochromic shift). On the other hand, the $n \rightarrow \pi$ absorption bands of the 2,2'-dimethoxyazobenzene is located at 454 nm. In the case of the UV-Vis spectra of **7**, this band was difficult to identify since it blends with the base of a $\pi \rightarrow \pi^*$ band. Nevertheless, the UV-Vis absorption profiles of the derivatives **7** is in accordance with the expected UV-Vis spectrum of azobenzene containing compounds.

Table 4.12 Characteristic $n \rightarrow \pi^*$ and $\pi \rightarrow \pi^*$ transition bands of derivatives (*t*)-**7** from UV-Vis spectroscopy in acetonitrile at 298 K.

Derivative	RX	$n \rightarrow \pi^*$ Transition		$\pi \rightarrow \pi^*$ Transition	
		λ_{\max} (nm)	ϵ ($M^{-1} \text{ cm}^{-1}$)	λ_{\max} (nm)	ϵ ($M^{-1} \text{ cm}^{-1}$)
(t)-7c	<i>n</i> -butoxy	486	347	349	4880
				286	9440
(t)-7f	hexylthio	496	242	349	5290
				294	7600
(t)-7g	chloro	481	498	363	4200
				304	5760
(t)-7i	phenoxy	484	520	350	5220
				296	6610
(t)-7k	4'- <i>tert</i> -butylphenoxy	450	783	352	5370
				297	7960
(t)-7m	3,5-bis(trifluoromethyl)phenoxy	494	25	357	5930
				298	9300
(t)-7n	perfluorophenoxy	478	453	361	4930
				289	9980

Additionally, the UV-Vis spectrum of the *cis*-isomer of the derivative **7c** ((*c*)-**7c**) in acetonitrile was obtained (Figure 4.21). As expected, the UV-Vis spectrum of the *cis*-isomeric forms display $\pi \rightarrow \pi^*$ absorption bands with lower absorptivities in comparison with the *trans*-isomer UV-Vis spectrum. Meanwhile, the $n \rightarrow \pi^*$ band of the *cis*-isomer show slightly higher absorptivities than those observed in the *trans*-isomer. The thermal reversions of the *cis*-isomer of derivative **7c** to its *trans*-isomeric form was monitored recording the UV-Vis spectra until all derivative **7c** was in solution as a *trans*-isomer. Two isosbestic points were identified at 262 and 427 nm ($\epsilon = 3193$ and $585 \text{ M}^{-1} \text{ cm}^{-1}$, respectively).

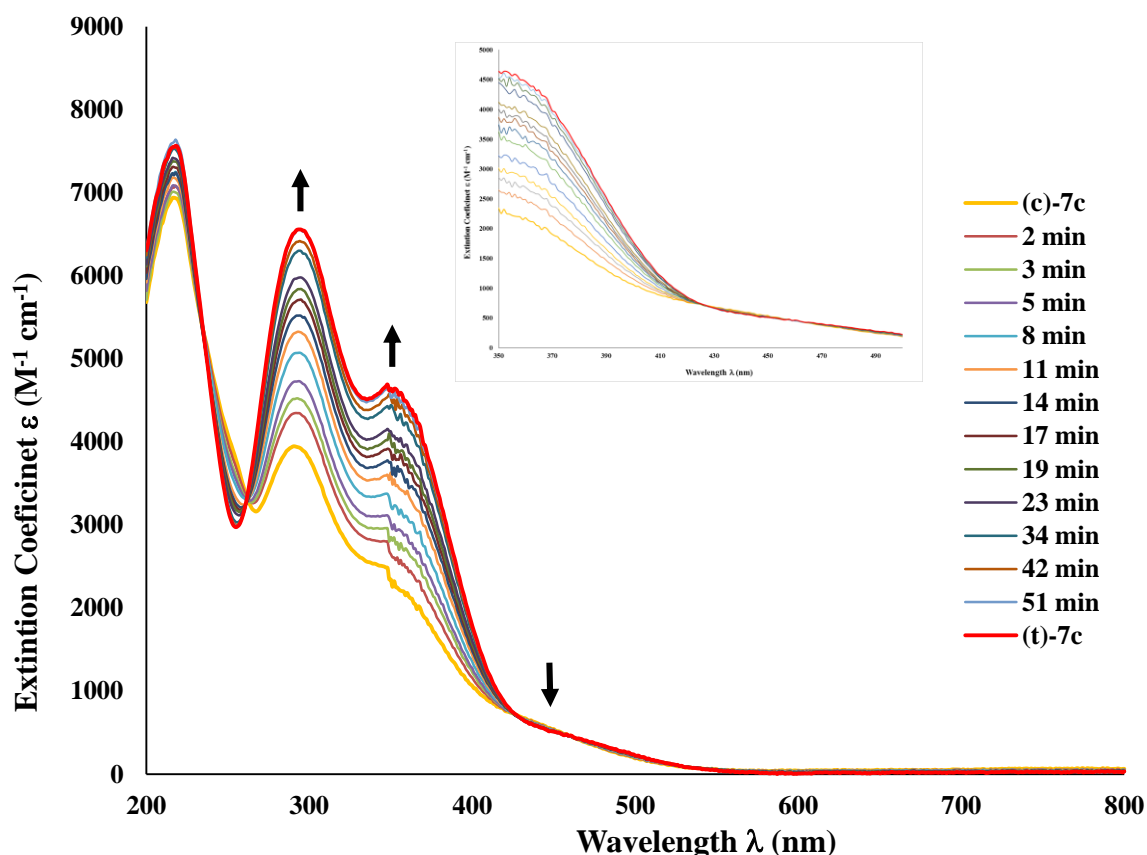


Figure 4.21 UV-Vis absorption spectra of (*c*)-**7c** and its thermal reversion to (*t*)-**7c** in acetonitrile at 298 K (**7c** total concentration = $1.26 \times 10^{-4} \text{ M}$). Inset figure: isosbestic point at 427 nm.

Table 4.13 Characteristic $n \rightarrow \pi^*$ and $\pi \rightarrow \pi^*$ transition bands of derivative (c)-7c from UV-Vis spectroscopy in acetonitrile at 298 K.

Compound	RX	$n \rightarrow \pi^*$ Transition		$\pi \rightarrow \pi^*$ Transition		Isosbestic Point	
		λ_{\max} (nm)	ϵ ($M^{-1} \text{ cm}^{-1}$)	λ_{\max} (nm)	ϵ ($M^{-1} \text{ cm}^{-1}$)	λ (nm)	ϵ ($M^{-1} \text{ cm}^{-1}$)
(c)-7c	<i>n</i> -butoxy	445	456	348	2362	427	585
				291	3828	262	3190

4.2.5 Photoisomerization Trans to Cis

The photoisomerization of the *trans* isomeric forms of derivatives **7** were carried out. The experiment conditions were the same ones employed during the photoisomerization of derivatives (*t*)-**4a-p**; i.e. UV light centered at 360 nm and three different solvent systems (CDCl_3 , toluene- d_8 and CD_3CN). Similarly to derivatives **4a-p**, the *cis*-isomers of derivatives **7** are differentiated from their *trans*-isomeric form by a new set of signals in the ^1H NMR spectrum located upfield (Figures 4.22 and 4.23). This upfield shift is in agreement with the location of most of the phenyl hydrogen atoms in the shielding cone of the triazine ring.

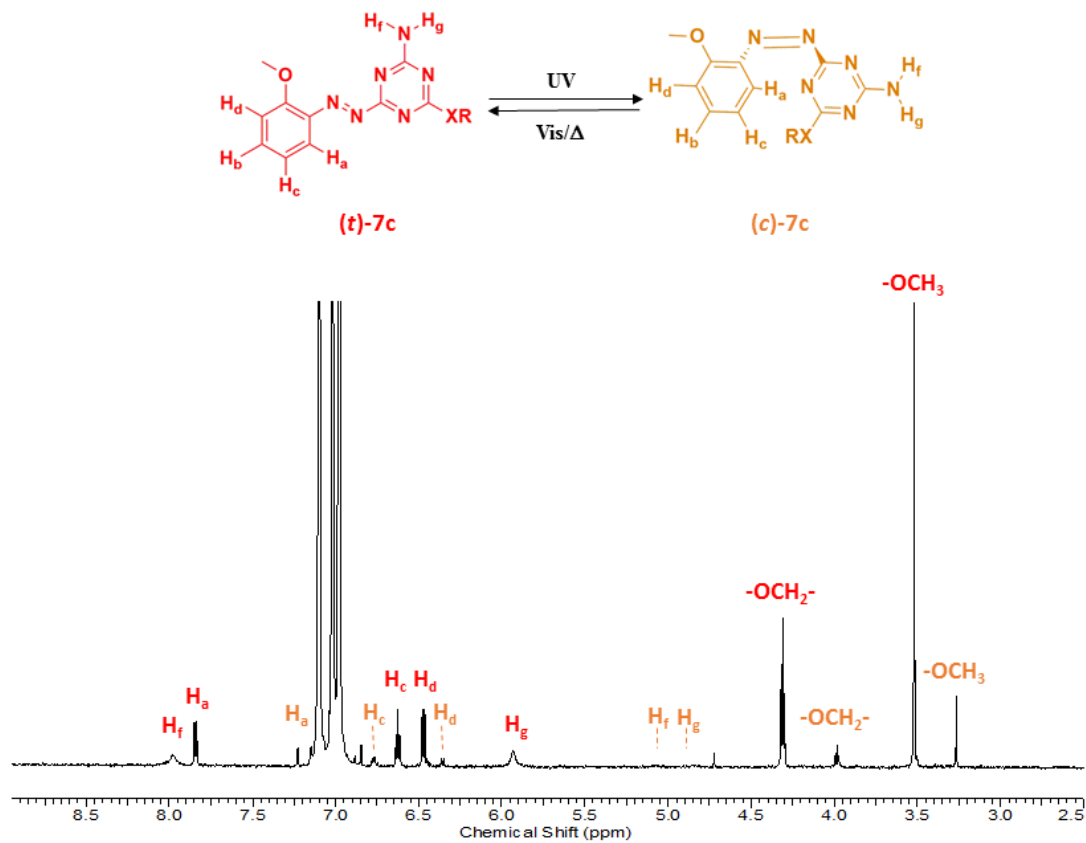


Figure 4.22 ^1H NMR spectra displaying derivative **7c** at PSS in toluene- d_8 at 298 K. RX = *n*-butoxy.

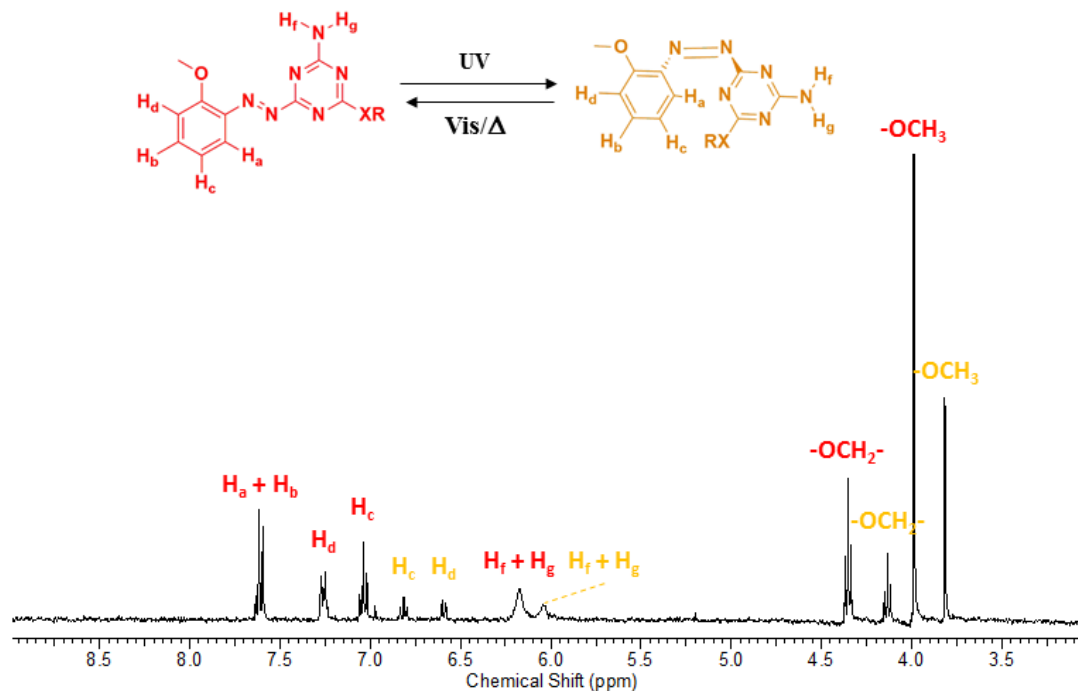


Figure 4.23 ^1H NMR spectra displaying derivative **7c** at PSS in toluene- d_8 at 298 K. RX = *n*-butoxy.

The *trans*- to *cis*- interconversion yields for derivatives **7** were calculated from the *cis/trans* integration ratio of the methoxy moiety. Table 4.14 shows the *trans*- to *cis*- interconversion yields. It is important to note that contrary to derivatives **4a-p**, the photoisomerization of (*t*)-**7** in CDCl_3 solution did not take place since the ^1H NMR spectrum of all (*t*)-**7** tested in this solvent did not change after continuous irradiation of UV light for a period of up to 3 h. On the other hand, from the three derivatives **7** soluble in toluene- d_8 (butoxy **7c**, hexylthiol **7f** and perfluorophenoxy **7n**) the butoxy derivative **7c** was the only one that showed *trans*- to *cis*- interconversion with 26% yield. This interconversion yield is slightly higher than that reported for the butoxy derivative **4c** in toluene- d_8 (22% yield). Lastly, with the exception of the chloro derivative **7g**, all derivatives **7** dissolved in CD_3CN exhibited photochromism with *trans*- to *cis*-

interconversion yields from 7 to 32 % yield. The lowest photoisomerization yield corresponded to the perfluorophenoxy derivative **7n**; and, the highest yield corresponded to the *n*-butoxy derivative **7c**. Overall, the photoisomerization yields obtained in CD₃CN for **7** were comparable to the yields observed for **4** in the same solvent system.

Table 4.14 *Trans* to *cis* interconversion yields at PSS after irradiation with UV Light (360 nm) at 298 K.

Derivative	RX	<i>trans</i> to <i>cis</i> conversion in CDCl ₃ (%)	<i>trans</i> to <i>cis</i> conversion in Toluene- <i>d</i> ₈ (%)	<i>trans</i> to <i>cis</i> conversion in CD ₃ CN (%)
7c	<i>n</i> -butoxy	0	26	32
7f	Hexylthio	0	0	26
7g	Chloro	0	-	0
7i	Phenoxy	0	-	15
7k	4'- <i>tert</i> -butylphenoxy	0	-	21
7m	3',5'-bis(trifluoromethyl)phenoxy	0	-	24
7n	Perfluorophenoxy	0	0	7

- Compound not soluble in the solvent system used.

The response of derivatives **7** to alternating light stimuli was tested through a photodegradation experiment similar to that described in Chapter 3 (Section 3.2.2, Figure 3.7). A toluene-*d*₈ solution of **7c** ($[7c] = 9.11 \times 10^{-4}$ M) was exposed to UV light (centered at 360 nm for 1h) and visible light ($\lambda > 400$ nm for 10 min) in an alternate manner. After each UV/Vis light irradiation, a ¹H NMR spectrum was acquired to confirm the presence or absence of *cis*-isomer and to record the N-H chemical shift of the *trans*-isomer. Once 5 cycles of UV/Vis light irradiation were completed, the sample was exposed to natural light

at room temperature for 72 h to latter record a last ^1H NMR spectrum (*cis*- to *trans*- thermal reversion, Figure 4.24). The average response after UV light irradiation for **7c** was an N-H chemical shift at 5.61 ppm; meanwhile, the average response after visible light irradiation was 5.66 ppm. In both cases, deviations from the average value were no larger than 0.01 ppm. In a similar manner as observed in the photodegradation experiment of **4c**, the ^1H NMR spectrum of **7c** after thermal reversion showed an amino proton chemical shift lower than the chemical shift prior the experiment. Likewise, no traces of *cis*-isomer or side product(s) were observed in the last spectrum. The last chemical shift observed corresponds to a **7c** solution which concentration decreased by 11% (i.e. 9.80×10^{-5} M). This difference falls in the limit of the NMR spectrometer resolution.

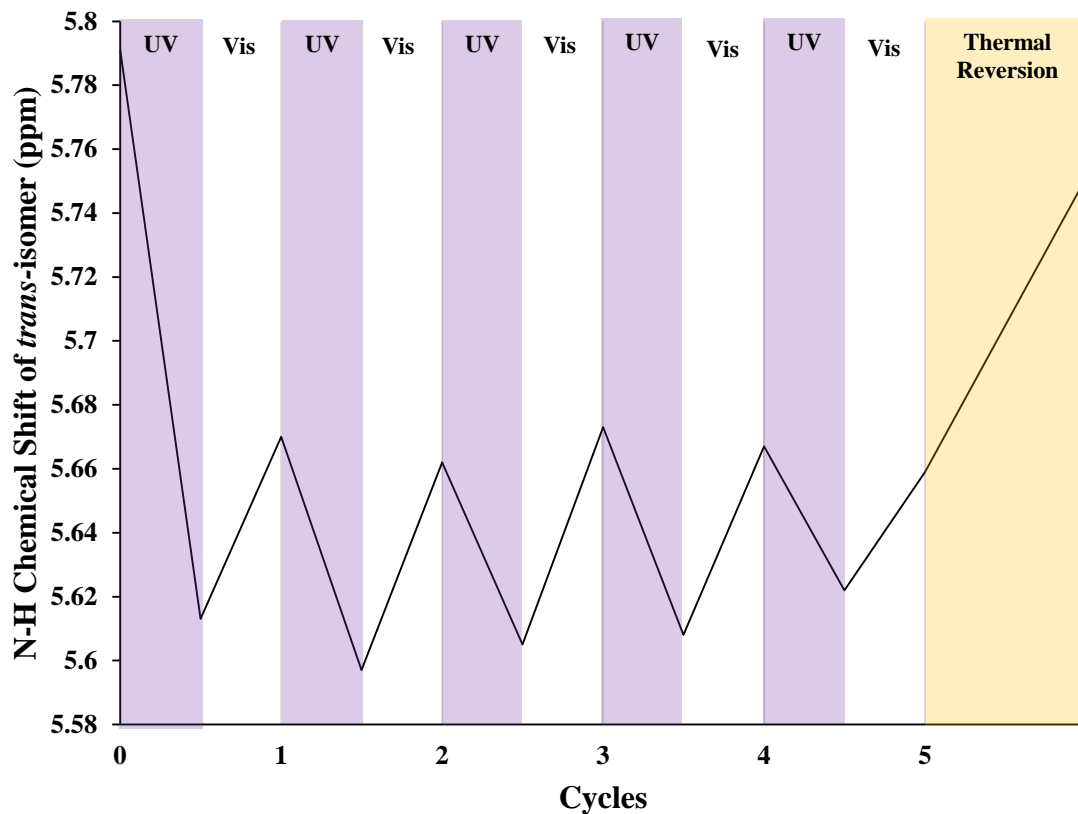


Figure 4.24 Cyclization plot of **7c** ($[7c] = 9.11 \times 10^{-4} \text{ M}$). Purple areas correspond to the N-H chemical shift change after UV light irradiation (centered at 360 nm for 1h). White areas correspond to the N-H chemical shift change after visible light irradiation ($\lambda > 400$ nm for 10 minutes). Yellow area correspond to the N-H chemical shift observed after thermal reversion of the solution over 72h.

4.2.6 Complexation Constants in Solution After Photoisomerization

Once the photophysical properties of the derivatives **7** were evaluated (UV-Vis absorption spectra and *trans*- to *cis*- interconversion yields at the photostationary state) we turned to the study of the complex equilibria after photoisomerization takes place. In this sense, we recall all the possible monomers and dimers in solution once (*c*)-**7** is present (Figure 4.25).

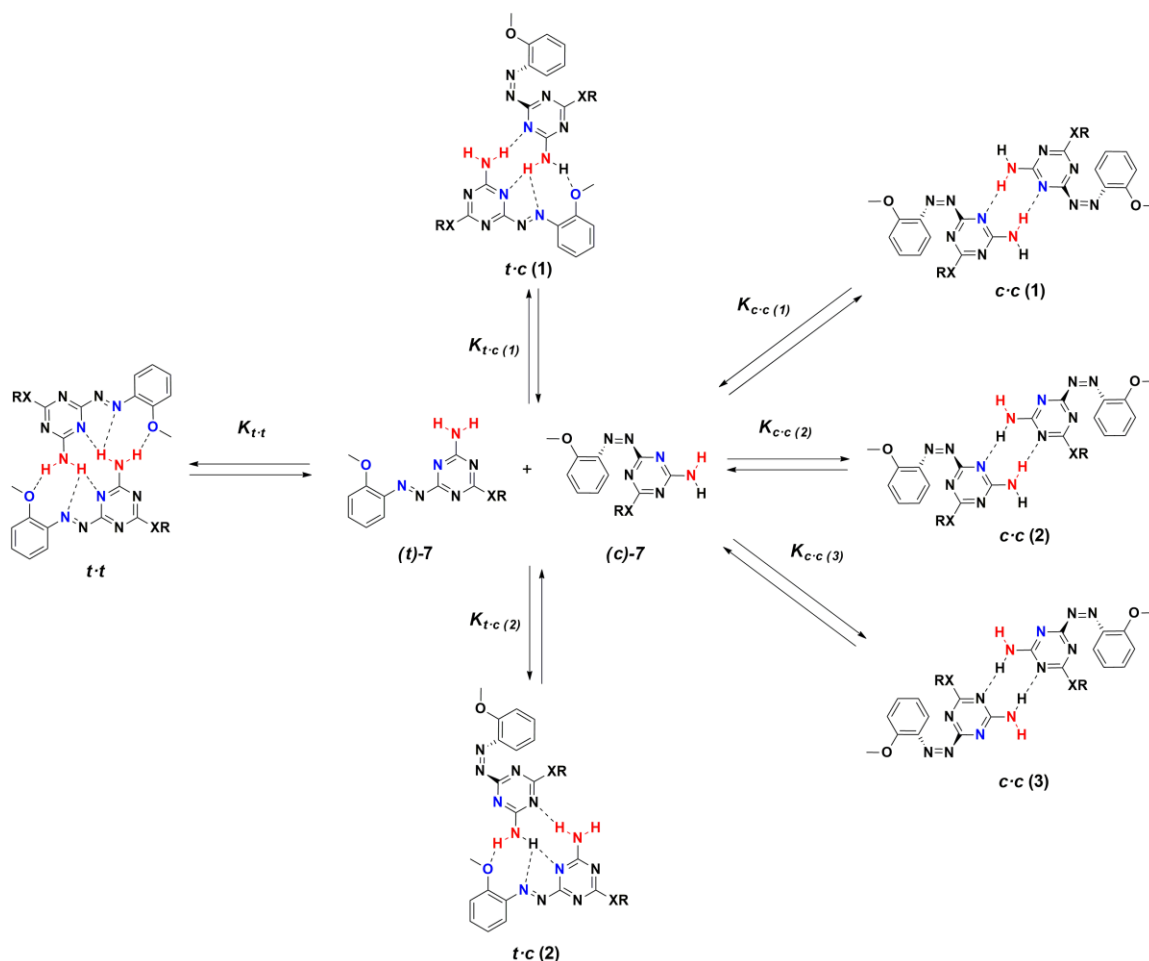


Figure 4.25 Hypothetical complexation equilibria present in mixed *cis/trans* solutions of derivatives **7** in non-polar solvents.

In the same way as **4a-p**, a *cis/trans* mixture of **7** in solution is prone to organize into different dimer structures. The *trans*-isomer was conceived to show one (and only one) stable dimer structure (*t-t* dimer in Figure 4.25). However, once photoisomerization occurs the exclusion of two hydrogen bond acceptors provides to the *cis*-isomer two triazine ring edges with an **AD** array (*(c)-7* in Figure 4.25). This particularity brings the possibility of more than one structural arrangement for the *cis-cis* dimer and the *trans-cis* complex. It is not possible to determine which of all *cis-cis* dimer and *trans-cis* complex structures are the most energetically favored. Neither is it possible to isolate the contribution of all equilibria to the composite *cis-cis* dimerization constant (K_{c-c}) and *trans-cis* complexation constant (K_{t-c}).

Based on the similarities with the **4a-p** derivatives, we decided to employ the mathematical model described in Chapter 3 (Section 3.2.3). Again we presume that the *cis-cis* dimerization constants for **7** are no greater than the dimerization constant of their counterpart derivatives **5**. Moving on to the sole soluble and photoswitchable example, butoxy derivative **7c** has a free energy of *trans-trans* dimerization in toluene- d_8 at room temperature of $-19.62 \text{ kJ mol}^{-1}$, meanwhile the butoxy derivative **5c** has a free energy of dimerization in toluene- d_8 of $-7.16 \text{ kJ mol}^{-1}$. The difference between both equilibria is large enough (at least 12 kJ mol^{-1}) to discard the *cis-cis* dimer contribution to the distribution of the total concentration of *cis*-isomer in solution at the concentrations we are examining.

Up to this point, it was assumed that the assessment method for the *trans-cis* complexation constant (K_{t-c}) for **7** would be similar to that employed for **4a-p**. However,

7 exhibited a significant difference that forced us to perform the reversion experiments in a different way than that settled for **4a-p**. This difference was the *cis*- to *trans*- thermal reversions observed for derivatives **7** in toluene-*d*₈ solution were approximately 10 fold faster than **4a-c** (Sections 3.2.4 and 4.2.7). A more detailed discussion with the corresponding constant values of the *cis*- to *trans*- thermal reversion rate are part of the following section; however, it is important to outline that the reversion rate of **7** (more specifically **7c**) did not allow us to obtain enough data for a reliable estimation of $K_{t.c}$. To overcome this inconvenience, it was necessary to carry out the reversion experiments at lower temperature since the reversion rate is thermally dependent.⁹ This strategy required the determination of the *trans-trans* dimerization constant at the same temperature that the reversion experiments would be performed. The chosen temperature to carry out the dilution and reversion experiments was -10 °C (or 263 K, Figure 4.26). The butoxy derivative **7c** was the only derivative examined as it was the only one to switch in toluene-*d*₈.

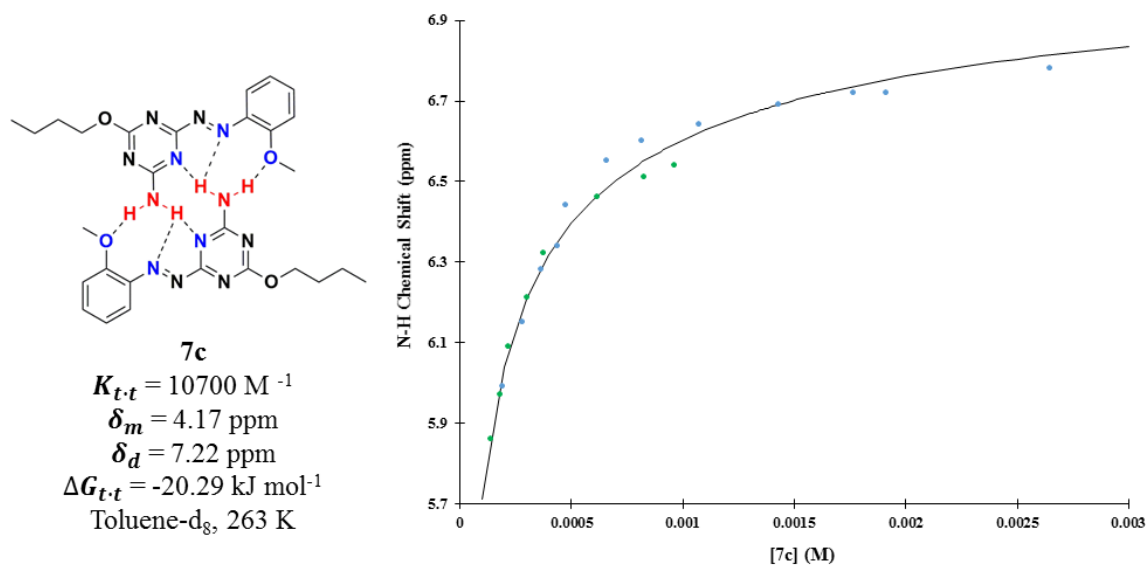


Figure 4.26 Dimerization isotherm of **7c** with K_{t-t} value and free energy calculated from fitting of the data to a 1:1 dimerization model. Blue and green dots correspond to first and second separate dilution experiments, respectively. Solid line corresponds to the theoretical dilution curve obtained from the average K_{t-t} of two separate dilution experiments.

Once the dimerization constant and the chemical shift values of derivative **7c** as monomer and dimer in toluene- d_8 solution at $-10 \text{ }^\circ\text{C}$ were determined, we performed reversion experiments. For this purpose we were able to isolate derivative **7c** as approximately 50% *cis*-isomer in the solid state. This way, a freshly prepared *cis/trans* **7c** solution was submitted to ^1H NMR spectroscopy at $-10 \text{ }^\circ\text{C}$ to record the chemical shift of the amino protons, as well as the *cis/trans* ratio in solution as the thermal reversion was taking place (Figure 4.27). As expected, the thermal reversion rate at $-10 \text{ }^\circ\text{C}$ was lower than at room temperature ($25 \text{ }^\circ\text{C}$); therefore, we were able to obtain a large enough number of data points to employ in the K_{t-c} calculation (Figure 4.28).

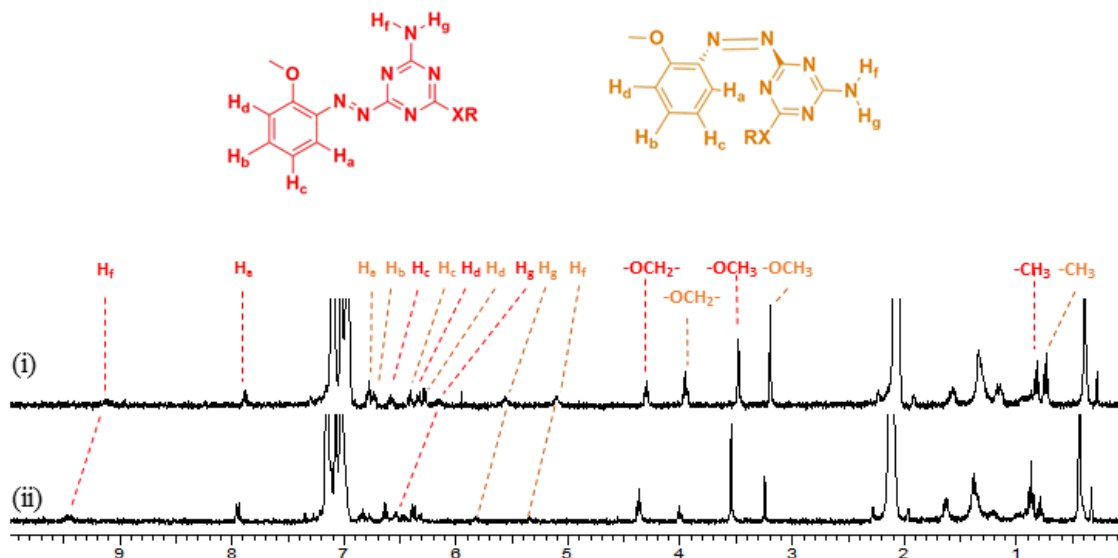


Figure 4.27 ^1H NMR spectra displaying the concentration-dependent behavior of **7c** in toluene- d_8 at 263 K. Total concentration $[\mathbf{7c}] = 5.84 \times 10^{-3}$ M, (i) $[c]_0/[t]_0 = 1.11$ (ii) $[c]_0/[t]_0 = 0.33$.

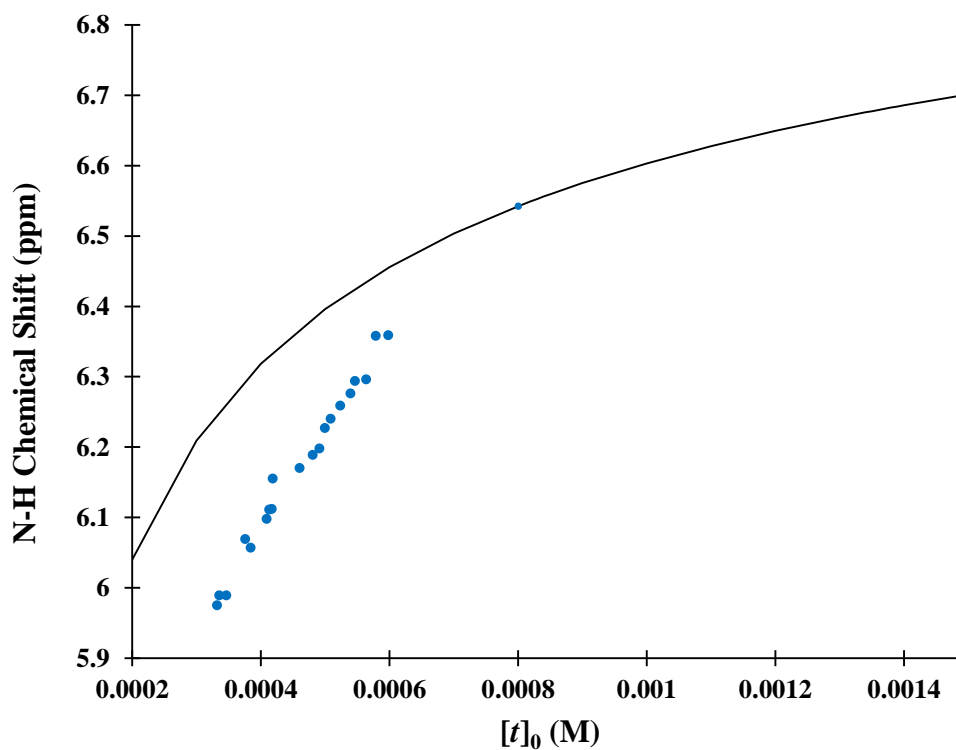


Figure 4.28 Relationship between δ_{obs} vs $[t]_0$ during three thermal reversion experiments of derivative **7c**. Blue dots correspond to a reversion curve obtained from a reversion experiment ($[\mathbf{7c}] = 8.8 \times 10^{-4}$ M). Solid line corresponds to the theoretical dilution curve obtained from the average of two separate dilution experiments with (t)-**7c**.

The data collected from the reversion experiments were used in the mathematical model described in Chapter 3 (Section 3.2.3) in order to obtain K_{t-c} and δ_{tc} . It is important to recall that this mathematical model is based on the interdependency of K_{t-c} and δ_{tc} values; therefore, for a set of δ_{obs} values at different *cis/trans* ratios with a fixed **7c** total concentration in solution there must be only one pair of K_{t-c} and δ_{tc} values common to all data points (i.e. the convergence point at Figure 4.29). From our calculations, such values were obtained through the minimum CV (coefficient of variation) for each δ_{tc} value employed (i.e. a vertical slice in Figure 4.30 plot). Table 4.15 displays the calculated K_{t-t} , K_{t-c} , δ_m , δ_d and δ_{tc} for butoxy derivative **7c** at -10 °C. An important point to note in Table 4.15 is the free energy difference between the *trans-trans* dimer and the *trans-cis* dimer which is 4.41 kJ mol⁻¹. This difference is comparable to that reported for the butoxy derivative **4c** in Chapter 3 (Section 3.2.3) which is 4.46 kJ mol⁻¹.

In order to have as complete as possible a description of all equilibria present in a *cis/trans* mixture toluene-*d*₈ solution of **7c** at -10 °C, the dimerization constant of butoxy **5c** was determined under the same solvent and temperature conditions. It is important to recall that the K_{t-t} value of **5c** is an approximation of the maximum value expected for the dimerization constant of the *cis*-isomeric form of butoxy derivative **7c**, which is 68 M⁻¹ ($\Delta G_{t-t} = -9.23$ kJ mol⁻¹). From this K_{c-c} approximation it can be assumed that the *cis-cis* dimer of **7c** is at least 11 kJ mol⁻¹ less stable than the *trans-trans* isomer ($\Delta\Delta G = 11.06$ kJ mol⁻¹). Likewise, the calculated ΔG_{t-c} for **7c** at -10 °C via our mathematical model is in agreement with the expected stability of the *trans-cis* complex (i.e. the average of the ΔG_{t-t} values of **7c** and **5c** at -10 °C, which is -14.76 kJ mol⁻¹), since the difference between the

calculated and the expected free energies of such complex is approximately 1 kJ mol^{-1}
 $(\Delta\Delta G_{t,c} = 1.13 \text{ kJ mol}^{-1})$

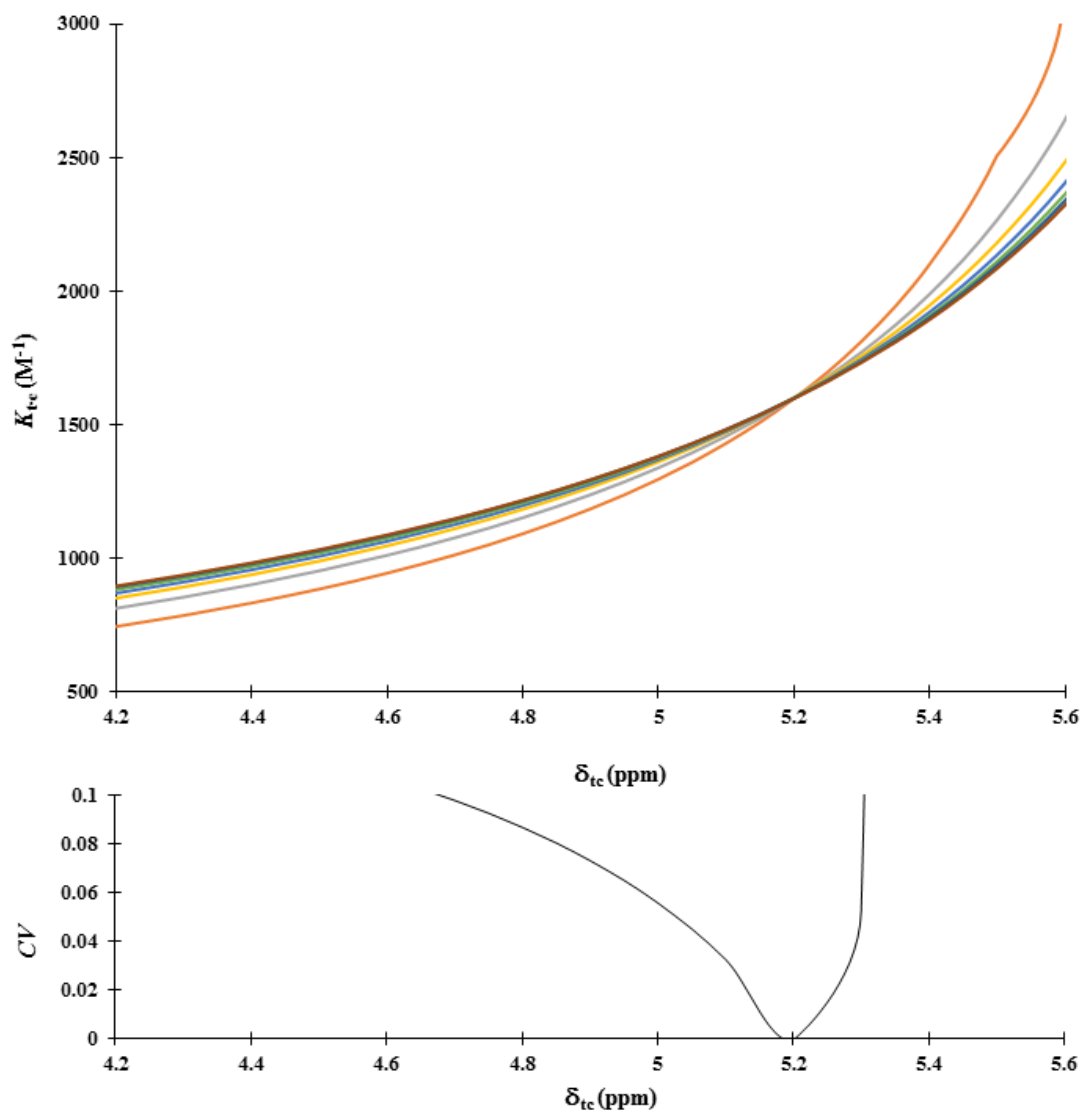


Figure 4.29 Top Plot: Theoretical $K_{t,c}$ vs δ_{tc} curves for the set of δ_{obs} from the least squares curve that describes the third reversion experiment of derivative **7c** (red dots in Figure 4.31, $[7c] = 1.47 \times 10^{-3} \text{ M}$). Bottom Plot: Theoretical CV vs δ_{tc} curve for the set of $K_{t,c}$ calculated from the third reversion experiment of derivative **7c** (red dots at Figure 4.31, $[7c] = 1.47 \times 10^{-3} \text{ M}$).

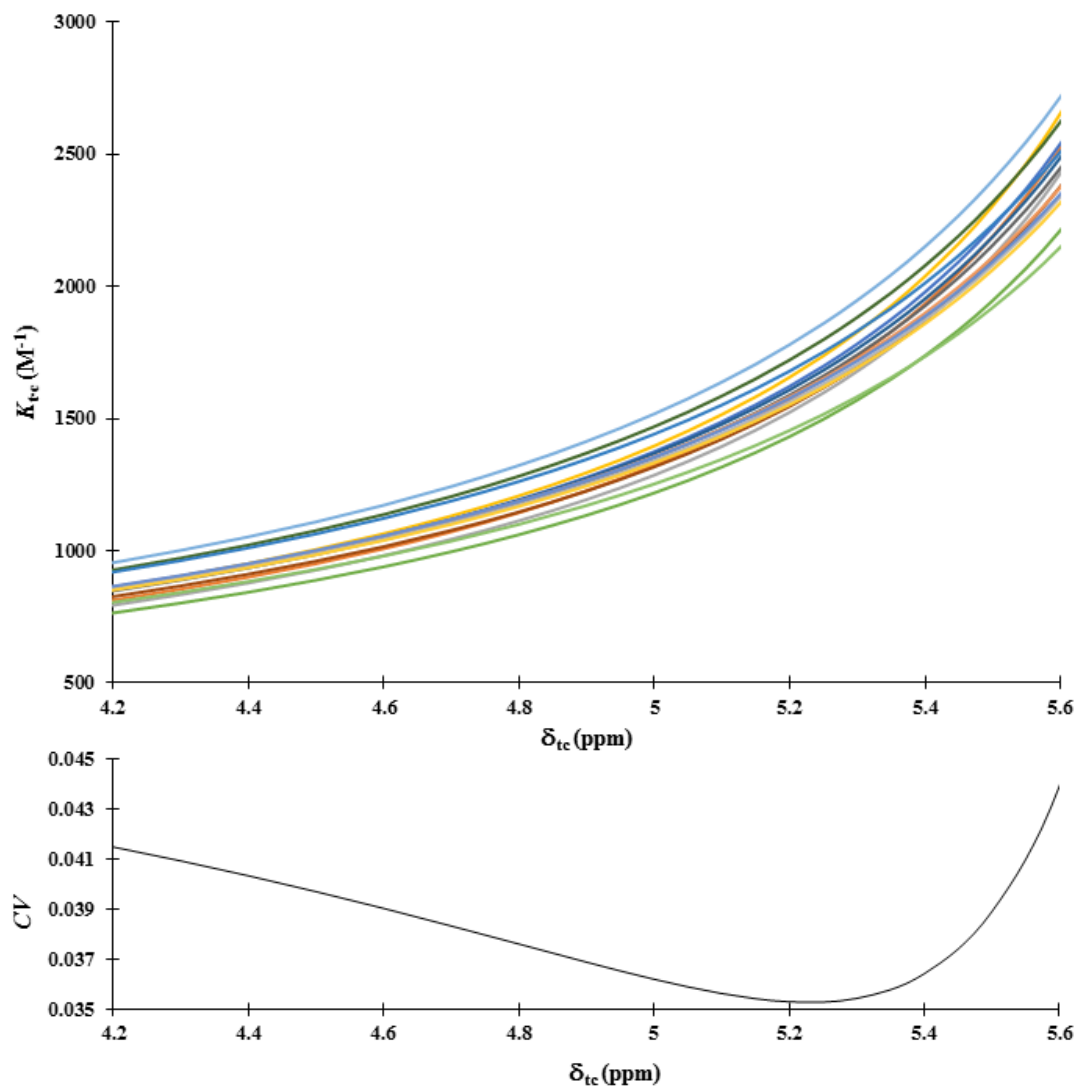


Figure 4.30 Top Plot: K_{t-c} vs δ_{t-c} curves for the set of δ_{Obs} from the third reversion experiment of derivative **7c** (red dots in Figure 4.31, $[7c] = 1.47 \times 10^{-3} M$). Bottom Plot: CV vs δ_{t-c} curve for the set of K_{t-c} calculated from the third reversion experiment of derivative **7c** (red dots at Figure 4.31, $[7c] = 1.47 \times 10^{-3} M$).

Table 4.15 Dimerization constant ($K_{t,t}$), complexation constant ($K_{t,c}$), free energy of dimerization ($\Delta G_{t,t}$), free energy of complexation ($\Delta G_{t,c}$), calculated chemical shifts of monomer (δ_m), dimer (δ_d) and complex (δ_{tc}) species studied in Toluene- d_8 at 263 K.

$K_{t,t}$ in Toluene- d_8 (M^{-1}) ^a	$\Delta G_{t,t}$ ($kJmol^{-1}$)	δ_m (ppm) ^a	δ_d (ppm) ^a	$K_{t,c}$ in Toluene- d_8 (M^{-1}) ^a	$\Delta G_{t,c}$ ($kJmol^{-1}$)	δ_{tc} (ppm) ^a
10700 ± 1100	-20.29 ± 0.23	4.17^b	7.22^b	1430 ± 198	-15.88 ± 0.29	5.20 ± 0.02

^a Average values obtained using Equation 5 from Chapter 2 (Section 2.3.2). Errors calculated from two times the standard deviation to give a 95% of confidence interval.

^b Chemical shift of the amino proton located upfield at the 1H NMR spectra.

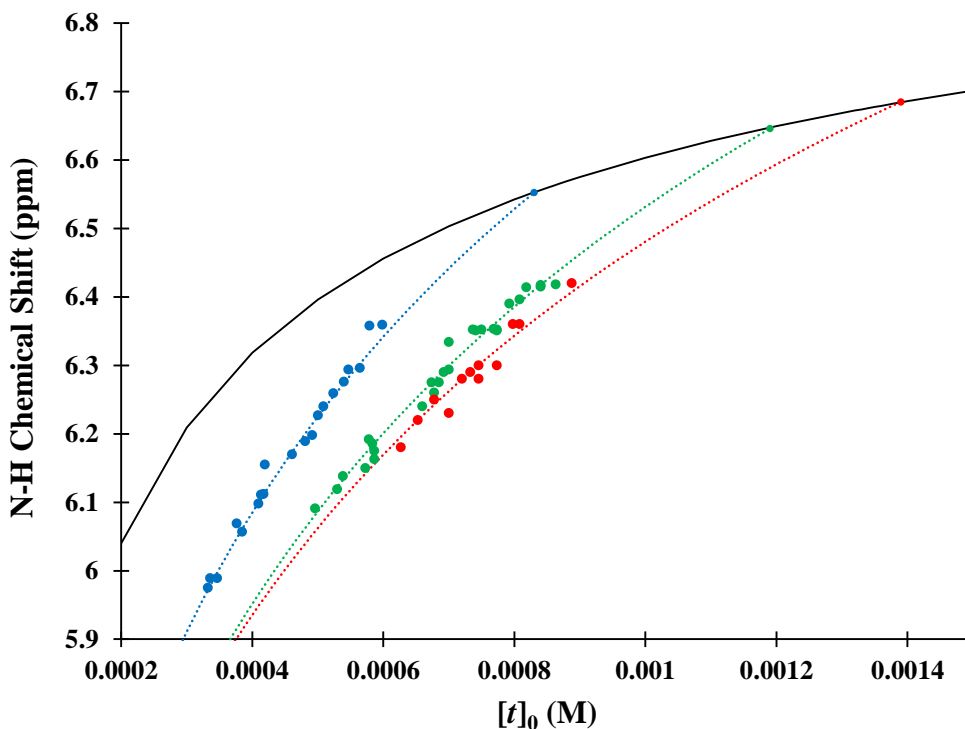


Figure 4.31 Relationship between δ_{obs} vs $[t]_0$ through three reversion experiments of the derivative **7c**. Blue, green and red dots correspond to first, second and third separate reversion experiments, respectively. Blue, green and red dashed lines correspond to the predicted δ_{obs} vs $[t]_0$ plots for the first, second and third reversion experiments with the expected $\overline{\Delta G}$ values (sample standard deviations of 0.006, 0.003, 0.01 ppm, respectively).

Solid line corresponds to the dilution curve obtained from the average of two separate dilution experiments.

Finally, all the equilibrium constants displayed in Table 4.15 and the approximation of the K_{c-c} for derivative **7c** allowed us to obtain a full picture of all the species involved in solution in a *cis/trans* mixture at different ratios; and create a speciation diagram (Figure 4.32). Similarly to derivatives **4c**, **4f** and **4k**, the speciation diagram for derivative **7c** was calculated on the basis of two scenarios: 1) when there is no *cis*-dimer in solution ($K_{c-c}=0$, solid lines) and, 2) when there is *cis*-dimer in solution ($K_{c-c} = 68 \text{ M}^{-1}$, dotted-star marked lines).

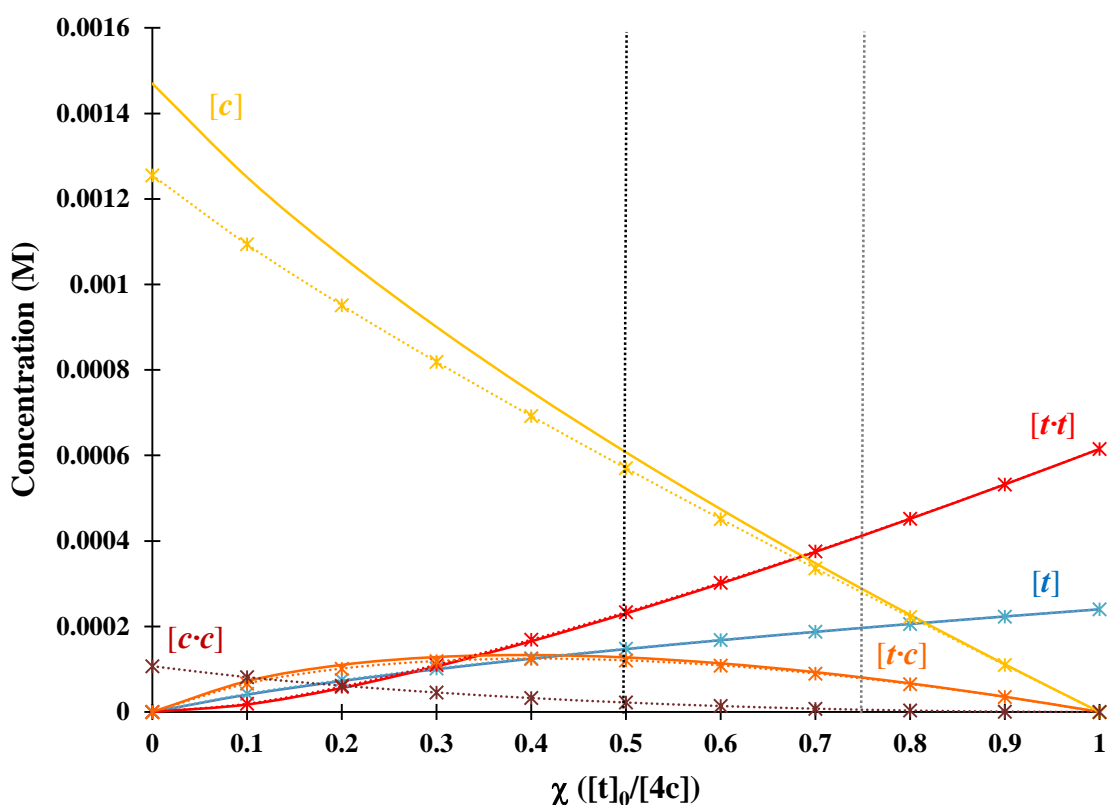


Figure 4.32 Theoretical speciation diagram of derivative **7c** at the third reversion experiment (red dots at Figure 4.31, $[7c] = 1.47 \times 10^{-3} \text{ M}$) at 263 K. Solid lines correspond to the first scenario ($K_{c-c} = 0$) and dotted-star marked lines correspond to the second scenario ($K_{c-c} = 68 \text{ M}^{-1}$) respectively. Blue, red, orange, yellow and brown colors correspond to $[t]$, $[t \cdot t]$, $[t \cdot c]$, $[c]$, and $[c \cdot c]$, respectively. Black dotted line corresponds to maximum *cis/trans* ratio in reversion experiment. Grey dotted line corresponds to *cis/trans* ratio at PSS.

Figure 4.32 shows that there are no significant differences between the concentrations of each dimer and monomer in solution when both scenarios are compared. The largest difference in concentration is approximately 4 % in *trans-cis* complex concentration ($[t \cdot c]$) between both scenarios over the total concentration of *trans*-isomer ($[t]_0$). This difference is expected when there is 90% *cis*-isomer in solution ($\chi = 0.1$ in Figure 4.32) and decreases as the total concentration of *trans*-isomer increases. This observation led us to conclude that discarding the *cis-cis* dimerization from the calculation of K_{t-c} does not have a significant impact in the full description of the species distribution at the employed concentrations. In other words, taking into account the starting *cis/trans* ratio during our reversion experiments was approximately 1 (black dotted line in Figure 4.32), the largest concentration difference between both scenarios is 0.96 % in the *trans-cis* complex concentration over the total concentration of *trans*-isomer ($[t]_0$) which is insignificant in the context of the total amount of derivative **7c** in solution.

4.2.7 Cis to Trans Reversion Kinetics

As mentioned in the previous section, the thermal reversion rate of **7c** in toluene- d_8 was considerably higher than those observed in the derivatives **4a-p** tested at room temperature. A more detailed analysis of the *cis/trans* ratio change in solution as time passed allowed us to calculate the rate of the thermal reversion **7c** at room temperature. In this sense, the *cis-* to *trans-* thermal reversion follows a first order reaction model (Equations 15 and 16 in Chapter 3, Section 3.2.4) with a k value of $2.62 \pm 1.88 \times 10^{-3} \text{ s}^{-1}$ (Figure 4.33). Compared with the thermal reversion rates reported for the **4a-p** derivatives

tested (**4c**, **4f** and **4k**) the calculated rate constant of derivative **7c** is at least 5 times higher; and more specifically, compared with the butoxy derivative **4c**, k value for butoxy **7c** is 8 times higher.

The same kinetic study was performed for the *cis*- to *trans*- thermal reversion of derivative **7c** at $-10\text{ }^{\circ}\text{C}$ (263 K). At this temperature the thermal reversion rate calculated from three separate reversion experiments is $8.47 \pm 1.54 \times 10^{-5}\text{ s}^{-1}$ (Figure 4.34). At $-10\text{ }^{\circ}\text{C}$ the thermal reversion of **7c** has a slower rate than those observed for **4c**, **4f** and **4k** derivatives at room temperature; i.e. butoxy **4c** thermal reversion rate at room temperature is four times higher than butoxy **7c** at $-10\text{ }^{\circ}\text{C}$.

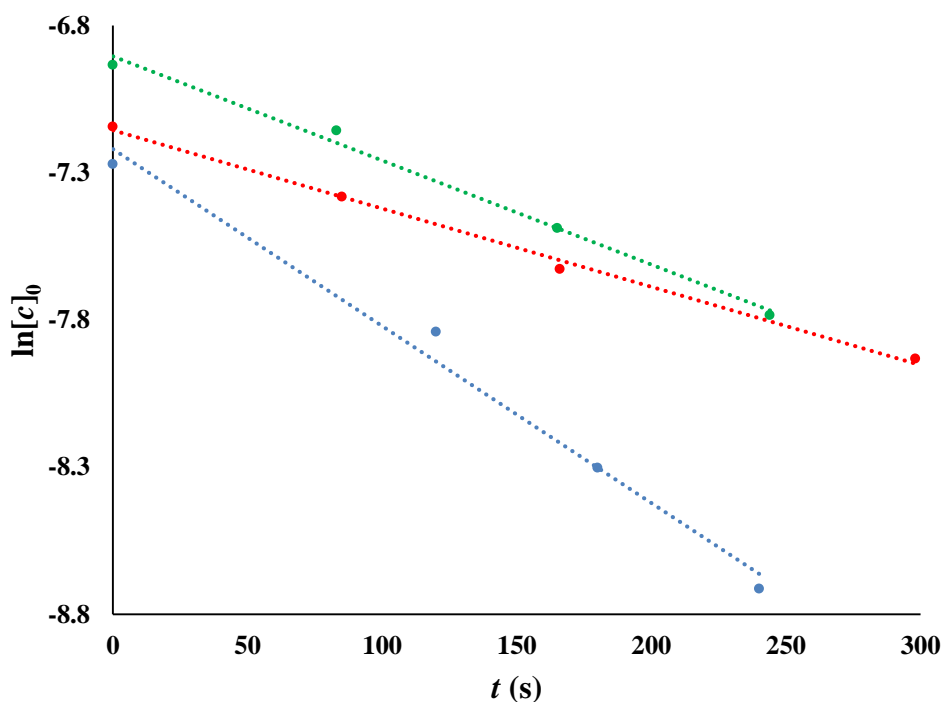


Figure 4.33 Decay profiles of (*c*)-**7c** isomer in toluene- d_8 at 298 K. Blue, red and green dots correspond to first, second and third separate reversion experiments ($r = -0.9934$, -0.9966 , -0.9981) respectively. Blue, red and green dashed lines correspond to the calculated values obtained by linear least squares regression of the first, second and third separate reversion experiments, respectively.

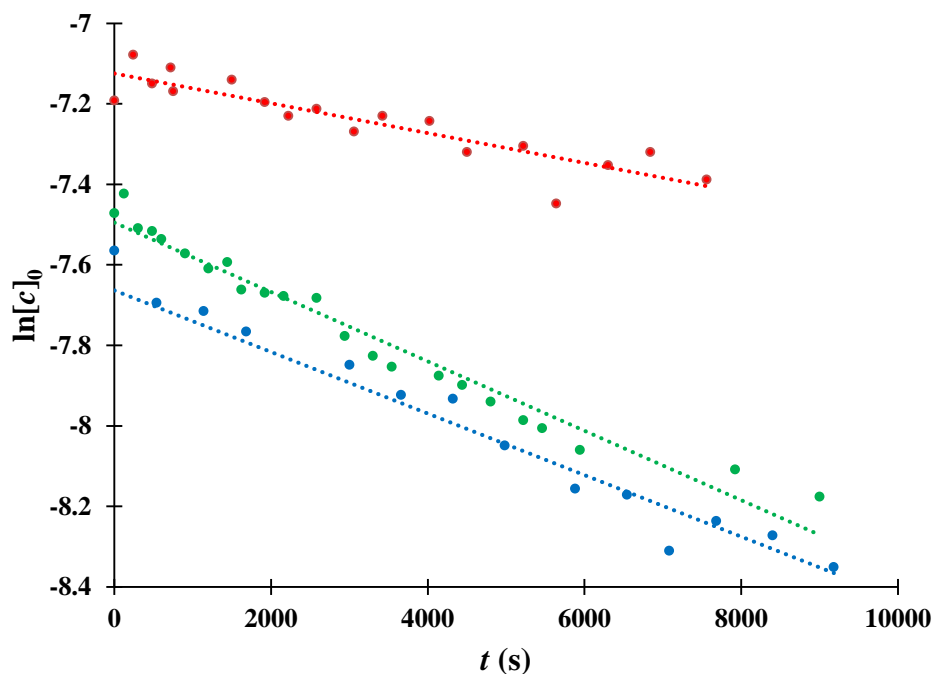


Figure 4.34 Decay profiles of (c)-7c isomer in toluene- d_8 at 263 K. Blue, green and red dots correspond to first, second and third separate reversion experiments ($r = -0.9816$, -0.9574 and -0.9885), respectively. Blue, green and red dashed lines correspond to the calculated values obtained by linear least squares regression of the first, second and third separate reversion experiments, respectively.

4.3 Summary and Conclusions

A new marginally improved library of self-complementary hydrogen bond **DDAAA** arrays (**7**) were synthesized and characterized. The improvement over **4a-p** presented in Chapter 2 and 3 lies in the change of an acceptor group; the pyridyl ring in derivatives **4a-p** was replaced by a 2-methoxyphenyl group. The reasoning behind this change was to provide an acceptor group in closer physical proximity to the amino protons than in **4a-p**. It was anticipated that the hydrogen bond interaction between this acceptor site and the amino protons would provide more stable dimer structures. Dimerization constants of derivatives **7** were obtained at room temperature in two solvent systems: CDCl_3 and toluene- d_8 . In the first solvent, dimerization constants ranged from 36 to 309 M^{-1} ; meanwhile, in toluene- d_8 dimerization constants varied from 2400 to 5600 M^{-1} . In both solvents employed, derivatives **7** generally displayed $K_{t,t}$ values higher than those obtained for derivatives **4a-p**. This difference is more evident in toluene- d_8 (a non-competitive solvent) and supports the idea of a more stable dimer structure due to the change of the pyridyl ring for a 2-methoxyphenyl group. In addition, similarly to **4a-p**, the presence of electron withdrawing RX groups in derivatives **7** resulted in larger dimerization constants. The energetic contribution of the methoxy acceptors in each solvent system employed was estimated at 5 and 11 kJ mol^{-1} in CDCl_3 and toluene- d_8 , respectively. This contribution is significantly higher than that estimated for derivatives **4a-p** which is in accordance with the improved arrangement. It was possible to confirm the dimerization of **7c**, **7f**, and **7n** in the solid state by single crystal X-ray diffraction. In all these structures, hydrogen bond interactions between the amino group and triazine, azo and methoxy moieties were observed as expected. A special case was the 4'-*tert*-butylphenoxy

derivative **7k** in the solid state since it was observed as an infinite hydrogen bonded chain. However, in this structure the hydrogen bond interactions present were the similar to those observed for **7c**, **7f**, and **7n** dimers in the solid state. The intermolecular distances between the interacting sites in derivatives **7c**, **7f**, **7k** and **7n** complex structures were shorter than those noted in the dimer structures of derivatives **4a**, **4d**, **4f** and **4k** in the solid state. This observation is in agreement with the larger dimerization constants for derivatives **7** compared with derivatives **4a-p**.

Regarding the photochemical properties, the *trans*-isomer UV-Vis absorption spectra of derivatives **7** are characterized by one $n \rightarrow \pi^*$ band (maximum absorption ≈ 481 nm) and two $\pi \rightarrow \pi^*$ bands (maximum absorptions at ≈ 354 nm and ≈ 295 nm). Conversely, the *cis*-isomer of butoxy derivative **7c** has a UV-Vis absorption spectrum with a $n \rightarrow \pi^*$ band higher in absorptivity and $\pi \rightarrow \pi^*$ bands lower in absorptivity compared with the *trans*-isomer. The presence of an isosbestic point thru the *cis*- to *trans*- thermal reversion of derivative **7c** confirms that no intermediates are involved during this isomerization. The percentages of interconversion from *trans*- to *cis*- at the photostationary state for all derivatives **7** were obtained in three different solvent systems: CDCl_3 , toluene- d_8 and acetonitrile. In CDCl_3 no photoisomerization was noted and in toluene- d_8 the butoxy derivative **7c** was the only one that showed *trans*- to *cis*- photoisomerization (26% yield). The acetonitrile solutions of all **7** displayed *trans*- to *cis*- photoisomerization with yields of interconversion that ranged from 7 to 32 %. In order to characterize the species distribution in a *cis/trans* mixture in solution the same mathematical model described in Chapter 3 was applied to butoxy derivative **7c** at -10 °C. At this temperature, butoxy derivative **7c** has a $K_{t,t}$ value of 10700 M^{-1} and a calculated $K_{t,c}$ value of 1400 M^{-1} . The

free energy difference between the *trans-trans* dimer and the *trans-cis* complex is similar to that observed in the butoxy derivative **4c**. Finally, the stability of (**c**)-**7c** in toluene-*d*₈ solution was studied at two temperatures: room temperature and -10 °C (263 K). The thermal reversion from *cis*- to *trans*-isomer proceeds as first order reaction with rate constants of $2.62 \times 10^{-3} \text{ s}^{-1}$ and $8.47 \times 10^{-5} \text{ s}^{-1}$ at 25 and -10 °C, respectively.

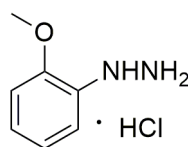
4.4 Experimental Methodology

4.4.1 Generalities

All experiments were performed in ambient atmospheric conditions unless otherwise indicated. Chemicals were purchased from Alfa Aesar, Sigma-Aldrich, and Oakwood Products and used as received. Solvents (acetone, acetonitrile, butanol, chloroform, dichloromethane, diethyl ether, diisopropyl ether, dimethyl formamide, ethyl acetate, hexanes, methanol, tetrahydrofuran, and toluene) were obtained from Caledon Laboratories, Fisher Chemicals, Sigma-Aldrich and VWR Analytical. In the case of inert atmosphere conditions, solvents were dried using an Innovative Technology Inc. Controlled Atmospheres Solvent Purification System that utilizes dual alumina columns (SPS-400-5), or purchased from Sigma-Aldrich and used as received. Reactions were monitored by thin-layer chromatography (TLC) on pre-coated TLC-sheets POLYGRAM®SIL G/UV₂₅₄. Column chromatography was performed with SiliCycle®SiliaFlash® F60, 40-63 μm 60 Å. Nuclear Magnetic Resonance spectra were recorded on Mercury 400 MHz, INOVA 400 MHz and INOVA 600 MHz spectrometers

(^1H = 400.08 MHz, 399.77 MHz and 599.32 MHz; ^{13}C { ^1H } = 100.52 MHz and 150.78 MHz respectively). ^1H and ^{13}C spectra were referenced relative to Me_4Si using the residual non-deuterated NMR solvent signal (^1H : CHCl_3 , $\delta = 7.26$ ppm, $(\text{CHD}_2)_2\text{SO}$, $\delta = 2.50$ ppm, $(\text{CHD}_2)\text{C}_6\text{D}_5$, $\delta = 2.09$ ppm, ; ^{13}C { ^1H }: CHCl_3 , $\delta = 77.0$ ppm, $(\text{CHD}_2)_2\text{SO}$, $\delta = 39.5$ ppm). Solvents for NMR spectroscopy (Chloroform-*d*, DMSO-*d*₆, and Toluene-*d*₈) were purchased from Cambridge Isotope Laboratories and Sigma-Aldrich. Mass spectra were recorded using an electron ionization Finnigan MAT 8200 spectrometer at an ionizing voltage of 70 eV. X-Ray diffraction data were collected on Bruker Apex II and Nonius Kappa CCD X-Ray diffractometers using graphite monochromatic Mo-K α radiation ($\gamma = 0.71073$ Å) and Cu-K α radiation ($\gamma = 1.54178$ Å), respectively. ^1H NMR dilution experiments, photostationary state experiments and ^1H NMR reversion experiments were performed as described in Chapters 2 and 3 (Sections 2.5.3, 3.4.2 and 3.4.4).

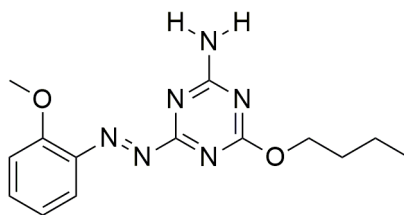
4.4.2 Synthetic Methods



Synthesis of (2-methoxyphenyl)hydrazine hydrochloride. Synthetic procedure as reported by Li and coworkers.¹⁰ In a round bottom flask a suspension of *o*-anisidine (2.46 g, 20 mmol) in concentrated hydrochloric acid (40 mL) is prepared and cooled down to -10 °C. To this suspension, a solution of NaNO_2 (1.39 g, 20.2 mmol) in distilled water (10 mL) was added dropwise keeping the suspension at a temperature below 0 °C. Once

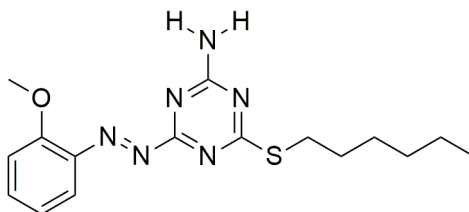
all NaNO_2 solution was added, the reaction mixture was stirred for 30 minutes at $0\text{ }^\circ\text{C}$. In a separate flask, a solution of $\text{SnCl}_2\cdot\text{H}_2\text{O}$ (9.12 g, 40.4 mmol) in concentrated hydrochloric acid (15 mL) was prepared and added all at once to the reaction mixture. The reaction mixture was stirred overnight and allowed to warm to room temperature. The product was filtered, washed with 1M HCl solution and dichloromethane and dried by vacuum filtration and. Yield = 3.45 g, 99%. EI-HRMS: Calc. for $\text{C}_7\text{H}_{10}\text{N}_2\text{O}$: 138.0793, Found: 138.0793. ^1H NMR (400 MHz, DMSO-d_6): δ (ppm) 10.04 (bs 3H), 7.57 (bs, 1H), 7.06 (m, 1H), 6.88-7.01 (m, 3H), 3.82 (s, 3H). ^{13}C NMR (100 MHz, DMSO-d_6): δ (ppm) 147.8, 134.2, 122.4, 120.6, 114.6, 111.0, 55.7.

General procedure for synthesis of (*E*)-4-((2-methoxyphenyl)diazenyl)-1,3,5-triazin-2-amine derivatives (7). In a clean, dry round bottom flask 4-chloro-1,3,5-triazin-2-amine derivative (2) (1 eq.), (2-methoxyphenyl)hydrazine hydrochloride (1 eq.) and potassium carbonate (2 eq.) were mixed with 100 mL of THF. The reaction mixture was refluxed for 12 h, cooled and the solvent removed under reduced pressure. The crude material was poured into 50 mL of distilled water and the intermediate was extracted with 3 x 50 mL of dichloromethane. The organic phase was dried over sodium sulfate and the drying agent was removed by gravity filtration. One equivalent of (diacetoxy)iodobenzene was added to the intermediate solution and stirred overnight at room temperature. Solvent was removed under reduced pressure and the product was purified by flash chromatography using a solvent mixture 1:1 hexanes : diethyl ether as eluent.



Synthesis of (*E*)-4-butoxy-6-((2-methoxyphenyl)diazenyl)-1,3,5-triazin-2-amine, 7c.

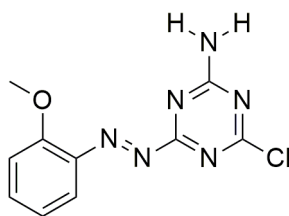
Synthesis performed according to general procedure for product **7**; wherein the 4-chloro-1,3,5-triazin-2-amine derivative is **2c**. Yield = 12%. EI-HRMS: Calc. for C₁₄H₂₀N₆O₂ (M+2H): 304.1648 Found: 304.1644. ¹H NMR (400 MHz, CDCl₃) = δ (ppm) 9.19 (bs, 1H)**, 7.82 (dd, 1H, *J* = 8.2, 2.0 Hz), 7.57 (ddd, 1H, *J* = 8.2, 7.4, 2.0 Hz), 7.13 (dd, 1H, *J* = 7.4, 1.2 Hz), 7.01 (ddd, 1H, *J* = 7.4, 7.4, 1.2 Hz), 6.53 (bs, 1H)**, 5.66 (bs, 1H)*, 5.47 (bs, 1H)*, 4.44 (t, 2H, *J* = 6.2 Hz), 4.08 (s, 3H), 1.78 (m, 2H, *J* = 7.8, 6.2 Hz), 1.49 (m, 2H, *J* = 7.8, 7.4 Hz), 0.97 (t, 3H, *J* = 7.4 Hz), *NH free monomer, **NH dimer. ¹³C NMR (100 MHz, CDCl₃) = δ (ppm) 174.6, 172.3, 169.2, 158.5, 141.4, 135.8, 120.9, 117.0, 112.8, 67.8, 56.0, 30.6, 19.0, 13.7.



Synthesis of (*E*)-4-(hexylthio)-6-((2-methoxyphenyl)diazenyl)-1,3,5-triazin-2-amine,

7f. Synthesis performed according to general procedure for product **7**; wherein the 4-chloro-1,3,5-triazin-2-amine derivative is **2f**. Yield = 50%. EI-HRMS: Calc. for C₁₆H₂₄N₆OS (M+2H): 348.1732 Found: 348.1723. ¹H NMR (400 MHz, CDCl₃) = δ (ppm) 9.38 (bs, 1H)**, 7.84 (dd, 1H, *J* = 8.2, 1.6 Hz), 7.58 (ddd, 1H, *J* = 8.6, 8.2, 1.6 Hz), 7.15

(d, 1H, $J = 8.6$ Hz), 7.02 (dd, 1H, $J = 8.6, 8.2$ Hz), 6.56 (bs, 1H)**, 5.47 (bs, 1H)*, 5.46 (bs, 1H)*, 4.12 (s, 3H), 3.17 (t, 2H, $J = 7.4$ Hz), 1.74 (m, 2H, $J = 7.4, 7.0$ Hz), 1.31-1.47 (m, 6H), 0.89 (t, 3H, $J = 7.0$ Hz), *NH free monomer, **NH dimer. ^{13}C NMR (100 MHz, CDCl_3) = δ (ppm) 184.1, 171.3, 166.5, 158.5, 141.5, 135.8, 121.0, 117.1, 112.8, 55.9, 31.3, 30.3, 28.9, 28.5, 22.5, 14.0.



Synthesis of (E)-4-chloro-6-((2-methoxyphenyl)diazenyl)-1,3,5-triazin-2-amine, 7g.

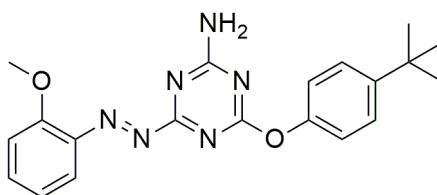
Synthesis performed according to general procedure for product **7**; wherein the 4-chloro-1,3,5-triazin-2-amine derivative is **1**. Yield = 12 %. EI-HRMS: Calc. for $\text{C}_{10}\text{H}_{11}\text{N}_6\text{O}$ ($\text{M}+2\text{H}$): 266.0683 Found: 266.0680. ^1H NMR (400 MHz, CDCl_3) = δ (ppm) 7.82 (d, 1H, $J = 7.0$ Hz), 7.69 (bs, 1H)**, 7.61 (m, 1H), 7.14 (d, 1H, $J = 8.8$ Hz), 7.02 (m, 1H), 6.46 (bs, 1H)**, 5.77 (bs, 1H)*, 5.72 (bs, 1H)*, 4.09 (s, 3H), *NH free monomer, **NH dimer. ^{13}C NMR (100 MHz, CDCl_3) = δ (ppm) 174.4, 170.4, 168.1, 167.0, 140.8, 120.6, 116.0, 114.0, 102.4, 56.0.



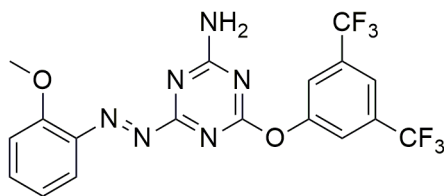
Synthesis of (E)-4-((2-methoxyphenyl)diazenyl)-6-phenoxy-1,3,5-triazin-2-amine, 7i.

Synthesis performed according to general procedure for product **7**; wherein the 4-chloro-

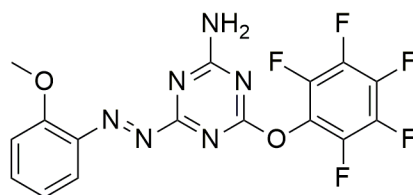
1,3,5-triazin-2-amine derivative is **2i**. Yield = 78%. EI-HRMS: Calc. for $C_{16}H_{16}N_6O_2$ (M+2H): 324.1335 Found: 324.1329. 1H NMR (400 MHz, $CDCl_3$) = δ (ppm) 8.56 (bs, 1H)**, 7.82 (dd, 1H, $J = 7.6, 1.8$ Hz), 7.57 (ddd, 1H, $J = 8.2, 7.6, 1.8$ Hz), 7.43 (m, 2H), 7.27 (m, 1H), 7.23 (m, 2H), 7.12 (d, 1H, $J = 8.2$ Hz), 7.01 (dd, 1H, $J = 7.6, 7.6$ Hz), 6.55 (bs, 1H)**, 5.69 (bs, 1H)*, 5.48 (bs, 1H)*, 3.97 (s, 3H), *NH free monomer, **NH dimer. ^{13}C NMR (100 MHz, $CDCl_3$) = δ (ppm) 175.4, 172.7, 169.3, 158.8, 152.1, 141.5, 136.0, 129.4, 125.7, 121.9, 120.9, 117.2, 112.8, 55.9.



Synthesis of (E)-4-(4-(tert-butyl)phenoxy)-6-((2-methoxyphenyl)diazenyl)-1,3,5-triazin-2-amine, 7k. Synthesis performed according to general procedure for product **7**; wherein the 4-chloro-1,3,5-triazin-2-amine derivative is **2k**. Yield = 14%. EI-HRMS: Calc. for $C_{20}H_{24}N_6O_2$ (M+2H): 380.1961 Found: 380.1960. 1H NMR (400 MHz, $CDCl_3$) = δ (ppm) 8.83 (bs, 1H)**, 7.81 (dd, 1H, $J = 8.2, 1.6$ Hz), 7.56 (ddd, 1H, $J = 8.6, 7.4, 2.0$ Hz), 7.42 (m, 2H), 7.14 (m, 2H), 7.11 (d, 1H, $J = 8.6$ Hz), 7.01 (ddd, 1H, $J = 8.2, 7.4, 1.6$ Hz), 6.55 (bs, 1H)**, 5.66 (bs, 1H)*, 5.49 (bs, 1H)*, 4.00 (s, 3H), 1.35 (s, 9H), *NH free monomer, **NH dimer. ^{13}C NMR (100 MHz, $CDCl_3$) = δ (ppm) 175.4, 172.8, 169.3, 158.7, 149.7, 148.5, 141.5, 135.9, 126.3, 121.1, 120.9, 117.2, 112.8, 55.9, 34.5, 31.5.



Synthesis of (*E*)-4-(3,5-bis(trifluoromethyl)phenoxy)-6-((2-methoxyphenyl)diazenyl)-1,3,5-triazin-2-amine, **7m.** Synthesis performed according to general procedure for product **7**; wherein the 4-chloro-1,3,5-triazin-2-amine derivative is **2m**. Yield = 21%. EI-HRMS: Calc. for $C_{18}H_{14}F_6N_6O_2$ ($M+2H$): 460.1082 Found: 460.1081. 1H NMR (400 MHz, $CDCl_3$) = δ (ppm) 8.36 (bs, 1H)**, 7.82 (dd, 1H, $J = 8.2, 2.0$ Hz), 7.80 (s, 1H), 7.73 (s, 2H), 7.59 (ddd, 1H, $J = 8.8, 8.8, 1.8$ Hz), 7.13 (d, 1H, $J = 8.8$ Hz), 7.02 (dd, 1H, $J = 7.6, 7.6$ Hz), 6.38 (bs, 1H)**, 5.74 (bs, 1H)*, 5.54 (bs, 1H)*, 4.00 (s, 3H), *NH free monomer, **NH dimer. ^{13}C NMR (100 MHz, $CDCl_3$) = δ (ppm) 201.8, 190.2, 171.3, 169.2, 164.2, 158.1, 152.9, 140.8, 135.7, 131.7, 124.0, 120.6, 116.0, 114.0, 56.0. ^{19}F NMR (376.42 MHz, $DMSO-d_6$) = δ (ppm) -61.18.



Synthesis of (*E*)-4-((2-methoxyphenyl)diazenyl)-6-(perfluorophenoxy)-1,3,5-triazin-2-amine, **7n.** Synthesis performed according to general procedure for product **7**; wherein the 4-chloro-1,3,5-triazin-2-amine derivative is **2n**. Yield = 50%. EI-HRMS: Calc. for $C_{16}H_{11}F_5N_6O_2$: 414.0864 Found: 414.0857. 1H NMR (400 MHz, $CDCl_3$) = δ (ppm) 8.78 (bs, 1H)**, 7.81 (dd, 1H, $J = 8.2, 2.0$ Hz), 7.60 (dd, 1H, $J = 7.0, 1.6$ Hz), 7.15 (d, 1H, $J = 8.2$ Hz), 7.03 (dd, 1H, $J = 8.2$ Hz), 6.44 (bs, 1H)**, 5.76 (bs, 1H)*, 5.56 (bs, 1H)*, 4.06 (s,

3H), *NH free monomer, **NH dimer. ^{13}C NMR (100 MHz, CDCl_3) = δ (ppm) 175.4, 169.4, 159.0, 141.5, 136.6, 121.0, 117.2, 113.0, 56.0. ^{19}F NMR (376.42 MHz, DMSO-d_6) = δ (ppm) -152.2 (d, 2H, $J = 17.2$ Hz), -158.42 (t, 1H, $J = 22.4$ Hz), -162.58 (dd, 2H, $J = 242.4, 17.2$ Hz).

4.4.3 Synthesis of (Z)-4-butoxy-6-((2-methoxyphenyl)diazenyl)-1,3,5-triazin-2-amine, (c)-7c.

Approximately 160 mL of a 10^{-2} M solution of a derivative **7** in dichloromethane was prepared and distributed between 16 test tubes. Each test tube containing the derivative **7** solution was purged with N_2 in order to avoid side reactions with O_2 present in solution. The 16 test tubes were placed in the photoreactor and irradiated using lamps with radiation centered at 360 nm for 3 hours. After irradiation, the solution was cooled down to -78° and the solvent was removed employing a constant air flow to yield a mixture of *cis* and *trans* isomers. The *cis*-isomer was isolated through flash chromatography with 1:1 hexanes : diethyl ether mixture as eluent. Once the first fraction (*cis* isomer) was obtained, it was cooled down to -78° to remove the solvent mixture with the aid of a constant air flow. In all cases, the *cis*-isomer was a yellow powder that was stored in a vial wrapped with black in the freezer to prevent thermal and photochemical reversion.

4.5 References

- (1) Arnett, E. M.; Joris, L.; Mitchell, E.; Murty, T. S. S. R.; Gorrie, T. M.; Schleyer, P. v. R. *J. Am. Chem. Soc.*, **1970**, *92* (8), 2365.
- (2) Berthelot, M.; Laurence, C.; Safar, M. *J. Chem. Soc., Perkin Trans. 2*, **1998**, 283.
- (3) Jeffrey, G. A.; Maluszynska, H. *J. Mol. Struct.*, **1986**, *147* (1-2), 127.
- (4) Jeffrey, G. A.; Maluszynska, H.; Mitra, J. *Int. J. Biol. Macromol.*, **1985**, *7* (6), 336.
- (5) Jeffrey, G. A. *An Introduction to Hydrogen Bonding*; Oxford University Press: New York, 1997.
- (6) Desiraju, G. R. *Angew. Chem. Int. Ed. Engl.*, **2007**, *46* (44), 8342.
- (7) Sartorius, J.; Schneider, H.-J. *Chem. Eur. J.*, **1996**, *2* (11), 1446.
- (8) Yamamoto, S.; Nishimura, N.; Hasegawa, S. *Bull. Chem. Soc. Jpn.*, **1971**, *44* (8), 2018.
- (9) Koźlecki, T.; Wilk, K. A.; Gancarz, R. *J. Photochem. Photobiol. A Chem.*, **1998**, *116* (3), 229.
- (10) Xu, R.; Xia, R.; Luo, M.; Xu, X.; Cheng, J.; Shao, X.; Li, Z. *J. Agric. Food Chem.*, **2014**, *62* (2), 381.

Chapter 5

5 Conclusions and Outlook

5.1 Conclusions

Azoaromatic compounds are well-known photoswitches with a variety of applications in materials science. Conversely, the heteroaromatic counterparts have had less attention in this area, regardless that they exhibit similar photochromic properties. This allowed a niche of opportunity we have explored in this thesis. We were able to obtain azoheteroaromatic self-complementary hydrogen bond arrays, derivatives **4** and **7**. The novelty of these arrays lies in the function of the azo group as a hydrogen bond acceptor, in addition to a means of structural change in the supramolecular array by UV-Vis light irradiation. Specifically, these systems were design to form a stable **DDAAA-AAADD** array when they are present as *trans*-isomers.

Through ^1H NMR dilution experiments we observed the effect of solvent systems and the electronic influence of the substituents employed in the *trans*-dimer stability. In addition, thanks to the X-ray crystal structures of four derivatives from our first system proposed (piperidine **4a**, octyloxy **4d**, hexylthiol **4f** and *tert*-butylphenoxy **4k** derivatives) we were able to corroborate the dimer structure expected. From these dimer structures in the solid state we noted that the pyridyl nitrogen acceptor site was not optimally aligned with an amino group acceptor for a strong hydrogen bond interaction between these sites. Therefore, we changed the pyridyl ring for a methoxyphenyl group. The methoxy group *ortho*- to the azo moiety was anticipated to be closer to the amino group in the dimer

structure. Comparing derivatives **7** with **4a-p** we observed a marginal improvement in the stability of the *trans*-dimer structures in solution for the former systems; specifically in toluene-*d*₈ solution. In addition, the X-ray crystal structures of the dimers of butoxy **7c**, hexylthiol **7f**, *tert*-butylphenoxy **7k** and perfluorophenoxy **7n** confirmed intermolecular distances from the methoxy oxygen acceptor to an amino's proton shorter than those observed for the pyridyl nitrogen acceptor to the same proton in derivatives **4** dimers in the solid state.

Regarding the photophysical properties of all these azoheteroaromatic self-complementary hydrogen bond arrays, *trans*- to *cis*- photoisomerizations proceed with interconversion yields lower than 35%. The presence of *cis*-isomer in a solution of **4** or **7** induces a change in the system through the addition of two further equilibria: *cis-cis* dimerization and *trans-cis* complexation. Based on the number of hydrogen bond interactions expected in the *cis-cis* dimer, it was assumed that the stability of this dimer would be significantly lower compared with the *trans-trans* dimer and the *trans-cis* complex; therefore, the contribution of the *cis-cis* dimerization equilibrium into the species distribution was discarded. In this way, we were able to calculate the *trans-cis* complexation constants of butoxy **4c**, hexylthiol **4f**, *tert*-butylphenoxy **4k** and butoxy **7c** (the first three at 298 K and the last one at 263 K). Thanks to these complexation constants it is possible to obtain the speciation diagrams of **4c**, **4f**, **4k** and **7c** as the *cis/trans* ratio in solution changes.

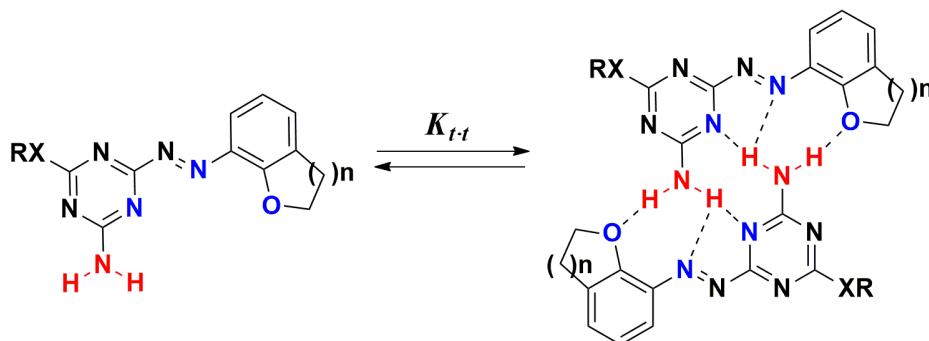
5.2 Outlook

The calculation of the *trans-cis* complexation constant (K_{t-c}) of butoxy **7c** at -10 °C was a good exercise that provided us the energetic differences between the *trans-trans* dimer and the *trans-cis* complex stabilities at low temperature. However, the impossibility to calculate this constant at room temperature is a disappointment since we are not able to compare with derivatives **4c**, **4f** and **4k** at the same temperature. For this reason, it would be interesting to attempt the calculation of K_{t-c} for **7c** at room temperature by extrapolation. This is, to calculate the *trans-cis* complexation constant of this system at different temperatures below room temperature (0, 5 and 10 °C) where the thermal reversion rate would allow the collection of a larger and reliable amount of data. Through the Van't Hoff equation (Equation 1) K_{t-c} for **7c** at 25 °C could be calculated.

$$\ln K_{t-c} = -\frac{\Delta H^0}{RT} + \frac{\Delta S^0}{R} \quad \text{Equation 1}$$

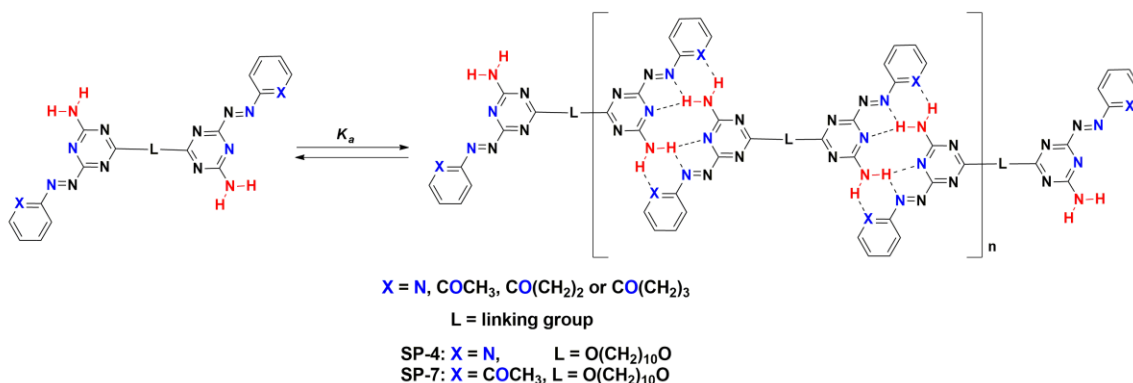
As described in Chapter 1 (Section 1.6), the preorganization of the monomeric units that participate in a supramolecular structure have a positive effect improving the molecular recognition process. In this sense, the rotational freedom of the methoxy group in **7** is an important issue to consider since it can impede the access to the oxygen acceptor atom in a hydrogen bond interaction. Therefore, the ether group *ortho*- to the azo moiety should be fixed as a cyclic ether (or ester) in order to expose the oxygen acceptor site (Scheme 5.1). A six member cyclic ether (n = 2) would be ideal considering that the ring constrains on the intermolecular distance and angle between the amino protons and the oxygen atom in the dimer structure. However, it would be also interesting to see if in a

five-member ring ether ($n = 1$) the dimer stability is improved due to preorganization regardless of the possible deviation from linearity between the interacting sites.



Scheme 5.1 Preorganized photo-isomerizable self-complementary hydrogen bond arrays ($n = 1$ or 2)

Finally, the synthesis of supramolecular polymers including these photo-isomerizable self-complementary hydrogen bond arrays would provide opportunities for further studies. As an example, the addition of these systems could be as terminal binding groups wherein the linkage could be a long chain diol (Scheme 5.2). The synthesis and characterization of the supramolecular polymers SP-4 and SP-7 in Scheme 5.1 is currently being developed in our group.



Scheme 5.2 Proposed inclusion of photo-isomerizable self-complementary hydrogen bond arrays.

Curriculum Vitae

- Name:** Iamnica Janic Linares Mendez
- Post-secondary Education and Degrees:** Universidad Autonoma de San Luis Potosi
San Luis Potosi, S.L.P, Mexico
2003-2008 B.A.
- Universidad Nacional Autonoma de Mexico
Mexico City, Mexico
2008-2010 M.A.
- The University of Western Ontario
London, Ontario, Canada
2011-2016 Ph.D.
- Honours and Awards:** Western Graduate Research Scholarship Graduate Scholarship
2011-2016
Graduate oral presentation (First Place). Organic: Advances in Molecular Recognition, CSC 2014
International Summer Science Research UASLP 2007
National Summer Research AMC 2006
- Related Work Experience:** Teaching Assistant
The University of Western Ontario
2011-2016

Conference Presentations:

- Linares, I. J.;** Pleizier, J. S.; Wisner, J. A.* Synthesis and Characterization of Photoisomerizable Self-Complementary Hydrogen Bond Arrays. 97th Canadian Chemistry Conference Exhibition, Vancouver BC – June 1-5, 2014 (Oral).
- Linares, I. J.;** Pleizier, J. S.; Wisner, J. A.* Synthesis and Characterization of Photoisomerizable Self-Complementary Hydrogen Bond Arrays. 96th Canadian Chemistry Conference Exhibition, Quebec QC – May 26-30, 2013 (Poster).
- Linares, I. J.;** Cuevas, G. E.* Design and synthesis of bisaryl bicyclic [N.M.L.] alkylketones with π - π interactions. 44^o Chemistry Mexican Congress, Puebla, Puebla – September 26-30, 2009 (Poster).